Mathematical models of influenza A virus infection: Elucidating the impact of host cell factors and defective interfering particles on virus growth

Dissertation

zur Erlangung des akademischen Grades

Doktoringenieurin

(Dr.-Ing.)

von   Tanja Laske, M. Sc.
geboren am   24. September 1988 in Magdeburg

genehmigt durch die Fakultät für Verfahrens- und Systemtechnik
der Otto-von-Guericke-Universität Magdeburg

Promotionskommission: Prof. Dr.-Ing. Kai Sundmacher
Prof. Dr.-Ing. Udo Reichl
Prof. Dr. Lars Kaderali
Dr. Ruian Ke

eingereicht am: 27. Mai 2021
Promotionskolloquium am: 16. November 2021

Auf Versuche ist mehr Gewicht zu legen als auf das Urteil der Dummheit,
welches immer Vorurteile gegen die Natur zu spinnen pflegt.

Otto von Guericke

Abstract

Influenza viruses, with the influenza A virus (IAV) being their most prominent representative, are major human pathogens that pose an ongoing burden on global public health and economics. They cause a disease of the respiratory tract, that affects up to 20 % of the global population and costs up to 650 000 lives during seasonal epidemics every year. Most importantly, the emergence of new virus variants from wild life reservoirs or by virus mutation are a continuous threat due to their potential of causing an influenza pandemic. To successfully counteract the burden related to influenza infections, we have to gain a detailed understanding of the viral life cycle and develop potent prophylactic and therapeutic strategies.

This thesis shows how mathematical models of IAV infection can improve our quantitative and mechanistic understanding of the viral life cycle at the intracellular and the cell population level. More precisely, we explore options to improve the production of influenza vaccines and novel virus-based antivirals by investigating the impact of host cell factors and defective interfering particles (DIPs) on virus growth. While the timely and sufficient supply of vaccines and antivirals is of utmost importance in the fight against influenza, we still struggle to determine and release bottlenecks that limit high yields of biopharmaceutical production processes.

The most sustainable measure to limit spread of IAV-related diseases is annual vaccination. The growing global demand for low-cost vaccines requires the establishment of high-yield production processes. Thus, the first part of this thesis addresses the question how cell culture-based vaccine production can be optimized using the option of cell line engineering. For this, novel vaccine producer cell lines can be engineered by manipulating the gene expression of host cell factors relevant for virus replication. To address this option *in silico*, we employed a deterministic intracellular model of IAV infection, previously developed by the Bioprocess Engineering (BPE) group, to identify potential bottlenecks in the viral life cycle. Model predictions indicate that steps of viral RNA synthesis, its regulation, and particle assembly and virus budding are promising targets for cell line engineering. The importance of these steps was confirmed in four of five candidate cell lines that overexpressed one selected gene. Those showed small, but reproducible changes in early dynamics of viral RNA synthesis and virus release. Model-based analysis suggests, however, that overexpression of the selected host cell factors negatively influences specific viral RNA synthesis rates. Still, virus yields were rescued by an increase in the virus release rate. Based on parameter estimations, we predicted that there is a

potential benefit associated with overexpressing multiple host cell genes in one cell line, which was validated qualitatively in experiments. Overall, this model-based study on IAV replication dynamics in engineered cell lines provides a step forward in the quantitative characterization of IAV-host cell interactions. Furthermore, it suggests targets for gene editing and indicates that overexpression of multiple host cell factors may be beneficial for the design of novel producer cell lines.

Like many other viral pathogens, IAVs can form DIPs which reduce virus production by competing with the replication of their standard virus (STV). Despite considerable efforts by many research groups, the molecular mechanisms of interference are still not fully understood. In the second part of this thesis, we, thus, aim to shed light on DIP-STV interactions using extended versions of our intracellular IAV model. In particular, we derive three models that account for different interference hypotheses speculating that DIPs have an advantage at the stages of either viral RNA replication, or its regulation, or progeny release. According to *in silico* analyses evaluating intracellular dynamics of viral genomes and proteins during various infection scenarios, we show that defective interfering RNAs (DI RNAs) with a replication advantage are the strongest antagonists of virus growth. Most intriguingly, the model accounting for this hypothesis can reproduce experimental data, obtained from yield reduction assays and studies testing different co-infection timings, without explicit model fitting. This can be related to the strong competition of those DI RNAs for viral resources needed to form replication-competent genomes. In contrast, DI RNAs that hijack either regulatory steps of the viral life cycle or viral progeny release, interfere less efficiently with STV growth. Nonetheless, comparing simulations for the growth of DIPs with a deletion in different genome segments suggests that DI RNAs derived from polymerase-encoding genes are more competitive than others, independent of their mode of interference. However, for DI RNAs derived from other segments, the interference at stages of RNA synthesis regulation and virus release can even compromise DIP growth. These investigations, thus, help to elucidate the interference mechanisms of DI RNAs and provide novel hypotheses on why certain DI RNAs are more abundant in virus preparations. Furthermore, the various *in silico* results presented here can contribute to the design of future experiments that allow to discriminate DI RNAs with different modes of interference.

In case of DIPs, an improved understanding of their molecular growth mechanisms can directly contribute to the development of novel antiviral agents. In particular, the characteristics related to the reduction in STV yields and induction of the immune response related to DIP co-infection open exciting possibilities in both the clinical and bioprocessing research areas. Previous studies of the BPE group have shown that DIPs hamper optimization of vaccine production in continuous cultures of IAV by

inducing periodic drops in viral titers. However, by performing *in silico* experiments with a simple within-host model, we did not find an economically reasonable option to revert losses in productivity related to DIP growth. Nonetheless, such continuous cultivation systems allow to evaluate STV and DIP replication dynamics over extended time periods. In particular, we used a novel continuous cultivation system, that enables head-to-head comparisons of virus growth at different experimental conditions, to determine characteristics of DIP co-infection related to different residence times of the bioprocess. For this, we extended the within-host model with respect to the obtained experimental data, which allowed interesting insights into crucial infection parameters. For instance, modeling suggests that both STV inactivation and virus degradation have to be taken into account to achieve good agreement of model simulations with the experimental data for the longer of the two residence times. Most intriguingly, we found that only by accounting for STV- and DIP-specific infection rates, the model is able describe the virus growth dynamics reasonably well. Hence, although we did not find a cost-effective way to diminish DIP-induced oscillations in viral titers, continuous production systems represent a valuable tool for model-aided investigations on DIP growth on longer time scales. This can be highly relevant in making informed predictions on DIP-associated virus evolution and pathogenicity of IAVs.

Together, mathematical models and simulation approaches presented in this thesis provide valuable insights into factors that represent significant bottlenecks during production of viral biopharmaceuticals needed in the fight against influenza infections. In particular, the intracellular models employed to study the impact of selected host cell factors and DIPs are indispensable in formulating future research questions. Even though we still lack a comprehensive picture of the IAV life cylce, modeling made a significant contribution in providing a step forward in the quantitative characterization of both virus-host cell as well as DIP-STV interactions.

Zusammenfassung

Influenzaviren, mit dem Influenza-A-virus (IAV) als prominentestem Vertreter, sind relevante menschliche Krankheitserreger, die eine fortwährende Belastung für die globale öffentliche Gesundheit und Wirtschaft darstellen. Sie verursachen eine Erkrankung der Atemwege, auch bekannt als Virusgrippe, die jährlich bis zu 20 % der Weltbevölkerung betrifft und während saisonaler Epidemien bis zu 650 000 Leben fordert. Vor allem das Auftauchen neuer Virusvarianten aus Wildtierreservoiren oder durch Virusmutationen ist eine ständige Bedrohung, da diese eine Influenza-Pandemie auslösen können. Um der Bedrohung durch Influenza-Infektionen erfolgreich entgegenzuwirken, müssen wir ein detailliertes Verständnis des viralen Lebenszyklus gewinnen, welches die Entwicklung wirksamer antiviraler Strategien vorantreiben kann.

Diese Doktorarbeit zeigt, wie mathematische Modelle der IAV-Infektion unser quantitatives und mechanistisches Verständnis des viralen Lebenszykluses auf der intrazellulären und der Zellpopulationsebene verbessern können. Genauer gesagt erforschen wir Möglichkeiten zur Verbesserung der Produktion von Influenza-Impfstoffen und neuartigen Virus-basierten antiviralen Wirkstoffen, indem wir den Einfluss von Wirtszellfaktoren und defekten Viruspartikeln (DIPs) auf das Viruswachstum untersuchen. Während die rechtzeitige und ausreichende Versorgung mit Impfstoffen und antiviralen Mitteln im Kampf gegen die Virusgrippe von größter Bedeutung ist, gibt es noch nennenswerte Limitationen in deren Herstellungsprozessen, die dringend ermittelt und beseitigt werden müssen, um die Produktausbeuten zu steigern.

Die nachhaltigste Maßnahme zur Eindämmung von IAV-bedingten Krankheiten ist die jährliche Impfung. Die wachsende globale Nachfrage nach kostengünstigen Impfstoffen erfordert die Etablierung von Produktionsprozessen mit hoher Ausbeute. Der erste Teil dieser Arbeit beschäftigt sich deshalb mit der Frage, wie die Zellkultur-basierte Impfstoffproduktion durch gezielte genetische Modifikation der Produktionszelllinien gesteigert werden kann. Dabei soll in den Zelllinien die Expression solcher Gene manipuliert werden, welche einen signifikanten Einfluss auf die Virusreplikation haben. Um diese Option *in silico* zu testen, verwenden wir ein deterministisches intrazelluläres Modell der IAV-Infektion, das zuvor von der BPE-Gruppe entwickelt wurde, um mögliche Engpässe im viralen Lebenszyklus zu identifizieren. Modellvorhersagen deuten darauf hin, dass die Schritte der viralen RNA-Synthese, deren Regulation sowie der Freisetzung von Tochterviren vielversprechende Ziele für die Genmanipulation der Zelllinien darstellen. Die Bedeutung dieser Schritte wurde in vier von fünf Kandidaten-Zelllinien bestätigt,

die jeweils ein ausgewähltes Gen überexprimierten. Diese zeigten kleine, aber reproduzierbare Veränderungen in der frühen Dynamik der RNA-Synthese und der Virusfreisetzung. Eine Modell-basierte Analyse deutete jedoch darauf hin, dass die Überexpression der ausgewählten Wirtszellfaktoren die spezifischen RNA-Syntheseraten negativ beeinflusste. Dennoch konnten die Virusausbeuten durch eine Erhöhung der Virusfreisetzungsrate mindestens auf das Niveau der parentalen Zelllinie, also der Zelllinie ohne Genmodifikation, gebracht werden. Basierend auf Parameterschätzungen konnten wir des Weiteren vorhersagen, dass es einen potenziellen Vorteil für die Virusproduktion geben könnte, wenn in einer Zelllinie mehrere Wirtszellfaktoren gleichzeitig überexprimiert werden, was in Experimenten qualitativ validiert wurde. Insgesamt stellt diese Modell-basierte Studie zur IAV-Replikation in Zelllinien mit Genmanipulationen einen Fortschritt in der quantitativen Charakterisierung von IAV-Wirtszell-Interaktionen dar. Darüber hinaus schlägt sie limitierende Schritte im Replikationszyklus vor, welche mittels genetischer Manipulation der Produktionszelllinie überwunden werden könnten, und zeigt, dass die Überexpression mehrerer Wirtszellfaktoren für das Design neuartiger Produktionszelllinie von Vorteil sein kann.

Wie viele andere virale Pathogene können IAVs DIPs bilden, welche mit der Replikation ihres Wildtyp-Virus (STV) konkurrieren und damit die Virusproduktion reduzieren. Trotz erheblicher Anstrengungen vieler Forschergruppen ist der molekulare Mechanismus dieser Interferenz noch weitgehend ungeklärt. Im zweiten Teil dieser Arbeit versuchen wir deshalb, die DIP-STV-Interaktionen mit Hilfe erweiterter Versionen unseres intrazellulären IAV-Modells zu untersuchen. Insbesondere leiten wir drei Modelle her, die verschiedene Interferenzhypothesen berücksichtigen, die beispielsweise darüber spekulieren, dass DIPs entweder bei den Schritten der RNA-Replikation, deren Regulation oder der Freisetzung von defekten Tochterviren einen Vorteil haben. Anhand von *in silico*-Analysen, welche die intrazelluläre Dynamik von viralen Genomen und Proteinen während verschiedener Infektionsszenarien auswerten, zeigen wir, dass DIPs mit einem Replikationsvorteil die stärksten Antagonisten des Viruswachstums sind. Insbesondere kann das Modell, das diese Hypothese berücksichtigt, Ergebnisse experimenteller Studien reproduzieren, welche die Reduktion der Virusausbeute sowie des Einflusses des Zeitpunkts der Ko-Infektion untersuchen, ohne das explizite Parameteranpassungen nötig sind. Dies kann mit der starken Konkurrenzfähigkeit dieser DIPs erklärt werden, wodurch virale Ressourcen, die zur Bildung replikationskompetenter Genome benötigt werden, sehr schnell verbraucht werden. Im Gegensatz dazu stören DIPs das STV-Wachstum weniger effizient, wenn sie einen Vorteil in regulatorischen Schritten des viralen Lebenszyklus und bei der Freisetzung von Tochterviren haben. Der Vergleich von Simulationen für das Wachstum von DIPs mit einer Deletion in verschiedenen Genomsegmenten

deutet des Weiteren darauf hin, dass defekte virale Genome (DI RNAs), die von Polymerase-kodierenden Genen abstammen, konkurrenzfähiger sind als andere, was unabhängig von der Art des Interferenzmechanismus ist. Im Gegensatz dazu, kann es für DI RNAs, die von anderen Segmenten abstammen, sogar nachteilig sein, wenn diese mit der Regulation der RNA-Synthese oder der Virusfreisetzung interferieren. Unsere Untersuchungen helfen folglich dabei, die Interferenzmechanismen von DI RNAs aufzuklären und neue Hypothesen darüber zu formulieren, warum bestimmte DI RNAs in Viruspräparaten häufiger vorkommen als andere. Darüber hinaus können die verschiedenen hier vorgestellten *in silico*-Ergebnisse zum Design zukünftiger Experimente beitragen, die es erlauben, DI RNAs mit unterschiedlichen Interferenzmechanismen zu unterscheiden.

In Bezug auf DIPs trägt ein verbessertes Verständnis ihrer molekularen Wachstumsmechanismen direkt zur Entwicklung verbesserter antiviraler Wirkstoffe bei. Insbesondere eröffnen die Eigenschaften der DIPs, die mit der Reduzierung der STV-Ausbeute und der Induktion der Immunantwort im Zusammenhang stehen, spannende Möglichkeiten in der klinischen und der biotechnologischen Forschung. Frühere Studien der BPE-Gruppe haben gezeigt, dass DIPs die Optimierung der Impfstoffproduktion in kontinuierlichen Kulturen von IAV behindern, indem sie periodische Oszillationen im Virustiter induzieren. Bei der Durchführung von *in silico*-Experimenten mit einem einfachen Zellpopulations-Modell fanden wir jedoch keine wirtschaftlich sinnvolle Option, um Produktivitätsverluste im Zusammenhang mit dem DIP-Wachstum zu verhindern. Darüber hinaus wurden Daten aus einem neuen kontinuierlichen Kultivierungssystem untersucht, das direkte Vergleiche der STV- und DIP-Replikationsdynamik über längere Zeiträume ermöglicht, um verschiedene Charakteristika der DIP-Ko-Infektion in Bezug auf die Verweilzeit des Produktionsprozesses zu bestimmen. Hierfür haben wir das Zellpopulations-Modell im Hinblick auf die neuen experimentellen Daten erweitert, was interessante Einblicke in entscheidende Infektionsparameter ermöglichte. Die Modellierung legt zum Beispiel nahe, dass sowohl die STV-Inaktivierung als auch die Degradation von Viren berücksichtigt werden müssen, um eine gute Übereinstimmung der Modellsimulationen mit den experimentellen Daten für die längere der beiden Verweilzeiten zu erreichen. Besonders interessant ist, dass das Modell nur durch die Berücksichtigung von STV- und DIP-spezifischen Infektionsraten in der Lage ist, die Dynamik der Virusreplikation korrekt wiederzugeben. Obwohl wir also keinen kosteneffektiven Weg gefunden haben, um DIP-induzierte Oszillationen in den Viruskonzentrationen zu verringern, stellen kontinuierliche Produktionssysteme ein wertvolles Werkzeug für Modell-gestützte Untersuchungen zum DIP-Wachstum über einen längeren Zeitraum dar. Dies ist

höchstrelevant, um fundierte Vorhersagen über die DIP-assoziierte Evolution und Pathogenität von IAVs zu treffen.

Zusammengenommen liefern die in dieser Arbeit vorgestellten mathematischen Modelle und Simulationsansätze wertvolle Einblicke in Faktoren, die signifikante Limitationen bei der Produktion von viralen Biopharmazeutika darstellen, die dringend im Kampf gegen Influenza-Infektionen benötigt werden. Insbesondere die intrazellulären Modelle, mit denen der Einfluss ausgewählter Wirtszellfaktoren und DIPs auf das Viruswachstum untersucht wurde, sind für die Formulierung zukünftiger Forschungsfragen unerlässlich. Auch wenn uns noch ein umfassendes Bild des IAV-Lebenszyklus fehlt, hat die Modellierung einen wesentlichen Beitrag zur quantitativen Charakterisierung sowohl der Virus-Wirtszell- als auch der DIP-STV-Interaktionen geleistet.

Contents

List of Abbreviations

BPE	Bioprocess Engineering
CB	cell bioreactor
CHX	cycloheximide
CRM1	chromosome region maintenance 1 protein
cRNA	complementary RNA
cRNP	complementary ribonucleoprotein
COVID-19	coronavirus disease 2019
DDE	delay differential equation
DI	defective interfering
DI RNA	defective interfering RNA
DIP	defective interfering particle
ER	endoplasmic reticulum
FACS	fluorescence-activated cell sorting
FI	fluorescence intensity
FL	full-length
FM	fresh medium reservoir
HA	hemagglutinin
HBV	hepatitis B virus
HCV	hepatitis C virus
HIV	human immunodeficiency virus
IAV	influenza A virus
IFN	interferon
IRF7	interferon regulatory factor 7
M1	matrix protein 1
M2	matrix protein 2
MDCK	Madin-Darby Canine Kidney
MGO	cell lines overexpressing multiple host cell genes
MOI	multiplicity of infection
MODIP	multiplicity of DIPs
mRNA	messenger RNA
MVA	modified Vaccinia virus Ankara
mvRNA	mini viral RNA
NA	neuraminidase
NEP	nuclear export protein
NIP	non-infectious particle
NLS	nuclear localization signal
NP	nucleoprotein
NS1	non-structural protein 1
ODE	ordinary differential equation
OP7	over-proportional segment 7
PA	polymerase acidic protein
PB1	polymerase basic protein 1
PB2	polymerase basic protein 2
Pol II	cellular RNA polymerase II
p.i.	post infection
RAB11	Ras-related protein Rab-11

RdRp	RNA-dependent RNA polymerase
RNA	ribonucleic acid
RNAi	RNA interference
RNP	ribonucleoprotein
RT	residence time
RT-qPCR	quantitative reverse transcription polymerase chain reaction
S1	segment 1
S3	segment 3
S4	segment 4
S5	segment 5
S6	segment 6
S7	segment 7
S8	segment 8
SGO	cell lines overexpressing a single host cell gene
SSR	sum of squared residuals
STV	standard virus
STY	space-time yield
svRNA	small viral RNA
TCID$_{50}$	50 % tissue culture infective dose
TIP	therapeutic interfering particle
VB	virus bioreactor
vRNA	viral RNA
vRNP	viral ribonucleoprotein
VSV	vesicular stomatitis virus

List of Symbols

Symbol	Unit	Description
α	–	significance level
δ	h^{-1}	death rate of infected cells
θ	–	parameter vector
λ	cells/(ml $\cdot$ h)	cell growth (supply) rate
μ	h^{-1}	specific growth rate of target cells
σ_i	–	standard deviation of measurement at time point i
σ_s	–	maximum value of species s
$\sigma_{s,c}$	–	standard deviation of species s at condition c
σ_Y	–	standard deviation of quantity Y
B_{hi}	sites	number of free high-affinity binding sites
B_{lo}	sites	number of free low-affinity binding sites
$B_{\mathrm{hi}}^{\mathrm{tot}}$	sites	total number of high-affinity binding sites
$B_{\mathrm{lo}}^{\mathrm{tot}}$	sites	total number of low-affinity binding sites
c	h^{-1}	virus clearance rate
C_{Ery}	cells/ml	concentration of erythrocytes
C_{V}	virions/ml	concentration of virus particles
Cp	molecules/cell	number of (nuclear) cRNPs
Cp_{k}	molecules/cell	number of (nuclear) cRNPs of segment k
d	h^{-1}	cell death rate
D	h^{-1}	dilution rate of the virus bioreactor
$D_{\mathrm{hi}}^{\mathrm{Att}}$	virions/cell	DIPs attached to B_{hi}
$D_{\mathrm{lo}}^{\mathrm{Att}}$	virions/cell	DIPs attached to B_{lo}
D_{Rib}	nucleotides	distance between two adjacent ribosomes on an mRNA
D^{cyt}	molecules/cell	defective complex of parental vRNPs in the cytoplasm
$D_{\mathrm{Cplx}}^{\mathrm{cyt}}$	molecules/cell	defective complex of progeny vRNPs in the cytoplasm
D^{En}	virions/cell	number of DIPs in endosomes
D^{Ex}	virions/cell	number of DIPs in extracellular medium
D^{Rel}	virions/cell	number of progeny DIPs
f	–	fraction of DIPs produced by an STV-infected cell
F_{Adv}	–	growth advantage of a DI RNA
F_{CB}	ml/h	flow rate from CB to VB
F_{Fus}	–	fraction of fusion-competent virions
F_{FM}	ml/h	flow rate from FM to VB
F_{H}	ml/h	harvest flow rate
F_{Inf}	cells/virion	infection efficiency

Symbol	Unit	Description
F_{Spl_7}	–	fraction of M2-encoding mRNAs
F_{Spl_8}	–	fraction of NEP-encoding mRNAs
$frac_{\mathrm{Int}}^{\mathrm{nuc}}$	%	relative fluorescence intensity of the nucleus
$frac_{\mathrm{Rnp}}^{\mathrm{nuc}}$	%	fraction of nuclear vRNPs
I	cells/ml	concentration of infected cells
I_{c}	cells/ml	concentration of coinfected cells
I_{d}	cells/ml	concentration of DIP-infected cells
I_{s}	cells/ml	concentration of STV-infected cells
j	–	$\in \{\mathrm{PB2, PB1, PA, RdRp, HA, NP, NA, M1, M2, NEP}\}$
K_{i}	molecules	inhibitor dissociation constant
K_{VRel}	virions	influence of protein concentration on virus release
k^{Apo}	h^{-1}	apoptosis rate of infected cells
$k_{\mathrm{hi}}^{\mathrm{Att}}$	$(\mathrm{site} \cdot \mathrm{h})^{-1}$	attachment rate to high-affinity binding sites
$k_{\mathrm{lo}}^{\mathrm{Att}}$	$(\mathrm{site} \cdot \mathrm{h})^{-1}$	attachment rate to low-affinity binding sites
$k_{\mathrm{M1}}^{\mathrm{Bind}}$	$(\mathrm{molecule} \cdot \mathrm{h})^{-1}$	binding rate of M1 to nuclear vRNPs
$k_{\mathrm{NP}}^{\mathrm{Bind}}$	$(\mathrm{molecule} \cdot \mathrm{h})^{-1}$	binding rate of NP to RdRp-RNA complexes
$k_{\mathrm{RdRp}}^{\mathrm{Bind}}$	$(\mathrm{molecule} \cdot \mathrm{h})^{-1}$	binding rate of RdRp complexes to vRNA/cRNA
k^{Cplx}	$\mathrm{molecule}^{-7} \cdot \mathrm{h}^{-1}$	formation rate of complexes containing eight vRNPs
$k_{\mathrm{En}}^{\mathrm{Deg}}$	h^{-1}	degradation rate of virions in lysosomes
$k_{\mathrm{M}}^{\mathrm{Deg}}$	h^{-1}	degradation rate of mRNAs
$k_{\mathrm{R}}^{\mathrm{Deg}}$	h^{-1}	degradation rate of naked cRNA/vRNA
$k_{\mathrm{Rnp}}^{\mathrm{Deg}}$	h^{-1}	degradation rate of RNPs
$k_{\mathrm{RRdRp}}^{\mathrm{Deg}}$	h^{-1}	degradation rate of RdRp-RNA complexes
$k_{\mathrm{V}}^{\mathrm{Deg}}$	h^{-1}	degradation rate of infectious virions
$k_{\mathrm{Vs}}^{\mathrm{Deg}}$	h^{-1}	degradation rate of STVs
$k_{\mathrm{hi}}^{\mathrm{Dis}}$	h^{-1}	detachment rate from high-affinity binding sites
$k_{\mathrm{lo}}^{\mathrm{Dis}}$	h^{-1}	detachment rate from low-affinity binding sites
k^{En}	h^{-1}	endocytosis rate
$k_{\mathrm{hi}}^{\mathrm{Eq}}$	site^{-1}	equilibrium constant of high-affinity binding sites
$k_{\mathrm{lo}}^{\mathrm{Eq}}$	site^{-1}	equilibrium constant of low-affinity binding sites
k^{Exp}	$(\mathrm{molecule} \cdot \mathrm{h})^{-1}$	rate of NEP binding and nuclear export
k^{Fus}	h^{-1}	fusion rate
k^{Imp}	h^{-1}	nuclear import rate
k^{Inf}	$\mathrm{ml}/(\mathrm{virion} \cdot \mathrm{h})$	virus infection rate
$k_{\mathrm{D}}^{\mathrm{Inf}}$	$\mathrm{ml}/(\mathrm{virion} \cdot \mathrm{h})$	DIP infection rate
$k_{\mathrm{S}}^{\mathrm{Inf}}$	$\mathrm{ml}/(\mathrm{virion} \cdot \mathrm{h})$	STV infection rate
k^{Prod}	$\mathrm{virions}/(\mathrm{cell} \cdot \mathrm{h})$	virus production rate
$k_{\mathrm{Vs}}^{\mathrm{Prod}}$	$\mathrm{virions}/(\mathrm{cell} \cdot \mathrm{h})$	production rate of STVs by I_{s}
$k_{\mathrm{Vd}}^{\mathrm{Prod,Ic}}$	$\mathrm{virions}/(\mathrm{cell} \cdot \mathrm{h})$	production rate of DIPs by I_{c}
$k_{\mathrm{Vd}}^{\mathrm{Prod,Is}}$	$\mathrm{virions}/(\mathrm{cell} \cdot \mathrm{h})$	*de novo* production rate of DIPs by I_{s}
$k_{\mathrm{V_{Ni}}}^{\mathrm{Prod,Ic}}$	$\mathrm{virions}/(\mathrm{cell} \cdot \mathrm{h})$	production rate of NIPs by I_{c}

Symbol	Unit	Description
$k_{V_{Ni}}^{\text{Prod,Is}}$	virions/(cell · h)	production rate of NIPs by I_s
k^{RdRp}	molecules^{-2} · h^{-1}	formation rate of polymerase complexes
k^{Rel}	virions/(molecule · h)	virus (or STV) release rate
$k_{\max}^{\text{Rel}}$	virions/(cell · h)	maximum virus release rate
$k_{\text{C}}^{\text{Syn}}$	h^{-1}	cRNA synthesis rate
$k_{\text{M}}^{\text{Syn}}$	nucleotides/h	mRNA synthesis rate
$k_{\text{P}}^{\text{Syn}}$	nucleotides/h	protein synthesis rate
$k_{\text{V}}^{\text{Syn}}$	h^{-1}	vRNA synthesis rate
L_k	nucleotides	length of the mRNA of segment k
L^{V}	nucleotides	average length of a vRNA
L_k^{V}	nucleotides	length of the vRNA of segment k
$M(\gamma)$	–	characteristic of the system output γ
MOI	virions/cell	multiplicity of infection
N_c	–	number of experimental c conditions
N_{P_j}	molecules/virion	number of proteins of type j in a virus particle
N_s	–	number of measured species s
N_t	–	number of measured time points
$N_{\text{M1}}^{\text{Nuc}}$	nucleotides	number of nucleotides bound by on M1 molecule
$N_{\text{NEP}}^{\text{Nuc}}$	nucleotides	number of nucleotides bound by on NEP molecule
$N_{\text{NP}}^{\text{Nuc}}$	nucleotides	number of nucleotides bound by on NP molecule
$\bar{p}$	–	mean parameter value
P_j	molecules/cell	number of proteins of type j
R^{C}	molecules/cell	number of naked cRNAs
R_k^{C}	molecules/cell	number of naked cRNAs of segment k
$R_{\text{RdRp}}^{\text{C}}$	molecules/cell	number of RdRp-cRNA complexes
$R_{\text{RdRp},k}^{\text{C}}$	molecules/cell	number of RdRp-cRNA complexes of segment k
$R_{\text{tot}}^{\text{C}}$	molecules/cell	total number of cRNAs in a cell
R_k^{M}	molecules/cell	number of mRNA of segment k
r^{Rel}	virions/(cell · h)	virus (or STV) release rate
$r_{\text{D}}^{\text{Rel}}$	virions/(cell · h)	DIP release rate
R^{V}	molecules/cell	number of naked vRNAs
R_k^{V}	molecules/cell	number of naked vRNAs of segment k
$R_{\text{RdRp}}^{\text{V}}$	molecules/cell	number of RdRp-vRNA complexes
$R_{\text{RdRp},k}^{\text{V}}$	molecules/cell	number of RdRp-vRNA complexes of segment k
$R_{\text{tot}}^{\text{V}}$	molecules/cell	total number of vRNAs in a cell
$R_{\text{tot}}^{\text{V}}$	molecules/cell	total number of vRNAs of segment k in a cell
$R_{\text{DIP/STV}}$	–	DIP-to-STV ratio
Rnp^{cyt}	molecules/cell	total number of vRNPs in the cytoplasm
Rnp^{nuc}	molecules/cell	total number of vRNPs in the nucleus
RT	h	residence time
S_{θ}^M	–	sensitivity coefficient

Symbol	Unit	Description
STY	virions/(ml $\cdot$ h)	space-time yield
t	h	time
T	cells/ml	concentration of uninfected target cells
T_0	cells/ml	initial target cell concentration
T_{CB}	cells/ml	target cell concentration in the CB
T_{in}	cells/ml	target cell concentration in the feed
V	virions/ml	concentration of virus particles
$V_{\mathrm{hi}}^{\mathrm{Att}}$	virions/cell	virions (or STVs) attached to B_{hi}
$V_{\mathrm{lo}}^{\mathrm{Att}}$	virions/cell	virions (or STVs) attached to B_{lo}
V_{d}	virions/ml	concentration of DIPs
V_{d0}	virions/ml	initial concentration of DIPs
V_{Ni}	virions/ml	concentration of NIPs
V_{Ni0}	virions/ml	initial concentration of NIPs
V_{s}	virions/ml	concentration of STVs
V_{s0}	virions/ml	initial concentration of STVs
V_{total}	virions/ml	number of total virus particles
V_{VB}	ml	working volume of VB
V^{cyt}	molecules/cell	complex of eight parental vRNPs in the cytoplasm
$V_{\mathrm{Cplx}}^{\mathrm{cyt}}$	molecules/cell	complex of eight progeny vRNPs in the cytoplasm
V^{En}	virions/cell	number of virions (or STVs) in endosomes
V^{Ex}	virions/cell	number of virions (or STVs) in extracellular medium
V^{Rel}	virions/cell	number of progeny virions (or STVs)
Vp^{cyt}	molecules/cell	number of cytoplasmic vRNPs
$Vp_{\mathrm{k}}^{\mathrm{cyt}}$	molecules/cell	number of cytoplasmic vRNPs of segment k
$Vp_{\mathrm{M1}}^{\mathrm{cyt}}$	molecules/cell	number of cytoplasmic M1-NEP-vRNP complexes
$Vp_{\mathrm{M1,k}}^{\mathrm{cyt}}$	molecules/cell	cytoplasmic M1-NEP-vRNP complexes of segment k
Vp^{nuc}	molecules/cell	number of nuclear vRNPs
$Vp_{\mathrm{k}}^{\mathrm{nuc}}$	molecules/cell	number of nuclear vRNPs of segment k
$Vp_{\mathrm{M1}}^{\mathrm{nuc}}$	molecules/cell	number of nuclear M1-vRNP complexes
$Vp_{\mathrm{M1,k}}^{\mathrm{nuc}}$	molecules/cell	nuclear M1-vRNP complexes of segment k
x_i	–	measurement value at time point t_i
y	–	vector of experimental observations
$y_{s,c}$	–	model output of species s at condition c
$y_{s,c}^D$	–	measurement of species s at condition c
Z	–	Gauss test statistic

Chapter 1

Introduction

Before the COVID-19 pandemic, the greatest pandemic potential was expected from influenza viruses. With global lock-downs, including social distancing and restrictions in traveling, the number of reported influenza cases was below baseline in the season of 2020/2021 [1]. However, usually, influenza viruses represent a significant threat to public health and economics by infecting up to 20 % of the global population in annual epidemics, which results in 3–5 million severe cases of disease and 290 000–650 000 deaths each year [2, 3]. Influenza viruses have a broad host tropism and a highly variable genome, allowing them to evade the host immune response and cross species barriers. This continuous evolution of the virus enables re-infection of the same host and fosters the emergence of new virus variants with the potential to cause the next influenza pandemic.

Influenza viruses are obligate intracellular parasites and their natural reservoir are wild aquatic birds. Besides poultry, influenza viruses can also infect many other host species, such as pigs, horses and dogs [3, 4]. Hence, the virus can spread through migratory birds that may infect domestic animals which are in close contact to humans. In particular, influenza viruses cause a contagious disease of the upper respiratory tract in humans, which causes symptoms such as head- and body ache, rhinitis, cough and high fever. In immune-competent individuals, seasonal virus strains cause a mild infection which is cleared within one or two weeks. However, more severe infections can reach the lower respiratory tract causing pneumonia, which might be further accompanied by bacterial or other airborne viral infections. In particular, risk groups, such as the very young and the elderly, pregnant women and those with a compromised immune system or other co-morbidity, are prone to develop the most severe infections.

Together with the most devastating influenza pandemic of 1918, which cost about 50 million lives worldwide [5], five noticeable pandemic outbreaks of influenza occurred in past 100 years, most recently in 2009 [3, 6]. Thus, the emergence of a pandemic virus strain is expected regularly, and was estimated to occur on average every 50 to 60 years [7]. Normally prevalent influenza virus strains circulate for several years, such that the human population acquires strain-specific adaptive immunity, which can prevent infection or, at least, decrease severity of the disease. In contrast, pandemic viruses are antigenically different and, thus, spread rapidly through the immunological naïve population. This results in increased numbers of hospitalizations and severe cases of disease. To save lives,

antiviral drugs can be administered that support viral clearance. However, influenza viruses can acquire drug-resistance through mutations, rendering the antiviral ineffective. Thus, the most efficient and sustainable way to avoid spreading of influenza is to induce adaptive immunity by vaccination. Since the prevalence of the circulating virus strains changes over the time, optimal protection is only guaranteed by repeated annual vaccinations. For this, the composition of influenza vaccines is updated every year according to recommendations by the World Health Organization. To meet the related growing global demand for influenza vaccines and, furthermore, guarantee a sufficient and timely supply of vaccines during a pandemic, efficient and reliable vaccine production processes are required. Accordingly, cell culture-based vaccine production systems are becoming increasingly important and represent a valuable alternative to conventional egg-based production systems.

To improve both, preventive and therapeutic treatment of influenza, we need a profound knowledge and deep understanding of virus replication mechanisms and the virus-host cell interactions on the molecular level. Since the virus encodes only a few proteins, it heavily relies on the infected host cell to provide resources and the cellular biosynthetic machinery to support virus growth. This dependency represents the Achilles heel of the virus. Thus, multiple research studies striving to identify relevant host factors, for instance, by genome-wide RNA interference (RNAi) screening, were conducted in recent years [8, 9]. Originally, those studies aim to identify cellular targets for novel antiviral treatment strategies that avoid the emergence of drug-resistant virus strains [10]. Likewise, the knowledge on relevant host cell factors also harbors the potential of improving cell culture-based vaccine production processes. For this, we anticipate that certain host cell factors are limiting the maximum number of virions released from a cell. This hypothesis is based on previous investigations showing that only a small fraction of available cellular resources is required for the production of progeny virions [11]. In addition, significant intracellular concentrations of viral components, such as viral genomes, are detectable at time points when virus release is already decreasing [12]. This indicates that producer cell lines would be capable of releasing significantly higher amounts of virus. Thus, the identification of crucial host cell factors that control virus growth provides a promising option to improve vaccine production processes. For instance, it would be interesting to test whether the expression of such key factors could be manipulated by cell line engineering in order to release cellular bottlenecks. Moreover, other factors can influence the productivity of the viral life cycle. One of them is provided by the virus itself in form of predatory viral sub-populations that originate as natural byproducts of virus replication. In particular, viral deletion mutants, i.e., DIPs, act as competitive inhibitors during virus replication, which can decrease viral yields significantly [13]. Likewise, DIPs

hamper process optimization by inducing oscillations in virus concentrations obtained during continuous cultures of infected producer cells [14]. However, please note, that DIPs might represent a biopharmaceutical product themselves. Since they limit viral spread, they can potentially serve as a novel antiviral agent [15]. To either reduce the impact of DIPs on vaccine production or provide process conditions in support of DIP growth requires a detailed understanding of their replication and how their interfere with the growth of their parental virus.

The major challenge in addressing research questions, such as outlined above, is the complexity of virus-host cell systems. While increasing amounts of data hold the promise of providing increased understanding of such complex biological systems, we need to translate measurements into robust mechanistic knowledge that allows to predict the behavior of such systems. For this, the discipline of computational systems biology provides means to describe and simulate complex biological systems with the help of mathematical models. In particular, infection research has benefited from virus dynamics modeling, which, for instance, helped to inform decision making in public health by describing viral spread in host populations [16, 17]. Furthermore, principles applied by within-host infection models can also be used to describe virus production in cell culture-based bioprocesses and suggest strategies for process optimization. However, we strive to not only describe the spread of viruses in cell cultures, but to understand virus production in the smallest unit of the infection cycle, i.e., a single infected cell. For this, the BPE group has developed strikingly detailed descriptions of the intracellular viral life cycle in influenza virus-infected cell cultures, which elucidated important regulatory mechanisms of virus replication [11, 18].

In order to explore options for the optimization of virus production processes, this thesis aims to elucidate the impact of host cell factors and DIPs on virus growth by employing different single-cell and within-host models of influenza virus infection. For this, we use the single-cell model previously developed by the BPE group [18] to identify bottlenecks in virus replication that could be targeted by cell line engineering to increase virus yields. Furthermore, we inform the model on the impact of selected host cell factors on virus growth and develop simulation approaches that allow to predict the production phenotype of novel engineered cell lines. In addition, we use the single-cell model to predict *in silico* how DIPs influence virus replication. For this, we implement different hypotheses on DIP interference into the intracellular model and test them with respect to virus release measurements reported in literature. Finally, we translate the mechanism of interference to a within-host model describing DIP co-infection that allows to capture the dynamics of virus concentrations in continuous vaccine production processes. Further model analyses enable us to evaluate options for process manipulation and discuss the

suitability of such processes to either produce vaccines or DIP-based biopharmaceuticals.

    This introduction is followed by a literature review of influenza viruses, viral vaccine production and on mathematical models of virus infection (Chapter 2). Subsequently, we describe the model and simulation approaches employed to investigate the impact of selected host cell factors and DIPs on virus replication on the intracellular and cell population level (Chapter 3). We, then, present the results of our model-based investigations on intracellular virus replication, which are followed by the within-host modeling results that solely focus on DIP growth during continuous virus cultivation (Chapter 4). Conclusions and outlook of this thesis are given in Chapter 5 and Chapter 6, respectively.

CHAPTER 2

Theoretical Background

This chapter introduces important aspects of influenza viruses and the molecular mechanisms of their replication as well as their DIPs. To motivate the optimization of animal cell culture processes for the production of virus-based biopharmaceuticals, we will provide a brief summary of virus production systems. Finally, we will give an overview on mathematical modeling of virus dynamics and theories applied for model construction and analysis.

2.1. Influenza A virus infection

Influenza viruses are obligate intracellular parasites and require a host cell to replicate their genome and form progeny virus particles. They are member of the *Orthomyxoviridae* family and are classified as either type A, B, C, or the recently identified type D (reviewed in [3, 19, 20]). In humans, mainly infections with the viruses of type A and B cause an infectious respiratory disease, named influenza or the common flu, that spreads in seasonal epidemics and, occasionally, leads to pandemic outbreaks. In particular, strains of IAV were responsible for the pandemic outbreaks of the last century and, thus, will be the main focus of this thesis.

2.1.1. Virus structure and morphology

IAVs are enveloped viruses that contain eight, negative-sense, single-stranded viral RNA (vRNA) gene segments. Their wide host tropism is related to the variability of their surface glycoproteins hemagglutinin (HA) and neuraminidase (NA), which are also used to distinguish different IAV strains. Each strain receives a unique name according to a systematic nomenclature using virus type, species from which the virus was isolated (if non-human), location of isolation, number of the isolate, year of the isolation, and subtype of HA and NA. For instance, the reference strain A/PR/8/34 (H1N1), widely used in research and process development, is the isolate number 8 of a human IAV isolated in Puerto Rico in 1934 that possesses both HA and NA of subtype 1. While there are 18 HA and 11 NA known subtypes that allow numerous possible subtype combinations, the H1N1, H2N2 and H3N2 subtypes of IAVs have consistently established in humans

and also caused the influenza pandemics of the last century (reviewed in [3, 20]). The following paragraphs will give an overview on the structural characteristics of IAVs.

Virion and genome structure   Morphologically, IAVs appear either as spherical particles with an average diameter of about 100 nm, or as filaments with up to 30 µm in length [21, 22]. The viral envelope is derived from the lipid membrane of the host cell during the budding process and contains the viral transmembrane proteins HA, NA and matrix protein 2 (M2). Furthermore, host membrane proteins may be also incorporated into the viral envelope, likely through lipid recruitment at the viral budding site [20]. The matrix protein 1 (M1) forms an inner layer beneath the lipid membrane supporting the viral envelope. Furthermore, M1 associates with the viral genome segments inside the virus particle. The viral genome is not incorporated as naked vRNA but in form of viral ribonucleoproteins (vRNPs). Within the vRNP, the vRNA is encapsidated by one copy of the heterotrimeric viral polymerase, i.e., viral RNA-dependent RNA polymerase (RdRp) and numerous copies of the viral nucleoprotein (NP). In particular, the viral polymerase consists of three subunits, i.e., the polymerase basic protein 1 (PB1), polymerase basic protein 2 (PB2) and the polymerase acidic protein (PA). It binds to a helical hairpin structure that forms between the highly conserved 5' and 3' ends of the vRNA. Thus, the encapsidated vRNA forms a rod-shaped secondary structure, with the polymerase at one end and a loop at the other, which represents the minimal replicative unit of the virus (see Figure 2.1 and reviews by [3, 19, 20, 23–25]). Moreover, the eight genome segments adopt a "1+7" configuration inside the virus particle with one core segment that is surrounded by the remaining seven segments [27, 28]. This configuration seems to follow an inherent mechanisms that is also observed for other influenza virus types [29]. Interestingly, a recent study showed that, in case one genome segment has a packaging defect, the virus particles contain an increased number of cellular ribosomal RNAs that, seemingly, "fill up" the gap left by the missing vRNP [28].

Genome organization   The length of the eight genome segments ranges from 890–2341 nucleotides for the A/PR/8/34 strain [30]. They encode for 10 essential viral proteins and multiple accessory proteins, which are either virus strain-specific or only occur under laboratory conditions (Figure 2.2). To overcome the limited coding capacity of their genome, influenza viruses employ mechanisms such as alternative open reading frames, alternative splicing and ribosomal frame shifting, which allows to increase the number of viral proteins encoded per segment [31, 32]. The three polymerase subunits PB1, PB2 and PA are encoded by the longest segments 1 to 3. The surface glycoproteins HA and NA are encoded by segment 4 and 6, respectively. Furthermore NP is synthesized from segment 5, and M1 and the non-structural protein 1 (NS1) are located on the
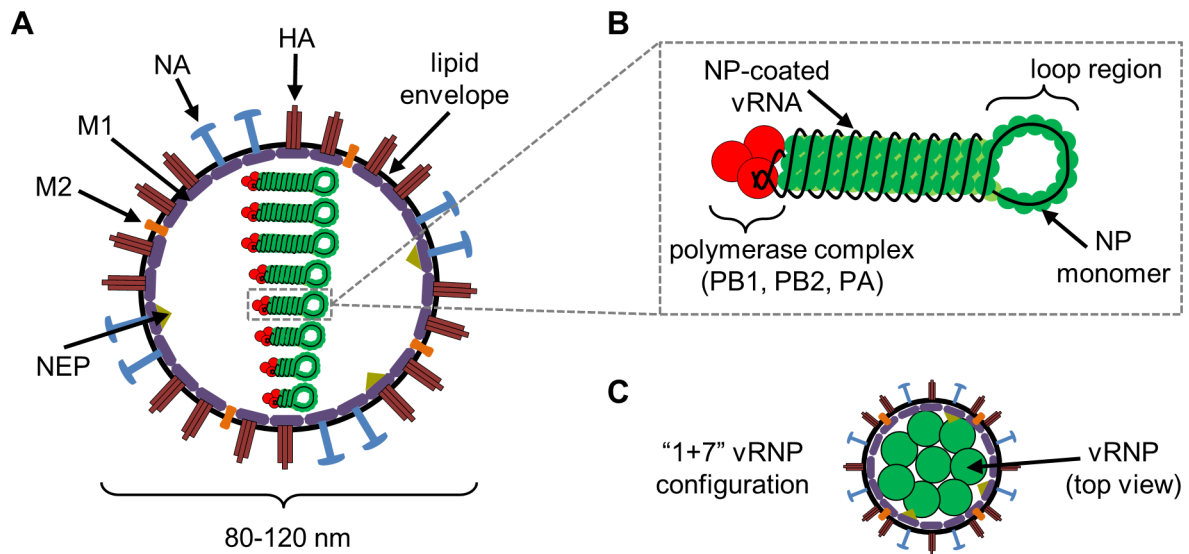
Figure 2.1.: Virus particle and genome structure. (A) Schematic diagram of a spherical influenza A virus particle. (B) Scheme of an influenza viral ribonucleoprotein (vRNP). (C) Top view of a virus cross-section showing the "1+7" configuration of vRNPs. PB - polymerase basic protein, PA - polymerase acidic protein, HA - hemagglutinin, NP - nucleoprotein, NA - neuraminidase, M - matrix protein, NEP - nuclear export protein. Figure adapted from [3, 19, 20]. Figure elements taken from [26].
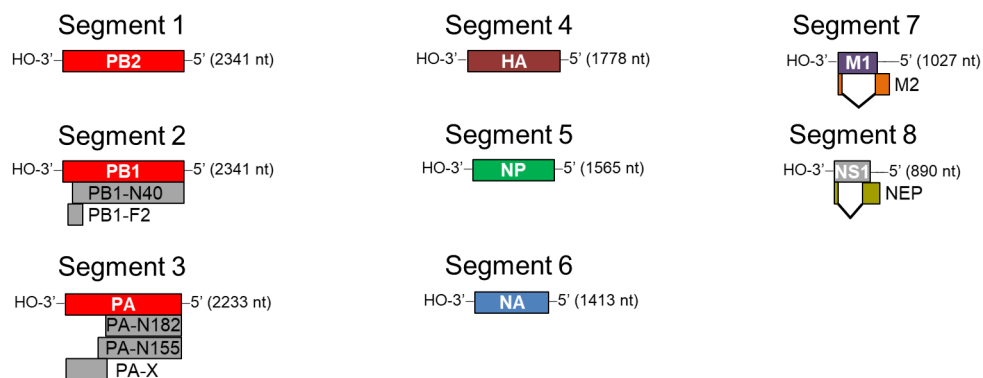

Figure 2.2.: Viral genome organization. Genome segments of the influenza A/PR/8/34 strain. Boxes represent the encoded proteins and lines at the termini symbolize the non-coding regions. Introns of the spliced mRNAs of segments 7 and 8 are indicated by V-shapes. The smaller coding regions (grey boxes, black letters) represent accessory proteins found in many strains, whereas those that are less prevalent (PB2-S1, M42, and NS3) are not illustrated. NS 1 nonstructural protein 1. Color code is in accordance to Figure 2.1. Figure adapted from [19, 20, 31]. Figure elements taken from [26].

two smallest segments 7 and 8, respectively. Two essential proteins, also derived from segments 7 and 8 by alternative splicing, are M2 and the nuclear export protein (NEP), respectively.

In response to infection, the host cell activates antiviral mechanisms, such as the RIG-I/interferon signaling pathway, to counteract virus replication [33, 34]. Thus, to complete its life cycle successfully, the virus requires not only its major proteins that are, for instance, responsible to replicate the viral genome and form the structural elements of the viral progeny. In addition, non-structural, multi-functional viral proteins are in place to modulate the host response in such way that it allows the virus to exploit the host cell machinery. This role has been attributed to proteins such as NS1, PB1-F2 and PA-X (reviewed in [35]). Interestingly, a recent study revealed that a peptide encoded by a deletion mutant of the segment 1 can also influence the antiviral response, showing that the virus might even employ further mechanisms, such as open reading frames in RNA deletion mutants, to enlarge its coding capacity [36].

2.1.2. The intracellular viral life cycle

In birds, the natural reservoir of influenza viruses, the virus replicates in epithelial cells of the intestinal tract, whereas in humans and mammals, influenza viruses preferentially infect epithelial cells of the respiratory tract causing typical disease symptoms. Moreover, influenza viruses also infect macrophages and dendritic cells. However, in those cells, virus replication is limited and rather results in the activation of the immune response than in significant release of viral progeny [3]. Details of the viral life cycle are shown in Figure 2.3 and will be explained in the following paragraphs.

Virus attachment and uptake   To enter its host cell, the virus binds to sialic acids at the cellular surface, a process mediated by the HA protein. Upon binding, the virus particle is internalized by receptor-mediated endocytosis, followed by endosomal trafficking and acidification (reviewed in [19, 38, 39]). The latter induces structural changes in the HA protein, which cause the fusion of the virus envelope with that of the endosome, such that the virion has access to the cytoplasm. Endosomal acidification also activates the viral M2 ion channels [40] that import protons to the inside of the virus particle, which is followed by viral uncoating, i.e., the dissociation of vRNPs from the M1 (reviewed in [19, 38, 39, 41]). Consequently, the eight genomic vRNPs which are free of M1, are released into the cytoplasm.

Nuclear import of vRNPs   Upon uncoating, the viral genomes traffic to the host cell's nucleus, where they replicate and transcribe their genome. In particular, there is evidence
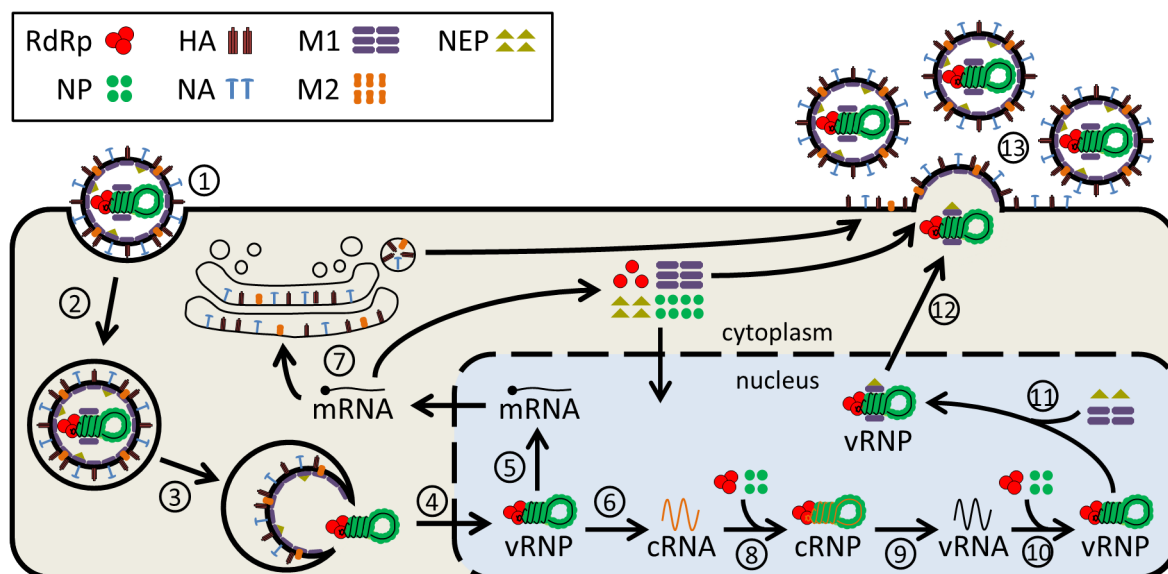
Figure 2.3.: Scheme of the influenza A virus life cycle. For the sake of simplicity, only one of the eight vRNPs is depicted and non-structural proteins were omitted. Different steps are assigned by numbers (see text for details): (1) attachment, (2) endocytosis, (3) fusion in late endosomes, (4) nuclear import, (5) transcription, (6) replication (cRNA synthesis), (7) protein translation, (8) cRNA encapsidation, (9) replication (vRNA synthesis), (10) vRNA encapsidation, (11) M1 and NEP binding, (12) nuclear export, (13) virus assembly and budding. Figure adapted from Heldt *et al.* [37].

that the eight vRNPs remain associated in a joint complex and only separate when they reach the nucleoplasm [42]. Multiple studies revealed that cytoplasmic vRNPs efficiently engage the host nuclear import pathway to reach the nucleoplasm [20, 43]. Due to their size, vRNPs require energy-driven transport by the host cell's nuclear import machinery to reach the inside of the nucleus (reviewed in [20, 24, 39, 43–46]). To interact with the nuclear transport receptors, viral components require a nuclear localization signal (NLS) which has been found in all viral proteins associated with the vRNPs [46]. While for the nuclear import of the vRNPs only the NLS of the NP is relevant [19, 39, 47, 48], individual viral proteins, such as the viral polymerase subunits, require their own NLS for cytoplasmic-nuclear trafficking later in infection. Depending on the viral cargo, different host nuclear import factors are recruited [39, 43, 46]. On the viral side, the most important regulator of cytoplasmic-nuclear trafficking is M1. When associated to vRNPs, M1 masks the NLS of NP, which prevents nuclear vRNP import unless M1 dissociates from the viral genome [49]. Hence, M1 release during uncoating is necessary to allow nuclear import of parental vRNPs. Furthermore, nuclear daughter vRNPs bound by M1 traffic to the cytoplasm and cannot re-enter the nucleus [50–52], which is a pre-requisite for viral progeny release.

Viral mRNA synthesis   Upon successful viral entry, viral messenger RNA (mRNA) synthesis occurs first independent of *de novo* synthesized viral proteins. This primary transcription is carried out in *cis* by the resident viral polymerase of the vRNP using its own vRNA as a template [53]. Furthermore, the initiation of viral mRNA synthesis depends on the interaction of the viral polymerase with the cellular RNA polymerase II (Pol II), which facilitates the so-called cap-snatching (reviewed by [19, 23, 25, 43]). For this, a 5' capped ribonucleic acid (RNA) primer is derived from host pre-mRNAs, which significantly increases the initiation efficiency of viral mRNA synthesis [20]. After elongation, each viral transcript is polyadenylated when the viral polymerase transcribes a short poly-uridine sequence of the vRNA 5' end, which involves stuttering of the polymerase and finally terminates mRNA synthesis. Due to their 5' cap and 3' poly(A)-tail, viral transcripts mimic host cell mRNAs, which facilitates their access to cellular nuclear export factors as well as the splicing and translational machinery of the cell [23, 54].

Viral protein translation   Cytoplasmic viral mRNAs are translated by cellular ribosomes for which they compete with cellular transcripts for active translation sites. To this end, the virus has evolved several mechanisms to draw resources away from host cell protein translation. This so-called host shut-off does not only involve preferential access to ribosomes but also degradation of the Pol II later in infection [19, 55]. To compensate for the limited coding capacity of the virus genome, some viral mRNAs are spliced prior to nuclear export (Figure 2.2), where timing of the expression of spliced and unspliced mRNAs seems to be linked to the functionality of the encoded proteins [19, 20]. For some of the *de novo* synthesized proteins, their translation is followed by import to the nucleus, where they are required for ribonucleoprotein (RNP) assembly, RNA replication and other processes [45, 46]. In contrast, the viral surface proteins with transmembrane domains, HA, NA and M2, are translated at endoplasmic reticulum (ER)-associated ribosomes and later travel to the host cell plasma membrane to form the viral envelope. At the ER and Golgi apparatus, important post-translational modifications, such as glycosylation and proteolytic cleavage, take place, which support the correct folding and functionality of those proteins [20].

Viral RNA replication   For the amplification of the viral genome, the virus employs a third RNA species, which is a complementary RNA (cRNA) of positive polarity. In contrast to the viral mRNA, this replication intermediate provides a full-length copy of the vRNA and is synthesized without the use of a 5' capped RNA primer or a 3' poly(A) tail. Since the vRNA of the parental vRNP encodes both mRNA and cRNA, that are ultimately designated for different purposes, the question is how the synthesis of

those two positive-strand RNAs is coordinated (reviewed in [19, 23, 25, 56]). While this is still a matter of ongoing research, there are two main hypotheses that were established during the past decades of research. On one hand, there is experimental evidence that the polymerase might switch from mRNA to cRNA synthesis later in infection, which is triggered by the increasing number of soluble NP molecules [57]. This so-called switching hypothesis was, however, challenged by findings of Vreede and colleagues [58, 59], who describe that vRNPs synthesize both positive-strand RNA species simultaneously. Importantly, nascent cRNAs are being degraded by cellular nucleases until they are stabilized by viral polymerases and NP, i.e., until they form complementary ribonucleoproteins (cRNPs), and cRNA accumulation becomes evident. Besides the switching and stabilization hypotheses, other studies suggest that transcription is carried out in *cis* by the vRNP-resident polymerase, whereas RNA replication is mainly driven in *trans* by the soluble polymerases [53, 60]. Of note, multiple other studies have been carried out revealing the impact of cellular [43, 61, 62] and viral factors [63–68] on viral RNA synthesis and its regulation. Using mathematical single-cell models, our group revealed that intracellular RNA dynamics can be reproduced best by accounting for the stabilization hypothesis [18, 26], which is why we continue to employ this mechanism in current models. When present in their stabilized form, cRNPs serve as template for *de novo* vRNA synthesis, likely catalyzed by the soluble viral polymerases [53]. Following vRNA synthesis, assembly of vRNPs through encapsidation by polymerases and multiple copies of NP is analogous to cRNP formation. Replication-competent vRNPs then serve again as template for mRNA and cRNA synthesis, such that the three RNA species engage in an autocatalytic cycle.

Nuclear export of vRNPs To complete the replication cycle and form progeny viruses, vRNPs need to leave the nucleus and traffic to the cellular plasma membrane. For this, the two viral proteins M1 and NEP are responsible in mitigating nuclear vRNP export together with the cellular export machinery (reviewed in [19, 20, 43]). Similar to vRNP import, the export of large molecules requires active transport involving the nuclear export receptor chromosome region maintenance 1 protein (CRM1) and cellular nucleoporins. To interact with those cellular factors, vRNPs are directed toward CRM1 via a "daisy chain" of M1 and NEP. For this, M1 associates with the vRNP and NEP, while NEP recruits CRM1 through its nuclear export signal [65, 69, 70]. It has been hypothesized that the initial formation of an M1-vRNP complex shuts down the transcriptive and replicative activity of the vRNPs [71–76], which is required to facilitate their export. Opposed to the "daisy chain" model, Brunotte and colleagues proposed an alternative mechanism, where NEP directly binds the vRNP-resident polymerase and does not only facilitate

binding of M1 to the NEP-vRNP complex but is also required to efficiently shut down vRNP activity [77, 78]. Although the two models propose ambiguous roles of M1 and NEP, they clearly underline their importance and joint action in driving nuclear export. Importantly, M1 and NEP are expressed late during infection, such that vRNP export only occurs after a complete round of replication preventing a pre-mature shut down of viral transcription and replication [19, 79].

Particle assembly and release   Ultimately, the eight viral genomes and the viral structural proteins, HA, NA, M1 and M2, assemble at the cellular plasma membrane to form progeny virions. To orchestrate this process, multiple mechanisms are required that facilitate the concentration of the viral components at the plasma membrane and induce membrane curvature and scission (reviewed in [19, 20, 24, 43, 80]). Several studies revealed that virions bud from lipid rafts, cellular membrane domains that are rich in sphingolipids and cholesterol (e.g. [81]). HA and NA localize at those rafts, accumulate and form distinct clusters and patches, which likely facilitates the recruitment of cytosolic M1 [19, 20]. Here, oligomerized M1 acts as a membrane-bending protein and induces curvature of the membrane and the formation of a budding site. Furthermore, M1 associates with vRNPs located at the plasma membrane, and, thus, provides a link between the viral membrane proteins and the vRNP complex inside the virus particle, which drives the incorporation of vRNPs during bud extension. Additionally, M2 seems to support the capturing of vRNPs [19], however, it rather accumulates at the boundary of the budding domain and further bends the membrane of the budding virion [20, 40]. In particular, M2 is responsible for the formation of a "bud neck" and promotes membrane scission by decreasing the distance between the two opposed membranes [82]. Importantly, the successful budding of particles also relies on the sialidase activity of the NA, which removes local sialic acid residues and, thus, prevents binding of HA to the cell surface [20].

Cytoplasmic vRNP trafficking and packaging   Upon nuclear export, vRNPs associate with Ras-related protein Rab-11 (RAB11)-positive recycling endosomes at the microtubule organizing center in the perinuclear region. Then, while being associated with the recycling endosome, the vRNPs are actively shuttled to the plasma membrane via the cellular microtubuli network. At the budding site, vRNPs are extracted from the recycling endosome, supported through the recruitment by M1 [43]. While RAB11 is the major host factor promoting vRNP cytoplasmic trafficking [83], further host factors are supporting their vesicular transport [24, 43]. Furthermore, there is evidence that vRNPs can reach the plasma membrane independent of host cell proteins or the cytoskeleton, e.g. through vRNP-intrinsic lipid recruitment or by diffusion [19, 24]. However, likely, vRNP traffic occurs mostly in an organized manner, since this facilitates their co-localization and

orientation before they are incorporated into budding particles [24, 43]. In particular, the step of genome packaging is crucial for the formation of progeny virions which are only replication-competent in case at least one copy of each genome segment is incorporated.

While it has been proposed that the packaging of vRNPs might occur randomly, several lines of evidence suggest that it rather follows a hierarchical segment-specific mechanism (reviewed in [84, 85]). In particular, electron microscopical and electron tomography studies show that the eight vRNPs organize in a "1+7" configuration, where a core segment is surrounded by seven other segments [24, 27, 28, 86–89]. The formation of this vRNP-packaging complex is driven through inter-segment interactions by the bundling and packaging signals of each vRNA [84, 90], facilitated by the secondary structure of the vRNPs [91]. This allows to bring specific segments together and increases the likelihood that only one copy of each segment is incorporated into the budding virion. Further support for a segment-specific packaging mechanisms comes from a study using vRNA-like reporter segments showing that homologous segments compete for the incorporation into the vRNP-packaging complex [92]. Nonetheless, a noticeable fraction of virus progeny carry only an incomplete set of genomes [93]. Hence, even though vRNP packaging is regulated by several mechanisms, it might still present a bottleneck in the formation of infectious virus particles.

2.1.3. Defective interfering particles

Virus populations are heterogeneous and highly divers in their properties such as genome sequence and biological activity [94–99]. Mostly, virological research is concerned with infectious and replication-competent virus particles, i.e., those virions that successfully enter the host cell and form progeny particles, since they represent the primary source of viral pathogenicity. However, large proportions of a viral population may be considered as non-infectious and consist of particles that do not directly contribute to the formation of viral progeny but exert other biological functions. One important class of such non-infectious particles was discovered in experiments by Henle and Henle [100] as well as by Preben von Magnus [101] in the mid 1900s. They describe that some inactive influenza virus particles limit the replication of infectious virions. For instance, during undiluted serial passaging of influenza viruses in eggs, von Magnus observed a drop in the ratio of infectious to non-infectious virus particles, which became known as the "von Magnus effect". While von Magnus attributed this phenomenon to so-called "incomplete" particles [102], only later the term "defective interfering" (DI) particle and its definition were introduced by Huang and Baltimore [103]. Firstly, DIPs are defective, since they require co-infection by the fully infectious STV to complete the viral replication cycle. Secondly, DIPs interfere with virus replication during co-infection and replicate at

the expense of their STV, reducing the number of infectious progeny. In particular, the latter represents a therapeutic potential of DIPs. While IAVs can mutate to evade the host immune response or antiviral drug treatment, it is unlikely that the virus can acquire mutations that counteract DIP interference. This is related to the fact that STVs and DIPs employ the same molecular mechanisms to replicate their genome. Consequently, any mutation that reduces the replication of DIPs will also affect STV propagation [104]. Hence, DIPs might serve as a novel antiviral agent that can overcome limitations of conventional vaccination and treatment with antiviral drugs (reviewed by [15, 105]). Today, we know that DIPs are formed by almost all viruses [15, 106–108], play a role in both laboratory experiments as well as *in vivo* scenarios [15, 109–111], and impact production and efficacy of biopharmaceutical products [13, 112]. In particular, state-of-the art sequencing techniques and genetic engineering allow improved characterization of DIPs and viral sub-populations in general, which helps to improve our understanding of their role in the viral life cycle and supports rational design of virus-based antivirals. Below, we will give a brief overview on origin, structure, function and potential therapeutic use of DI RNAs.

Origin and structure of DI RNAs   Morphology and structural viral components of influenza DIPs are identical to their cognate STVs. In particular, they are antigenically identical, which makes it difficult to distinguish the two particle species with conventional virological assays, such as the HA assay. However, DIPs are unable to complete the viral life cycle since they lack essential viral genes due to the incorporation of one or more deletion mutant genome segments during packaging. Such sub-genomic segments arise during errors in virus replication, where the viral polymerase detaches from its template and translocates to a position further downstream of the RNA sequence (reviewed by [113–116]). Likely, this process is facilitated by the secondary structure of the vRNPs bringing distant sequence regions in close physical proximity, resulting in a largely symmetrical internal deletion close to the termini of the segment (Figure 2.4, [117]). The deleted gene segments typically retain the terminal ends of the cognate full-length (FL) sequence, i.e., the 3' and 5' ends and the non-coding region, which contain the promotor region and the packaging signals, and parts of the adjacent coding region [84, 115]. While the deleted segment is significantly shorter compared to its cognate FL segment, it might still encode truncated DI peptides [36, 119]. The internal deletions vary in size and seem to occure randomly, since, thus far, there is no clear indication for a preferential breaking point or common nucleotide composition around the deletion site [13, 115, 116]. IAV DIP preparations usually contain multiple DI RNAs that can originate from either one of the genome segments, whereas, so far, no sub-genomic RNAs of segment 7 were

described [14, 84, 120, 121]. The most abundant DI RNAs of IAV originate from segments 1–3, which encode the three polymerase subunits [110, 117, 120, 122]. Since those are the longest of the eight IAV genome segments, internal deletions can result in very short polymerase-derived DI RNAs with only up to 300 nt, which corresponds to only about 15 % of their parental FL segment in length (reviewed by [84, 115]). In particular, this substantial difference in length of DI RNAs has lead to the common assumption that their reduced length is the main source for their interfering potential (see below).

Besides DI RNAs with single internal deletions, defective sub-genomic RNAs also exist in other forms. Those include such with multiple deletions; copy-back/panhandle genomes and snap-back/hairpin genomes, where parts of the sequence are copied in reverse complement; mosaic or complex defective genomes that arise by partial recombination
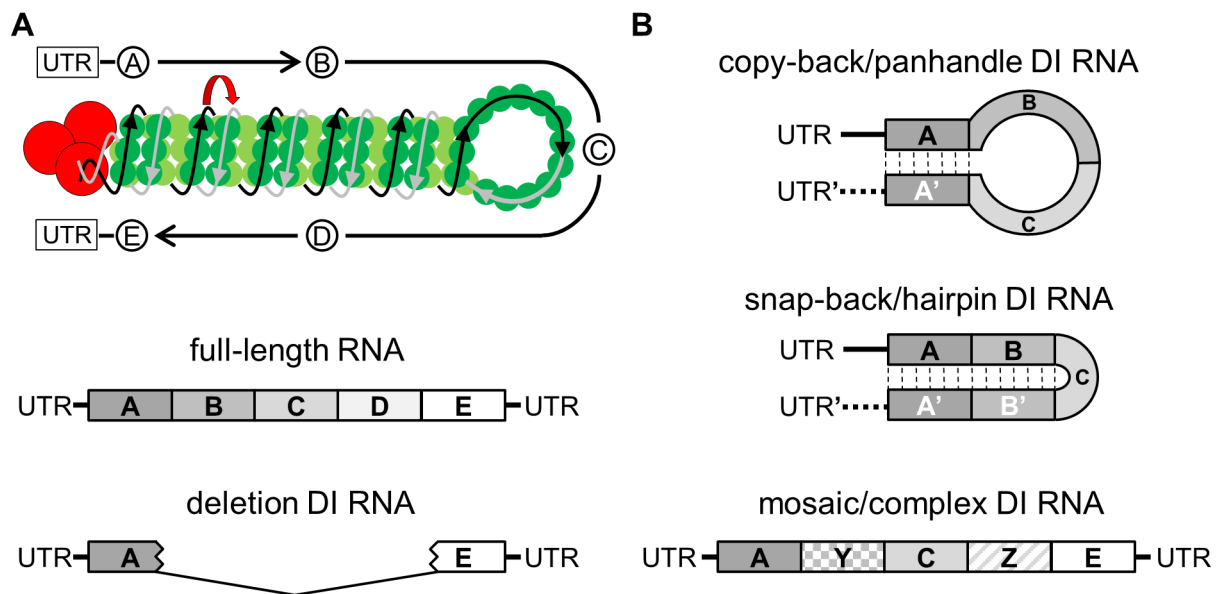

Figure 2.4.: Schematic diagram of full-length and DI RNA structures. (A) Structure of an influenza virus full-length segment, depicted as vRNP and in its linear form, respectively, containing the untranslated regions (UTR) with promotor sequences and packaging signals, and the coding sequence elements A–E. The deletion DI RNA (bottom) is potentially generated *de novo* by a translocation of the viral polymerase between adjacent regions of the RNA template which are present in a double-helical conformation. While the polymerase reads the template RNA it can dissociate from element A and reattaches to element E, respectively (red arrow), without copying the entire sequence. Consequently, parts of the internal coding region are deleted, as indicated by the V-shape in the linear DI RNA sequence. (B) Structures of DI RNA forms reported in literature. For instance, copy-back and snap-back DI RNAs contain complementary copies of sequence elements, represented by A' and B', respectively. Complementary sequence elements can hybridize and give rise to either panhandle or hairpin RNA structures. Mosaic genomes represent recombinations (or rearrangements) of various regions coming from the parental full-length RNA, or host RNA, denoted by sequence elements Y and Z. Figure adapted from [13, 15, 26, 105, 107, 108, 116, 118].

with other viral or cellular genome parts; or (hyper-)mutated genomes (reviewed by [15, 105, 107, 108, 116, 118]). For instance, while no deleted form of the IAV segment 7 was described previously, our group discovered a hyper-mutated version of this segment which shows a DI-like interfering phenotype [123], referred to as over-proportional segment 7 (OP7).

Modes of interference and competition To replicate their genome and form progeny particles, DIPs depend on the co-infection by their cognate STV. In particular, high multiplicity of infection (MOI) scenarios facilitate DIP propagation by increasing the chance of a co-infection of a host cell. During co-infection, the DI RNAs replicate at the expense of the STV by taking advantage of the missing viral proteins complemented *in trans* by the STV. During co-replication, the DI virus uses up viral and cellular resources without contributing to the pool of functional viral proteins and, thus, inhibits the formation of STV progeny. However, the molecular mechanisms involved in this inhibition are still not fully understood (reviewed in [13, 105, 107, 108, 115, 118]).

The most common assumption is that DI RNAs have an advantage over FL RNAs due to their reduced length. For instance, the preferential amplification of sub-genomic RNAs observed in experiments lead to the hypotheses that the viral polymerase can produce more copies of short RNAs per unit of time [105, 115, 119, 124]. In particular, Odagiri and colleagues proposed that the advantage in RNA replication occurs at the stage of cRNA synthesis [125]. Consequently, the DI RNAs might outnumber the FL RNAs resulting in a decrease of STV formation. Moreover, it was speculated that the DI RNAs' potential to accumulate to unusually high copy numbers stems from the loss of, yet unknown, regulatory elements that are normally present in FL RNAs. Furthermore, DI RNAs have to be packaged into progeny particles to successfully propagate and infect new host cells. For this, the DI RNAs have to retain the terminal ends of the FL sequence, which contain the packaging signals. However, since DI segments are smaller compared to their cognate full-length segment, it was hypothesized that they could be packaged more easily into budding particles or may exclude FL segments from packaging considering that vRNP incorporation occurs in a segment-specific manner (reviewed in [115]).

In particular, support for a simple length-dependent advantage of DI RNAs during RNA synthesis comes from a mini-replicon study using luciferase-expressing virus-like vRNAs [126]. Here, the shorter of two reporter vRNAs suppressed luciferase expression more efficiently. Furthermore, also the the eight FL vRNAs were evaluated for their potential to reduce luciferase expression. Interestingly, the shorter the FL segment, the more efficiently luciferase expression was inhibited. In addition, this study showed that the replication of virus-like RNAs was limited by the availability of viral polymerases.

This agrees well with experimental findings of an *in vitro*, cell-free RNA assay of vesicular stomatitis virus (VSV), which revealed that DI and FL RNAs compete for components of the viral polymerase complex [127]. While very short DI RNAs seem to have an advantage in RNA synthesis compared to their parental FL RNAs, not all IAV DI RNAs accumulate to high levels in host cells [124]. However, some experiments showed that DI segments might also be preferentially packaged into progeny particles, such that the DI-to-FL RNA ratio in progeny particles is higher compared to that ratio on the intracellular level [124, 128, 129]. Consequently, co-infected host cells showed almost exclusive DIP release although decent amounts of FL RNAs were present inside the cells. Hence, length might not be the only determinant for an efficient interference. For instance, Rao and Huang also reported that during simultaneous co-infection of host cells by three VSV DI RNAs of different lengths, the longest of them was the most successful competitor, which might be related to the presence of particular sequence parts [130]. Likewise, also the dual-luciferase reporter assay by Widjaja and colleagues revealed that the interfering potential of IAV-like vRNAs was influenced by the parts of the coding and non-coding region that were retained in the deleted RNA sequence [126]. While the nucleotide sequence might influence the replication and packaging of DI segments, the retained 5' and 3' ends also allow the synthesis of truncated polypeptides encoded by DI vRNAs [119, 131], which were suggested to play a role for the viral life cycle and/or the DI vRNA's interfering potential [36]. However, so far, we lack a direct correlation between DI polypeptide expression and an enhanced DI RNA synthesis [115].

While there are multiple aspects of DI RNA interference, the most intriguing feature in DIP co-infections is the limitation of STV growth and, thus, a reduction of infectious virus particle release. However, since DIP reproduction is directly depending on the availability of functional proteins supplied by the STV, highly competitive DIPs, that quickly diminish STV replication, interfere with their own propagation, i.e, they are self-interfering. The latter can be referred to as a parasitic behavior towards their STV, which leads to the rapid extinction of both virus types. On the contrary, less competitive DIPs, which may be referred to as symbiotic, attenuate virus growth, however, still support viral spread. Such symbiotic DIPs have been related to the a reduction in disease symptoms during infection, which supports the mobility of the infected host and, thus, even improve viral spread compared to DIP-free infections, e.g. described for dengue virus [132]. Besides, attenuation of disease symptoms may also prevent the virus-induced death of host organisms which would otherwise decrease the host population size. For instance, severe disease outcomes in pandemic influenza infections can be related to a reduced abundance of DIPs [133]. Furthermore, DIPs may facilitate the establishment and/or maintenance of persistent infections [103, 118, 134].

Therapeutic potential of DIPs Since the late 1980s, DIPs have been evaluated as novel prophylactic and therapeutic antiviral agent [15, 105, 135–138]. Conventional antiviral drugs applied to treat acute influenza infections, such as NA and M2 inhibitors, exhibit a selective pressure on influenza viruses. Thus, circulating strains have acquired resistance against some of the conventional antiviral drugs, rendering them ineffective [139–143]. Opposed to that, the administration of DIPs holds the promise of overcoming those limitations of conventional antiviral drugs since the emergence of DIP-resistant virus strains is less likely [15, 104, 136]. Thus, acute infections could be treated without increasing the selective pressure on wild-type influenza strains since DI RNAs hijack conserved mechanisms of virus replication.

So far, influenza virus DIPs have been demonstrated to impair virus growth *in vitro* and *in vivo*, and to protect mice and ferrets from a lethal challenge of STVs from various influenza virus strains [15, 135, 144–148]. Furthermore, experimental observations convey that, in the presence of DIP co-infection, the induction of the cellular innate immune response was enhanced [33, 108, 111, 118, 144, 147–149]. In particular, this has been related to a preferential binding of RIG-I, a host cell factor that leads to the activation of interferon (IFN), to the short DI RNAs [150]. Moreover, the DIP-related induction of the immune response, including antibody production [144, 147, 148], represents an additional benefit in protecting the host organisms from homologous, and even non-homologous, virus infections of the respiratory tract [136, 151]. However, a recent, systematic evaluation of IFN induction during influenza infections revealed that naked, i.e., not NP-encapsidated, mini viral RNAs (mvRNAs) of 56–125 nt in length are triggering the RIG-I-mediated activation of IFN even more efficiently than DI RNAs [152]. However, the presence of DI RNAs might indirectly cause accumulation of mvRNAs, since they can induce an imbalance of NP and polymerases when competing for limiting viral factors with the FL RNAs (explained above). Such imbalance causes a dysregulation of RNA replication that is associated with preferential accumulation of mvRNAs, and, thus, induction of IFN expession [152]. Hence, it is yet to be clarified whether DIP-related protection comes mainly from enhanced DI RNA replication or improved IFN activation, or both.

While the exact mechanisms of DIP interference and protection are still elusive, the application of DIPs as a co-replicating antiviral represents a promising, innovative alternative to conventional drugs. To facilitate (pre-)clinical trials, large amounts of DIPs can be produced in stirred tank bioreactors under controlled conditions. In particular, genetic engineering of trans-complementing producer cell lines allows the generation of STV-free DIP preparations [153–155], facilitating the supply of safe and well-characterized DIPs, also termed as therapeutic interfering particles (TIPs). While the repertoire of

possible application scenarios of such TIPs keeps expanding, e.g. for the treatment of cancer (reviewed in [108]), the fact that TIPs represent a biological active, transmissible and live virus-based therapeutic agent might complicate approval for the use in humans, which requires further tuning by genetic engineering techniques. In addition, Harding and colleagues proposed a TIP system using a synthetic, mutated IAV strain that mimics DIP interference at the stage of genome packaging and already showed protection from lethal infections in animal experiments [156]. Thus, despite the mysteries related to their formation and propagation, DIPs have already inspired new antiviral strategies beyond their own mode of action.

2.2. Influenza vaccine production

Influenza virus infections have a significant impact on global public health and economics. While effective antiviral drugs for the treatment of influenza are available, vaccination is still the most effective and successful measure to prevent spreading of the disease. However, influenza viruses are highly variable [157], and the selection pressure from the host immune response together with the application of antiviral drugs causes a continuous evolution of the virus (antigenic shift, antigenic drift). In particular, mutations of the surface antigens HA and NA pose a significant challenge in battling IAV infections since they enable re-infection of the same host. Hence, the composition of the influenza vaccines are updated annually according to recommendations by the World Health Organization. Currently, two IAV subtypes (H1N1, H3N2) and two lineages of influenza B viruses (Victoria, Yamagata) are circulating in humans (reviewed in [3, 20]). Accordingly, many vaccine formulations contain two representatives of IAV and at least one of the influenza B virus strains. While the majority of vaccines is still produced in embryonated chicken eggs, the use of animal cells together with genetic engineering techniques opened various alternatives that lead to the market-introduction of novel cell culture-derived influenza vaccines (reviewed in [158–160]). Here, we give a brief overview on the different types of vaccines, and outline the different production techniques as well as avenues to process optimization.

Current and future influenza vaccines Traditionally, influenza vaccines are available in inactivated or live-attenuated form. The first generation of influenza vaccines was chemically inactivated and purified whole virus particles, with the first vaccine candidate developed in the 1930s and licensed in the 1940s in the USA (reviewed by [3, 161], [162]). Furthermore, influenza vaccines are available in the form of virosomes or virus-like particles as well as split virus particles, and, nowadays most commonly, viral sub-units that serve as antigens [159, 160, 163]. Upon chemical inactivation, so-called split vaccines are generated by further disintegrating the virus particles using detergents, e.g. Fluarix® by GSK [164]. For sub-unit vaccines only HA and NA are purified from the remaining viral components, e.g. Optaflu® by Novartis [165]. Compared to whole virus particle-based vaccines, split and sub-unit vaccines suffer from both decreased efficacy and duration of protection. To increase immunogenicity of inactivated vaccines, they can be complemented with adjuvants [166]. For instance, during the influenza pandemic of 2009, Germany allowed the use of MF59 to overcome limitations in vaccine dose supply, i.e., to enable the use of less antigen per dose [3]. While inactivated vaccines are administered by intramuscular injection, live attenuated vaccines are delivered intranasally, e.g. through sprays (FluMist® by AstraZeneca, previously MedImmune, 2003 [167]). For this,

cold-adapted virus strains are used that can infect the nasal epithelium and replicate in the upper respiratory tract, however, cannot affect the lower respiratory tract. By mimicking the natural infection, a long-lasting, cross-protective immune response can be induced in the upper respiratory tract, the natural initial replication site [3, 160].

A drawback of the seasonal influenza vaccines is that they have to be updated annually and there is the potential risk of a vaccine mismatch, rendering the vaccine ineffective [3, 160, 168–170]. Hence, to increase robustness of the induced immunity, there are efforts toward developing a universal influenza vaccine. This is based on viral peptides corresponding to the less variable components of the virus, i.e., the stalk region of the HA or extracellular domains of the M2 protein. Alternatively, also M1 or NP or even combinations of multiple conserved proteins as vaccine is being evaluated, which may induce a more cross-protective immune response [159, 160, 171].

To facilitate seasonal influenza vaccine production and avoid vaccine mismatches, novel vaccines are developed using recombinant proteins, viral vectors, peptides as well as RNA and DNA vaccines (reviewed by [3, 159, 160, 172, 173]). For instance, in 2013, a recombinant influenza vaccine was introduced, which was produced by the baculovirus expression system in insect cells [163]. For this, infected cells express recombinant HA without the need to generate or adapt influenza seed virus strains. Furthermore, peptide antigens can be synthesized chemically in a cell-free system, which improves their safety and feasibility for large-scale production. However, while the production of such novel vaccines might be faster and cheaper, there are limitations regarding their stability, delivery and efficacy [174]. In particular, many of them are poorly immunogenic when administered without immunostimulators. Thus, the new generation of vaccines also requires the development of safe and potent adjuvants that improve their immunogenicity [160].

Egg-based vaccine production Traditionally, influenza vaccines are produced in embryonated chicken eggs, which led to the licensing of the first inactivated influenza vaccine in 1945 in the USA [3, 161]. Until today, egg-based influenza vaccine production has been constantly optimized and also automated, which allows the cost-effective delivery of safe influenza vaccines [160, 175]. Furthermore, the long track of experience, standardization and record of vaccinations gained over more than half a century is beneficial with respect to regulatory approvals. While the majority of influenza vaccines are produced in egg-based processes, certain risks of the method remain. In particular, the logistics of providing a sufficient amount of vaccine-grade eggs are complex and might be impaired by egg pathogens as well as an avian influenza outbreak among the chicken layer flocks [161, 175, 176]. While it is already challenging to provide sufficient amounts

of vaccine-grade eggs during the annual influenza seasons, egg-based production alone is too slow to meet the global demand in vaccine doses in case of a rapidly evolving influenza pandemic. Furthermore, some influenza strains only replicate poorly in eggs and require adaptation, e.g. H3N2 [159, 160]. While, since the 1960s, the application of A/PR/8/34-based high-growth reassortants has been facilitating the adaptation of circulating strains to grow in eggs, some viruses might require multiple egg passages to attain sufficient growth performance. However, during passaging, the virus can acquire mutations, e.g. in the HA, which can result in a mismatch of the vaccine strain with the circulating strain and can render the vaccine ineffective [160, 161, 177]. Thus, a main goal of current influenza vaccine research and development is to decrease the dependency on egg-based processes in order to guarantee a sufficient and timely supply in case of a pandemic outbreak.

Cell-culture based vaccine production To overcome drawbacks of egg-based production systems, the application of cell culture technologies represents a promising alternative. After the first vaccine produced in cell culture revolutionized the vaccine manufacturing field (Vero-grown polio vaccine, 1955 [178]), cell culture was also explored for the production of influenza vaccines in the second half of the 20$^{\text{th}}$ century [179]. Several continuous cell lines have shown applicability for influenza virus propagation, such as Madin-Darby Canine Kidney (MDCK), Vero, HEK-293, PBS-1 cells and designer cell lines, such as PER.C6®, AGE1.CR®, EB14®/EB66®, and CAP® [180–183]. Today, the MDCK cell line is the "working horse" of influenza virus vaccine research and manufacturing [175, 180, 184]. A big concern in applying immortalized animal cell lines is their potential tumorigenicity and oncogenicity, and contamination with pathogens, which has also been evaluated for several MDCK cell lines to show their suitability for vaccine production [185–187]. Thus, in 2001, a major accomplishment was the approval of Influvac®, the first human influenza vaccine in the EU that was produced in an adherent MDCK cell line [188]. To facilitate large-scale production, adherent cell lines can be adapted to growth in suspension. One successful example for this approach is the first MDCK suspension cell line developed in 1997 [189], that was used later by Novartis to produce seasonal influenza vaccines (Optaflu®, commercialized in 2007 [165]). The same cell line is still used today for vaccine production (Flucelvax®) by Sequirus in the USA [190]. Since proprietary cell lines are excluded for the use in academia, research groups started to develop their own MDCK suspension cell lines [191–194]. In particular, the MDCK.SUS2 cell line has been extensively applied by our group [193–197] and, hence, modeling of an MDCK.SUS2-based process will be also covered by parts of this thesis.

The production process is separated in a cell growth phase and an infection/production

phase. First, cells are grown to high cell concentrations in large-scale cultivation systems, such as stirred tank bioreactors, and are subsequently infected by high-growth vaccine strains at a low MOI. While for adherent producer cell lines an increasing surface must be provided during the cell growth phase, e.g. by using microcarriers, suspension cells can be scaled-up more easily by simply increasing the process volume [180]. Furthermore, the application of suspension cell lines also facilitates process optimization and intensification (see below).

In summary, cell culture-based production processes are independent of the availability of vaccine-grade eggs and allow production in a closed, sterile and controlled system. Furthermore, mutations in the HA protein, as observed in egg-passaged viruses, are absent in cell-derived vaccines [160, 198]. Importantly, cell-culture based production systems can be scaled-up more easily and can, theoretically, allow to respond quickly to an increased demand in vaccine doses in case of a pandemic outbreak [177]. However, to guarantee safety and reproducibility, cell lines are grown in chemically defined culture media [180], which can result in lower virus yields compared to egg-based processes. While high costs arise for manufacturers during establishment, validation and approval of a novel process, the combination of high cost and low productivity can render a transition to cell-based production financially unattractive [159, 175, 176]. Thus, the further optimization of cell culture based production processes is of utmost importance.

Routes to process optimization   While cell-culture-based production holds the promise of guaranteeing a sufficient and timely supply of a large number of vaccine doses [176, 199], there is still room for process optimization. On one hand, the process setup itself can be optimized. In particular, suspension cell lines [182, 183, 193, 200] have been explored in recent years that can be applied in high-cell density processes that allow the production of more vaccine doses in smaller volumes [196, 201–203]. On the other hand, either the vaccine strain or the cell substrate itself can be further optimized. While, for instance, in MDCK cells, most human influenza viruses grow efficiently, it might be still required to generate high-growth reassortant strains and adapt the virus to the producer cell line to achieve sufficient growth performance [161]. While the A/PR/8/34 virus is the traditional backbone for high-growth reassortants, genetic engineering techniques allow even further optimization of so-called master seed viruses, e.g. by manipulating the viral polymerase, genome packaging and virus release (reviewed in [160]). Such backbones are subsequently combined with the HA and NA genome segments from the circulating viruses by reverse genetics, similar to what has been established to generate high-growth reassortants for egg-based processes [161]. The optimization of the cell substrate itself is subject of ongoing research. Here, the two main options are the picking of high-yield

clones from cell populations [186] or genetic engineering of cells. For the latter, the downregulation of antiviral factors, such as interferon regulatory factor 7 (IRF7) [204], can lead to increased IAV yields in MDCK cells. Likewise, in the case of poliovirus production, knockdown of antiviral host cell factors in Vero cells was also reported to result in significantly increased virus yields [205]. Another option is to overexpress host cell factors that support virus growth, e.g. sialic acids that serve as receptors used by the virus to enter cells [206, 207]. To optimize virus yields, the overexpression of relevant host cell factors was also explored by our group. Thus, the evaluation of cell lines over-expressing relevant host cell factors for IAV replication is also covered by parts of this thesis.

2.3. Mathematical models of virus infection

Mathematical modeling of biological systems aims to elucidate mechanisms underlying the principles of biology. Also in virology, mathematical models have become a crucial instrument for data analysis and interpretation by transferring biological knowledge into logical structures that reproduce experimentally observed phenomena. Furthermore, the quantitative understanding of infectious disease dynamics has supported fundamental advancements in infection research, for instance, in predicting outcomes of antiviral therapy. Moreover, model construction, data integration, *in silico* experiments and model-driven experiments, form an iterative cycle that allows to generate, test and (in)validate new hypotheses on biological mechanisms involved in disease biology [208–210].

In the first part of this section, we give an overview on models used to describe the dynamics of virus growth at different scales with a focus on IAV models. The second part will deal briefly with theoretical aspects of model analysis techniques.

2.3.1. Model classes and scales of infection

Mathematical models exist in a variety of forms. While the simplest ones consist only of a few equations, more complex models are comprised of tens of equations and use various mathematical techniques. Depending on the research question, simple and complex models can be equally helpful. However, a growing set of equations is also related to increasing computational costs and the risk of over-fitting a system. Thus, the complexity in constructing of mathematical models in infections research, as well as in any other discipline, is guided by their purpose, available information, i.e., biological knowledge and experimental data, and the computational cost. Still, while models studying molecular mechanisms at the single-cell level and those that serve for disease control on the epidemiological scale are built for different purposes (Figure 2.5), they jointly follow common modeling principles and simplifying assumptions. In the following, we outline different types of models used in infection research with a primary focus on models used to describe influenza virus infection dynamics.

Classification and common modeling assumptions The major groups of mathematical models are deterministic and stochastic models which describe the timely and/or spatial progression of an infection process. Depending on the purpose of the model, the different modeling approaches can also be combined to form hybrid frameworks. Typically, virus growth dynamics are described by deterministic continuous models built of a set of ordinary differential equations (ODEs), which are of particular
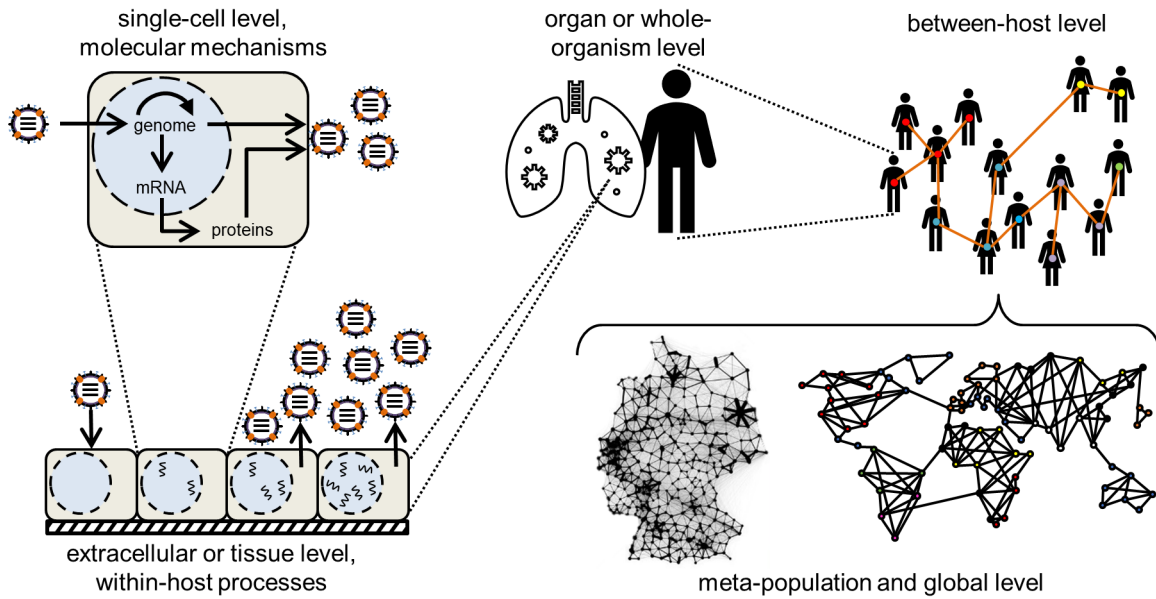
Figure 2.5.: Scales of infection. Modeling of viral infection processes and spread occurs at multiple scales. At the intracellular level, models capture molecular details on replication and virus-host cell interactions. Within-host models help to elucidate crucial infection parameters and support improved antiviral treatment at the patient level. At the host population level, virus dynamics models can describe infectious disease spreading in defined cohorts or communities, as well as on the global population scale by incorporating aspects of mobility, such as air travel. The latter are of particular interest to study and predict public health interventions, which is of utmost importance to understand how diseases can be stopped and pandemics prevented. Figure adapted from [17, 210]. Mobility network map of Germany taken from [211].

interest for this present work. Besides, numerous infection studies have also incorporated the stochasticity of virus-host cell systems and accounted for the randomness inherent in biochemical reactions. Furthermore, infection models make use of various mathematical techniques. One study presented a boolean model, i.e., network-based model, where each model species represents a "switch" that is either active or inactive [212]. Alternatively, cellular automaton models [213–217], population balance models [218, 219], and agent-based models (reviewed in [220, 221]) can successfully describe viral spread in cell cultures and tissues, and capture virus infection in heterogeneous systems comprised of various cell types, e.g. required to incorporate the immune response or multi-pathogen infections (reviewed in [222]). Furthermore, we can subdivide the different available models according to which facet of the infection process they are focusing on. While some focus on describing mechanisms on the molecular scale and intracellular virus replication, others cover a broader spatial and temporal scale and analyze virus dynamics on the within-host or between-host level (reviewed by [17, 223], see below).

Without further mentioning, deterministic models of viral infection, which are the most wide-spread type of virus dynamics models, make use of some common, simplifying

assumptions (reviewed by [209]). For instance, models uncouple viral kinetics from other host cell processes. This also includes the assumption that host cell resources are not limited during the course of infection, which allows to focus on essential steps of virus replication. In addition, most models assume that infected systems are well-mixed, i.e., that they are spatially homogeneous and transport processes are fast, such that they do not influence the reaction kinetics. Furthermore, the majority of reaction kinetics is described by the law of mass action, which treats all reacting species as equilibrated, such that most processes are expressed by a single reaction rate that is directly proportional to the product of the concentrations of the reacting species (see below). We will also frequently apply this principle in our models.

Within-host models Within-host models primarily focus on the main players and events of infection. Accordingly, the standard deterministic within-host model of virus growth (Figure 2.6 A, [224]) describes three species which are uninfected cells T, infected cells I and free virus particles V, whose concentrations change over time according to the following equations.

$$\frac{\mathrm{d}T}{\mathrm{d}t} = \lambda - dT - k^{\mathrm{Inf}}TV, \tag{2.3.1}$$

$$\frac{\mathrm{d}I}{\mathrm{d}t} = k^{\mathrm{Inf}}TV - \delta I, \tag{2.3.2}$$

$$\frac{\mathrm{d}V}{\mathrm{d}t} = k^{\mathrm{Prod}}I - cV, \tag{2.3.3}$$

where the number of uninfected cells constantly increases with rate λ, and decreases due to cell death at rate dT and the cells' interaction with infectious virions V. For the latter, infection occurs at rate $k^{\mathrm{Inf}}TV$, which follows mass action kinetics and is proportional to the product of the abundances of uninfected cells T and free virus particles V, respectively. Infected cells produce virus particles with a rate proportional to their abundance $k^{\mathrm{Prod}}I$ and die at rate δI. Free virus particles are removed from the system at rate cV. Equations 2.3.1–2.3.3 represent the basis of several models used to examine measurement data from clinical trials and infected cell cultures (reviewed in [225, 226]), and which can be extended to account for various hypotheses on virus replication, virus evolution, virus persistence, and predict the outcome of antiviral treatment, the host immune response and vaccination campaigns [210, 223, 224, 227]. An important feature of those simple within-host models is the target cell-limitation, i.e., the phasing out of virus production when the population of susceptible target cells is depleted [223, 228]. While the first within-host models described virus dynamics of human immunodeficiency virus (HIV) (reviewed in [229–231]), their principles also apply
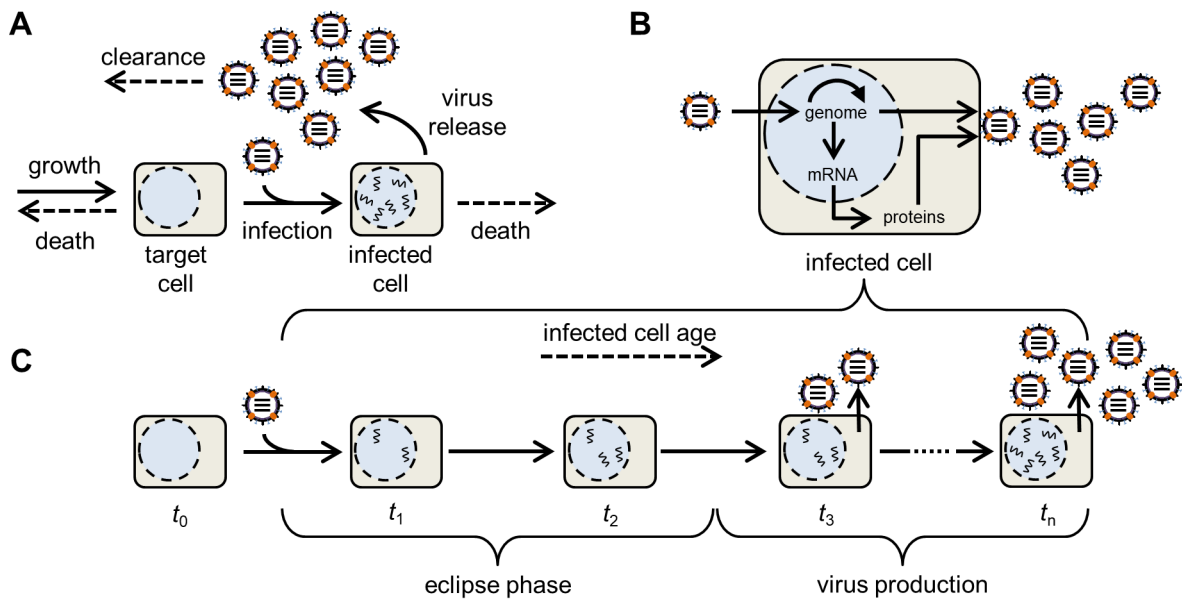
Figure 2.6.: Schemes of virus dynamics models. (A) Standard model of within-host virus dynamics. Susceptible target cells are constantly supplied, can die, or become infected by free virus particles. Infected cells produce viral progeny and undergo virus-induced cell death. Progeny virions infect new target cells or are removed/cleared from the system. (B) Simplified model scheme of the intracellular IAV life cycle. Viral genomes enter the nucleus and synthesize new genome copies and viral transcripts (mRNA). The latter are translated to viral proteins needed to package the viral genomes and form progeny particles. (C) Simplified schematic of a multi-scale frame work using age-segregation of infected cells based on the interlinked single-cell model shown in (B). Furthermore, within-host processes of infection shown in (A) also apply to infected cells in (C).

for other virus-host cell systems (reviewed in [222]). Today, various within-host models describing the virus dynamics of a number of different human viruses are available, e.g., hepatitis B virus (HBV) and hepatitis C virus (HCV) and influenza virus, which were, more recently, followed up by models for Ebola, Dengue and Zika viruses [223, 232, 233].

An iconic contribution to the field of within-host models of virus dynamics was made by Perelson and colleagues whose model-based analysis of measurement data from HIV-positive patients under antiviral treatment uncovered that HIV would rapidly acquire drug resistance through mutations [234, 235]. This lead to the development of combination treatments and, thus, contributed significantly to the fight against HIV. Accordingly, the simulation of antiviral therapy is an important application of successor within-host models, such as for HBV and HCV (reviewed in [223, 226, 236, 237]). While chronic HIV and hepatitis infections and their treatment can last for months and even years, influenza infections are acute and span a much shorter time scale of only a few days. Hence, within-host models of influenza virus dynamics (reviewed in [16, 228]) might have to include the eclipse phase, i.e., the delay between the time point of infection

and the onset of virus release, during which viral components accumulate inside the host [238, 239]. This can be accounted for by delay differential equations (DDEs) or by considering two classes of infected cells: one that is in the eclipse phase and not yet virus-production, and the second, that is releasing progeny viruses. While the latter represents virus production in a more realistic way, models without eclipse phase are able to describe measurement data equally well [239, 240]. In accordance to previous studies, the investigation and prediction of antiviral treatment is also an important application of within-host models of influenza infection [223, 240–243]. For this, modeling studies also suggest a combination therapy to avoid the emergence of drug-resistant virus mutants [244, 245]. To fully describe the progression of influenza *in vivo*, some models also account for the immune response of the host which plays an important role in clearing the virus from the respiratory tract in animals and humans [208, 240, 246, 247]. Thus, several aspects of the immune system, such as the interferon response [223, 240, 248, 249], have already been incorporated into modeling frame works and researchers still strive to obtain a comprehensive mathematical description of the immune system dynamics in response to influenza infections [208, 222, 250, 251].

In addition, within-host models lend themselves well to describe the progression of infection in cell culture experiments and cell culture-based vaccine production. In contrast to *in vivo* infections, experiments in cell culture systems are conducted in a controlled environment and can be frequently sampled. In addition, virus replication can be evaluated in response to system perturbations, which helps to improve our mechanistic understanding of the infection process. Furthermore, they can be applied to estimate antiviral drug efficacy [241] and to perform quantitative comparison of virus replication properties of different virus strains [216, 252]. In particular, the target cell-limitation (explained above) is highly relevant in cell culture systems. In accordance, early models of influenza vaccine production in MDCK cells developed by Möhler *et al.* showed that the virus yield in cell culture is limited by the available number of susceptible target cells [253]. In addition, also the rates of virus production and virus-induced death of infected cells were identified as crucial parameters to optimize virus yields. Moreover, Möhler compared simulations of the model with and without time-delay of virus production by accounting for the eclipse phase with a DDE, and found that virus dynamics were described equally well by both models. This DDE model was extended by Schulze-Horsel *et al.* who implemented an additional DDE to also account for the dynamics of infected cells that undergo virus-induced cell death with a time delay [254]. The model parameters were estimated from flow cytometry data with a high time resolution, which allowed to determine the percentage of uninfected and infected cells, and cells that had undergone virus-induced cell death (apoptosis). Furthermore, the

fluorescence intensity can be used to track the progression of infection, since it increases over time with an increasing number of intracellular viral proteins. Based on this, Sidorenko *et al.* proposed a stochastic population balance model in which the cells' degree of infection is dependent on accumulation and release of viral proteins [255, 256]. For this, they converted the fluorescence intensity measurements into viral protein concentration which was compared to the model simulations to reproduce the corresponding distribution of infected cells. Similarly, also Müller *et al.* used the degree of fluorescence as an internal coordinate to account for the progression of infection in a deterministic population balance model with eclipse phase [219]. Their model nicely reproduces the waves of infection with increasing fluorescence intensity during eclipse phase until onset of virus release and decreased intensity of cells at the end of their productive phase. In particular, the model was calibrated against experimental data from low MOI infections, which are highly relevant in vaccine production (Section 2.2). Clearly, the implementation of such internal coordinates is a step toward describing infection progression by linking cell-to-cell transmission at the host cell population level with events of virus replication at the intracellular level. Models focusing on the latter will be introduced below.

Single-cell models   In contrast to unstructured within-host models, intracellular models of virus replication describe the one-step growth of an individual infected cell, i.e., a single cycle of replication from virus attachment to release of viral progeny (Figure 2.6 B). For this, different state variables are used to describe steps of virus replication in different compartments of the cell. To build comprehensive mathematical frameworks of intracellular virus replication, researchers have been developing mechanistic and quantitative descriptions of particular aspects of the viral life cycle for more than 50 years. This includes models that study virus particle adsorption to cells, virus entry, transcription, RNA splicing, protein translation, genome replication, assembly of virus particles, packaging of virus particles, and release or budding of progeny virus particles from cells (reviewed by [209]). The earliest intracellular models describe the replication of bacteriophages [209, 257] and served as a basis for several other models of human and animal viruses that are available today and contribute to our understanding of the timing and productivity of virus replication steps at the cellular level. They also allow to study how viruses hijack their host cells' biosynthetic machinery and test hypotheses on potential drug targets. The first comprehensive description of the entire life cycle of a human virus was developed by Reddy and Yin for HIV-1 infection [258]. Furthermore, models describing (parts of) the intracellular replication cycle of Semliki Forest virus [259], poliovirus [260], vesicular stomatitis virus [261, 262], baculovirus [263, 264], HBV [265], HCV [266–270], herpes simplex virus 1 [271] and IAV

were developed [11, 18, 272, 273] (reviewed by [209]) and, recently, this list was extended by a model for intracellular Dengue virus replication [274].

For IAV, the first mathematical descriptions of the life cycle focused on virus attachment and entry processes [272, 275]. Later, Sidorenko *et al.* provided the first detailed model of the IAV life cycle to describe virus growth in MDCK cells for vaccine production [11]. This model covered steps of virus attachment and internalization, synthesis of viral genomes and proteins, vRNP packaging and progeny release. Furthermore, this model was used to predict the demand for cellular resources, i.e., nucleotides and amino acids, to produce progeny virions. The model simulations reproduced the virus dynamics well and allowed to test hypotheses that would allow to improve virus yields. However, model parameters, such as RNA and protein synthesis rates, had to be based on text book values due to the limited amount of intracellular virus replication data at that time. Sidorenko's model was further refined in the work of Heldt *et al.* who accounted for well-informed mechanisms of RNA replication and added further details, such as splicing of particular viral transcripts [18]. Furthermore, the model was informed by integrating data on intracellular RNA replication dynamics, which allowed to test competing hypotheses on the regulation of RNA replication. Besides the model by Bazhan and co-workers ([276] in Russian, reviewed by [209]), the model by Heldt *et al.* is the most detailed mathematical description of the IAV life cycle and provides, in large parts, the basis for work conducted within the scope of this thesis and other studies by our group. Among those is a stochastic model of the intracellular IAV life cycle that gives insights into the sources of heterogeneity in virus release of infected cells [277]. In particular, the segmentation of the viral genome provides a source of noise in the replication cycle resulting in numerous unproductive infections, e.g., due to loss of a genome segment early in the life cycle. Furthermore, this stochastic model was also employed to elucidate hypotheses on segment-specific regulation of viral replication by small viral RNAs (svRNAs) [26, 277].

In addition, the deterministic intracellular model described by Heldt *et al.* [18] was integrated into the population scale of virus infection that lead to the development of IAV multi-scale models [37, 278]. Below we will shortly outline multi-scale models available for virus dynamics research.

Multi-scale models Multi-scale infection models describe the infection process by interlinking the within-host level with the single-cell level (Figure 2.6 C). This significantly increases model complexity, however, it also provides a more realistic description of virus growth. For instance, while simple within-host models have to take assumptions on whether or not to account for the eclipse phase of virus release, a multi-scale model readily incorporates the eclipse phase due to its underlying single-cell level which times the

onset of virus release depending on the intracellular kinetics of viral genome and protein synthesis. In contrast, simple within-host models usually have a hard-coded eclipse phase expressed by specific model parameters, which might be difficult to estimate [238].

As explained earlier, the consideration of an internal coordinate, such as degree of infection, by populations balance models [219, 255, 256] provided a first step into this direction. Furthermore, Haseltine and Rawlings formulated a population balance modeling framework to cover both, within-host and single-cell level, and also addressed the challenge of computational cost related to the simulation of such multi-scale model [218, 279]. Moreover, multi-scale models can significantly improve predictions on antiviral drug treatment that targets steps of the intracellular life cycle. For instance works by Guedj *et al.* showed that only a multi-scale approach, that tracks the infection age of cells, can capture viral load data from HCV-positive patients, even though their intracellular description focused on viral genome synthesis only [280, 281]. For HCV, such models by Guedj and other authors [282–284] served well in comparing antiviral drug treatment regimens and modes of action of direct-acting antivirals (reviewed by [223]).

Heldt *et al.* presented a age-seggregated multi-scale model for IAV growth, which combines the intracellular life cycle [18] with cell-to-cell transmission in cell cultures [37]. This model was used to test the impact of putative direct-acting antivirals to predict the outcome of antiviral treatment regimens. For this, most promising antiviral targets to reduce viral load were viral RNA transcription, replication and protein synthesis as well as nuclear export of genomes and virus release. Opposed to that, interfering with early steps in virus replication, i.e., virus entry, only caused a delay in virus release. Furthermore, this study showed that some treatment regimens can be disadvantageous causing an increase in viral titers. This finding underlines the importance of a comprehensive understanding of the virus replication dynamics at the intracellular level. In a follow-up study, this multi-scale model of IAV growth was further refined by our group to capture data from cell cultures infected at different initial conditions [278].

Furthermore, multi-scale models may extend to tissue/organ or whole-organism scale, combining temporal and spatial aspects of the infection process aiming to describe the entire life cycle of the viruses from infection to onset of disease. Moreover, multiple scales of infection are required to build realistic epidemiological models, linking within-host and between-host level, which can be used to study disease spreading and public health interventions [17, 223, 285–287]. For the latter, the classical epidemiological models describing populations of susceptible, infected and recovered individuals (SIR models) are extended to describe spreading of a disease taking into account also the mobility and contact network of individuals [211, 288].

2.3.2. Model analysis techniques

As explained in the previous section, the majority of virus infection models relies on mass action kinetics and can consist of large ODE systems. In addition to implementing reasonable mechanisms of the infection process into mathematical models, their parameterization plays an important role in making meaningful predictions. Parameter values are typically estimated from experimental data, i.e., by fitting the simulated model states to their corresponding measurement value. In some cases, this procedure can be challenging and cause noticeable uncertainty in parameter values. Consequently, the model can only provide unrealistic predictions on the underlying biological systems. To cope with this challenge, parameter estimation procedures are usually followed-up by a model analysis in order to quantify parameter uncertainty and show routes to further improve model construction or experimental design. In the following, we briefly outline the basis of the underlying theories of model analysis techniques applied in this thesis. In addition, Chapter 3 (Models and Methods) provides further details on how model analysis was performed on the various data-model-pairs investigated within the scope of this thesis.

Parameter sensitivity A model parameter is considered sensitive when its perturbation causes a change in the simulation result of at least one of the state variables of the model [289]. For instance, the local sensitivity of a parameter can be assessed using the following coefficient:

$$S_\theta^M = \frac{\delta M\left(\gamma\right)/M\left(\gamma\right)}{\delta\theta/\theta}, \tag{2.3.4}$$

which quantifies the impact of a change in the parameter θ, denoted as $\delta\theta$, on a particular quantity M of the the model output γ, where $\delta M\left(\gamma\right)$ and $M\left(\gamma\right)$ are the model quantities recorded with and without parameter perturbation, respectively [290]. To quantify the change in the model response, different characteristics of the system output can be used, such as the area under the curve, values of state variables in steady-state or at a particular time point relevant for the observed system [290]. Moreover, the weighted sum of squared residuals (SSR) can be used as such characteristic quantity.

$$\frac{\delta M\left(\gamma\right)}{M\left(\gamma\right)} \equiv \frac{1}{N_c N_s} \sum_{s,c} \left[\frac{1}{N_t} \sum_t \left(\frac{y_{s,c}\left(\theta,t\right) - y_{s,c}\left(\theta^\star,t\right)}{\sigma_s} \right)^2 \right], \tag{2.3.5}$$

where the residuals are calculated based on $y_{s,c}\left(\theta,t\right)$ and $y_{s,c}\left(\theta^\star,t\right)$ as the model output of species s in experiment c at time t in response to the original parameter value θ or the perturbed parameter value $\theta^\star$, respectively [291]. The residuals are further normalized by the maximum value of species s (σ_s) or by its standard deviation at the corresponding

experimental condition ($\sigma_{s,c}$), if available. Additionally, the SSR is normalized by the number of measured time points (N_t), number of measured species (N_s), and number of experimental conditions (N_c). Thus, the sensitivity coefficient is a measure of how well a parameter is defined given a particular set of experimental data. For this, a low sensitivity coefficient indicates an ill-defined, i.e., non-identifiable, parameter. Note, that the identifiability of a parameter is not only defined by its local sensitivity, but can be also influenced by other effects, such as parameter correlations and redundancies [289]. To avoid non-identifiability of parameters, the model complexity and the number of parameters should be chosen with respect to the available measurement data. Ideally, each model state can be calibrated against a particular measurement species assessed in multiple independent experiments. According to Gutenkunst *et al.*, mathematical models of biological systems commonly suffer from poorly constrained parameters. Nonetheless, those models can capture measurement data reasonably well and allow for meaningful predictions [291]. Most importantly, the thorough analysis of the underlying model structure together with sensitivity analysis and *in silico* experiments can help to reveal biological mechanisms that are not immediately evident from the experimental data. Moreover, parameter correlations can also help to identify insufficient experimental design or measurement data. For instance, in infection models, a correlation between infection and production rate, or production and clearance rate, shows that the data does not allow to distinguish between those processes. Consequently, new experiments can be designed that allow to assess the kinetics of those processes individually, which continuously drives the systems biological cycle of model-experiment exchange [208].

Parameter confidence intervals   While many models comprise "sloppy" parameters they can still yield insightful simulations and predictions [208, 291]. Yet, in some cases, it might be relevant to estimate a parameter precisely and the confidence of its value needs to be determined. To assess the accuracy of parameter values, several mathematical methods can be applied [289, 292]. In this thesis, we focus on bootstrap algorithms for inferring parameter confidence intervals (reviewed by [292, 293]).

Bootstrapping relies on Monte Carlo sampling and allows to derive the parameter distribution through random re-samples of the available experimental data. For this, we draw a random sample of a species measured in n independent experiments $y = (x_1, x_2, \ldots, x_n)$ and fit the model to this bootstrap sample. Note, that we can also derive Monte Carlo samples from a time series of measurements by drawing a sample value at each time point t_i from a normal distribution $\mathcal{N}(x_i, \sigma_i^2)$ with x_i as the actual measurement and σ_i as its standard deviation. Subsequently, we also obtain a bootstrap sample $y^\star = (x_1^\star, x_2^\star, \ldots, x_n^\star)$ that can be subjected to model fitting. Consequently, we determine

a parameter estimate $\theta^\star$ with respect to the corresponding bootstrap sample $y^\star$. This procedure is performed repeatedly to derive an estimate of the underlying distribution of parameter values for which we can determine the confidence interval. Given a significance level α, we can apply the percentile method where the confidence intervals are equivalent to the central interval between the $100 \cdot \alpha/2$ and the $100 \cdot (1 - \alpha/2)$ percentiles of the estimated parameter distribution [293].

<div align="center">

CHAPTER 3

Models and Methods

</div>

The models used in this thesis are mechanistic, deterministic models that describe the dynamics of IAV infections in animal cell cultures using ODEs. Here, we list and describe the ODEs of the single-cell models that were applied to account for either the impact of host cell factors or the impact of DIPs on virus replication. Furthermore, two descriptions of within-host dynamics of DIP growth in continuous cultivation are presented.

3.1. Intracellular virus replication and host cell factors

We based our analysis of the impact of host cell factors on IAV replication on a detailed mathematical description of the intracellular viral life cycle previously developed by the BPE group. That model was mainly calibrated against experimental data obtained from adherent infected MDCK cells [18] and will be presented in the first part of this section. To then predict virus replication and release for parental and genetically engineered A549 cells, we assumed that key steps of the viral life cycle do not change mechanistically, but only show differences in their kinetic parameter values and their dynamics due to a change in the host cell system. Further assumptions and variables added to the model to account for the impact of the host cell on virus replication are outlined in the second part of this section. The latter approach was published in the Journal *PLoS Computational Biology* by Laske and Bachmann *et al.* [294] and parts of this publication are used here and throughout this thesis.

3.1.1. Single-cell model of intracellular virus replication

In the following paragraphs, we list the equations of the ODE model used to simulate IAV replication in a single cell. This model is identical to a model that was previously published by Heldt *et al.* [18]. A scheme of the model is shown in Chapter 2 this thesis in Figure 2.3.

Virus entry The binding of extracellular virus particles V^{Ex} to binding sites of high-affinity B_{hi} and low-affinity B_{lo} is based on investigations by

Nunes-Correia *et al.* [272] and described by the following equations.

$$\frac{\mathrm{d}V^{\mathrm{Ex}}}{\mathrm{d}t} = k_{\mathrm{hi}}^{\mathrm{Dis}} V_{\mathrm{hi}}^{\mathrm{Att}} + k_{\mathrm{lo}}^{\mathrm{Dis}} V_{\mathrm{lo}}^{\mathrm{Att}} - \left(k_{\mathrm{hi}}^{\mathrm{Att}} B_{\mathrm{hi}} + k_{\mathrm{lo}}^{\mathrm{Att}} B_{\mathrm{lo}} \right) V^{\mathrm{Ex}}, \tag{3.1.1}$$

$$\text{with} \quad B_{\mathrm{n}} = B_{\mathrm{n}}^{\mathrm{tot}} - V_{\mathrm{n}}^{\mathrm{Att}}, \quad n \in \{\mathrm{hi}, \mathrm{lo}\}. \tag{3.1.2}$$

Here, the number of extracellular virions V^{Ex} is equal to the MOI, i.e., the number of infectious virus particles added at time of infection. Virions attach to free binding sites B_{n} with rate $k_{\mathrm{n}}^{\mathrm{Att}}$. In accordance to Nunes-Correira *et al.* [272], fast recycling of receptors is assumed, such that the total number of binding sites $B_{\mathrm{n}}^{\mathrm{tot}}$ follows from the conservation Equation (3.1.2). Attached virions $V_{\mathrm{n}}^{\mathrm{Att}}$ either dissociate from binding sites B_{n} with rate $k_{\mathrm{n}}^{\mathrm{Dis}}$ or are taken up by the cell via receptor-mediated endocytosis with rate k^{En}. Then, virions in endosomes V^{En} can either fuse with the endosomal membrane and the viral genome is released to the cytoplasm V^{cyt}, or, virions in endosomes are degraded with rate $k_{\mathrm{En}}^{\mathrm{Deg}}$.

$$\frac{\mathrm{d}V_{\mathrm{n}}^{\mathrm{Att}}}{\mathrm{d}t} = k_{\mathrm{n}}^{\mathrm{Att}} B_{\mathrm{n}} V^{\mathrm{Ex}} - \left(k_{\mathrm{n}}^{\mathrm{Dis}} + k^{\mathrm{En}} \right) V_{\mathrm{n}}^{\mathrm{Att}}, \tag{3.1.3}$$

$$\frac{\mathrm{d}V^{\mathrm{En}}}{\mathrm{d}t} = k^{\mathrm{En}} \left(V_{\mathrm{hi}}^{\mathrm{Att}} + V_{\mathrm{lo}}^{\mathrm{Att}} \right) - \left(k^{\mathrm{Fus}} + k_{\mathrm{En}}^{\mathrm{Deg}} \right) V^{\mathrm{En}}, \tag{3.1.4}$$

$$\text{with} \quad k_{\mathrm{n}}^{\mathrm{Dis}} = \frac{k_{\mathrm{n}}^{\mathrm{Att}}}{k_{\mathrm{n}}^{\mathrm{Eq}}} \quad \text{and} \quad k_{\mathrm{En}}^{\mathrm{Deg}} = \frac{1 - F_{\mathrm{Fus}}}{F_{\mathrm{Fus}}} k^{\mathrm{Fus}}, \quad 0 < F_{\mathrm{Fus}} \leq 1, \tag{3.1.5}$$

where fusion of virions in endosomes occurs with rate k^{Fus} which combines the processes of trafficking and acidification of the early endosomes, fusion of the viral and endosomal membrane and uncoating of the virus particle. Furthermore, we accounted for the experimental finding that only a fraction of virions are able to fuse [50, 295], which is expressed as the fraction of fusion-competent virions F_{Fus}.

Viral RNA replication Upon fusion, vRNPs are released to the cytoplasm Vp^{cyt} and imported to the nucleus with rate k^{Imp} [44, 52]. Here, nuclear vRNPs Vp^{nuc} are template for viral mRNA R^{M} and cRNA R^{C} [59], where cRNAs serve as replication intermediate and are template for vRNA synthesis. Note, that cRNAs and vRNAs are rapidly degraded unless they are stabilized in ribonucleoprotein complexes, cRNPs and vRNPs, respectively [58]. For this, encapsidation of cRNAs and vRNAs occurs by, first, binding of the viral polymerase with rate $k_{\mathrm{RdRp}}^{\mathrm{Bind}}$ and, secondly, binding of multiple copies of NP with rate $k_{\mathrm{NP}}^{\mathrm{Bind}}$. Experimental findings convey that the majority of vRNAs (and cRNAs) of different genome segments show similar levels throughout infection [296, 297]. Based on those findings, here, replication of individual segments was neglected. Toward the end

of virus replication, nuclear vRNPs Vp^{nuc} are bound by M1 and NEP, which mediates nuclear export of vRNPs [45]. According to literature [71–73], binding of M1 inhibits the transcriptase activity of vRNPs. Once bound by M1, the M1-vRNP complexes do not serve as template for RNA synthesis any longer. Together, virus replication can be described by the following equations:

$$\frac{\mathrm{d}Vp^{\text{cyt}}}{\mathrm{d}t} = 8k^{\text{Fus}}V^{\text{En}} - k^{\text{Imp}}Vp^{\text{cyt}}, \tag{3.1.6}$$

$$\frac{\mathrm{d}Vp^{\text{nuc}}}{\mathrm{d}t} = k^{\text{Imp}}Vp^{\text{cyt}} + k_{\text{NP}}^{\text{Bind}}P_{\text{NP}}R_{\text{RdRp}}^{\text{V}} - \left(k_{\text{M1}}^{\text{Bind}}P_{\text{M1}} + k_{\text{Rnp}}^{\text{Deg}}\right)Vp^{\text{nuc}}, \tag{3.1.7}$$

$$\frac{\mathrm{d}R^{\text{V}}}{\mathrm{d}t} = k_{\text{V}}^{\text{Syn}}Cp - k_{\text{RdRp}}^{\text{Bind}}P_{\text{RdRp}}R^{\text{V}} - k_{\text{R}}^{\text{Deg}}R^{\text{V}}, \tag{3.1.8}$$

$$\frac{\mathrm{d}R_{\text{RdRp}}^{\text{V}}}{\mathrm{d}t} = k_{\text{RdRp}}^{\text{Bind}}P_{\text{RdRp}}R^{\text{V}} - k_{\text{NP}}^{\text{Bind}}P_{\text{NP}}R_{\text{RdRp}}^{\text{V}} - k_{\text{RRdRp}}^{\text{Deg}}R_{\text{RdRp}}^{\text{V}}, \tag{3.1.9}$$

$$\frac{\mathrm{d}Vp_{\text{M1}}^{\text{nuc}}}{\mathrm{d}t} = k_{\text{M1}}^{\text{Bind}}P_{\text{M1}}Vp^{\text{nuc}} - \left(k^{\text{Exp}}P_{\text{NEP}} + k_{\text{Rnp}}^{\text{Deg}}\right)Vp_{\text{M1}}^{\text{nuc}}, \tag{3.1.10}$$

$$\frac{\mathrm{d}Vp_{\text{M1}}^{\text{cyt}}}{\mathrm{d}t} = k^{\text{Exp}}P_{\text{NEP}}Vp_{\text{M1}}^{\text{nuc}} - 8r^{\text{Rel}} - k_{\text{Rnp}}^{\text{Deg}}Vp_{\text{M1}}^{\text{cyt}}, \tag{3.1.11}$$

$$\frac{\mathrm{d}R^{\text{C}}}{\mathrm{d}t} = k_{\text{C}}^{\text{Syn}}Vp^{\text{nuc}} - k_{\text{RdRp}}^{\text{Bind}}P_{\text{RdRp}}R^{\text{C}} - k_{\text{R}}^{\text{Deg}}R^{\text{C}}, \tag{3.1.12}$$

$$\frac{\mathrm{d}R_{\text{RdRp}}^{\text{C}}}{\mathrm{d}t} = k_{\text{RdRp}}^{\text{Bind}}P_{\text{RdRp}}R^{\text{C}} - k_{\text{NP}}^{\text{Bind}}P_{\text{NP}}R_{\text{RdRp}}^{\text{C}} - k_{\text{RRdRp}}^{\text{Deg}}R_{\text{RdRp}}^{\text{C}}, \tag{3.1.13}$$

$$\frac{\mathrm{d}Cp}{\mathrm{d}t} = k_{\text{NP}}^{\text{Bind}}P_{\text{NP}}R_{\text{RdRp}}^{\text{C}} - k_{\text{Rnp}}^{\text{Deg}}Cp, \tag{3.1.14}$$

where $k_{\text{V}}^{\text{Syn}}$ and $k_{\text{C}}^{\text{Syn}}$ are the rates of vRNA and cRNA synthesis, in Equation (3.1.8) and Equation (3.1.12), respectively. Nascent RNAs are degraded by nucleases with rate $k_{\text{R}}^{\text{Deg}}$ or bind to viral polymerases P_{RdRp} as a first step of encapsidation. Those intermediate complexes ($R_{\text{RdRp}}^{\text{C}}$, $R_{\text{RdRp}}^{\text{V}}$) can degrade with rate $k_{\text{RRdRp}}^{\text{Deg}}$ before they are finally stabilized by binding of NP (P_{NP}). RNPs are still sensitive to digestion by RNases [298], however, decay at a low rate $k_{\text{Rnp}}^{\text{Deg}}$. This assumption was, however, dropped for incoming cytoplasmic vRNPs (Equation (3.1.6)) to account for experimental findings that vRNA levels are constant in cells treated with the translation inhibitor cycloheximide (CHX) [58]. Nuclear export of M1-vRNP complexes $Vp_{\text{M1}}^{\text{nuc}}$ is mediated by binding of NEP P_{NEP} and lumped into the nuclear export rate k^{Exp} in Equation (3.1.10). The cytoplasmic NEP-M1-vRNP complexes $Vp_{\text{M1}}^{\text{cyt}}$ then traffic to the plasma membrane, where virus progeny are assembled and released (see Equation (3.1.26)).

Viral mRNA and protein synthesis   Based on experimental findings, viral mRNA levels of different genome segments differ significantly during infections [296, 297]. Thus, and opposed to vRNA and cRNA synthesis (Equations (3.1.6)–(3.1.14)), viral mRNA synthesis from nuclear vRNPs Vp^{nuc} is modeled individually for each genome segment k.

$$\frac{\mathrm{d}R_{\mathrm{k}}^{\mathrm{M}}}{\mathrm{d}t} = \frac{k_{\mathrm{M}}^{\mathrm{Syn}}}{L_{\mathrm{k}}}\frac{Vp^{\mathrm{nuc}}}{8} - k_{\mathrm{M}}^{\mathrm{Deg}}R_{\mathrm{k}}^{\mathrm{M}}, \quad k = 1,\ldots,8, \tag{3.1.15}$$

where the the total number of Vp^{nuc} is divided by eight to calculate the number of available vRNPs of each individual genome segment. Since nuclear export of viral mRNAs is fast [299], this process is neglected and assumed that mRNAs are instantly available for translation. According to experiments, protein synthesis is directly proportional to the corresponding mRNA levels [300]. Here, we considered only the production of structural proteins and assumed a homogeneous distribution of molecules in the cell. The polymerase subunits PB2, PB1 and PA are translated from mRNAs $R_{\mathrm{k}}^{\mathrm{M}}$ of segments 1–3, respectively. They form the hetero-trimeric viral polymerase complex P_{RdRp} , that is attaching to nascent strands of vRNAs R^{V} and cRNAs R^{C}.

$$\frac{\mathrm{d}P_{\mathrm{PB1}}}{\mathrm{d}t} = \frac{k_{\mathrm{P}}^{\mathrm{Syn}}}{D_{\mathrm{Rib}}}R_2^{\mathrm{M}} - k^{\mathrm{RdRp}}P_{\mathrm{PB1}}P_{\mathrm{PB2}}P_{\mathrm{PA}}, \tag{3.1.16}$$

$$\frac{\mathrm{d}P_{\mathrm{PB2}}}{\mathrm{d}t} = \frac{k_{\mathrm{P}}^{\mathrm{Syn}}}{D_{\mathrm{Rib}}}R_1^{\mathrm{M}} - k^{\mathrm{RdRp}}P_{\mathrm{PB1}}P_{\mathrm{PB2}}P_{\mathrm{PA}}, \tag{3.1.17}$$

$$\frac{\mathrm{d}P_{\mathrm{PA}}}{\mathrm{d}t} = \frac{k_{\mathrm{P}}^{\mathrm{Syn}}}{D_{\mathrm{Rib}}}R_3^{\mathrm{M}} - k^{\mathrm{RdRp}}P_{\mathrm{PB1}}P_{\mathrm{PB2}}P_{\mathrm{PA}}, \tag{3.1.18}$$

$$\frac{\mathrm{d}P_{\mathrm{RdRp}}}{\mathrm{d}t} = k^{\mathrm{RdRp}}P_{\mathrm{PB1}}P_{\mathrm{PB2}}P_{\mathrm{PA}} - k_{\mathrm{RdRp}}^{\mathrm{Bind}}P_{\mathrm{RdRp}}\left(R^{\mathrm{V}} + R^{\mathrm{C}}\right) - (N_{\mathrm{P_{RdRp}}} - 8)r^{\mathrm{Rel}}. \tag{3.1.19}$$

Furthermore, NP proteins, encoded by segment 5, are required to form replication-competent RNPs, which participate in viral replication and transcription. In particular, vRNPs are also exported from the nucleus upon binding of M1 and NEP, encoded by spliced mRNAs of segment 7 $(1 - F_{\mathrm{Spl_7}})$ and segment 8 $(F_{\mathrm{Spl_8}})$, respectively.

$$\frac{\mathrm{d}P_{\mathrm{NP}}}{\mathrm{d}t} = \frac{k_{\mathrm{P}}^{\mathrm{Syn}}}{D_{\mathrm{Rib}}}R_5^{\mathrm{M}} - \frac{L^{\mathrm{V}}}{N_{\mathrm{NP}}^{\mathrm{Nuc}}}k_{\mathrm{NP}}^{\mathrm{Bind}}P_{\mathrm{NP}}\left(R_{\mathrm{RdRp}}^{\mathrm{V}} + R_{\mathrm{RdRp}}^{\mathrm{C}}\right) - (N_{\mathrm{P_{NP}}} - 8\frac{L^{\mathrm{V}}}{N_{\mathrm{NP}}^{\mathrm{Nuc}}})r^{\mathrm{Rel}}, \tag{3.1.20}$$

$$\frac{\mathrm{d}P_{\mathrm{M1}}}{\mathrm{d}t} = \frac{k_{\mathrm{P}}^{\mathrm{Syn}}}{D_{\mathrm{Rib}}}\left(1 - F_{\mathrm{Spl_7}}\right)R_7^{\mathrm{M}} - \frac{L^{\mathrm{V}}}{N_{\mathrm{M1}}^{\mathrm{Nuc}}}k_{\mathrm{M1}}^{\mathrm{Bind}}P_{\mathrm{M1}}Vp^{\mathrm{nuc}} - (N_{\mathrm{P_{M1}}} - 8\frac{L^{\mathrm{V}}}{N_{\mathrm{M1}}^{\mathrm{Nuc}}})r^{\mathrm{Rel}}, \tag{3.1.21}$$

$$\frac{\mathrm{d}P_{\mathrm{NEP}}}{\mathrm{d}t} = \frac{k_{\mathrm{P}}^{\mathrm{Syn}}}{D_{\mathrm{Rib}}}F_{\mathrm{Spl_8}}R_8^{\mathrm{M}} - \frac{L^{\mathrm{V}}}{N_{\mathrm{NEP}}^{\mathrm{Nuc}}}k^{\mathrm{Exp}}P_{\mathrm{NEP}}Vp_{\mathrm{M1}}^{\mathrm{nuc}} - (N_{\mathrm{P_{NEP}}} - 8\frac{L^{\mathrm{V}}}{N_{\mathrm{NEP}}^{\mathrm{Nuc}}})r^{\mathrm{Rel}}. \tag{3.1.22}$$

The viral surface proteins HA, NA and M2, which are encoded by segment 4, segment 6 and segment 7, respectively, are required for the formation of progeny virus particles and leave the cell during virus release. For M2, the splicing of segment 7 is accounted for by including the fraction of spliced M2-mRNA F_{Spl7}. The M1 and other viral proteins are also incorporated into budding virions and leave the cell with release rate r^{Rel}.

$$\frac{\mathrm{d}P_{\text{HA}}}{\mathrm{d}t} = \frac{k_P^{\text{Syn}}}{D_{\text{Rib}}} R_4^{\text{M}} - N_{P_{\text{HA}}} r^{\text{Rel}}, \tag{3.1.23}$$

$$\frac{\mathrm{d}P_{\text{NA}}}{\mathrm{d}t} = \frac{k_P^{\text{Syn}}}{D_{\text{Rib}}} R_6^{\text{M}} - N_{P_{\text{NA}}} r^{\text{Rel}}, \tag{3.1.24}$$

$$\frac{\mathrm{d}P_{\text{M2}}}{\mathrm{d}t} = \frac{k_P^{\text{Syn}}}{D_{\text{Rib}}} F_{\text{Spl7}} R_7^{\text{M}} - N_{P_{\text{M2}}} r^{\text{Rel}}. \tag{3.1.25}$$

To account for experimental findings [296], we implemented a negative correlation between the length of an mRNA and its abundance. For this, we implemented a length-dependent mRNA synthesis rate k_M^{Syn} which is scaled with the length L_i of its corresponding, unspliced mRNA of segment i in Equation (3.1.15). Besides, we assume that all mRNAs degrade with the same rate k_M^{Deg}. During protein synthesis k_P^{Syn}, multiple ribosomes can bind to an individual mRNA. This was accounted for by implementing the distance between two adjacent ribosomes D_{Rib} [301]. The number of proteins N_{P_j} of species j that leave the cell due to virus budding is based on literature values and the stoichiometry of virus replication. For instance, measurements showed that the number of polymerases in a virion is greater than eight, i.e., the eight polymerases attached to the daughter vRNPs [30]. Hence, the difference was accounted for by $(N_{P_{\text{RdRp}}} - 8)$ in Equation (3.1.19). Similarly, the amount of viral proteins in NEP-M1-vRNP complexes was determined by referring the number of nucleotides bound by the respective proteins, $N_{\text{NP}}^{\text{Nuc}}$, $N_{\text{M1}}^{\text{Nuc}}$, and $N_{\text{NEP}}^{\text{Nuc}}$, to the average length of the vRNAs L_V (Equations (3.1.20)–(3.1.22)).

Virus assembly and release   After nuclear export, progeny vRNPs $Vp_{\text{M1}}^{\text{cyt}}$ and structural viral proteins P_j assemble at the plasma membrane to form progeny particles. For this, a simple description is used, where the number of released virions V^{Rel} directly depends on the virus release rate k^{Rel}, the number of availabe $Vp_{\text{M1}}^{\text{cyt}}$ and P_j that influence virus release in a Michaelis-Menten-like fashion.

$$\frac{\mathrm{d}V^{\text{Rel}}}{\mathrm{d}t} = r^{\text{Rel}} = k^{\text{Rel}} Vp_{\text{M1}}^{\text{cyt}} \prod_j \frac{P_j}{P_j + K_{V^{\text{Rel}}} N_{P_j}}, \tag{3.1.26}$$

$$\text{with} \quad j \in \{\text{RdRp}, \text{HA}, \text{NP}, \text{NA}, \text{M1}, \text{M2}, \text{NEP}\},$$

for which sufficient amounts of proteins of type j to form one virion N_{P_j} have to be present. Here, half the maximum release rate is reached when enough proteins are available to form the number of K_{VRel} virions. To account for the observation that the expression of NA at the cell membrane cleaves sialic acids and prevents superinfection [302], we neglected re-infection of a cell by progeny virions.

3.1.2. Modeling virus-host cell interactions in A549 cells

Based on the mathematical description of IAV replication in Section 3.1.1 [18], we analyzed the impact of specific host cell factors on virus replication in A549 cells. In general, we assume that cellular resources, such as amino acids, nucleotides, ribosomes as well as other host cell factors are abundant and do not limit virus replication, which was assumed previously in several other research studies [11, 209, 257, 262, 266]. However, due to the change in the host cell system, we re-parameterized the model to measurements obtained from infected A549 cells for nuclear vRNP import, viral replication, viral transcription and virus release based on experimental data obtained for infected A549 cells (Figure 4.1, Section 4.1.1). Subsequently, we used the A549-based model to analyze and predict changes in virus replication in cell lines overexpressing a single host cell factor or multiple host cell factors simultaneously, namely CEACAM6, FANCG, NXF1, PLD2, XAB2. For this, we took several assumptions and performed simple model extensions, which will be outlined in the following paragraphs.

Nuclear import of viral genomes   As an extension of the original version of this model (Section 3.1.1, [18]), we computed the percentage of nuclear vRNPs $frac_{Rnp}^{nuc}$ to fit measurements of nuclear vRNP import obtained by imaging flow cytometry (Figure 4.4, Section 4.1.2).

$$Rnp^{cyt} = 8V^{En} + Vp^{cyt} + Vp_{M1}^{cyt}, \tag{3.1.27}$$

$$Rnp^{nuc} = Vp^{nuc} + Vp_{M1}^{nuc}, \tag{3.1.28}$$

$$frac_{Rnp}^{nuc} = \left(\frac{Rnp^{nuc}}{Rnp^{nuc} + Rnp^{cyt}} \right) \cdot 100, \tag{3.1.29}$$

where Rnp^{cyt} and Rnp^{nuc} denote all vRNPs within the cytoplasm and nucleus of the cell, respectively.

Model variables for segment-specific RNA levels   In order to estimate RNA synthesis rates, we compared measurements of intracellular RNA levels to simulated values. For this, we determined the total number of vRNAs (R_{tot}^{V}) and cRNAs (R_{tot}^{C}) by summation

over all viral components that contain the respective RNA species.

$$R_{\mathrm{tot}}^{\mathrm{V}} = 8 \left(V_{\mathrm{hi}}^{\mathrm{Att}} + V_{\mathrm{lo}}^{\mathrm{Att}} + V^{\mathrm{En}} \right) + Vp^{\mathrm{cyt}} + Vp^{\mathrm{nuc}} + R^{\mathrm{V}} + R_{\mathrm{RdRp}}^{\mathrm{V}} + Vp_{\mathrm{M1}}^{\mathrm{nuc}} + Vp_{\mathrm{M1}}^{\mathrm{cyt}}, \quad (3.1.30)$$

$$R_{\mathrm{tot}}^{\mathrm{C}} = R^{\mathrm{C}} + R_{\mathrm{RdRp}}^{\mathrm{C}} + Cp. \tag{3.1.31}$$

Since the original model does not distinguish replication of individual genome segments, the simulated RNA level of a specific segment is obtained by dividing $R_{\mathrm{tot}}^{\mathrm{V}}$ and $R_{\mathrm{tot}}^{\mathrm{C}}$ by eight, which can be compared to quantitative reverse transcription polymerase chain reaction (RT-qPCR) measurements, e.g. of segment 5 in Figure 4.1 (Section 4.1.1).

Estimation of parameters and parameter uncertainties Model parameters were estimated in two subsequent steps. First, the nuclear import rate k^{Imp} was estimated by fitting the simulated fraction of nuclear vRNPs $frac_{\mathrm{Rnp}}^{\mathrm{nuc}}$ to the mean of the relative fluorescence intensity (FI) of the nucleus $frac_{\mathrm{Int}}^{\mathrm{nuc}}$ determined by imaging flow cytometry (Figure 4.4, Section 4.1.2). For this, we assumed that the relative increase in FI of the nucleus is directly correlated to the increase in the fraction of nuclear vRNPs caused by nuclear import of the viral genomes which can be stained by a specific antibody. In our experiments, we observed an offset for $frac_{\mathrm{Int}}^{\mathrm{nuc}}$ of approximately $50\,\%$ at the time point of infection, which is related to the background signal of the nucleus and normally comprises between 40–60 % of the cell's area evaluated during image analysis. To account for this background signal, we applied an offset to the simulation values of $frac_{\mathrm{Rnp}}^{\mathrm{nuc}}$. Since offset values differed slightly between cell lines and showed occasionally high standard errors (Figure 4.4, Section 4.1.2), we also estimated this offset value and optimized it with respect to the arithmetic mean and standard error of the first measurement point at zero h post infection (p.i.) for each cell line. To fit with parameter set θ, we minimized the least-squares prediction error for all available data points at time point t weighted with the maximum measurement value:

$$\min_{\theta} \sum_{t=t_0}^{t_{end}} \left(\frac{frac_{\mathrm{Rnp}}^{\mathrm{nuc}}(t) - frac_{\mathrm{Int}}^{\mathrm{nuc}}(t)}{\max(frac_{\mathrm{Int}}^{\mathrm{nuc}})} \right)^2. \tag{3.1.32}$$

After optimization of the nuclear import rate k^{Imp}, we fitted our model to intracellular measurements of vRNA, cRNA and mRNA levels obtained from experiments at MOI 50 as well as to progeny particle numbers per cell for experiments at MOI 1 (Figure 4.5 and Figure 4.6, Section 4.1.2). The corresponding set of kinetic parameters θ was estimated simultaneously by minimizing the least-squares prediction error based on the decadic logarithm of all state variables n, whereby the error of each variable s was weighted with

its maximum measurement value:

$$\min_{\theta} \sum_{s}^{n} \sum_{t=t_1}^{t_{end}} \left(\frac{\log_{10}\left(y_s\left(t\right)\right) - \log_{10}\left(y_s^D\left(t\right)\right)}{\max(\log_{10}\left(y_s^D\right))} \right)^2, \tag{3.1.33}$$

where y_s and y_s^D denote the simulated and measured values of variable s, respectively. To synchronize infection and facilitate parameter inference, infections experiments were conducted at a high MOI. Thus, due to the high virus concentration at time of infection, RT-qPCR already detected vRNA copies as soon as 1 h p.i. (Figure 4.5 bottom panel, Section 4.1.2). This value cannot be caused by an immediate uptake of all virions but rather relates to vRNAs inside virus particles and/or free vRNAs attached to the cells. Therefore, we applied the intracellular vRNA measurement value at 1 h p.i. as an offset to the simulated amount of vRNAs, as done before similarly in another modeling study of our group [37]. In contrast to this previous study, we did not apply offsets to viral mRNA and cRNA levels, as these RNA species are not part of virus particles and are usually not present in the seed virus supernatant. In particular, cRNA levels at 1 h p.i. were below or close to one copy per cell and have no significant impact on simulation results. Finally, approximately 10 copies of mRNA per cell were detected at 1 h p.i. Since mRNA synthesis starts as early as vRNPs reach the nucleus, these mRNAs are a product of primary transcription and cannot be considered as a plain mRNA offset. The parameter distributions were determined by parametric bootstrapping performing multiple model fits to 3000 random re-samples of the experimental data according to their mean and standard deviation, as detailed elsewhere [293]. We set the medians of the resulting parameter distributions as parameter optima to perform simulations. For the SGO candidate FANCG, only duplicate measurements of the intracellular viral RNA were available. Therefore, we considered a relative standard error of 50 %, which was the average relative standard error of all other RNA measurements performed in this study.

***In silico* analysis of cell lines overexpressing a single host cell gene** The modeling approaches in this work used to simulate virus replication in genetically engineered cell lines are based on the simplifying assumption that each step of the virus life cycle is directly dependent on the presence of relevant host cell factors and that their influence is changed by manipulating the expression of the corresponding genes. For instance, if a host cell factor crucial for vRNA synthesis is knocked down, the efficiency of vRNA synthesis is reduced as well, resulting in a lower vRNA synthesis rate. When the same host cell factor is overexpressed, vRNA replication is enhanced, which results in a higher vRNA synthesis rate. Using this assumption, we determined the optimal value for individual kinetic parameters of the model by maximizing the number of released progeny virions at

24 h p.i. To predict biologically reasonable values, we constrained the parameter search by a lower bound of factor 0.2 and an upper bound of factor 5 of the original parameter values, respectively.

In silico analysis of cell lines overexpressing multiple host cell genes Cell lines analyzed in this study were genetically modified by lentiviruses to modify the expression of host cell factors relevant for IAV replication. Gene editing constructs delivered by lentiviruses are integrated at different chromosomal locations, showing patterns of favored target sites depending on transcriptional activity [303, 304]. However, we can anticipate that individual cells within a transduced cell population will show heterogeneity with respect to levels of relative overexpression. Consequently, the transduction of more than one overexpression construct leads to an even larger heterogeneity in gene expression levels. To simulate IAV production of cell lines overexpressing multiple host cell genes (MGO), we account for the integration of multiple gene constructs by randomly compiling new parameterizations of the single-cell model. More precisely, we assume that IAV can propagate in an individual cell of an MGO population with random combinations of kinetic parameters as determined before in detailed characterizations of populations of cell lines overexpressing a single host cell gene (SGO). In addition, to account for the adverse impacts by off-target effects during lentiviral transduction, we also included the parameter set of the unmodified parental A549 cell line for randomization. To facilitate the interpretation of simulation results for MGOs, we simulated IAV replication with randomly assembled parameter sets for a single-cell infection at MOI 1 for 48 h p.i. In a next step, we evaluated each simulation with respect to maximum virus yield and the time point of first virus release, i.e., the time p.i. when the first simulated virus particle was released ($V^{\mathrm{Rel}} \geq 1$). To assure that a sufficient number of simulations was performed that would allow reasonable conclusions on MGO single cell infections, we repeated simulations with randomized parameter sets n times until the relative difference between the mean of $n-1$ and mean of n simulated maximum virus yields reached 1×10^{-8}.

Simulation and computation Model Equations (3.1.1)–(3.1.26) were solved numerically using the CVODE routine from SUNDIALS [305] on a Linux-based system. Values of the model parameters of the original single-cell model (Section 3.1.1, [18]) and those for the different A549 cell lines are given in the appendix Table A.1 and Table A.3, respectively. Model files and experimental data were handled within the Systems Biology Toolbox 2 [306] for MATLAB (version 8.0.0.783 R2012b). Parameter values were estimated by the least-squares method as explained before (see paragraph "Parameter estimation"), using the global stochastic optimization algorithm fSSm [307].

Statistics   To determine the significance level of differences in parameter distributions between parental A549 and SGOs we performed a one-sided Z test (Gauss test) with mean $\bar{p}$ and variance σ^2 determined from the empiric parameter distributions to compute the following test statistic Z:

$$Z = \frac{\bar{p}_{A549} - \bar{p}_{SGO}}{\sqrt{\frac{\sigma^2_{A549}}{n} + \frac{\sigma^2_{SGO}}{m}}}. \tag{3.1.34}$$

For this, the variance is usually normalized by the sample sizes n and m. However, we set the sample sizes to one instead of 3000 for the number of bootstrapped re-samples, since the artificially high sample size is otherwise biasing the test result. This was also done previously by others to compare parameters of mutant to wild type viruses [252]. Following their approach, we generally assume that parameters are normally distributed. Only if parameter distributions followed a log-normal form, namely the vRNA synthesis rate k_V^{Syn} and the virus release rate k^{Rel}, the test statistics were calculated based on the decadic logarithm of these parameters. To determine statistical significance in differences of measurements from SGOs and the parental A549 cell line, the Kruskal-Wallis test was performed as available in MATLAB (version 8.0.0.783 R2012b).

3.2. Intracellular replication of viral deletion mutants

The mathematical single-cell models used to describe the replication of influenza defective interfering (DI) RNAs are extensions of the model of intracellular IAV replication introduced in the previous section (Equations (3.1.1)–(3.1.26), [18]). To account for different modes of DI RNA interference, we implemented three different mechanisms to describe an advantage of the DI RNA at the corresponding steps of the viral life cycle. First, we will present the extended version of the basic single-cell model that, unlike [18], explicitly accounts for the replication of individual genome segments. Second, we will present additional equations that were used to account for the different modes of interference. Here, the approach to model an enhanced DI RNA synthesis was developed in a joint work with colleagues of the BPE group [26, 308] and published in the *Virus Research* article by Laske and Heldt *et al.* (2016) [309].

3.2.1. Basic model of intracellular DI RNA replication

The following equations describe the replication of a DI RNA of segment 1 (S1), encoding PB2. We first chose to model a DI S1 as a representative of the DI RNAs originating from the polymerase-encoding genome segments which are the most abundant DI RNAs found in virus preparations [120, 122]. A complete list of model equations accounting for growth of RNA deletion mutants of S1 as well as of segments 4–8 can be found in the appendix (Section B.5 and Section B.6).

Virus entry Since STV and DIPs are antigenically identical, we assumed that uptake of both STVs and DIPs follows the same mechanisms. Here, entry of STVs is described according to Equations (3.1.1)–(3.1.4) and we added similar equations for the entry of DIPs.

$$\frac{\mathrm{d}D^{\mathrm{Ex}}}{\mathrm{d}t} = k_{\mathrm{hi}}^{\mathrm{Dis}} D_{\mathrm{hi}}^{\mathrm{Att}} + k_{\mathrm{lo}}^{\mathrm{Dis}} D_{\mathrm{lo}}^{\mathrm{Att}} - \left(k_{\mathrm{hi}}^{\mathrm{Att}} B_{\mathrm{hi}} + k_{\mathrm{lo}}^{\mathrm{Att}} B_{\mathrm{lo}} \right) D^{\mathrm{Ex}}, \tag{3.2.1}$$

$$\text{for} \quad B_{\mathrm{n}} = B_{\mathrm{n}}^{\mathrm{tot}} - V_{\mathrm{n}}^{\mathrm{Att}} - D_{\mathrm{n}}^{\mathrm{Att}}, \quad n \in \{\mathrm{hi}, \mathrm{lo}\}, \tag{3.2.2}$$

$$\frac{\mathrm{d}D_{\mathrm{n}}^{\mathrm{Att}}}{\mathrm{d}t} = k_{\mathrm{n}}^{\mathrm{Att}} B_{\mathrm{n}} D^{\mathrm{Ex}} - \left(k_{\mathrm{n}}^{\mathrm{Dis}} + k^{\mathrm{En}} \right) D_{\mathrm{n}}^{\mathrm{Att}}, \tag{3.2.3}$$

$$\frac{\mathrm{d}D^{\mathrm{En}}}{\mathrm{d}t} = k^{\mathrm{En}} \left(D_{\mathrm{hi}}^{\mathrm{Att}} + D_{\mathrm{lo}}^{\mathrm{Att}} \right) - \left(k^{\mathrm{Fus}} + k_{\mathrm{En}}^{\mathrm{Deg}} \right) D^{\mathrm{En}}, \tag{3.2.4}$$

where V and D denote STVs and DIPs, respectively. During receptor-mediated endocytosis of the virions, we assume fast recycling of receptors, such that the number of free binding sites B_{n} follows from the conservation Equation (3.2.2), where $V_{\mathrm{n}}^{\mathrm{Att}}$ and

D_n^{Att} denote the number of attached STVs and DIPs, respectively. Upon uptake, virions in endosomes, V^{En} and D^{En}, either degrade or fuse with the endosomal membrane. Upon fusion, virions release a complex of eight genome segments into the cytoplasm, V^{cyt} and D^{cyt}, respectively. To describe this process, we changed Equation (3.1.6) to Equation (3.2.5) to account for experimental findings showing that viral genomes from incoming particles stay associated until nuclear import occurs [42]. Accordingly, we added a similar equation for DIPs.

$$\frac{\mathrm{d}V^{\mathrm{cyt}}}{\mathrm{d}t} = k^{\mathrm{Fus}}V^{\mathrm{En}} - k^{\mathrm{Imp}}V^{\mathrm{cyt}}, \tag{3.2.5}$$

$$\frac{\mathrm{d}D^{\mathrm{cyt}}}{\mathrm{d}t} = k^{\mathrm{Fus}}D^{\mathrm{En}} - k^{\mathrm{Imp}}D^{\mathrm{cyt}}, \tag{3.2.6}$$

where V^{cyt} comprises a set of eight FL segments and D^{cyt} harbors FL segments 2–8 and one copy of a DI S1.

Viral RNA replication   Once the cytoplasmic vRNP complexes are imported into the nucleus, the genome segments are transcribed and replicated individually. For this, we extended the corresponding model Equations (3.1.7)–(3.1.14) [18] to explicitly account for the dynamics of vRNPs and cRNPs of each FL segment and the DI segment.

$$\frac{\mathrm{d}Vp_k^{\mathrm{nuc}}}{\mathrm{d}t} = k^{\mathrm{Imp}}V^{\mathrm{cyt}} + k^{\mathrm{Imp}}D^{\mathrm{cyt}} + k_{\mathrm{NP}}^{\mathrm{Bind}}P_{\mathrm{NP}}R_{\mathrm{RdRp,k}}^{\mathrm{V}} - \left(k_{\mathrm{M1}}^{\mathrm{Bind}}P_{\mathrm{M1}} + k_{\mathrm{Rnp}}^{\mathrm{Deg}}\right)Vp_k^{\mathrm{nuc}}, \tag{3.2.7}$$

$$\text{for} \quad k = 2, \ldots, 8 \quad \text{and}$$

$$\frac{\mathrm{d}Vp_1^{\mathrm{nuc}}}{\mathrm{d}t} = k^{\mathrm{Imp}}V^{\mathrm{cyt}} + k_{\mathrm{NP}}^{\mathrm{Bind}}P_{\mathrm{NP}}R_{\mathrm{RdRp,1}}^{\mathrm{V}} - \left(k_{\mathrm{M1}}^{\mathrm{Bind}}P_{\mathrm{M1}} + k_{\mathrm{Rnp}}^{\mathrm{Deg}}\right)Vp_1^{\mathrm{nuc}}, \tag{3.2.8}$$

$$\frac{\mathrm{d}Vp_9^{\mathrm{nuc}}}{\mathrm{d}t} = k^{\mathrm{Imp}}D^{\mathrm{cyt}} + k_{\mathrm{NP}}^{\mathrm{Bind}}P_{\mathrm{NP}}R_{\mathrm{RdRp,9}}^{\mathrm{V}} - \left(k_{\mathrm{M1}}^{\mathrm{Bind}}P_{\mathrm{M1}} + k_{\mathrm{Rnp}}^{\mathrm{Deg}}\right)Vp_9^{\mathrm{nuc}}, \tag{3.2.9}$$

where Vp_k^{nuc} are nuclear vRNPs of segment k, where $k = 1, \ldots, 8$ denote the FL segments and $k = 9$ the DI S1, respectively. Accordingly, dynamics of cRNA and vRNA synthesis of the individual segments k (R_k^{C}, R_k^{V}) and formation of cRNPs and vRNPs (Cp_k, Vp_k^{nuc}) as well as M1-vRNP complexes ($Vp_{\mathrm{M1,k}}^{\mathrm{nuc}}$) were modeled as in Equations (3.1.8)–(3.1.14).

$$\frac{\mathrm{d}R_k^{\mathrm{C}}}{\mathrm{d}t} = k_{\mathrm{C}}^{\mathrm{Syn}}Vp_k^{\mathrm{nuc}} - k_{\mathrm{RdRp}}^{\mathrm{Bind}}P_{\mathrm{RdRp}}R_k^{\mathrm{C}} - k_{\mathrm{R}}^{\mathrm{Deg}}R_k^{\mathrm{C}}, \tag{3.2.10}$$

$$\frac{\mathrm{d}Cp_k}{\mathrm{d}t} = k_{\mathrm{NP}}^{\mathrm{Bind}}P_{\mathrm{NP}}R_{\mathrm{RdRp,k}}^{\mathrm{C}} - k_{\mathrm{Rnp}}^{\mathrm{Deg}}Cp_k, \tag{3.2.11}$$

$$\frac{\mathrm{d}R_k^{\mathrm{V}}}{\mathrm{d}t} = k_{\mathrm{V}}^{\mathrm{Syn}}Cp_k - k_{\mathrm{RdRp}}^{\mathrm{Bind}}P_{\mathrm{RdRp}}R_k^{\mathrm{V}} - k_{\mathrm{R}}^{\mathrm{Deg}}R_k^{\mathrm{V}}, \tag{3.2.12}$$

$$\frac{\mathrm{d}Vp_{\mathrm{M1,k}}^{\mathrm{nuc}}}{\mathrm{d}t} = k_{\mathrm{M1}}^{\mathrm{Bind}}P_{\mathrm{M1}}Vp_{\mathrm{k}}^{\mathrm{nuc}} - \left(k^{\mathrm{Exp}}P_{\mathrm{NEP}} + k_{\mathrm{Rnp}}^{\mathrm{Deg}}\right)Vp_{\mathrm{M1,k}}^{\mathrm{nuc}}, \qquad (3.2.13)$$

$$\text{for} \quad k = 1, \ldots, 9.$$

Viral mRNA and protein synthesis To describe transcription of nuclear vRNPs into viral mRNA, we used Equation (3.1.15) [18].

$$\frac{\mathrm{d}R_{\mathrm{k}}^{\mathrm{M}}}{\mathrm{d}t} = \frac{k_{\mathrm{M}}^{\mathrm{Syn}}}{L_{\mathrm{k}}}Vp_{\mathrm{k}}^{\mathrm{nuc}} - k_{\mathrm{M}}^{\mathrm{Deg}}R_{\mathrm{k}}^{\mathrm{M}}, \quad k = 1, \ldots, 8, \qquad (3.2.14)$$

where mRNAs $R_{\mathrm{k}}^{\mathrm{M}}$ are synthesized from the FL vRNPs $Vp_{\mathrm{k}}^{\mathrm{nuc}}$ of segment k. Note, that we did neither account for the synthesis of DI mRNAs nor the translation thereof. On one hand, transcription and translation of DI genomes into truncated polypeptides has been described in literature (reviewed in [115]), and it was revealed that a polypeptide encoded by a DI S1 can, indeed, influence the IFN response of the host cell [36]. On the other hand, the functionality of DI polypeptides might be unique to a specific DI RNA candidate and may not directly impact virus replication. Therefore, and to provide a model that covers more general cases of DIP co-infection, we neglected the description of DI polypeptides.

Preliminary simulations revealed that DI RNA synthesis can rapidly deplete the pool of viral NP and polymerases [308], which blocks release of progeny when the virus release kinetics from the original model were applied, Equation (3.1.26) [18]. Thus, we revised our description for virus release and assumed that unbound NP, polymerases as well as NEP are dispensable for viral progeny formation. Instead, only NP, polymerases and NEP bound to vRNPs, as well as HA, NA, M1 and M2 are accounted for in the revised formulation of virus budding in Equation (3.2.20) and Equation (3.2.21). In addition, equations describing the viral protein dynamics (Equations (3.1.16)–(3.1.25)) were adjusted accordingly.

Virus release Prior to progeny release, we modeled the formation of cytoplasmic vRNP complexes containing eight genome segments with respect to experimental findings [86]. In particular, all of those complexes contain FL segments 2–8 ($Vp_{\mathrm{M1,2-8}}^{\mathrm{cyt}}$) and, furthermore, either an FL S1 ($Vp_{\mathrm{M1,1}}^{\mathrm{cyt}}$) or a DI S1 ($Vp_{\mathrm{M1,9}}^{\mathrm{cyt}}$), which we refer to as $V_{\mathrm{Cplx}}^{\mathrm{cyt}}$ and $D_{\mathrm{Cplx}}^{\mathrm{cyt}}$, respectively.

$$\begin{aligned}
\frac{\mathrm{d}Vp_{\mathrm{M1,k}}^{\mathrm{cyt}}}{\mathrm{d}t} = {}& k^{\mathrm{Exp}}P_{\mathrm{NEP}}Vp_{\mathrm{M1,k}}^{\mathrm{nuc}} - k^{\mathrm{Cplx}}Vp_{\mathrm{M1,1}}^{\mathrm{cyt}}\prod_{k}Vp_{\mathrm{M1,k}}^{\mathrm{cyt}} \\
& - k^{\mathrm{Cplx}}Vp_{\mathrm{M1,9}}^{\mathrm{cyt}}\prod_{k}Vp_{\mathrm{M1,k}}^{\mathrm{cyt}} - k_{\mathrm{Rnp}}^{\mathrm{Deg}}Vp_{\mathrm{M1,k}}^{\mathrm{cyt}}, \qquad (3.2.15)
\end{aligned}$$

$$\frac{\mathrm{d}Vp_{\mathrm{M1,1}}^{\mathrm{cyt}}}{\mathrm{d}t} = k^{\mathrm{Exp}}P_{\mathrm{NEP}}Vp_{\mathrm{M1,1}}^{\mathrm{nuc}} - k^{\mathrm{Cplx}}Vp_{\mathrm{M1,1}}^{\mathrm{cyt}}\prod_k Vp_{\mathrm{M1,k}}^{\mathrm{cyt}} - k_{\mathrm{Rnp}}^{\mathrm{Deg}}Vp_{\mathrm{M1,1}}^{\mathrm{cyt}}, \tag{3.2.16}$$

$$\frac{\mathrm{d}Vp_{\mathrm{M1,9}}^{\mathrm{cyt}}}{\mathrm{d}t} = k^{\mathrm{Exp}}P_{\mathrm{NEP}}Vp_{\mathrm{M1,9}}^{\mathrm{nuc}} - k^{\mathrm{Cplx}}Vp_{\mathrm{M1,9}}^{\mathrm{cyt}}\prod_k Vp_{\mathrm{M1,k}}^{\mathrm{cyt}} - k_{\mathrm{Rnp}}^{\mathrm{Deg}}Vp_{\mathrm{M1,9}}^{\mathrm{cyt}}, \tag{3.2.17}$$

$$\frac{\mathrm{d}V_{\mathrm{Cplx}}^{\mathrm{cyt}}}{\mathrm{d}t} = k^{\mathrm{Cplx}}Vp_{\mathrm{M1,1}}^{\mathrm{cyt}}\prod_k Vp_{\mathrm{M1,k}}^{\mathrm{cyt}} - r^{\mathrm{Rel}} - k_{\mathrm{Rnp}}^{\mathrm{Deg}}V_{\mathrm{Cplx}}^{\mathrm{cyt}}, \tag{3.2.18}$$

$$\frac{\mathrm{d}D_{\mathrm{Cplx}}^{\mathrm{cyt}}}{\mathrm{d}t} = k^{\mathrm{Cplx}}Vp_{\mathrm{M1,9}}^{\mathrm{cyt}}\prod_k Vp_{\mathrm{M1,k}}^{\mathrm{cyt}} - r_{\mathrm{D}}^{\mathrm{Rel}} - k_{\mathrm{Rnp}}^{\mathrm{Deg}}D_{\mathrm{Cplx}}^{\mathrm{cyt}}, \tag{3.2.19}$$

$$\text{for} \quad k = 2, \ldots, 8.$$

For this, we assume that vRNP complexes, $V_{\mathrm{Cplx}}^{\mathrm{cyt}}$ and $D_{\mathrm{Cplx}}^{\mathrm{cyt}}$, form rapidly with complex formation rate k^{Cplx} and can degrade with rate $k_{\mathrm{Rnp}}^{\mathrm{Deg}}$. For the sake of simplicity, we assume that DI vRNPs are packaging-competent, i.e., that they retain sequence elements required for incorporation into budding particles. Finally, vRNP complexes and viral proteins assemble at the cell membrane to form viral progeny. Here, the number of released STVs and DIPs (V^{Rel}, D^{Rel}) is directly dependent on the number of available vRNP complexes ($V_{\mathrm{Cplx}}^{\mathrm{cyt}}$, $D_{\mathrm{Cplx}}^{\mathrm{cyt}}$) and proteins P_{j} that influence the virus release kinetics in a Michaelis-Menten-like fashion.

$$\frac{\mathrm{d}V^{\mathrm{Rel}}}{\mathrm{d}t} = r^{\mathrm{Rel}} = 8k^{\mathrm{Rel}}V_{\mathrm{Cplx}}^{\mathrm{cyt}}\prod_j \frac{P_{\mathrm{j}}}{P_{\mathrm{j}} + K_{\mathrm{V^{Rel}}}N_{\mathrm{P_j}}}, \tag{3.2.20}$$

$$\frac{\mathrm{d}D^{\mathrm{Rel}}}{\mathrm{d}t} = r_{\mathrm{D}}^{\mathrm{Rel}} = 8k^{\mathrm{Rel}}D_{\mathrm{Cplx}}^{\mathrm{cyt}}\prod_j \frac{P_{\mathrm{j}}}{P_{\mathrm{j}} + K_{\mathrm{V^{Rel}}}N_{\mathrm{P_j}}}, \tag{3.2.21}$$

$$\text{with} \quad j \in \{\mathrm{HA, NA, M1, M2}\}.$$

In contrast to the previous description in Equation (3.1.26), we multiplied k^{Rel} by eight. This is necessary, since previously r^{Rel} was dependent on the total amount of cytoplasmic vRNPs ($Vp_{\mathrm{M1}}^{\mathrm{cyt}}$), whereas, here, it depends on the concentration of a vRNP complex that already contains a set of eight genome segments.

Important model variables   To evaluate the total number of FL vRNAs and DI vRNAs in simulations, we have to determine the sum of all corresponding vRNA-containing model species associated with an infected cell.

$$\begin{aligned} R_{\mathrm{tot,k}}^{\mathrm{V}} = &\; V_{\mathrm{hi}}^{\mathrm{Att}} + V_{\mathrm{lo}}^{\mathrm{Att}} + D_{\mathrm{hi}}^{\mathrm{Att}} + D_{\mathrm{lo}}^{\mathrm{Att}} + V^{\mathrm{En}} + V^{\mathrm{cyt}} + D^{\mathrm{En}} + D^{\mathrm{cyt}} \\ &+ R_{\mathrm{k}}^{\mathrm{V}} + R_{\mathrm{RdRp,k}}^{\mathrm{V}} + Vp_{\mathrm{k}}^{\mathrm{nuc}} + Vp_{\mathrm{M1,k}}^{\mathrm{nuc}} + Vp_{\mathrm{M1,k}}^{\mathrm{cyt}} + V_{\mathrm{Cplx}}^{\mathrm{cyt}} + D_{\mathrm{Cplx}}^{\mathrm{cyt}}, \end{aligned} \tag{3.2.22}$$

$$\text{for} \quad k = 2, \ldots, 8 \quad \text{and}$$

$$
\begin{aligned}
R_{\text{tot},1}^{\text{V}} = {} & V_{\text{hi}}^{\text{Att}} + V_{\text{lo}}^{\text{Att}} + V^{\text{En}} + V^{\text{cyt}} + R_1^{\text{V}} + R_{\text{RdRp},1}^{\text{V}} + V p_1^{\text{nuc}} \\
& + V p_{\text{M1},1}^{\text{nuc}} + V p_{\text{M1},1}^{\text{cyt}} + V_{\text{Cplx}}^{\text{cyt}},
\end{aligned}
\tag{3.2.23}
$$

$$
\begin{aligned}
R_{\text{tot},9}^{\text{V}} = {} & D_{\text{hi}}^{\text{Att}} + D_{\text{lo}}^{\text{Att}} + D^{\text{En}} + D^{\text{cyt}} + R_9^{\text{V}} + R_{\text{RdRp},9}^{\text{V}} + V p_9^{\text{nuc}} \\
& + V p_{\text{M1},9}^{\text{nuc}} + V p_{\text{M1},9}^{\text{cyt}} + D_{\text{Cplx}}^{\text{cyt}},
\end{aligned}
\tag{3.2.24}
$$

where $R_{\text{tot,k}}^{\text{V}}$ ($k = 2, \ldots, 8$) denotes all FL vRNAs except for FL S1, and $R_{\text{tot},1}^{\text{V}}$ and $R_{\text{tot},9}^{\text{V}}$ are the total number of FL S1 and DI S1, respectively.

3.2.2. Model extensions to account for different modes of interference

Since DI RNAs are significantly smaller compared to their FL counterparts, it is commonly believed the competitive advantage of DI RNAs is based on their reduced length. While it is most frequently proposed that DI RNAs posses an advantage in RNA synthesis, DI RNAs may also manipulate other steps of the viral life cycle, which allows them to out-compete their FL counterparts (reviewed in [115]). Here, we propose three possible model extensions that account for different modes of DI RNA interference.

Advantage factor   As a first approximation, we chose to base the advantage of DI RNAs over their FL counterparts on the respective FL-to-DI RNA length ratio.

$$F_{\text{Adv}} = \left(\frac{L_1^{\text{V}}}{L_9^{\text{V}}} - 1 \right), \tag{3.2.25}$$

where L_1^{V} and L_9^{V} are the length of the FL S1 and DI S1 vRNA, respectively. By implementing F_{Adv} at particular steps of the viral life cycle, we can account for advantages of the DI RNA during replication, regulation of replication or vRNP packaging, which is explained in the following.

Enhanced DI RNA synthesis   Based on findings by Odagiri and colleagues [125], we assumed that DI cRNAs possess a replication advantage over their FL counterparts. To implement this into our model, we adjusted Equation (3.2.10) for the DI segment to:

$$\frac{\mathrm{d} R_9^{\text{C}}}{\mathrm{d} t} = (F_{\text{Adv}} + 1)\, k_{\text{C}}^{\text{Syn}} V p_9^{\text{nuc}} - k_{\text{RdRp}}^{\text{Bind}} P_{\text{RdRp}} R_9^{\text{C}} - k_{\text{R}}^{\text{Deg}} R_9^{\text{C}}. \tag{3.2.26}$$

Due to their reduced length, DI cRNAs replicate faster than FL cRNAs which are synthesized with rate $k_{\text{C}}^{\text{Syn}}$. Here, F_{Adv} (Equation (3.2.25)) denotes the replication advantage with which the DI cRNA synthesis exceeds FL cRNA synthesis. For instance,

a DI segment which comprises half the length of its cognate FL segment replicates twice as fast.

Differential regulation of DI RNA synthesis Nayak and colleagues [115] speculated that DI RNAs might have lost yet unknown regulatory elements which got deleted from the FL RNA sequence. Hence, DI RNAs are able to reach intracellular copy numbers much higher compared to their FL counterparts. In our model, the most important regulatory step of RNA synthesis is the inactivation of vRNPs by binding of the M1, which shuts down viral RNA transcription and replication. Hence, we can account for an advantage of DI RNAs during regulation of DI RNA synthesis by reducing the binding rate of M1 to nuclear DI vRNPs. According to literature, M1 binds to vRNPs by interaction with NP [76] and, perhaps, with the vRNA [310]. For vRNP formation, we model that one NP molecule binds a fixed number of nucleotides in the vRNA [57]. Since DI RNAs are significantly shorter than their FL counterparts, fewer NP is bound in DI vRNPs, such that, also M1 binding might be less efficient. Thus, it seems reasonable to also assume a length-dependent M1 binding rate for DI vRNPs. To account for this, we adjusted Equation (3.2.9) and Equation (3.2.13) to:

$$\frac{\mathrm{d}Vp_9^{\mathrm{nuc}}}{\mathrm{d}t} = k^{\mathrm{Imp}}D^{\mathrm{cyt}} + k_{\mathrm{NP}}^{\mathrm{Bind}}P_{\mathrm{NP}}R_{\mathrm{RdRp},9}^{\mathrm{V}}$$
$$- \left(\frac{1}{F_{\mathrm{Adv}}+1}\right)k_{\mathrm{M1}}^{\mathrm{Bind}}P_{\mathrm{M1}}Vp_9^{\mathrm{nuc}} - k_{\mathrm{Rnp}}^{\mathrm{Deg}}Vp_9^{\mathrm{nuc}}, \tag{3.2.27}$$

$$\frac{\mathrm{d}Vp_{\mathrm{M1},9}^{\mathrm{nuc}}}{\mathrm{d}t} = \left(\frac{1}{F_{\mathrm{Adv}}+1}\right)k_{\mathrm{M1}}^{\mathrm{Bind}}P_{\mathrm{M1}}Vp_9^{\mathrm{nuc}} - \left(k^{\mathrm{Exp}}P_{\mathrm{NEP}} + k_{\mathrm{Rnp}}^{\mathrm{Deg}}\right)Vp_{\mathrm{M1},9}^{\mathrm{nuc}}, \tag{3.2.28}$$

where we used the reciprocal of F_{Adv} (Equation (3.2.25)) such that $k_{\mathrm{M1}}^{\mathrm{Bind}}$ for the DI vRNP (Vp_9^{nuc}) will be reduced by $50\,\%$ if the DI RNA comprises half the length of its corresponding FL segment.

Preferential packaging of DI vRNPs To model an advantage of DI vRNPs during packaging, we implemented a competitive inhibition of S1 vRNPs during assembly of viral progeny, which was previously proposed for FL segments [92]. For this, we re-modeled the virus release rate following the model for competitive inhibition based on the corresponding Michaelis-Menten equation for enzyme kinetics (e.g. [311, 312]).

$$v = v_{\mathrm{max}}\frac{S}{S + K_{\mathrm{m}}(1 + \frac{I}{K_{\mathrm{i}}})}, \tag{3.2.29}$$

with the maximal reaction rate v_{max} and the Michaelis-Menten constant K_{m}. The concentration of the substrate and inhibitor are denoted by S and I, respectively. The

dissociation constant of the inhibitor K_i is small for inhibitors with a high affinity to the enzyme, i.e., with a strong ability to inhibit substrate binding.

Furthermore, we used a different basic description of the virus release rate for both STV and DIPs, following a similar version for a DIP-free infection in [37].

$$\frac{dV^{\text{Rel}}}{dt} = r^{\text{Rel}} = k_{\max}^{\text{Rel}} \frac{\left(V_{\text{Cplx}}^{\text{cyt}} + Vp_{\text{M1,1}}^{\text{cyt}}\right)\left(\frac{Vp_{\text{M1,1}}^{\text{cyt}}}{1+Vp_{\text{M1,1}}^{\text{cyt}}}\right)}{Vp_{\text{M1,1}}^{\text{cyt}} + 8K_{V^{\text{Rel}}}\left(1 + \left(\frac{Vp_{\text{M1,9}}^{\text{cyt}}}{\left(\frac{1}{F_{\text{Adv}}+1}\right)K_i}\right)\right)}$$
$$\cdot \prod_j \frac{P_j}{P_j + K_{V^{\text{Rel}}}N_{P_j}}, \quad (3.2.30)$$

$$\frac{dD^{\text{Rel}}}{dt} = r_D^{\text{Rel}} = k_{\max}^{\text{Rel}} \frac{\left(V_{\text{Cplx}}^{\text{cyt}} + Vp_{\text{M1,9}}^{\text{cyt}}\right)\left(\frac{Vp_{\text{M1,9}}^{\text{cyt}}}{1+Vp_{\text{M1,9}}^{\text{cyt}}}\right)}{Vp_{\text{M1,9}}^{\text{cyt}} + 8K_{V^{\text{Rel}}}\left(1 + \left(\frac{Vp_{\text{M1,1}}^{\text{cyt}}}{\left(2-\left(\frac{1}{F_{\text{Adv}}+1}\right)\right)K_i}\right)\right)}$$
$$\cdot \prod_j \frac{P_j}{P_j + K_{V^{\text{Rel}}}N_{P_j}}, \quad (3.2.31)$$

$$\text{with} \quad j \in \{\text{HA}, \text{NA}, \text{M1}, \text{M2}\} \quad \text{and}$$
$$V_{\text{Cplx}}^{\text{cyt}} = \sum_k Vp_{\text{M1,k}}^{\text{cyt}}, \quad \text{for} \quad k = 2, \ldots, 8,$$

where virus release depends on the number of vRNPs of segments 2–8 in the cytoplasm ($V_{\text{Cplx}}^{\text{cyt}}$) and either the number of vRNPs of FL S1 ($Vp_{\text{M1,1}}^{\text{cyt}}$) or vRNPs of DI S1 ($Vp_{\text{M1,9}}^{\text{cyt}}$), for STVs and DIPs, respectively. Here, $K_{V^{\text{Rel}}}$ denotes the number of virus particles for which components must be present in order to reach half of the maximum release rate. The term of the form $K_{V^{\text{Rel}}}\left(1 + {}^I/_{K_i}\right)$, accounts for the competitive inhibition between S1 vRNPs, where the concentration of the inhibitor I denotes either the number of FL S1 ($Vp_{\text{M1,1}}^{\text{cyt}}$) that inhibit DIP formation, or the number of DI S1 ($Vp_{\text{M1,9}}^{\text{cyt}}$) that inhibit STV formation, respectively. In addition, we also implemented a length-dependency of the inhibitor dissociation constant K_i using F_{Adv} (Equation (3.2.25)). As a consequence, the term $K_{V^{\text{Rel}}}\left(1 + {}^I/_{K_i}\right)$ becomes large for short DI vRNPs, such that r^{Rel} is decreasing. Furthermore, we added the term $\left(Vp_{\text{M1,k}}^{\text{cyt}}/\left(1+Vp_{\text{M1,k}}^{\text{cyt}}\right)\right)$ to prevent release of virus progeny that carry an incomplete set of viral genomes in case an STV-free or DIP-free scenario is simulated, i.e., either no $Vp_{\text{M1,1}}^{\text{cyt}}$ or no $Vp_{\text{M1,9}}^{\text{cyt}}$ enter the cell at infection.

The additional parameters needed for the model of preferential packaging $k_{\max}^{\text{Rel}}$, $K_{V^{\text{Rel}}}$ and K_i were set such that the number of viral progeny released at 12 h p.i. as well as in steady state (300 h p.i.) was similar to that obtained with the other two co-infection models in a control scenario. For this, we simulated the models with a DI-like S1

comprising the same length as a FL S1 (2341 nt), and compared release of STVs and DIPs in case of a DIP-free infection at MOI 2 and for a co-infection at MOI 1 and MODIP 1. Parameter values were accepted when numbers of STVs and DIPs obtained with the model of preferential packaging did not deviate more than 1 % from the control model (Section 3.2.1).

Simulation and computation   Model files were handled in the Systems Biology Toolbox 2 [306] for MATLAB (version 8.0.0.783 R2012b). We solved the model equations numerically using the CVODE routine from SUNDIALS [305] on a Linux-based system. The values of kinetic parameters are listed in Table B.1 in the appendix.

3.3. Continuous production of influenza A virus

Using a two-stage bioreactor setup, Frensing and Heldt *et al.* [14] demonstrated that DIPs cause oscillations in virus titers in continuous cultures of influenza virus. The simple within-host infection model presented in that study describes the dynamics of DIPs and STVs, three infected cell populations and the population of uninfected target cells. For the sake of completeness, the model equations will be reproduced here in Section 3.3.1. Those are complemented by additional formulas related to relevant process parameters that can be manipulated to perform model-based process optimization (Section 4.3.1). Recently, an RT-qPCR method was developed by Wasik *et al.* that allows to distinguish a known form of DI RNA from its corresponding FL segment [313]. This opened the possibility to augment the Frensing-and-Heldt model [14] to also account for additional viral sub-populations, which is presented in Section 3.3.2. This extended model is used to describe data of two-stage bioreactor cultivations performed at different residence times. The latter was published by Tapia and Laske *et al.* [314] and parts of the original publication will be presented throughout this thesis as well (Section 4.3.2).

3.3.1. Basic model for virus growth in two-stage bioreactors

Frensing-and-Heldt model The mathematical model describing the replication of IAV in a continuous culture using a two-stage bioreactor system (Figure 3.1) is reproduced here to give a comprehensive overview of the models used in this thesis. In brief, batch cultures of avian AGE1.CR suspension cells were grown in the two stirred tank bioreactors until a cell concentration of 4–5×10^6 cells/mL was reached. Then, the virus bioreactor was infected with A/PR/8/34 (H1N1) at MOI 0.025 and the system was switched into continuous mode. While cells in the virus bioreactor undergo apoptosis during the virus production process, uninfected cells are continuously fed from the cell bioreactor to the virus bioreactor, continuously providing cell substrate for virus infection. Still, virus has to be added only once to the system since viable target cells will be infected by virus progeny already present in the virus bioreactor. The model by Frensing and Heldt *et al.* [14] focuses on describing concentrations of cells, infected cells and virus particles in the virus bioreactor. Here, ideal mixing is assumed for all state variables. The number of uninfected target cells T is the following.

$$\frac{\mathrm{d}T}{\mathrm{d}t} = \mu T - k^{\mathrm{Inf}} \left(V_{\mathrm{s}} + V_{\mathrm{d}} \right) T + D \left(T_{\mathrm{in}} - T \right), \tag{3.3.1}$$

where the number of uninfected cells T grow with rate μ and are infected by DIPs V_{d} and STVs V_{s} at rate k^{Inf}. The term $D \left(T_{\mathrm{in}} - T \right)$ considers the continuous feed of cells to, and
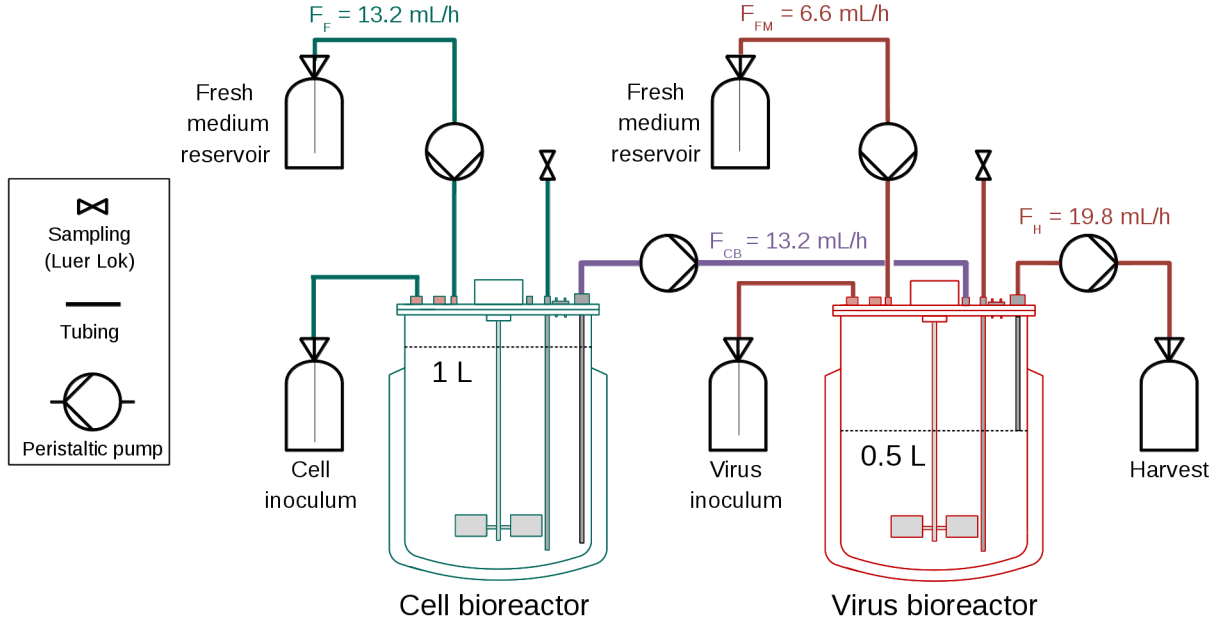
Figure 3.1.: Two-stage bioreactor system for continuous production of influenza A virus. Cell propagation and virus production are carried out separately in two bioreactors. For this, the suspension cells grow continuously in the cell bioreactor (green highlighting) that is supplied with fresh medium via F_F and feeds cell broth to the virus bioreactor (red highlighting) with rate F_CB. To avoid substrates limitation, fresh medium is supplied to the virus bioreactor with flow rate F_FM. In the virus bioreactor cells are infected with influenza A/PR/8/34 (H1N1) and produce virus progeny. Finally, the culture broth, consisting of cells, medium and viruses, is harvested with rate F_H. Using the flow rates depicted in this schematic, the virus bioreactor has an average residence time of 25.3 h. Schematic of Frensing and Heldt *et al.* (2013) [14] was adapted to the nomenclature of this thesis.

continuous harvest of cells from the virus bioreactor. The dilution rate D is determined by the flow rate of the harvest F_H and the working volume of the virus bioreactor V_VB.

$$D = \frac{F_\text{H}}{V_\text{VB}}, \tag{3.3.2}$$

$$\text{with } F_\text{H} = F_\text{CB} + F_\text{FM}, \tag{3.3.3}$$

where F_H is the sum of all feeding flow rates which include the feed from the cell bioreactor F_CB and from the fresh medium reservoir F_FM. Since the concentration of cells in the cell bioreactor T_CB reaches a constant steady-state value, we assume that the cell concentration in the feed T_in is independent of time and can be determined by the following equation.

$$T_\text{in} = \frac{T_\text{CB} F_\text{CB}}{F_\text{CB} + F_\text{FM}}, \tag{3.3.4}$$

where T_CB denotes the average cell concentration in the cell bioreactor. The population of infected cells consists of three sub-populations, namely, cells infected only by STVs I_s,

cells infected only by DIPs I_{d} and cells co-infected by both viruses I_{c}.

$$\frac{\mathrm{d}I_{\text{s}}}{\mathrm{d}t} = k^{\text{Inf}} V_{\text{s}} T - \left(k^{\text{Inf}} V_{\text{d}} + k^{\text{Apo}} \right) I_{\text{s}} - D I_{\text{s}}, \tag{3.3.5}$$

$$\frac{\mathrm{d}I_{\text{d}}}{\mathrm{d}t} = k^{\text{Inf}} V_{\text{d}} T - \left(k^{\text{Inf}} V_{\text{s}} - \mu \right) I_{\text{d}} - D I_{\text{d}}, \tag{3.3.6}$$

$$\frac{\mathrm{d}I_{\text{c}}}{\mathrm{d}t} = k^{\text{Inf}} \left(V_{\text{s}} I_{\text{d}} + V_{\text{d}} I_{\text{s}} \right) - k^{\text{Apo}} I_{\text{c}} - D I_{\text{c}}. \tag{3.3.7}$$

Target cells T are infected by either STVs V_{s} or DIPs V_{d} and form I_{s} and I_{d}, respectively (Equation (3.3.5) and Equation (3.3.6)). STV-only and DIP-only infected cells, I_{s} and I_{d}, can be superinfected by V_{d} and V_{s}, respectively, which results in co-infected cells I_{c} (Equation (3.3.7)). Due to virus replication, STV-only infected cells I_{s} and co-infected cells I_{c} undergo virus-induced cell death, i.e., apoptosis, with rate k^{Apo}. Since virus replication cannot take place in DIP-only infected cells I_{d}, Frensing and Heldt *et al.* [14] proposed that I_{d} continue to grow, giving rise to DIP-infected daughter cells. This assumption was also used by Kirkwood and Bangham in a previous mathematical description of DIP co-infection [315]. Finally, all infected cell sub-populations are continuously harvested from the virus bioreactor with rate D. The concentration of the two viral sub-populations, STVs V_{s} and DIPs V_{d}, is given by the following equations.

$$\frac{\mathrm{d}V_{\text{s}}}{\mathrm{d}t} = k^{\text{Prod}} I_{\text{s}} - \left(\frac{k^{\text{Inf}}}{F_{\text{Inf}}} \left(T + I_{\text{d}} + I_{\text{s}} + I_{\text{c}} \right) + k_{\text{V}}^{\text{Deg}} + D \right) V_{\text{s}}, \tag{3.3.8}$$

$$\frac{\mathrm{d}V_{\text{d}}}{\mathrm{d}t} = k^{\text{Prod}} I_{\text{c}} + f k^{\text{Prod}} I_{\text{s}} - \left(\frac{k^{\text{Inf}}}{F_{\text{Inf}}} \left(T + I_{\text{d}} + I_{\text{s}} + I_{\text{c}} \right) + k_{\text{V}}^{\text{Deg}} + D \right) V_{\text{d}}. \tag{3.3.9}$$

Here, STV-only infected cells I_{s} release STVs and a small fraction of DIPs generated *de novo* at rate k^{Prod} and $f k^{\text{Prod}}$, respectively. Since DIPs interfere with virus replication, co-infected cells I_{c} release only DIPs at rate k^{Prod}. Frensing and Heldt *et al.* [14] assumed that virus particles in the supernatant can infect all cell sub-populations. In particular, they assumed that one virion readily establishes an infection in a cell, expressed by an infection efficiency of $F_{\text{Inf}} = 1$. In the end, free virus particles either lyse with rate $k_{\text{V}}^{\text{Deg}}$ or are harvested with rate D.

Modeling different residence times   In simulations, we tested the option to dampen, or even prevent, oscillations in virus titers by manipulating the residence time (RT) of the virus bioreactor.

$$RT = \frac{1}{D}, \tag{3.3.10}$$

where the average RT of the virus bioreactor is the reciprocal of its dilution rate D (Equation (3.3.2)). For the sake of simplicity, we fixed the feed rate from the cell bioreactor to the virus bioreactor F_{CB} in Equation (3.3.3) and only adjusted the feed rate from the fresh medium reservoir to the virus bioreactor F_{FM}.

$$F_{FM} = DV_{VB} - F_{CB}. \tag{3.3.11}$$

If $F_{FM} = 0\,h^{-1}$, the dilution rate of the virus bioreactor is $D = 0.0264\ 1/h$, which is equivalent to the maximum RT of 37.9 h. For every RT tested, the concentration of cells in the feed T_{in} has to be adjusted accordingly (Equation (3.3.4)).

Productivity of continuous processes   One criterion to evaluate the productivity of the continuous process is the space-time yield (STY).

$$STY_X(t_n) = \frac{\sum_{t_0}^{t_n} (V_X F_H t_n)}{\sum_{t_0}^{t_n} (F_H t_n)\, t_n}, \tag{3.3.12}$$

where V_X is the virus concentration of interest. The product of the harvest flow rate F_H and elapsed time t_n is equivalent to the volume harvested from the virus bioreactor up to time point t_n of the process.

3.3.2. Extended model for virus growth in two-stage bioreactors

A/PR/8/34-delS1(1) model   Based on the study by Frensing and Heldt *et al.* [14], our group examined continuous production of IAV using a seed virus engineered by reverse genetics that contained a particular form of deleted RNA from segment 1 (DI S1), previously described by Dimmock *et al.* [145]. Since the sequences of DI S1 and its corresponding full-length segment 1 (FL S1) are known, it was possible to design an RT-qPCR method that could distinguish the two RNA species in virus samples [313, 314]. Furthermore, we determined the fraction of non-infectious particles (NIPs) from the measurements (see paragraph "Data conversion"). The Frensing-and-Heldt model [14] provided the basis to integrate those data.   However, to account for all viral sub-populations, we had to modify the original model, which is outlined in the following section. In the extended model, the concentration of uninfected target cells T is described by

$$\frac{dT}{dt} = \mu T - \left(k_S^{Inf}V_s + k_D^{Inf}V_d\right)T + D\left(T_{in} - T\right), \tag{3.3.13}$$

where target cells T grow at rate μ which is equal to the dilution rate D of the virus bioreactor. Furthermore, target cells are continuously fed from the cell bioreactor and harvested with rate D. The concentration of cells in the feed stream T_{in} is assumed

to be independent of time and can be determined by considering the average cell concentration in the cell bioreactor and the diluting effect of the fresh medium supply to the virus bioreactor (Equation (3.3.4)). A significant modification made to the Frensing-and-Heldt model [14] is that the infection of uninfected target cells T by either DIPs V_d or STVs V_s is modeled by considering the virus-dependent infection rates k_D^{Inf} and k_S^{Inf}, respectively. The following equations describe the concentration of the three infected cell sub-populations.

$$\frac{dI_s}{dt} = k_S^{Inf} V_s T - k_D^{Inf} V_d I_s - \left(k^{Apo} + D \right) I_s, \tag{3.3.14}$$

$$\frac{dI_d}{dt} = k_D^{Inf} V_d T - k_S^{Inf} V_s I_d - \left(k^{Apo} + D \right) I_d, \tag{3.3.15}$$

$$\frac{dI_c}{dt} = k_S^{Inf} V_s I_d + k_D^{Inf} V_d I_s - \left(k^{Apo} + D \right) I_c. \tag{3.3.16}$$

The target cells are infected via two routes: cells are infected by either STV or DIP first, and form I_s or I_d, respectively. Secondly, superinfection of I_s and I_d by DIPs and STVs, respectively, yields co-infected cells I_c (Equation (3.3.16)). For the sake of simplicity, we also assume that one virion is sufficient to cause a productive infection, and in case of DIPs, to readily interfere with STV replication. All infected cells can undergo virus-induced apoptosis with rate k^{Apo} and are harvested from the virus bioreactor with rate D. In contrast to Frensing and Heldt *et al.* [14], we assume that DIP-only infected cells I_d do not continue to grow and instead die due to virus-induced apoptosis like the other infected cell populations I_s and I_c. The dynamics of infectious STVs V_s, DIPs V_d and V_{Ni}, i.e., virions that contain an FL S1 but are non-infectious (NIPs), are the following.

$$\frac{dV_s}{dt} = k_{Vs}^{Prod} I_s - k_S^{Inf} V_s T - k_S^{Inf} V_s I_d - \left(k_{Vs}^{Deg} + D \right) V_s, \tag{3.3.17}$$

$$\frac{dV_d}{dt} = k_{Vd}^{Prod,Ic} I_c + k_{Vd}^{Prod,Is} I_s - k_D^{Inf} V_d T - k_D^{Inf} V_d I_s - \left(k_V^{Deg} + D \right) V_d, \tag{3.3.18}$$

$$\frac{dV_{Ni}}{dt} = k_{V_{Ni}}^{Prod,Is} I_s + k_{V_{Ni}}^{Prod,Ic} I_c + k_{Vs}^{Deg} V_s - \left(k_V^{Deg} + D \right) V_{Ni}, \tag{3.3.19}$$

considering that STV-infected cells I_s release virus particles that contain FL S1, both infectious V_s and non-infectious V_{Ni}, with rates k_{Vs}^{Prod} and $k_{V_{Ni}}^{Prod,Is}$, respectively. Due to errors in virus replication, DIPs V_d are also generated *de novo* by STV-infected cells I_s, which are released with rate $k_{Vd}^{Prod,Is}$. Since DIPs V_d are not replication-competent, DIP-only infected cells I_d cannot release any progeny DIPs. Certainly, the majority of DIPs V_d is produced by co-infected cells I_c with rate $k_{Vd}^{Prod,Ic}$. For the sake of simplicity, we defined that DIPs generated either *de novo* or by amplification are only of type DI S1. Furthermore, we did not limit I_c to only release DIPs, but also allowed the release of

non-infectious virions V_{Ni} with rate $k_{V_{\text{Ni}}}^{\text{Prod,Ic}}$. The number of V_{Ni} is furthermore increasing when previously infectious STVs V_{s} are inactivated with rate $k_{V_{\text{s}}}^{\text{Deg}}$, while both V_{d} and V_{Ni} deteriorate with the lysis rate k_{V}^{Deg}. In contrast to Frensing and Heldt *et al.* [14], we neglected superinfection of I_{s} and I_{c} by STVs as well as superinfection of I_{d} and I_{c} by DIPs, respectively.

Important model variables A characteristic value that can be determined from both the simulated and the experimental data is the DIP-to-STV ratio (Equation (3.3.20)). In our case, the calculation of this ratio is only based on the DI S1 measurements and does not account for other DIPs present in the virus samples.

$$R_{\text{DIP/STV}} = \frac{V_{\text{d}}}{V_{\text{s}}}, \tag{3.3.20}$$

where V_{d} denotes the number of DI S1 particles, as calculated by Equation (3.3.24), and V_{s} is the number of fully infectious FL S1-containing particles, determined by the $50\,\%$ tissue culture infective dose (TCID$_{50}$) assay, respectively. For the parameter estimation procedure, we also determined the total number of cells in the virus bioreactor as follows:

$$\text{cells}_{\text{total}} = T + I_{\text{s}} + I_{\text{d}} + I_{\text{c}}, \tag{3.3.21}$$

which can be compared to the cell concentration measurements during model fitting. Although it is possible to further distinguish STV-only, DIP-only and co-infected cells including their live and apoptotic forms based on the model, we do not yet have access to such data and, thus, focused on the measurements of the total cell count. To complement the parameter estimation procedure, we also calculated the number of total virus particles from the simulated virus concentrations by

$$V_{\text{total}} = V_{\text{s}} + V_{\text{d}} + V_{\text{Ni}}, \tag{3.3.22}$$

which was used to directly compare the simulated total virus concentration V_{total} with the experimental total virus concentration C_{V} which is based on the HA titer (Equation (3.3.23)). In contrast, the simulated V_{total} of the Frensing-and-Heldt model [14] is calculated by summation of V_{s} and V_{d}.

Data conversion The numbers of DI S1- and FL S1-containing particles from continuous cultivations are inferred with the help of the genome copy numbers (RT-qPCR measurements) and the HA titer. The latter is used first to determine the total virus

particle concentration C_V in a sample according to

$$C_V = C_{Ery} \cdot 10^{(\log_{10} HAU/100\mu L)}, \tag{3.3.23}$$

where C_{Ery} is the concentration of the chicken erythrocyte solution added to the HA assay ($2 \cdot 10^7$ cells/mL). For the conversion of the genome copy numbers to particle numbers, we assumed that every particle contains one copy of S1, which is either the deleted or the FL form. Hence, the sum of DI S1- and FL S1-containing particles denotes the maximum number of virions present in a sample, equivalent to the total virus particle concentration C_V. Using this assumption, we calculated the concentration of DI S1- and FL S1-containing particles by Equation (3.3.24) and Equation (3.3.25), respectively.

$$V_d = \frac{DI\,S1}{DI\,S1 + FL\,S1} \cdot C_V, \tag{3.3.24}$$

$$V_s + V_{Ni} = \frac{FL\,S1}{DI\,S1 + FL\,S1} \cdot C_V. \tag{3.3.25}$$

Furthermore, a differentiation between infectious FL S1-containing virions V_s and non-infectious FL S1-containing virions V_{Ni} is possible. Since we know the number of V_s, i.e., the TCID$_{50}$ titer, the number of non-infectious FL S1-containing virions can be easily determined by solving Equation (3.3.25) for V_{Ni}. For the details of the assaying procedures, see Tapia and Laske *et al.* [314] and references therein, e.g. [316–318].

Parameter estimation The ten kinetic parameters of the model were estimated by simultaneously fitting the simulated concentrations V_s, V_d, V_{Ni}, V_{total} and cells$_{total}$ to the corresponding measurements. For this, the weighted least-squares prediction error was minimized using the global stochastic optimization algorithm fSSm [307]. For the virus titers, the error was calculated based on the decadic logarithm of both the simulated and measured data according to Equation (3.1.33), while the error of the cell count was not logarithmized. Initial parameter guesses were selected according to Frensing and Heldt *et al.* [14].

Simulation and computation Model equations were solved numerically using the CVODE routine from SUNDIALS [305] on a Linux-based system. Experimental data and model files were managed using the Systems Biology Toolbox 2 [306] for MATLAB (version 8.0.0.783 R2012b). Model parameters and initial conditions are listed in Table 4.3.

CHAPTER 4

Results and Discussion

This thesis aims to improve our understanding on how relevant factors influence influenza virus replication. Investigations performed to address this research challenge focus on two major factors, namely, the impact of the host cell system and the virus itself. To elucidate virus-host cell interactions in more detail, we concentrated on the impact of host cell factors on the intracellular mechanisms of virus replication, which will be presented in the first section. Secondly, we will continue to study intracellular virus replication, however, in light of the impact of viral deletion mutants, i.e., DIPs, that are inherently present in heterogeneous virus populations. The third section is also dealing with the topic of virus growth in the presence of DIPs. In contrast to the other sections, it, however, serves to elucidate their impact at the within-host level during continuous culture of influenza viruses.

4.1. Modeling virus-host cell interactions on the single-cell level

IAVs depend on host cellular functions to complete their replication cycle. Our aim was to take advantage of this dependency and manipulate the expression of host cell factors that are relevant for IAV replication to improve virus production for vaccine manufacturing. Due to the complexity of virus-host cell interactions, mathematical models are required to complement the interpretation of infection experiments. Here, we used a re-calibrated model of IAV replication to predict and quantify changes in virus replication in genetically engineered A549 cells. Work shown in this section was conducted within the scope of the joint research project "Cell line development by systems biology" (CellSys). This section contains the results thereof, which were previously presented in *PLoS Computational Biology* by Laske and Bachmann *et al.* [294]. While the publication and this thesis focus on the modeling aspects of the project conducted to support a detailed analysis of the impact of five selected gene candidates, we addressed significantly more gene candidates throughout CellSys. For a comprehensive overview on the engineering, selection and screening of cell lines with genetic modifications in one or more host cell genes, the interested reader is referred to [319].

4.1.1. Identifying bottlenecks of virus replication in A549 cells

To allow a reasonable prediction of bottlenecks in the virus life cycle we first re-calibrated key kinetic parameters of our single-cell model of IAV replication to data sets obtained during infections of parental A549 cells. Then, a parameter study was performed to identify those steps of virus replication that are most promising to be manipulated by the expression of relevant host cell factors. While this *in silico* study seems by far too pragmatic it provided an important benchmark to later interpret changes in virus replication observed in genetically modified A549 cells.

Developing a model of virus growth in A549 cells The model of IAV replication used in this study is identical to a previously published description of the intracellular life cycle of IAV (Section 3.1, [18]). In general, we assume that basic mechanisms of IAV replication are similar in different host cell lines, but that values for key parameters of virus growth have to be adapted for each host cell system. While the previous model [18] was calibrated against various experimental data, mostly acquired from infected MDCK cells [297, 320], the re-calibration of the model used in this study was based on three sets of in-house experimental data from infected A549 cells (Figure 4.1). The available measurements allowed to estimate the kinetic parameters for nuclear import of vRNPs k^{Imp}, the synthesis of viral mRNA, cRNA and vRNA ($k_{\text{M}}^{\text{Syn}}$, $k_{\text{C}}^{\text{Syn}}$, $k_{\text{V}}^{\text{Syn}}$) as well as binding of M1 $k_{\text{M1}}^{\text{Bind}}$ and the release of viral progeny k^{Rel}. Statistical testing revealed that $k_{\text{C}}^{\text{Syn}}$ and $k_{\text{M1}}^{\text{Bind}}$ were not significantly different (p > 0.1) in A549 compared to MDCK cells (Table 4.1). However, $k_{\text{V}}^{\text{Syn}}$ was significantly increased and $k_{\text{M}}^{\text{Syn}}$ significantly reduced in A549 cells, respectively.

Table 4.1.: Comparison of key parameters of influenza A virus replication in adherent MDCK and A549 cells.

Parameter		Value MDCK cells [18]	Value A549 cells
k^{Imp}	(h^{-1})	6 [n.a.]	0.296
$k_{\text{V}}^{\text{Syn}}$	(h^{-1})	13.86 [****]	100.93
$k_{\text{C}}^{\text{Syn}}$	(h^{-1})	1.38	1.53
$k_{\text{M}}^{\text{Syn}}$	(nucleotides/h)	2.50×10^5 [***]	3.06×10^4
$k_{\text{M1}}^{\text{Bind}}$	$(\text{molecule} \cdot \text{h})^{-1}$	1.39×10^{-6}	1.82×10^{-6}
k^{Rel}	$(\text{virions}/(\text{molecule} \cdot \text{h}))$	3.70×10^{-3} [n.a.]	1.10×10^{-3}

[n.a.] not assessed (no bootstrap simulations in [18] available).
Asterisks indicate significant differences of the parameter values with respect to the A549 cell line using a one-sided Gauss test: [****] p ≤ 0.001, [***] p ≤ 0.01, [**] p ≤ 0.05, [*] p ≤ 0.1, no asterisk p > 0.1.
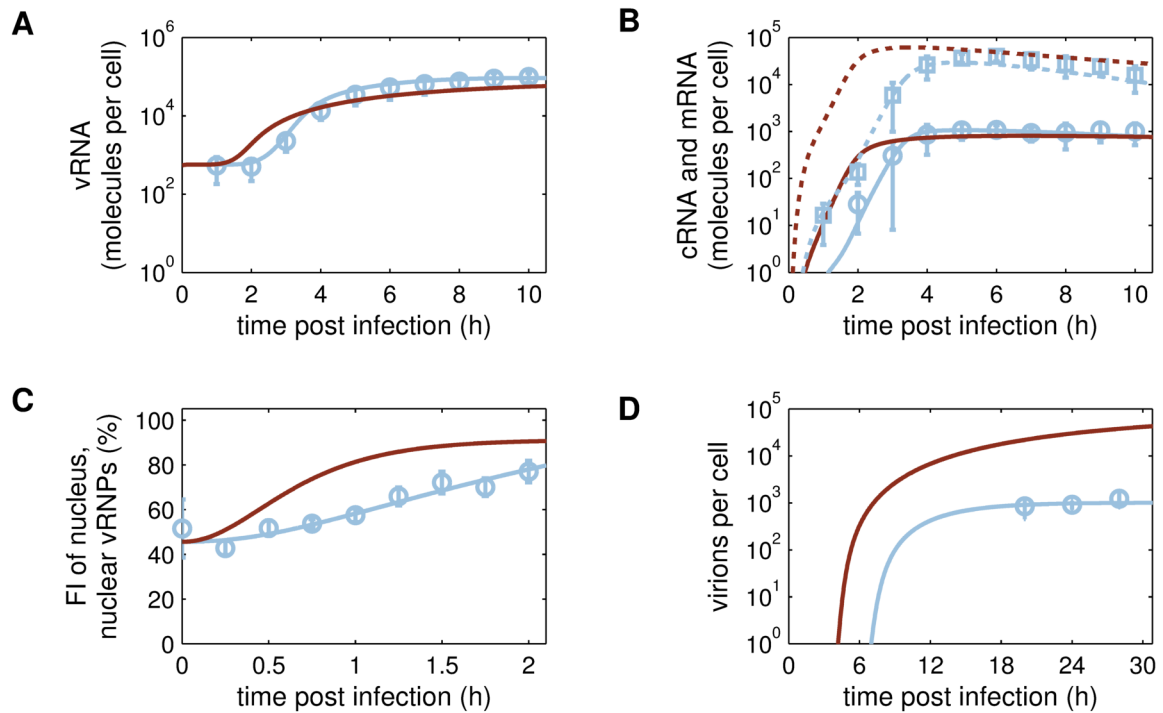
Figure 4.1.: Comparison of simulations of intracellular influenza A virus replication in MDCK and parental A549 cells. Model fit (blue lines) to experimental data (blue symbols ± standard deviation, n ≥ 4) for A549 and simulations for MDCK cells (brown lines) are shown, respectively. (A, B) Intracellular dynamics of viral RNA for a simulated infection at MOI 50 for vRNA and cRNA (circles, solid line) as well as for mRNA (squares, dashed line) in A549 cells and MDCK cells. (C) Nuclear import of viral genomes in cycloheximide-treated cells for a simulated infection at MOI 50. For A549 cells, the relative increase in fluorescence intensity (FI) of the nucleus was determined by imaging flow cytometry after co-staining of cells with DAPI and an vRNP-antibody (see Figure 4.4 for details). For better comparison, the simulated fraction of nuclear vRNPs in MDCK cells was scaled with respect to the nuclear vRNP offset determined for A549 cells. (D) Cell-specific virus release for a simulated infection at MOI 1. Figure taken from Laske and Bachmann *et al.* (2019) [294].

Computational approach to determine bottlenecks in virus growth Two simplifying assumptions were made to simulate the influence of host cell factors on IAV replication. First, we considered that each step in the virus life cycle was dependent on one host cell factor and secondly, that a change in the expression level of this host cell factor would directly translate into a change of the corresponding kinetic parameter value in our mathematical model for IAV replication. For instance, if a host cell factor involved in vRNA synthesis is overexpressed, vRNA replication is enhanced, resulting in a higher vRNA synthesis rate. Likewise, the downregulation of the same factor would result in a reduced vRNA synthesis rate. Based on these assumptions, we performed *in silico* engineering of A549 cells by perturbing each parameter of our model individually with the objective to maximize virus yield at 24 h p.i. The resulting pairs of optimized parameter values and model output are summarized in Table A.2 in the appendix.

Virus yield By comparing the simulated virus release of parental A549 cells to results obtained for *in silico* optimized cell lines (Figure 4.2), we observed three possible outcomes upon parameter perturbation: (i) virus release dynamics were not affected significantly, (ii) only onset of virus release was improved, starting at least 1 h earlier compared to the parental A549 cell line and (iii) virus release dynamics were affected significantly leading to an increase in final yield by at least two-fold. The latter was caused by perturbations of parameters that define the most promising targets for cell line engineering, namely steps of viral RNA synthesis, its regulation and virus release (Figure 4.2, green shaded subfigures). Interestingly, the model predicted that the upregulation of viral mRNA synthesis is beneficial for virus replication, whereas synthesis of viral cRNA and vRNA should be downregulated.

Viral RNA and protein levels To investigate this in greater detail we, next, compared the dynamics of the simulated intracellular viral RNAs and protein levels in both upregulation and downregulation scenarios to levels in parental A549 cells (Figure 4.3). We observed that changes of intracellular replication dynamics were most evident upon manipulation of viral mRNA synthesis (Figure 4.3, middle panel). Most importantly, the sole increase of the mRNA synthesis rate lead to a higher increase in vRNA levels than the upregulation of the vRNA synthesis rate itself (Figure 4.3, upper and middle panel second column). This strongly indicates that viral RNA replication in A549 cells is already saturated and only if more viral mRNA, and consequently, more viral proteins were available, more vRNA could be produced and virus release could be enhanced significantly. In addition, the modulation of regulatory steps, which is accounted for in our model by binding of M1 (negative regulator, see Section 3.1.1 for explanations), had only an impact on final RNA and protein levels rather than on the dynamics *per se* (Figure 4.3, bottom panel).
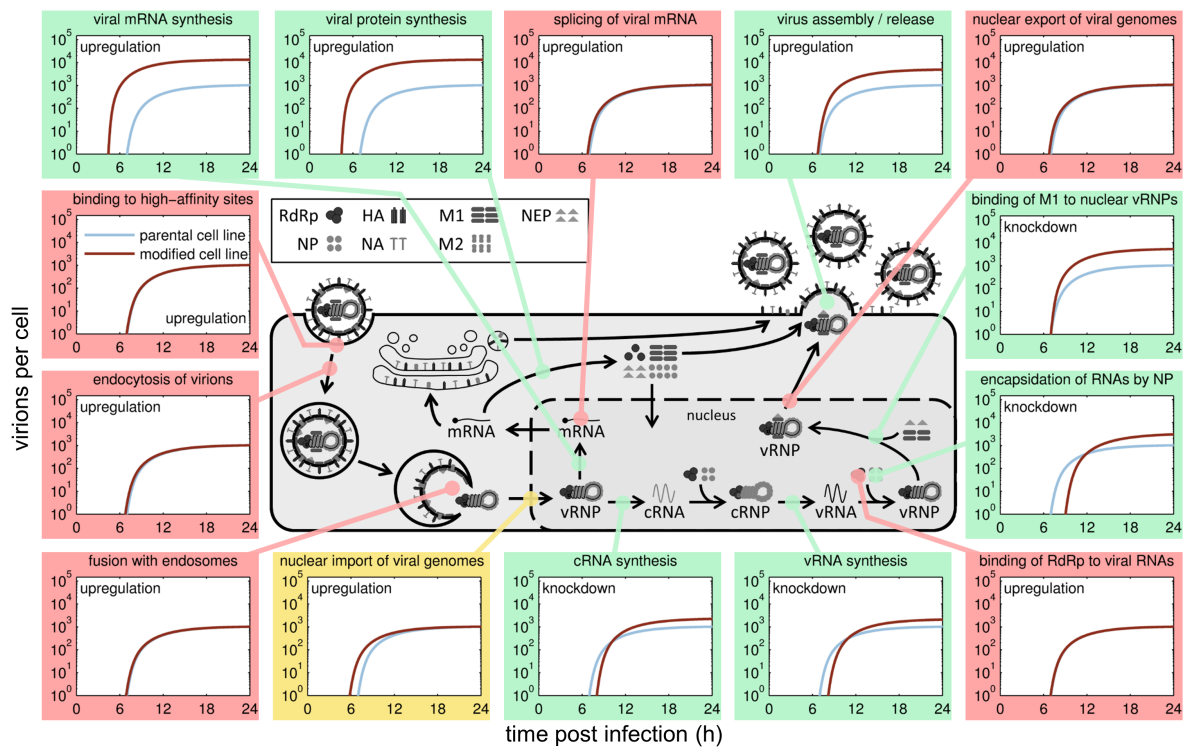
Figure 4.2.: Virus release dynamics in response to *in silico* manipulation of gene expression of host cell factors in A549 cells. We assume that the efficiency of individual steps in the influenza A virus (IAV) life cycle is directly dependent on host cell factors and their influence is changed upon knockdown or overexpression of the corresponding gene. We simulated manipulation of gene expression by perturbing the corresponding kinetic parameters of a model for intracellular replication of IAV in A549 cells, which is based on a model previously established by our group [18]. For a simulated infection at MOI 1, virus release of the parental A549 (blue solid line) and the engineered cell line (brown solid line) are shown for the most important steps of virus replication. Colors indicate whether perturbation of the corresponding step improved virus yield at 24 h p.i. by at least two-fold (green), had only an impact on the starting time point of virus release (yellow) or no impact (red). Scheme of IAV replication adapted from [37]. Pairs of optimized parameter values and model output are summarized in Table A.2 in the appendix. Figure taken from Laske and Bachmann *et al.* (2019) [294]. RdRp - RNA-dependent RNA polymerase, HA - hemagglutinin, NP - nucleoprotein, NA - neuraminidase, M - matrix protein, NEP - nuclear export protein.

4.1.2. Impact of selected host cell factors on virus replication

To validate our model predictions, we used lentiviral gene transfer to generate A549 cell populations that overexpress specific host cell genes relevant for IAV replication. The host cell factors CEACAM6, FANCG, NXF1, PLD2 and XAB2 were selected from a set of candidate genes determined previously by RNAi screening [321–324] and virus-host cell interaction studies [325, 326]. An overview of genes and their function in the IAV life cycle is given in the appendix (Table A.4). The resulting cell populations were subjected to fluorescence-activated cell sorting (FACS) to enrich cells that express
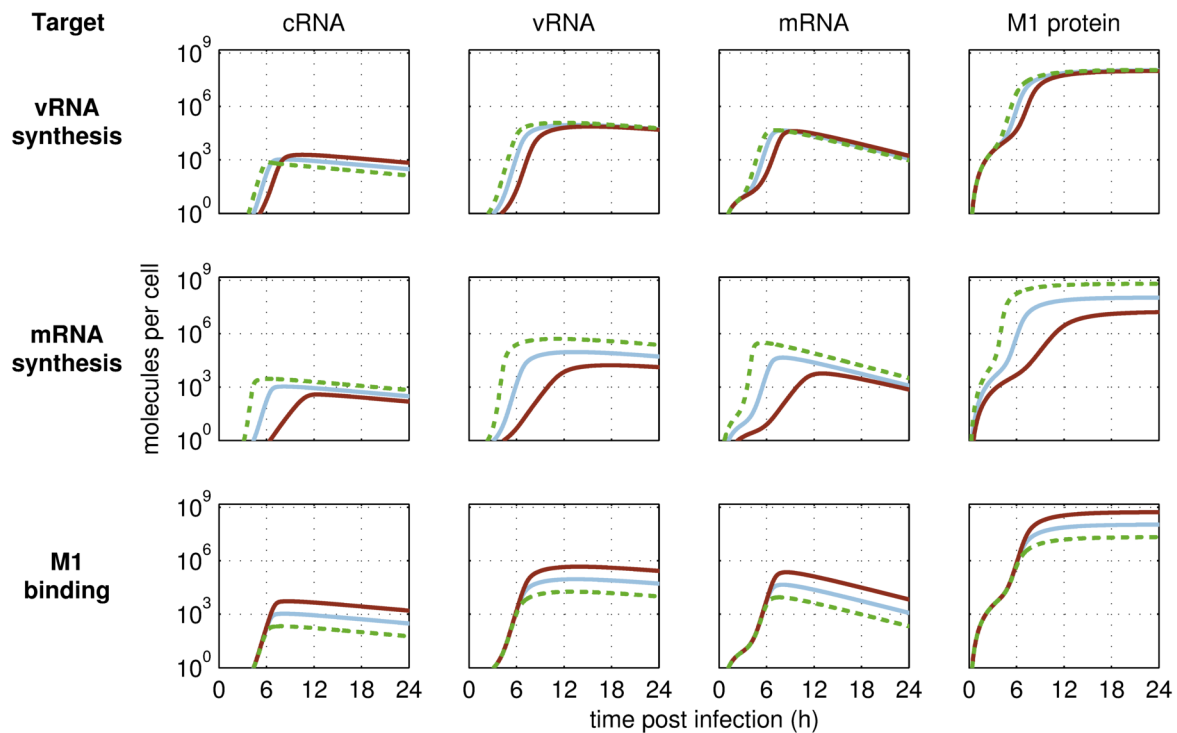
Figure 4.3.: Intracellular replication dynamics in response to *in silico* modifications of host cell gene expression in a single infected cell. Changes in levels of viral cRNA (column 1), vRNA (column 2), mRNA (column 3) and matrix protein 1 (M1, column 4) are shown for a simulated infection at MOI 1 for the parental A549 cell line (blue solid line) or upon targeting selected steps of virus replication, as indicated on the left-hand side, by either knockdown (brown solid line) or overexpression (green dashed line). Figure taken from Laske and Bachmann *et al.* (2019) [294].

the transduced gene based on eGFP, which is the co-expressed reporter gene. SGOs that showed stable gene overexpression were infected with A/PR/8/34 (H1N1) at a MOI of 10^{-4}, which is usually applied for vaccine production processes. We compared virus titers of each SGO to that of the parental A549 cell line at selected time points p.i. (Table A.5 in the appendix). Assuming that changes in virus release are associated with changes in intracellular mechanisms of virus replication, we selected SGOs for further characterization of intracellular virus replication based on their HA titer. To facilitate selection, we ranked the HA measurements for each time point and each cell line according to their relative increase compared to the parental A549 cell line. The measurement data and the corresponding ranking values revealed that HA titers of all SGOs were increased at early time points p.i., whereas none of the SGOs showed an increase greater than 20 % of the final HA titer at the usual time of harvest 72 h p.i (Table A.5 in the appendix). Thus, by modulating the expression level of those host cell genes, it was possible to influence the IAV release dynamics, however, the total virus yield was similar comparing SGOs to

their parental cell line. To get a quantitative understanding of changes in virus growth in IAV-infected SGOs compared to infected parental A549 cells and an eGFP transduction control, we fitted the single-cell model to measurements of nuclear vRNP import, RNA synthesis and virus release (Figures 4.4–4.6).

Nuclear import of vRNPs   We examined nuclear import of vRNPs in A549 cells with the help of imaging flow cytometry, which combines both the statistically relevant throughput of cell counts known from conventional flow cytometry and the information on localization of the fluorescence signal inside a single cell usually acquired by fluorescence microscopy. Cells were treated with CHX to inhibit translation, such that only incoming vRNPs, resulting from virus uptake, would be detected in infected cells co-stained with DAPI (nuclear staining) and an anti-vRNP antibody. Overall, the kinetics of nuclear vRNP import were similar in all tested cell lines (Figure 4.4). In particular, the transduction control (Figure 4.4 A) and the XAB2 SGO (Figure 4.4 F) showed exactly the same time course of nuclear vRNP import as the parental A549 cell line. FANCG and PLD2 SGOs showed slightly reduced levels (Figure 4.4 C and E), while CEACAM6 and NXF1 showed a slightly slower increase of relative nuclear fluorescence intensity over time (Figure 4.4 B and D). Using the mathematical single-cell model, we estimated the nuclear import rate of viral genomes k^{Imp} for each cell line. While the differences in the majority of the parameter values were statistically not significant ($p > 0.1$) with respect to the parental A549 cell line, we observed a trend showing a slight reduction ($p \leq 0.1$) of k^{Imp} for CEACAM6 and NXF1 SGOs (Figure 4.7).

Viral replication and transcription   Next, we analyzed the intracellular replication and transcription dynamics of IAV RNA by segment-specific RT-qPCR. Therefore, we infected A549 cells at MOI 50 and measured viral mRNA, cRNA and vRNA of segment 5, which encodes the viral NP. Overall, the dynamics of the three viral RNA species were similar in all five SGOs compared to the parental A549 cell line (Figure 4.5). A few trends ($p \leq 0.1$) were found in intracellular RNA measurements. In particular, viral mRNA levels in CEACAM6 (Figure 4.5, upper panel, B), NXF1 (Figure 4.5, upper panel, D), and PLD2 SGOs (Figure 4.5, upper panel, E) seemed to be reduced at time points ≤ 6 h p.i. Interestingly, viral cRNA levels were reduced significantly ($p \leq 0.05$) in the PLD2 SGO from 4 to 7 h p.i. (Figure 4.5, middle panel, E), while no significant differences in cRNA levels were evident for other SGOs. Although we observed a slight reduction in levels of mRNA and/or cRNA in some of the infected SGOs, the time courses of vRNA synthesis and the number of viral genome copies per cell were similar for the majority of the tested cell lines (Figure 4.5, bottom panel). Only the FANCG SGO is an exception, since vRNA levels in infected FANCG SGO cells were reduced as measured in two independent
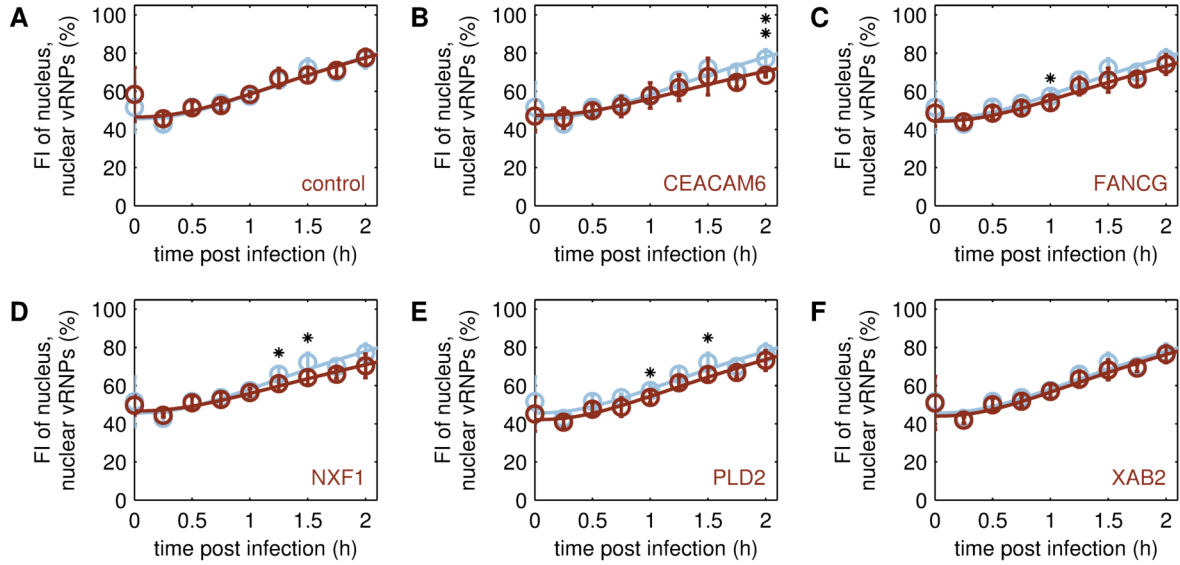
Figure 4.4.: Nuclear import of viral genomes in different A549 cell lines. Model fit (lines) to experimental data (circles $\pm$ standard deviation, n = 4) for the import of viral genomes (vRNPs) in cycloheximide-treated cell lines upon infection by A/PR/8/34 (H1N1) at MOI 50. Relative increase in fluorescence intensity (FI) of the nucleus was determined by imaging flow cytometry after co-staining of cells with DAPI and vRNP antibody. The nuclear import rate was estimated by fitting the simulated fraction of nuclear vRNPs to the averaged experimental data. To account for the background signal of the nucleus in images, an offset of approximately 50 % at 0 h p.i. was applied with respect to the experimental data obtained for parental A549 cells (A–F, blue), the transduction control (A, brown) and engineered cell lines overexpressing one of the following host cell factors: CEACAM6 (B, brown), FANCG (C, brown), NXF1 (D, brown), PLD2 (E, brown), XAB2 (F, brown). Statistical analysis of differences in relative FI levels with respect to the parental A549 cell line was performed by the Kruskal-Wallis test and is indicated by ** p $\leq$ 0.05, * p $\leq$ 0.1 and no asterisk for p > 0.1. Figure taken from Laske and Bachmann *et al.* (2019) [294].

experiments. Furthermore, viral mRNA and cRNA levels were also reduced in FANCG SGO cells. According to the Kruskal-Wallis test, the difference in the raw data compared to those of parental A549 cells was statistically not significant (p > 0.1). However, statistical testing could be performed on the empiric parameter distributions, generated upon multiple re-sampling of the intracellular viral RNA measurement data and repeated model fitting (Figure 4.7). For this, we fitted the time courses of the three RNA species simultaneously to estimate the synthesis rates of mRNA $k_{\text{M}}^{\text{Syn}}$, vRNA $k_{\text{V}}^{\text{Syn}}$, cRNA $k_{\text{C}}^{\text{Syn}}$ and the binding rate of the negative regulator M1 to vRNPs $k_{\text{M1}}^{\text{Bind}}$. In agreement with the experimental data, model-based analysis revealed that the mRNA synthesis rate $k_{\text{M}}^{\text{Syn}}$ and cRNA synthesis rate $k_{\text{C}}^{\text{Syn}}$ were reduced in most of the SGOs (Figure 4.7). In particular, both $k_{\text{M}}^{\text{Syn}}$ and $k_{\text{C}}^{\text{Syn}}$, were also reduced in the FANCG SGO. Furthermore, the synthesis rate of vRNA $k_{\text{V}}^{\text{Syn}}$ was estimated to be slightly higher in SGOs compared to the parental A549
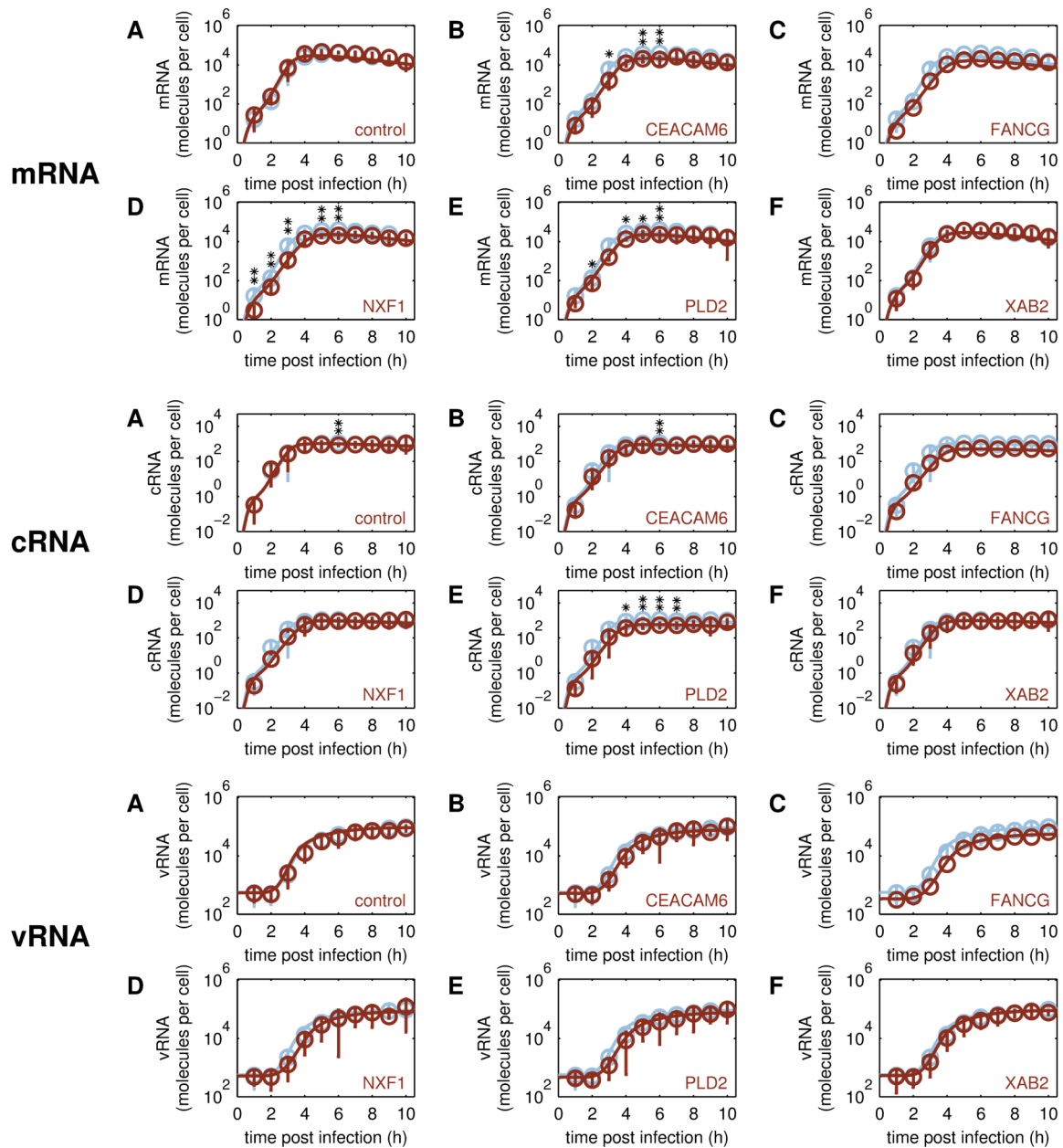
Figure 4.5.: Intracellular dynamics of viral RNA synthesis in different A549 cell lines. Model fit (lines) to experimental data (circles $\pm$ standard deviation, n = 4 or single circles for FANCG, n = 2) of viral mRNA (top panel), cRNA (middle panel), vRNA (bottom panel) of segment 5 (encoding NP) in cell lines infected by A/PR/8/34 (H1N1) at MOI 50. Viral RNA synthesis rates and M1 binding rate were estimated by fitting the simulated number of the three viral RNA species to averaged segment-specific RT-qPCR data. To account for the offset in vRNA measurements caused by free viral RNAs in the seed virus, we also implemented such offsets in our simulations with respect to the measurements obtained for parental A549 cells (A–F, blue), the transduction control (A, brown) and engineered cell lines overexpressing one of the following host cell factors: CEACAM6 (B, brown), FANCG (C, brown), NXF1 (D, brown), PLD2 (E, brown), XAB2 (F, brown). Statistical analysis of differences in RNA levels with respect to the parental A549 cell line was performed by the Kruskal-Wallis test and is indicated by ** $p \leq 0.05$, * $p \leq 0.1$ and no asterisk for $p > 0.1$. Figure taken from Laske and Bachmann *et al.* (2019) [294].

cell line. Since all three viral RNA species engage in an autocatalytic cycle, the synthesis rate of vRNA k_V^{Syn} has to be increased in order to maintain vRNA levels comparable to the parental A549 cell line and therefore compensates for reduction of either k_C^{Syn} or k_M^{Syn} in infected SGOs. However, the increase of k_V^{Syn} was not significant (p > 0.1) for any of the SGOs. Similarly, model-based analysis of the M1 binding rate k_{M1}^{Bind} in infected SGOs revealed no significant changes compared to the parental A549 cell line.

Virus release In addition to intracellular viral RNA levels, we also integrated experimental data of total virus release based on HA titer into our model to estimate the virus release rate k^{Rel} of SGOs (Figure 4.6). In contrast to our screening experiment for which cells were infected at MOI 10^{-4}, we had to apply a higher MOI for model fitting. This was necessary since our single-cell model cannot describe the progression of infections with multiple cycles in a cell population, which occur in low MOI scenarios. Therefore, we infected cells at MOI 1 and estimated the cell-specific virus release rate k^{Rel} with respect to the experimental data. Contrary to our expectations, the differences in
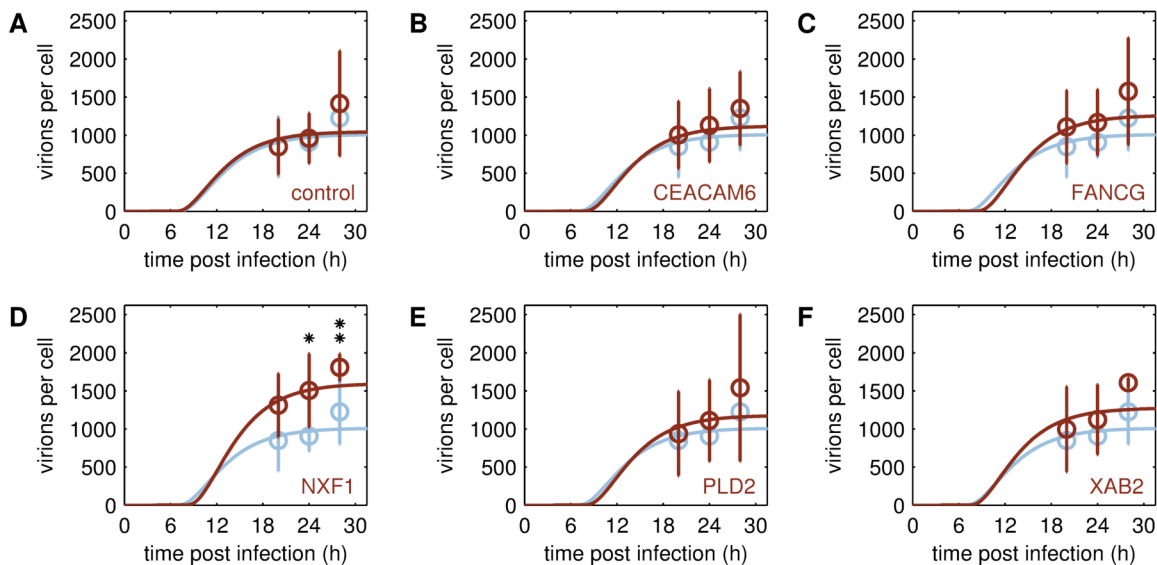
Figure 4.6.: Virus particle release of different A549 cell lines. Model fit (lines) to cell-specific numbers of released virions estimated from HA titer and maximum viable cell count (circles ± standard deviation, n ≥ 4) obtained from A/PR/8/34 (H1N1) infections at MOI 1. Simulated number of released virions was fitted to averaged cell-specific yield obtained for parental A549 cells (A–F, blue), the transduction control (A, brown) and engineered cell lines overexpressing one of the following host cell factors: CEACAM6 (B, brown), FANCG (C, brown), NXF1 (D, brown), PLD2 (E, brown), XAB2 (F, brown). Statistical analysis of differences in the cell-specific virus yield with respect to the parental A549 cell line was performed by the Kruskal-Wallis test and is indicated by ** p ≤ 0.05, * p ≤ 0.1 and no asterisk for p > 0.1. Figure taken from Laske and Bachmann *et al.* (2019) [294].

the number of released virions were even less pronounced in this experiment compared to the initial cell line screening (Table A.5 in the appendix). Only the NXF1 SGO showed significant differences in the number of released virions compared to the parental cell line (Figure 4.6 D), which is also in line with a noticeable ($p \leq 0.1$) increase of the virus release rate k^{Rel} compared to the parental A549 cell line (Figure 4.7). Interestingly, also other SGOs showed an increase of k^{Rel} of about two-fold. This can be explained by the model's architecture that leads to a compensation of the adverse/disadvantageous parameterization of viral replication and transcription through an increase in k^{Rel}, which finally allows the model to capture the cell-specific virus yield determined in experiments.

Simulation approach for cell lines overexpressing multiple genes   Although only NXF1 SGOs showed a promising increase in virus yield, it seemed that overexpression of host cell factors can influence IAV replication on the intracellular level. Thus, we also explored the possibility whether additive or even synergistic effects on IAV yield could be achieved by overexpressing multiple host cell factors simultaneously. At first, we investigated this option by a computational approach and simulated the virus release of single cells overexpressing different combinations of multiple host cell factors. We anticipated that integration of genes into the host chromosome is random and that gene constructs will be inserted at different chromosomal locations with different transcriptional
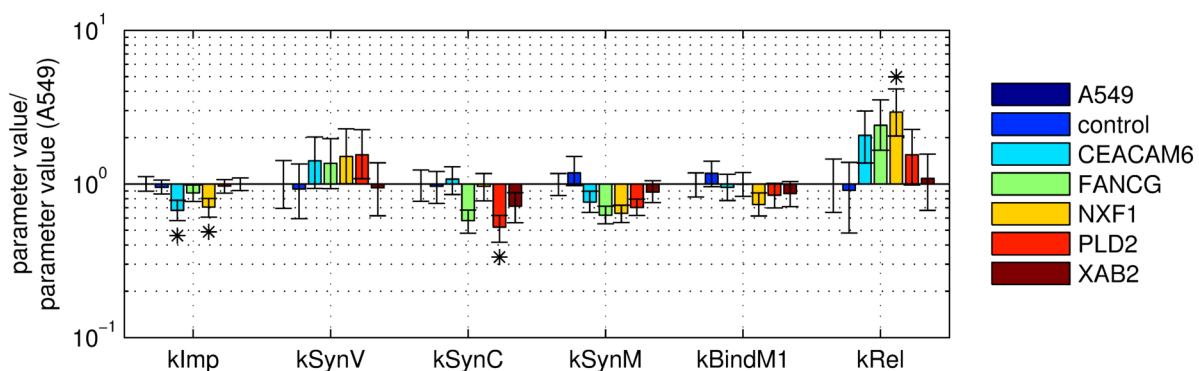
Figure 4.7.: Comparison of parameter values for viral kinetics obtained for A/PR/8/34 (H1N1) infections in different A459 cell lines. After fitting 3000 re-samples of the available experimental data, all parameter values were normalized to the median of each kinetic parameter obtained for parental A549 cells. Bars represent the normalized medians and error bars indicate the first and third normalized quartile of each parameter per cell line (for detailed boxplots see Figure A.3 in the appendix). Statistical analysis of differences in parameter values with respect to the parental A549 cell line was performed by a one-sided Z test (Gauss test) and is indicated by * $p \leq 0.1$ and no asterisk for $p > 0.1$. Figure taken from Laske and Bachmann *et al.* (2019) [294].

activities and, since transduction follows a Poisson distribution, not every cell will obtain the same number of the gene constructs. Together, these factors influence the strength of overexpression. In addition, the integration process can also have an impact on the gene expression through off-target effects. To account for all these scenarios, which involve some sort of randomness, we used randomized sets of parameters assembled based on the median values of the model parameters k^{Imp}, $k_{\mathrm{V}}^{\mathrm{Syn}}$, $k_{\mathrm{C}}^{\mathrm{Syn}}$, $k_{\mathrm{M}}^{\mathrm{Syn}}$, $k_{\mathrm{M1}}^{\mathrm{Bind}}$, and k^{Rel}, previously estimated from experimental data of infected SGOs and the parental A549 cell line (Table A.3 in the appendix). The parameter set of the latter was also included to account for off-target effects. For instance, the parameter set of an MGO may be composed of k^{Imp} of XAB2 SGOs, $k_{\mathrm{V}}^{\mathrm{Syn}}$ of PLD2 SGOs, $k_{\mathrm{C}}^{\mathrm{Syn}}$ of NXF1 SGOs, $k_{\mathrm{M}}^{\mathrm{Syn}}$ of FANCG SGOs, $k_{\mathrm{M1}}^{\mathrm{Bind}}$ of CEACAM6 SGOs, and k^{Rel} of the parental A549 cell line. We assume that all transduced genes can be expressed theoretically with the same probability, i.e., that there is an equal chance that kinetic parameters of the SGOs will be selected during randomization. Note, that even if all five candidate genes were transduced, not every MGO single cell will be a phenotypic mixture of all SGOs, but its parameter set could be k^{Imp} and $k_{\mathrm{V}}^{\mathrm{Syn}}$ of the parental A549 cell line, $k_{\mathrm{C}}^{\mathrm{Syn}}$ and $k_{\mathrm{M}}^{\mathrm{Syn}}$ of CEACAM6 SGOs and $k_{\mathrm{M1}}^{\mathrm{Bind}}$ and k^{Rel} of the NXF1 SGOs.

Simulation of virus growth in MGOs To generate *in silico* MGOs, we chose to randomize parameter sets of those SGOs that showed a beneficial change in parameters according to initial model predictions (Figure 4.2). Thus, we combined parameter sets of the top three candidates with the highest virus release rate k^{Rel} (CEACAM6 (C), FANCG (F) and NXF1 (N), CFN in Figure 4.8), the top three with the lowest cRNA synthesis rate $k_{\mathrm{C}}^{\mathrm{Syn}}$ (FANCG (F), PLD2 (P) and XAB2 (X), FPX in Figure 4.8), and the top three with the lowest M1 binding rate $k_{\mathrm{M1}}^{\mathrm{Bind}}$ (NXF1 (N), PLD2 (P), XAB2 (X), NPX in Figure 4.8). Finally, we also randomized parameter sets of all SGOs (CFNPX in Figure 4.8). In a Monte Carlo approach, we generated multiple randomized parameter sets according to the selected combinations of SGOs and simulated virus infection at MOI 1 for 48 h (Figure A.8 in the appendix). Finally, we evaluated every single-cell simulation for the time point at which the first simulated virus particle was released $\mathrm{t}(V^{\mathrm{Rel}} \geq 1)$ and for the fold change in the maximum number of released viral progeny (Figure 4.8). Interestingly, these model predictions revealed that a single cell overexpressing multiple genes can theoretically yield up to five-fold more virus progeny than its parental cell line if the underlying parameter set was k^{Imp} and $k_{\mathrm{M}}^{\mathrm{Syn}}$ of the parental A549 cell, $k_{\mathrm{V}}^{\mathrm{Syn}}$ of XAB2 SGOs, $k_{\mathrm{C}}^{\mathrm{Syn}}$ of PLD2 SGOs, and $k_{\mathrm{M1}}^{\mathrm{Bind}}$ and k^{Rel} of the NXF1 SGOs. In particular, the earlier virus release started, the higher was the fold increase in the number of viral progeny. While the time point of first virus release followed a
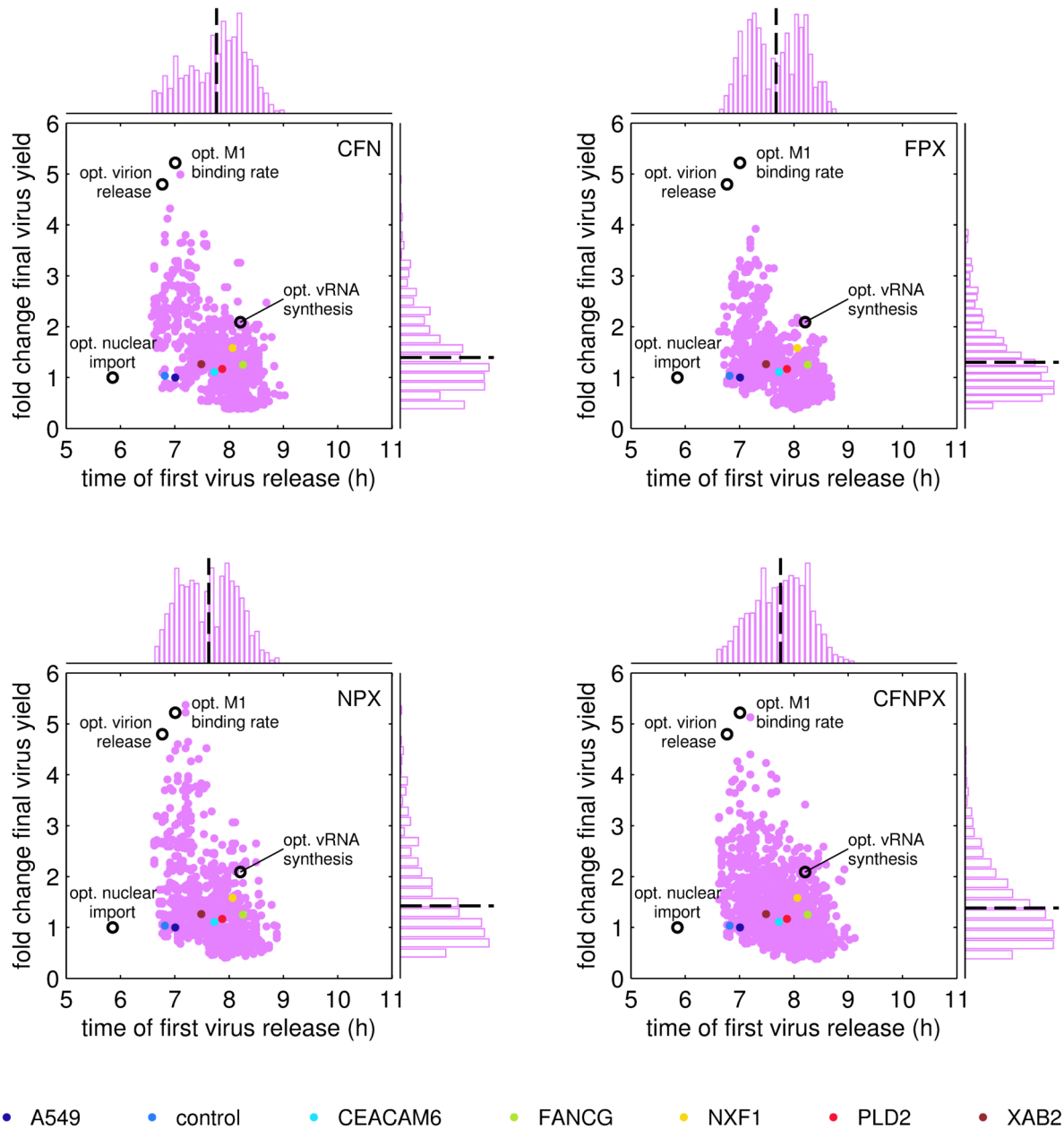
Figure 4.8.: Evaluation of the time point of first virus release and the fold change in virus yield for model predictions of cell lines overexpressing multiple and single host cell genes. Multiple gene overexpression cell lines (MGOs) were generated *in silico* by random assembly of kinetic parameter sets based on experimental single gene overexpression cell lines (SGOs), where letters in the upper right corner indicate which gene combinations were simulated (gene names are abbreviated as their first letter). For the resulting MGOs (pink dots) approximately every 10th of up to 2×10^4 model predictions is shown and compared to simulations with parameter sets experimentally determined for SGOs and parental A549 cells (dots, colors according to legend) at 48 h p.i. for a simulated infection at MOI 1, cell-specific virus yields were normalized to the one obtained for parental A549 cells. Open circles represent single-cell predictions using the indicated optimal parameter according to the analysis shown in Figure 4.2. Dashed lines in histograms indicate the arithmetic mean of the corresponding simulation readout. Figure taken from Laske and Bachmann *et al.* (2019) [294].

normal distribution, the fold change of virus release showed a log-normal distribution with highly productive cells as rare events. Overall, the combinations CFN, NPX and CFNPX showed similar distributions of the simulation read outs, whereas the combination of FPX resulted in a narrower distribution of virus yield with a slightly lower maximum fold increase of four-fold. Finally, this analysis revealed that highly productive cells are rare events in a heterogenous MGO population and their contribution to the population average is negligible, which leads to an increase of less than two-fold in the final virus yield (Figure 4.8, dashed line in vertical histograms).

Experimental MGOs The computational analysis of MGOs indicated that overexpressing multiple host cell factors could result in an earlier onset of virus release and, to some extent, also in an improvement of virus yield. To validate these model predictions, we generated populations of A549 cells in which individual cells express random combinations of selected host cell factors at various levels (Table A.8 in the appendix). In particular, we generated three independent cell populations (MGO 1–3) which provide random combinations of all five host cell factors CFNPX, which also covers the phenotypes of combinations CFN and NPX according to simulations (Figure 4.8). Furthermore, we generated MGO 4 in which the three factors FPX were randomly combined and which should show a slightly different phenotype compared to CFNPX. All MGOs were infected by IAV at MOI 10^{-4}. We chose this MOI according to the SGO screening experiment (Table A.5 in the appendix) since under these experimental conditions differences between cell lines were more pronounced than for infections at MOI 1 (Figure 4.6). Ranking of HA titers revealed that virus release of MGOs was increased at early time points, while final virus yield was not increased significantly in these cell populations compared to the parental A549 cell line (Table A.7 in the appendix). Of note, the impact of overexpressing single host cell genes on virus yield could be enhanced by overexpressing multiple of these host cell genes simultaneously, which partially confirms our model predictions on MGOs. In addition, MGO 4 was the only cell line showing less than 40 % increase in virus yield at 42 h p.i. compared to the parental A549 cell line. This supports the model prediction that the combination FPX results in a slightly less productive phenotype than other gene combinations.

Summary By assuming that relevant host cell factors have a direct impact on the kinetics of virus replication, we predicted that steps of viral RNA synthesis, their regulation and particle assembly and virus budding are promising targets for cell line engineering. The importance of these steps was confirmed in four of five SGOs that showed small, but reproducible changes in early dynamics of RNA synthesis and virus release. Model-based analysis suggests, however, that overexpression of the selected host

cell factors negatively influences specific RNA synthesis rates. Still, virus yields were rescued by an increase in the virus release rate. Based on parameter estimations obtained for SGOs, we predicted that there is a potential benefit associated with overexpressing multiple host cell genes in one cell line, which was validated experimentally.

4.1.3. Discussion of virus-host cell interactions in A549 cells

In Section 4.1 we re-calibrated a single-cell model for IAV replication to reproduce various data sets obtained from infected A549 cells. While the lung carcinoma cell line A549 is widely used as a model cell line for basic infection research of respiratory diseases, their cell-specific virus yields are smaller compared to MDCK cells which are highly suitable for vaccine production. While our initial model for the IAV life cycle was tailored to represent mostly data obtained from infected MDCK cells, we will first evaluate changes in key kinetic parameters comparing A549 and MDCK cells to better understand the difference in their production phenotype. Furthermore, we will make an attempt to decipher virus-host cell interactions in A549 cell lines overexpressing selected host cell factors. For this, we used our new A549-based model as a tool to quantify changes in key kinetic parameters of the engineered cells. Here, we discuss how those insights can help to rationally improve the model-based engineering and design of novel producer cell lines and how the process of identifying suitable gene candidates is inherently limiting this research avenue.

Bottlenecks of virus replication in A549 cells   To account for the influence of host cell factors on steps of the virus life cycle, we made the simplifying assumption that changes in host cell gene expression have a direct impact on kinetic parameters of our model. Although we did not explicitly model physical interactions between host cell factors or cellular pathways with viral components, we were able to identify targets for cell line engineering by evaluating changes in the cell-specific virus release upon parameter perturbations. According to our *in silico* analysis, both a significant increase in virus yield as well as an earlier onset of virus release could be expected if either viral transcription or translation were significantly enhanced. In contrast, the model predicted that various steps of virus replication need to be downregulated to achieve a higher cell-specific virus yield. For instance, the binding of M1 to nuclear vRNPs, which mediates the nuclear export of vRNPs, should be delayed. The lower the binding rate of M1 $k_{\mathrm{M1}}^{\mathrm{Bind}}$, the longer vRNPs serve as template for viral genome replication and transcription inside the nucleus. Accordingly, not only more viral genome copies but also mRNAs will be synthesized and, thus, higher viral protein levels will be achieved (Figure 4.3, bottom panel), which together will benefit virus yield. Furthermore, the model predicts that a decrease in the vRNA synthesis rate, in the cRNA synthesis rate, and a delayed binding of NP to naked viral RNA, needed to form replication-competent vRNPs and cRNPs, will cause an increase in virus yield (Figure 4.2). These three predictions seem counterintuitive since they cause a slowdown of viral replication. On the other hand, however, this strongly suggests that there is an imbalance between viral RNA replication and viral protein synthesis. While the synthesis of viral genomes is saturated, i.e., the RNA synthesis

rates are too high, the supply of viral proteins either needed to form RNPs (NP and polymerases) or needed for virus budding (HA and NA) represents a limiting step in A549 cells. Interestingly, Ueda and colleagues [327] made similar observations when comparing IAV growth in MDCK and A549 cells. While steps of viral replication were similar in both cell lines, A549 cells released fewer virions because both the maturation of glycoproteins and their transport to the plasma membrane were slower compared to MDCK cells. In line with that, parameter perturbation studies with the single cell model for MDCK cells did not point to bottlenecks in viral transcription and translation (Figure A.2 in the appendix). Indeed, the MDCK-based model is more sensitive to a change in the vRNA synthesis rate compared to a change in the protein synthesis rate, while the A549-based model is highly sensitive to changes in the protein synthesis rate (Figure A.1 in the appendix).

Virus release of cell lines overexpressing a single host cell gene We generated cell lines overexpressing host cell genes beneficial for virus replication previously identified by RNAi screening [321–324] and studies on virus-host cell interactions performed by other research groups [325, 326, 328, 329]. Overall, the maximum virus yield was similar in all A549 cell populations. However, the engineered cell populations released more virus particles at earlier time points compared to the parental cell line during infection studies performed at low MOI. To assure that target genes were stably overexpressed, we confirmed the expression of the functionally linked reporter gene coding for eGFP by flow cytometric measurements during cell culture maintenance (Figure A.4 in the appendix). Furthermore, we determined relative expression levels of the transgenes in SGOs by RT-qPCR (Table A.6 in the appendix). Although the overall number of virus progeny produced by engineered cells was not significantly higher compared to the parental cell line, we could not exclude that intracellular mechanisms of virus replication had changed due to the modulation of host cell gene expression. To elucidate this in greater detail, we investigated virus replication dynamics on the intracellular level both experimentally and computationally. With the help of the single-cell model, we quantified the changes in key kinetic parameters by fitting to the available experimental data. A detailed discussion of parameter changes in genetically engineered cell lines and their possible relation to the biological function of the corresponding host cell factors will be discussed in the following.

NXF1 In contrast to our initial model predictions (Figure 4.2), both nuclear import rate and viral mRNA synthesis rate were reduced in some SGOs compared to their parental A549 cell line. For instance, the viral mRNA synthesis rate in infected cells overexpressing the nuclear export factor NXF1 was only about 60 % of the one in parental A549 cells, which alone would lead to a reduction in virus yield by 50 %. Still, the

NXF1 SGO was the only cell line with a higher cell-specific virus yield when infected at MOI 1 (Figure 4.6 D). The model can only capture these experimental data by an increase in the virus release rate. Hence, the improved virus release rescues virus yields such that despite the adverse changes in viral RNA synthesis, the SGOs release equal or slightly higher amounts compared to the parental A549 cell line. It was reported that inhibition of NXF1 in A549 cells impairs nuclear export of viral mRNAs encoding for NP as well as the surface proteins HA and NA [328]. Upon overexpression of NXF1, viral mRNA export might be improved, which may lead to an earlier onset of translation, such that viral surface proteins are available earlier compared to the parental A549 cell line, which is less efficient in protein maturation and trafficking [327]. In the single-cell model, those steps are not explicitly modeled but lumped into a joint release mechanism that depends on the availability of viral proteins and genome copies in the cytoplasm (see Equation (3.1.26) in Section 3.1.1). In addition, the importance of the virus release mechanism was also shown by initial model predictions (Figure 4.2) that identified virus assembly and budding as kinetic bottleneck of virus production.

CEACAM6 The overall tendency that an increase in the virus release rate can compensate adverse changes in RNA synthesis steps was also observed for infected CEACAM6 SGO cells. In contrast to NXF1, CEACAM6 is not directly involved in steps of RNA synthesis but seems to interact with newly synthesized viral NA proteins during infection, which activates the Src/Akt survival pathway in A549 cells as shown by Gaur and colleagues [326]. In the same study, CEACAM6-silenced A549 cells showed reduced levels of viral genome copies and proteins. However, in our study, the overexpression of CEACAM6 was not beneficial for IAV replication. Accordingly, temporal upregulation of CEACAM6 instead of high abundance seems to be crucial for cellular survival signaling during infection. Furthermore, members of the CEACAM family are already upregulated upon infection by different influenza virus strains, as recently also shown for CEACAM1 and CEACAM5 [330]. In particular, CEACAM1 induction triggers the innate antiviral host cell response by suppression of the translational machinery and limits viral spread [331]. Taken together, the ambivalent role of the CEACAM family and, in particular, the functional role of CEACAM6 in cellular survival pathways, may support the finding that the overexpression of CEACAM6 can be disadvantageous for IAV replication. Still, it is remarkable that CEACAM6 SGO cells release equal amounts of progeny virions compared to parental A549 cells, indicating that despite a certain inhibition of replication, the virus maintains a basal level of reproduction.

PLD2 Except for cells lines overexpressing either NXF1 or CEACAM6, for which the nuclear import rate was slightly reduced ($p \leq 0.1$, calculated by one-sided Gauss test),

the nuclear import rate of vRNPs was similar in the other SGOs compared to parental A549 cells. For the PLD2 SGO, this was unexpected, since it is known that inhibition of PLD2 results in delayed virus entry and reduced viral titers [329]. Still, overexpressing PLD2 did neither improve virus entry nor virus release in our study. The only change in kinetic parameters, that was in agreement with initial model predictions (Figure 4.2) and should benefit virus yield, was the reduction of the cRNA synthesis rate by about 50 % compared to parental A549 cells. However, this alone would result in an increase of virus yield by only about 1.3-fold in simulations, a small improvement that is eliminated by a simultaneous decrease in the mRNA synthesis rate in PLD2 SGOs as determined from the experimental data (Figure 4.7).

FANCG   According to a mini-replicon study, the candidate FANCG interacts with the three viral polymerase subunits (PB2, PB1 and PA) and has a direct influence on polymerase activity [325]. In this particular assay, it was demonstrated that a FANCG knockdown resulted in a decrease of polymerase activity by 50 % while overexpression of FANCG showed a three-fold increase in polymerase activity. According to our initial model predictions, FANCG would have been the most promising candidate to improve virus yield, in particular, if the mRNA synthesis rate was increased (Figure 4.2). Surprisingly, all viral RNA species showed reduced levels in infected FANCG SGO cells. Although we have only performed two independent experiments to measure intracellular viral RNA levels in infected FANCG SGO cells, RNA copy numbers were lower compared to those in infected A549 cells in the same experiments as well as compared to the averaged RNA levels in A549 cells from all four independent experiments. Taken together, it seems that an overall increase of the viral polymerase activity results in imbalanced virus replication. Therefore, additional simulations were performed to test the effect of increasing all three or different combinations of the RNA synthesis rates simultaneously. However, by only increasing the vRNA synthesis rate, a reduction in virus yield is predicted (Figure A.5 in the appendix), while any other scenario leads to an either modest or significant increase in final yield in simulations (Figure A.6 and Figure A.7 in the appendix, respectively). Hence, our experimental observations together with the model-based analysis of this candidate are not in agreement with the study of Tafforeau and colleagues [325]. On the one hand, this may indicate that observations in an (artificial) mini-replicon assay can only give hints towards changes in mechanisms and that the observation in the context of an infection, i.e., including additional regulatory steps of replication and availability of cellular and viral precursor molecules, can be contradictory. On the other hand, FANCG also has a beneficial function for the host cell, since it is involved in DNA repair mechanisms. We could, therefore, speculate that damage

of cellular DNA induced by IAV infection [332] is reduced by overexpressing FANCG. However, we cannot exclude that FANCG plays a pro-viral role by interacting with the viral polymerase.

XAB2 Similar to FANCG, also XAB2 is involved in DNA repair mechanisms, in particular, in transcription-coupled DNA repair [333]. Furthermore, XAB2 was identified as a host restriction factor for IAV as well as for other viruses, e.g. West Nile virus, Vaccinia virus and HIV-1 [334]. In our study, however, the overexpression of this factor neither improved nor impaired viral reproduction.

Virus release of cell lines overexpressing multiple host cell genes In a few infected SGOs the change in various kinetic parameters should be beneficial for virus replication according to model predictions (Figure 4.2 and Figure 4.7), e.g. a decrease in cRNA synthesis rate upon overexpression of FANCG, PLD2 or XAB2, or an increase in the virus release rate upon overexpression of CEACAM6, FANCG or NXF1. Using a Monte Carlo approach, we performed single-cell simulations using randomized SGO parameter sets to predict virus release of MGOs. Those predictions revealed that the productivity of single cells follows a log-normal distribution with highly productive cells as rare events (Figure 4.8). This finding is supported by previous single-cell analyses performed by our group, which investigated the cell-specific productivity of MDCK cells infected by IAV. In particular, they demonstrated that there is a large variability in the productivity of individual cells and that only very few cells are highly productive and yield up to 10-fold higher titers compared to the cell population average [123, 277]. Furthermore, the most recent study showed that single-cell virus yields are log-normally distributed [123]. While MGO simulations suggest that particular combinations of genes have the potential to yield IAV titers similar to an *in silico* optimized cell line with an optimal virus release rate or M1 binding rate (open circles, Figure 4.8), we could not generate MGOs with an elevated overall HA titer. However, it has to be taken into account that all experimental data were acquired from cell populations of genetically modified cells with different combinations and expression levels of host cell genes. Thus, beneficial combinations of host cell factors in individual cell clones might be masked. More extensive screening would be required to identify and isolate individual cell clones, which reflect the features predicted *in silico*.

To improve model predictions for MGO populations and guide rational design of MGOs in the future, we investigated further computational approaches together with collaboration partners. For this, we used our initial assumption that MGOs should show a production phenotype that is a mixture of the underlying SGOs. In addition, we considered population balance modeling to describe the heterogeneity in the level of gene overexpression in genetically modified cell lines [335]. While with the single-cell

model, we only used the median values of the SGO parameter distributions, population balance modeling opens to possibility to reproduce the cell-to-cell variability by linking the distributions of kinetic parameters to those of the production phenotype. Using those assumptions, we evaluated different strategies to generate distributed parameter sets for MGOs based on the bootstrapped distributions of the kinetic parameters for SGOs [336, 337]. In particular, the most promising strategy combined SGO parameter distributions and additionally accounted for the relative level of overexpression of the corresponding genes to construct parameter distributions of MGOs. With this, population balance model simulations predicted that the process yield can be improved by up to one order of magnitude. In addition, the more genes were transduced *in silico* to generate MGOs, the more virus was produced, which supports the findings of our single-cell MGO simulations (Figure 4.8).

Applicability and limitations of the single-cell model   The present version of the mathematical model of IAV replication is most suited to describe the impact of host cell factors that act directly on individual steps of the virus life cycle, e.g. factors that modulate the activity of the polymerases. The assumption that the influence of such factors also directly impacts kinetic parameters of the model enabled the identification of bottlenecks in virus replication that could be modulated by cell line engineering. Similar model-based approaches were performed previously by others to compare the replicative properties of different influenza virus strains [252, 338], of different respiratory viruses [339] and virus replication with and without antiviral treatment [37, 284]. While Binder and colleagues [269] compared low and high permissive host cells for HCV replication that showed different intracellular basal concentrations of the same host cell factor, we applied the single cell model of IAV replication to quantify changes in key kinetic parameters of virus replication in cell lines overexpressing different host cell factors, which has not been reported before. Still, all these approaches have in common that they are solely computational, focusing on virus dynamics described by a fixed set of equations. As a result, in our study, similar 'patterns' of parameter changes were found for cell lines overexpressing host cell factors with very diverse functions, e.g. $k^{\mathrm{Imp}} \uparrow$, $k_{\mathrm{V}}^{\mathrm{Syn}} \rightarrow$, $k_{\mathrm{C}}^{\mathrm{Syn}} \rightarrow$, $k_{\mathrm{M}}^{\mathrm{Syn}} \downarrow$, $k_{\mathrm{M1}}^{\mathrm{Bind}} \rightarrow$ and $k^{\mathrm{Rel}} \uparrow$ for both NXF1 and CEACAM6. Therefore, this model-based analysis can only provide indications regarding the general impact of an overexpressed host cell factor. Clearly, further in-depth characterization of the impact of host cell factors on individual steps of virus replication is required on the molecular level to fully comprehend the biological implications of parameter changes determined in the present work. To neglect details of cellular processes and pathways, e.g. cellular transcription and translation or immune response, may limit model

predictions. On the contrary, the implementation of proposed functions of candidate host cell factors into the model may lead to biased interpretation of experimental data (self-fulfilling prophecies). In the future, more elaborate dynamic models on virus-host cell interactions should not only account for the viral life cycle but also include a mathematical description of the cellular pathways in which the considered host cell factors are involved. While Madrahimov and colleagues made an attempt to realize this in a boolean framework [212], they are neglecting quantitative and dynamic aspects of virus replication, which limits the applicability of their approach. In addition, the biological knowledge about how most host cell factors impact the viral life cycle is too sparse and even controversial to be readily implemented into a mathematical framework. To elucidate this in more detail can only be accomplished through experiments which analyze changes in the viral life cycle together with the dynamics of host cell factors and the activity of the corresponding cellular pathways. Regarding the further improvement of quantitative models for intracellular virus replication, this will probably be one of the most challenging tasks to be performed over the next decades. Moreover, we model virus dynamics in an average infected cell and do not account for stochastic effects that play a role at low molecule numbers, i.e., for low MOI infections. We can therefore only estimate parameters from experimental infections performed at high MOI (MOI ≥ 1), which ensures that the majority of cells is infected simultaneously. Thus, the infection propagates synchronously in the cell population and virus release reaches steady state within 24 h. In these high MOI scenarios, replication can also be affected adversely by introducing a high number of non-infectious virions, e.g. DIPs. There are already single-cell models available that also describes the impact of DIPs on virus replication (see Section 4.2, [309]). However, since the intracellular mechanisms of DIP interference remain elusive, we think that, now, the modeling of DIP propagation in engineered cell lines seems unreasonable but should be taken into account in future studies.

Limitations of targets identified by RNAi screens and target validation studies
Usually, the significance of cellular targets identified from loss-of-function studies is limited, e.g. due to inefficient knockdown or off-target effects that lead to identification of false positives and false negatives (discussed in [340–342]). In our study, we therefore chose host cell factors relevant for IAV replication that were not only identified in RNAi screens, but have also been described previously in additional studies, except for XAB2. Still, the importance of these factors is mostly inferred from loss-of-function studies and we simply assumed that if the knockdown of a host cell factor results in reduced virus growth, the overexpression of the same factor should improve virus replication. Overall, however, we found that most differences in both intracellular replication and progeny

virus release were noticeable, but not statistically significant compared to parental A549 cells. Only when infected at MOI 10^{-4}, engineered cell lines showed higher HA titers at early time points (see Table A.5 and Table A.7 in the appendix), while the HA titers of all cell lines were similar at time of harvest (72 h p.i.). Hence, we confirmed findings of screens for which changes in virus growth were evaluated at early time points (12–48 h p.i.) after infection at MOIs below one [321–324], where a single readout is useful to identify host cell factors that have a strong impact on early virus dynamics. Such factors are very interesting in the context of antiviral treatment, for which the interference with virus replication early during infection might promote viral clearance *in vivo*. Although they are required to complete the replication cycle successfully, such factors might not even limit viral replication at their basal expression level. Hence, their overexpression would not result in any measurable changes of intracellular mechanisms. To improve vaccine production, however, the expression of host cell factors should be increased which improve the maximum cell-specific productivity. For this purpose, screening designs should be re-considered to capture not only dynamics of virus growth but also virus yield at time of harvest. Since large scale high-throughput screens are costly, a first step might be the re-evaluation of already existing screens that considered multiple time points post infection, e.g. [343–345]. Recently, re-evaluation of primary data from various RNAi screens and different virus-host cell interaction studies, i.e., protein-protein interactions, transcriptomic and proteomic data, revealed and validated the impact of host cell factors on virus replication, that were previously unknown [345–347]. This highlights the importance of study design and subsequent bioinformatical analysis, which both strongly contribute to the identification of key host cell factors for intracellular virus replication and release. Beyond that challenge, we have no indication regarding the optimal level of gene (over)-expression required to achieve a positive impact on virus growth, while avoiding off-target effects. In our study, we used lentiviral transduction without control of the integration site and assumed that cells, for which insertion of the overexpression constructs was beneficial, will propagate well in culture. Indeed, we saw that transduction of different host cell factors resulted in different levels of overexpression (Table A.6 and Table A.6 in the appendix). Surprisingly, the cell line with a very low overexpression level of the host cell factor NXF1 was most promising with respect to early virus dynamics. In contrast, a high level of overexpression might stress the biosynthetic capacity of the cell, and result in a competition between expression of candidate genes and viral proteins. It is particularly known that the translation of viral proteins is the energetically most costly step of virus replication [348]. If the synthesis capacity of the cell is exploited by both overexpression of candidate genes and expression of viral proteins, cellular resources needed for virus growth might become limiting. Together,

this might explain the observation that SGOs, in particular those showing high expression levels of the candidate gene, produce the same or only slightly higher virus yields compared to the parental A549 cell line. However, experimental proof would be needed to support those speculations. To better control overexpression levels, it might be worthwhile to explore other gene editing methods, e.g. recombinase-mediated cassette exchange [349] or CRISPR/Cas9 [350], for target validation studies. As discussed before, some host cell factors are already enriched upon infection and it might be also insightful to follow their expression levels over time, e.g. done by [331, 347]. Based on such observations, the design of an inducible expression system [351, 352] that allows to control supply of host cell factors in a temporal manner could be promising if this is needed for their function. Clearly, to control level and timing of overexpression of pro-viral host cell factors during virus replication is a challenging task. In contrast, it might seem more promising to knockdown anti-viral factors based on readouts directly obtained from RNAi screening data. However, knockdown cell lines generated by our consortium performed even worse compared to the overexpression cell lines [319]. In addition, there was an initiative by other researchers to improve poliovirus production in Vero cells by cell line engineering. At first, the knockdown of host cell factors that inhibit virus replication was reported to result in a ten-fold increase in virus titers [205]. This promising result, however, could not be reproduced in a follow-up study using CRISPR/Cas9 for gene knockout [353]. Hence, to fully grasp the potential of host cell manipulation by knockdown and overexpression seems to require a more holistic understanding of the host cell system. For this, it is not only necessary to take a detailed look at molecular interactions between host and viral factors, but also analyze cellular interventions resulting from genetic manipulation, such as activating alternative cellular pathways that can help the cell to compensate measures of cell line engineering. While only a few proteins are responsible for maintaining cellular pathway homeostasis [354], genetic engineering will have little impact if expression of such host cell factors is manipulated, that are only in the periphery of the cellular pathway network.

Summary With regard to the optimization of influenza vaccine production, we and others have struggled to engineer cell lines with the aim of increasing cell-specific virus yields. Instead, we only observed an earlier onset of virus release for some of our candidate cell lines, whereas the maximum number of viral progeny was similar compared to the parental cell line. The fact that our findings for specific gene candidates contradict reports by other research groups underlines the challenge in obtaining and applying robust knowledge about virus-host cell interactions. As shown in a first attempt in this work, mechanistic models of the virus replication cycle are indispensable for the

evaluation and interpretation of infection data from engineered cell lines. Thus, we envision that screening approaches focusing on virus yield at harvest time points relevant in vaccine production supported by simulation studies using mathematical models for virus replication will enable the design of novel producer cell lines with the final goal to improve cell culture-based vaccine manufacturing. In addition, the combination of both, experimental and computational, approaches using data from well-defined experimental conditions will significantly deepen our understanding of intracellular mechanisms of virus-host cell interactions and, thus, support the development of measures in the fight against infectious diseases.

4.2. Modeling DIP growth on the single-cell level

In the previous section we have analyzed how molecular mechanisms of the viral life cycle can be influenced by host cell factors. Now, we will take a look at influencing factors that are inherent to the composition of the virus population itself. Virus populations comprise various virus particles with different biological features. Mostly, virus research is concerned with infectious virus particles, i.e., replication-competent particles, that propagate in host cells and cause disease. However, the majority of virus populations are replication-incompetent particles. They further split up into multiple sub-populations with different abilities to influence the outcome of virus infections. Here, we use mathematical models to analyze the impact of a specific viral sub-population called DIPs. They carry at least one genome segment with a significant internal deletion. Due to this defect they cannot complete a replication cycle by themselves and are dependent on the co-infection by an infectious virus, i.e., STV. During co-infection, DIPs act as molecular parasite of the STV and use joint resources to complete their replication cycle and, thus, replicate at the expense of the STV. Due to their ability to interfere with STV replication they could potentially serve as an antiviral. Thus, there is an increased interest in DIP-related research in both virology and biotechnology. However, there is a need to deepen the understanding of how DIPs interfere with STV replication on the molecular level. In the following we will analyze the impact of DIPs on the viral life cycle and elucidate molecular details related to their interfering potential.

4.2.1. Interference by viral deletion mutants

DI RNAs are sub-genomic RNAs of the IAV genome. They arise during conventional virus replication due to errors of the viral polymerase that cause an internal deletion of the FL genome. While it is commonly believed that interference by deleted RNAs is caused through a length-dependent advantage in RNA synthesis, DI RNAs could potentially also hijack other steps of the viral life cycle (reviewed by Nayak *et al.* (1985) [115]). To analyze hypotheses proposed in literature, we constructed three models accounting for different modes of DI RNA interference. For this, we used the mathematical single-cell model of IAV replication introduced in the previous chapter [18] and extended it with different mechanisms for DI RNA growth at particular steps of the viral life cycle. Results from simulated co-infections will be compared to available experimental data to reveal which mechanisms contribute to IAV DIPs' successful competition over their STV. Furthermore, we will challenge the most frequently proposed hypotheses on length-dependent DI RNA synthesis based on measurements of intracellular IAV replication dynamics. The single-cell model accounting for an advantage in DI RNA synthesis was developed in collaboration

with previous members of the BPE group [26, 308] and published in the *Virus Research* article by Laske and Heldt *et al.* (2016) [309]. Results from this publication will be reproduced here and used as a benchmark to allow a comprehensive comparison of the different hypotheses on the DI RNAs' mode of interference.

Length-dependent replication of influenza A virus RNA   In literature, it is commonly proposed that DI RNAs outcompete FL RNAs since the viral polymerase can synthesize more copies of the shorter DI RNAs. Indeed, the majority of DI RNAs that have been reported so far are significantly shorter than their corresponding FL RNAs (reviewed in [105, 115]). For instance, the promising antiviral candidate DI 244 [145] is a deletion mutant of the IAV S1, encoding PB2, and 395 nt long, which represents only 17 % of its parental FL segment in length. Thus, it seems reasonable to assume that more copies of DI 244 could be synthesized compared to its FL segment in a given time period. However, so far, it has not been demonstrated how exactly a reduction in length would translate into an increase in RNA synthesis rates. In addition, if length-dependent RNA synthesis is an inherent feature of IAV replication, differences in the RNA synthesis rates of the eight FL segments should also become evident during virus growth. Since the lengths of the FL segments span a range of 890–2341 nt [19], we anticipated a significant length-dependent difference in RNA synthesis rates as well as in segment-specific maximum RNA levels. Since cRNA synthesis was described as the source of the DI RNA's advantage, we analyzed cRNA measurements from IAV-infected MDCK cells and determined the segment-specific cRNA synthesis rates through linear regression of the data (Figure 4.9 A and B). The differences in cRNA synthesis rates were neither significant nor showing a clear trend related to segment length (Figure 4.9 D). Note, that the RT-qPCR method used here is not able to distinguish FL and DI genomes. Thus, the cRNA synthesis rate of segment 3 (S3), encoding PA, might represent an outlier due to the presence of DI RNAs that originate predominantly from the longest genome segments [120, 122] and are also present in the A/PR/8/34 seed virus [14, 121]. If S3 is excluded, a slight, however, still insignificant trend towards faster cRNA synthesis of shorter FL segments can be observed that qualitatively follows the model assumption by Laske and Heldt *et al.* [309] (dotted gray line in Figure 4.9 D, Equation (3.2.26), Section 3.2.2). To complement the analysis of the data, we also analyzed whether the maximum cRNA copy number of the individual segments reached in cells during infection shows a dependency on segment length (Figure 4.9 C). Although the individual segments show noticeable differences in their maximum levels, we did not observe a clear trend towards higher maximum levels of shorter FL segments. Here, a linear correlation of length and maximum cRNA levels becomes evident only if FL S3 and FL segment 8 (S8),
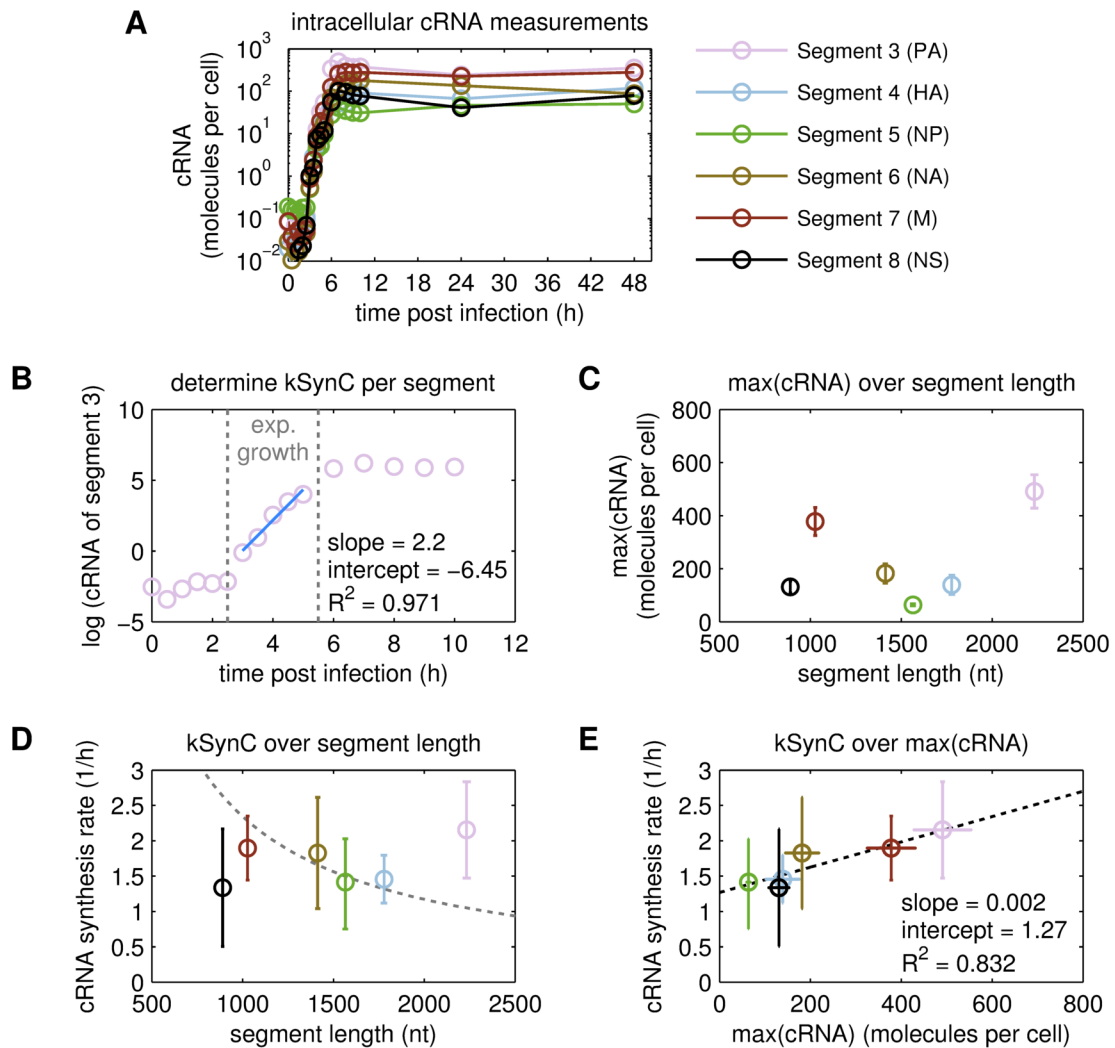
Figure 4.9.: Length-dependency of synthesis rates and maximum intracellular levels of influenza A virus full-length segments' cRNA. Adherent MDCK cells were infected by the influenza virus strain A/PR/8/34 (H1N1) at MOI 6 and intracellular viral cRNA levels were assessed by segment-specific RT-qPCR ($n = 3$). (A) Median cRNA values of the viral genome segments 3–8 (open circle, error bars were omitted for sake of simplicity). (B) Log-transformation (open circles) and linear regression (blue solid line) of median cRNA values were performed to determine the cRNA synthesis rate (kSynC) of each segment during the exponential growth phase (vertical gray dotted lines), exemplified using the cRNA measurements of segment 3. (C) Correlation of maximum intracellular cRNA levels and segment length (open circles, average $\pm$ standard deviation). (D) Correlation of kSynC and segment length (open circles). Error bars represent the 95 % confidence interval of the slope determined by linear regression, described in (B). The gray dashed line represents the DI RNAs' length-dependent cRNA synthesis rate proposed by Laske and Heldt *et al.* [309] to account for enhanced DI RNA replication (see Equation (3.2.26), Section 3.2.2). (E) Correlation of kSynC and the maximum intracellular cRNA levels of each segment (open circles, horizontal and vertical error bars as in (C) and (D), respectively). Linear regression was performed to examine consistency of the data analysis (black dotted line). Colors according to legend. Experiments conducted by Antje Pflugmacher, measurements of segment 5 published in [37]. Note, that segment 3 is used as a representative of the polymerase-encoding segments and, thus, analysis of segment 1 and segment 2 was omitted. Similar analyses were conducted for the viral mRNA and vRNA measurements of this study (Figure B.1 and Figure B.2 in the appendix).

i.e., the longest and the shortest FL segments, were excluded from the analysis. Finally, and to show consistency of our analysis, we also evaluated the correlation between the cRNA synthesis rate and the maximum cRNA copy number of the individual FL segments achieved during infection (Figure 4.9 E). As expected, we observed a noticeable, although insignificant, trend towards higher maximum cRNA levels for higher cRNA synthesis rates.

In brief, we did not find convincing evidence for the length-dependency of the FL cRNA synthesis rates. Nevertheless, the data convey that as soon as DI RNAs are present, e.g. in case of S3, different replication phenotypes become evident (Figure 4.9 C and D). Hence, we may hypothesize that conventional molecular mechanisms related to RNA replication do not apply equally to both FL and DI segments. While this seems to support the primary hypothesis on a DI RNA replication advantage, we decided to test whether features described for DIP co-infections could be reproduced in case the DI RNA hijacked other steps of the viral life cycle. For this, we built three models that account for different modes of interference exerted by the DI RNA. Details on model construction and simulation results will be presented in the following paragraphs.

Modeling different hypotheses on DI RNA interference Based on literature, we implemented three major hypotheses on the DI RNAs' mode of interference (reviewed by Nayak *et al.* [115]). Firstly, and most frequently proposed, is enhanced replication of DI RNAs due to their reduced length, which allows them to outcompete FL RNA growth during co-infection [119, 124, 125]. Secondly, it has been hypothesized that due to their deletion, DI RNAs might have lost crucial, yet unknown, regulatory parts of their sequence. Thus, DI RNAs can be possibly amplified to significantly higher levels compared to FL RNAs [115]. Thirdly, it was reported that the DI-to-FL RNA ratio was increased on the extracellular level compared to the intracellular level, suggesting that DI RNA segments might be preferentially packaged into progeny particles [124, 128, 129]. Since all of these steps are already described in great detail in our previously published model of the intracellular life cycle of IAV [18], it served as a substantial basis for further model extensions. Recently, we have proposed an augmented version of that model to account for the co-infection by DIPs with an enhanced DI cRNA synthesis [309]. In light of that study, we propose two further model variants for co-infection by DIPs, which account for the different molecular mechanisms of DI RNA interference described above (Figure 4.10). Overall, any of the proposed mechanisms could be related to the length of the DI RNA, i.e., the shorter a genomic RNA is, (i) the faster it is being copied, (ii) the more easily it is incorporated into progeny particles, (iii) the more sequence elements are lost that would usually be involved in the control of the replication and/or the packaging process.
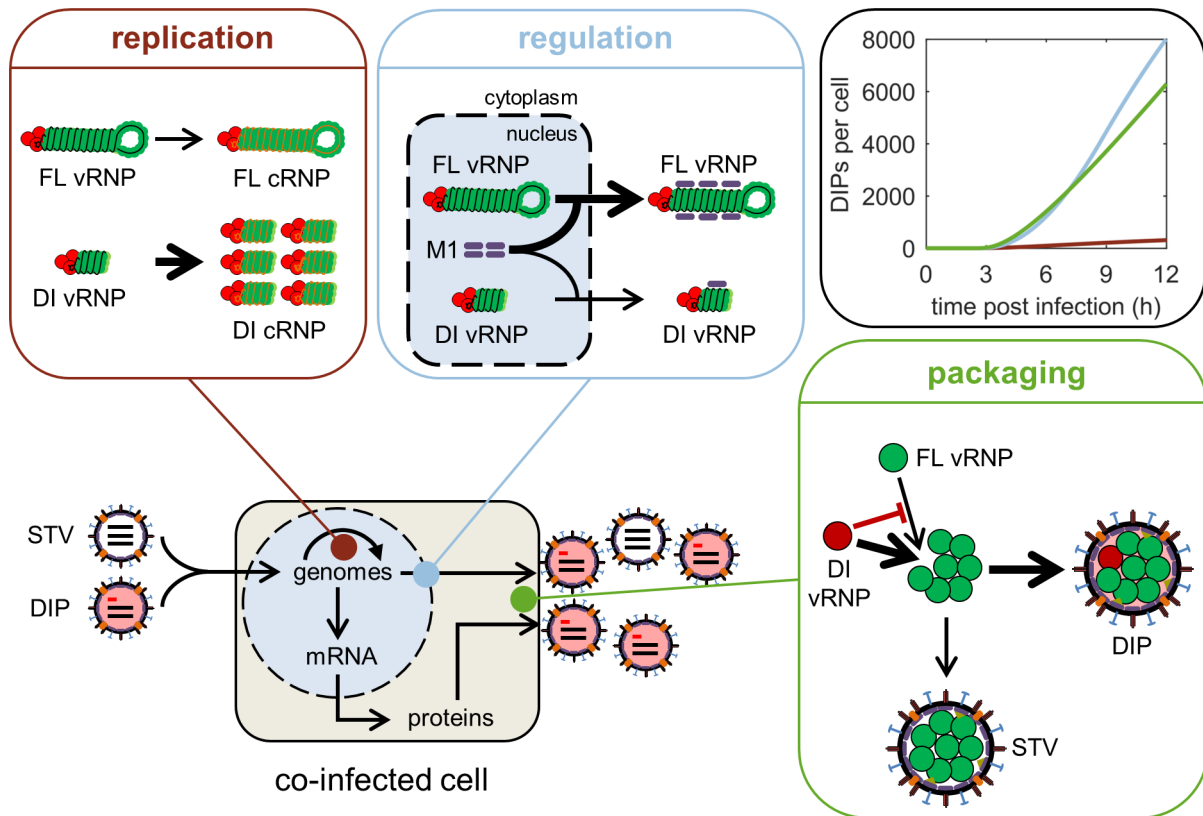
Figure 4.10.: Schematics of three single-cell model variants that account for different modes of DI RNA interference and the resulting DIP release dynamics. The figure in the bottom left corner shows a simplified model scheme of a single cell co-infected by a standard virus (STV) and a defective interfering particle (DIP). The three surrounding miniature schemes depict particular steps of the viral life cycle which are presumably hijacked by DI RNAs. They visualize how the DI RNAs exert different advantages either at the step of cRNA synthesis where more DI cRNAs are synthesized per unit time (brown box), or at the level of regulation of RNA synthesis, where they show reduced M1-mediated nuclear export (blue box), or at the stage of genome packaging, where they interfere with the incorporation of their cognate FL vRNPs into the "1+7" configuration of genome segments inside budding progeny particles through competitive inhibition (green box). To provide a first impression on how the different DI RNA's modes of interference influence model output, the DIP release profile of a cell simultaneously co-infected by 10 DIPs and 10 STVs is shown in the upper right corner (black box, color scheme according to the boxes of the miniature model schemes). The model variant describing enhanced DI cRNA synthesis follows the approach by Laske and Heldt *et al.* [309] (brown box).

While our single-cell model [18] does not explicitly account for the function of sequence elements we are still able to account for an increase in the DI RNA synthesis rate, a differential regulation of DI RNA replication and a preferential packaging of DI RNAs by including an advantage of the DI RNA at the respective steps in the viral life cycle. For the sake of simplicity, we based the model parameter accounting for the advantage F_{Adv} of all models on the FL-to-DI RNA length ratio (Equation (3.2.25), Section 3.2.2), which we did previously to model a length-dependent advantage in DI cRNA synthesis (Figure 4.10, [309]). However, please note, that we constructed the models in a way that easily allows to uncouple F_{Adv} from the RNA length (Section 3.2.2). To account for a differential regulation of DI RNA synthesis we modeled a length-dependent binding of the viral M1 to DI vRNPs. Upon binding of M1, vRNPs are exported from the host cell's nucleus and cannot serve as a template for replication any longer. If DI vRNPs could escape that mechanism and, thus, prolong their residence time inside the nucleus, they could replicate to higher levels compared to the FL segments. The elevated DI RNA levels achieved by an advantage in either replication or regulatory mechanisms already allow the DI RNA to form more progeny particles compared to its corresponding FL segment. As we have already shown with our model for DI RNAs with an advantage in replication [309], this is related to the inherent mass-action kinetics used to describe virus release (Equation (3.2.21), Section 3.2.1). To still characterize the impact of a sole packaging advantage we explicitly modeled a packaging mechanism that accounts for a competitive inhibition of the DI and the FL vRNPs during virus budding (Figure 4.10; Equation (3.2.31), Section 3.2.2). Here, DI vRNPs exert a length-dependent advantage in being incorporated into budding progeny particles and simultaneously inhibit the formation of FL segment-containing vRNP complexes.

In the following paragraphs, we compare the impact of the different DI RNA's mode of interference on the outcome of DIP co-infection. For this, we focused on simulating the growth of a known DI RNA candidate, referred to as DI 244 [145]. This DI RNA originated from FL S1 and is 395 nt long, which corresponds to a FL-to-DI RNA length ratio of 5.93. Thus, the DI S1 either replicates 5.93-fold faster, or, has a M1 binding rate which is reduced by 83.1 % compared to FL S1, or, has a dissociation constant increased by 83.1 % during DI vRNP incorporation into budding particles, while that of its corresponding FL vRNP is reduced by 83.1 %, respectively.

Impact of DIP co-infection on virus yield   To investigate the three different hypotheses on DI RNA interference in more detail, we performed simulated infections to compare virus release of STV-only infected, DIP-only infected and co-infected cells (Figure 4.11). For this, we also included a control simulation that describes the replication of a
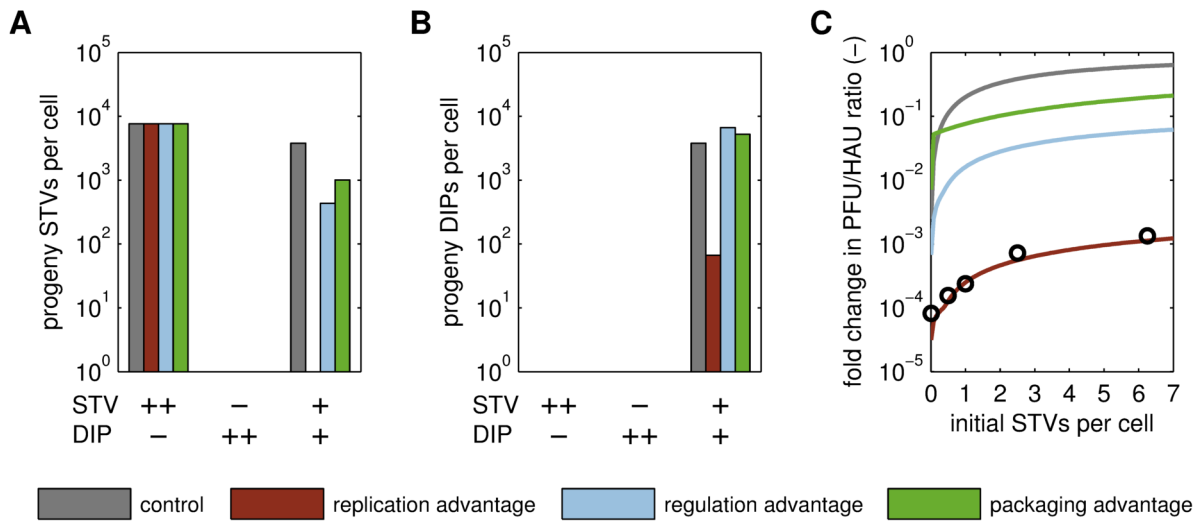
Figure 4.11.: DI RNA's mode of interference impacts the virus yield of DIP co-infections. Simulated number of progeny STVs (A) and DIPs (B) at 12 h p.i. for an infection of a cell by two STVs, two DIPs, or co-infection by one STV and one DIP. The DIP carries a defective segment 1 (DI S1, encoding PB2) with a length of 395 nt and has different advantages over its STV at different stages of the viral life cycle. Simulations of DI S1 are compared to those of a full-length DI-like S1 (2341 nt) that has no propagation advantage (control). (C) Comparing ratios of infectious to total virus particles, i.e., the ratio of plaque forming units (PFU) to hemagglutinating units (HAU) in experiments (open circles) and the ratio of STVs to total virus particles (sum of STVs and DIPs) in simulations (solid lines), of virus progeny at 24 h p.i. for a simultaneous co-infection of a cell by 4 DIPs and an increasing number of STVs added at time of infection. Results were normalized to the ratio obtained for an infection with 0.5 PFU/cell for measurements and 0.5 STV/cell for simulations. Colors according to legend. Model assumptions used to simulate the replication advantage are according to Laske and Heldt *et al.* [309]. Experimental data retrieved from Akkina *et al.* [355].

DIP carrying a DI-like S1 which is as long as its FL segment and which has no advantage in the viral life cycle. Firstly, all models release only STVs in the STV-only infected scenario (Figure 4.11 A, first column), where the amount of released progeny is equal to the control simulation. This is expected since our models only consider amplification of DI RNAs that enter the cell, while they do not account for *de novo* generation of DI RNAs during STV replication. Secondly, DIP-only infected cells do not release any viral progeny (Figure 4.11 A and B, second column). Hence, all models successfully reproduce a known feature of DIPs, which is their inability to replicate themselves in the absence of STVs that provide the genetic information to synthesize the missing viral proteins. Thirdly, only when co-infection occurs, DIPs are released by the co-infected cell (Figure 4.11 A and B, third column). As expected, the control simulation shows that both DIPs and STVs are released in equal amounts, each half of the yield achieved during STV-only infection. In contrast, simulations of models accounting for the different modes of interference result in different numbers of progeny

STVs and DIPs. Here, an infection by a DIP with a replication advantage lead to an exclusive release of DIP progeny and a significant decrease in total virus yield, which validates the results of Laske and Heldt *et al.* [309], who simulated infections with a DI S3. In contrast, cells co-infected by DIPs with an advantage in either regulation or packaging do still release STVs together with high amounts of DIPs. To complement the comparison of virus yields, we performed simulations to reproduce the experiment by Akkina *et al.* [355]. The authors reported that DIP-mediated reduction in virus particle production can be partially reverted by an increase in the number of infecting STVs. We performed simulations to reproduce this experimental setup *in silico* and determined the infectiousness of the progeny viruses, i.e., the ratio of infectious particles to total particles produced, which can be compared to the measurements (Figure 4.11 C). Overall, the model simulations reproduce the trend of the data which show that the infectiousness of progeny viruses is recovered when more STVs were added at time of infection. This improved productivity is related to the higher initial amounts of FL segments and, consequently, an improved FL RNA replication and synthesis of functional viral proteins to overcome the shortcomings of a DIP co-infection. Note, however, that the influence of DIP replication cannot be reverted efficiently and only less than 1 % of infectiousness was achieved compared to an STV-only infection. Thus, the DIPs used in the experiment seem to be highly potent in interfering with STV replication. This experimental finding is reproduced best by the model that assumes the DI RNA exerts an advantage in replication (Figure 4.11 C, reproduction of [309]). To obtain a deeper understanding of the differences related to the other modes of interference in this *in silico* experiment, we also investigated the virus release dynamics of cells infected by a fixed multiplicity of DIPs (MODIP) in combination with an increasing multiplicity of STVs, i.e., MOI (Figure B.3 in the appendix). Here, it became immediately evident that an increase in MOI only has a minor impact on the number of released STV progeny when cells were co-infected by a DIP exerting an advantage in replication (Figure B.3 in the appendix, second column). Instead, mostly DIPs benefit from the increased amounts of functional viral material, which lead to both, an earlier onset of release and a higher maximum virus yield when the MOI was increased. In contrast, cells infected by DIPs with an advantage in either regulation or packaging showed a significant increase in STV yields with an increasing MOI (Figure B.3 in the appendix, third and fourth columns). However, while STV yields recover by up to two orders of magnitude, the numbers of DIP progeny remain largely unaffected and reach values comparable to the control simulation. Furthermore, we systematically analyzed various MOI-to-MODIP ratios and found that large initial amounts of defective virus with an advantage in RNA synthesis have an adverse impact on DIP production and cause an overall decrease in total virus yields (Figure B.4 D in the

appendix). In contrast, cells co-infected by DIPs with an advantage in either regulation or packaging release decent amounts of DIP progeny even in high MODIP scenarios. In particular, co-infections by DIPs with an advantage in regulation result in high amounts of DIP progeny over the entire range of tested MOI-to-MODIP ratios (Figure B.4 F in the appendix). Likewise, also cells co-infected by DIPs with an advantage in packaging can yield higher DIP amounts with an increase in MODIP. Once more, the virus release profile of cells co-infected by DIPs with an advantage in packaging is qualitatively similar to the control simulation, i.e., to co-infections by a DI-like S1 DIP, with the obvious difference that significantly fewer STVs are released (Figure B.4 G in the appendix).

Dynamics of intracellular viral RNA and protein levels   To better understand how the three different advantages of DI RNAs, which we proposed in the previous paragraph, translate into the ability to interfere with STV replication, we compared vRNA and protein levels in STV-only and co-infected cells (Figure 4.12). In case the DI S1 exerts an advantage in replication we observe a reduction in FL vRNA levels by two orders of magnitude (Figure 4.12, upper panel). Interestingly, this does not occur in a segment-specific manner, such that both the parental FL S1 as well as the FL S5, for which no DI RNA is present, show reduced vRNA levels. This overall reduction in FL segments is accompanied by an excessive amplification of the DI vRNA whose levels are three orders of magnitude higher than those of its corresponding FL segment. Strikingly, this increase in DI vRNA and a simultaneous decrease in FL vRNA levels is an exclusive feature of the model accounting for enhanced DI cRNA synthesis (approach according to [309]). The models accounting for either an advantage in regulation or packaging do not predict a significant decrease in FL segment levels. In particular, levels of FL S5 are identical to those of an STV-only infection within the tested time window (Figure 4.12, middle and bottom panel). However, those two models predict distinct DI S1 vRNA dynamics. Here, the model accounting for a regulation advantage predicts an increase in DI vRNA levels by two orders of magnitude compared to its FL segment. In particular, differential accumulation of the DI S1 becomes evident upon approximately 3 h p.i. (Figure 4.12, middle panel). This is related to the impact of regulatory mechanism through M1-mediated nuclear export of vRNPs. While now, FL vRNPs are exported and cannot serve as template for RNA synthesis any longer, DI vRNPs, that escape M1-binding, reside in the nucleus and keep accumulating. Opposed to that, the model accounting for an advantage in DI vRNP packaging does not predict elevated DI vRNA levels. This is expected since such DI vRNPs will only interfere with their FL counterparts at the stage of virus budding.

Furthermore, we evaluated differences in viral protein levels during STV-only and
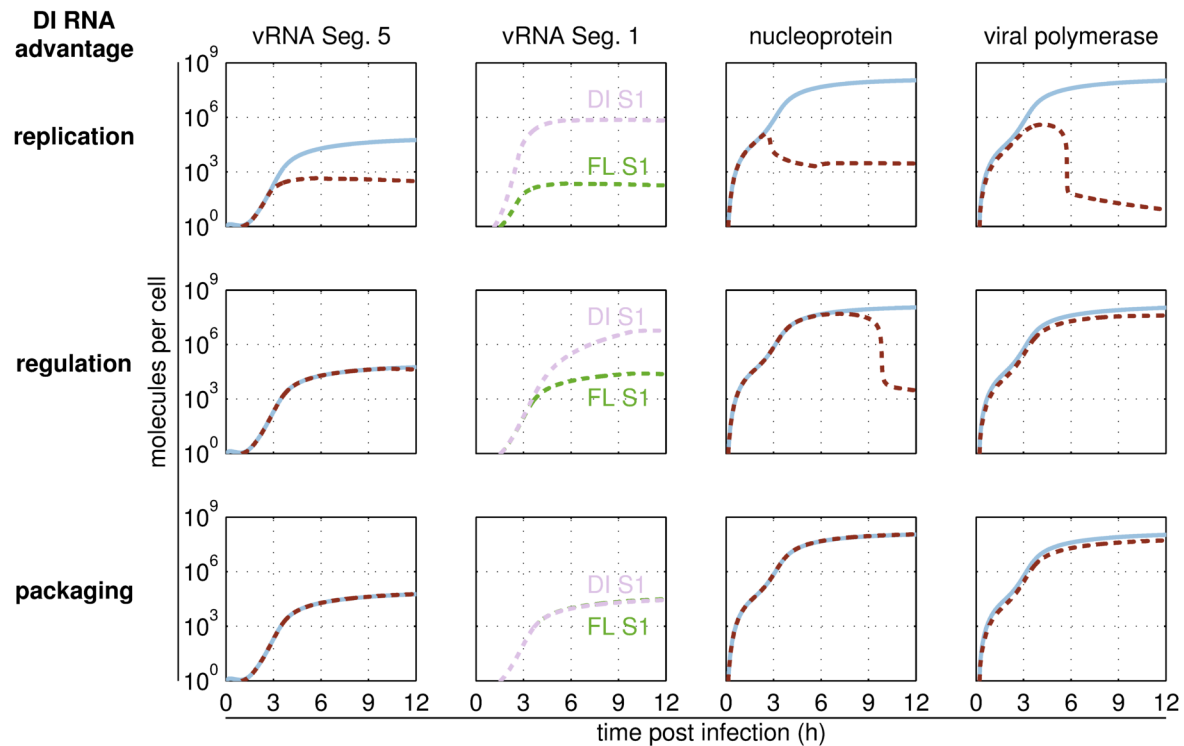
Figure 4.12.: Different modes of interference influence the competition between DI and FL segments for viral resources. Simulated infection of a cell by either two STVs (solid lines) or by one STV and one DIP (dashed lines). Infection occurs simultaneously at 0 h p.i. The DIP carries a defective segment 1 (S1, encoding PB2) which is 395 nt long and can exert different advantages over its FL segment at particular steps of the viral life cycle, as indicated on the left hand side (bold letters). First and second column show the intracellular dynamics of segment 5 vRNA (encoding NP) and S1, respectively. Columns three and four show levels of unbound NP and unbound viral polymerases, respectively. Model assumptions used to simulate an advantage in DI RNA replication (upper panel) are according to Laske and Heldt *et al.* [309].

co-infection. In general, we can state that the stronger the impact of the different DI RNAs was on RNA synthesis, the stronger is their impact on protein levels. In particular, levels of the viral NP and the viral polymerase, which are needed for RNA encapsidation, i.e., for the formation of replication-competent vRNPs and cRNPs, were significantly reduced in case the cell was co-infected by a DIP with an advantage in replication (Figure 4.12, upper panel). During co-infections by DIPs with an advantage in regulation, we only observed a significant reduction in NP levels later during infection, while polymerase levels were only slightly reduced (Figure 4.12, middle panel). This difference is related to the fact that several copies of NP are needed to encapsidate a single RNA, while only one polymerase complex per RNA is required. Since DI RNAs with an advantage in regulation exceed FL segment levels later during infection (explained above), the corresponding drop in NP levels is delayed as well (Figure 4.12, middle panel). Moreover, simulated co-infections by DIPs with a packaging advantage did not show a significant difference in viral protein

levels. Only the amount of polymerases was slightly reduced since the DI RNA originates from a polymerase-encoding segment such that only half of the initial amount of FL S1 was added at time of infection compared to an STV-only infection (Figure 4.12, bottom panel).

In summary, DI RNAs with an advantage in replication interfere most efficiently with STV replication. They replicate to high levels and rapidly deplete the pool of NP and polymerases and, thus, hamper FL RNA encapsidation. This observation is in accordance to the hypothesis that DIPs act as molecular parasites of their corresponding STV and sequester joint viral or cellular resources [105]. While DI RNAs with an advantage in RNA replication are interfering strongly and replicate at the expense of the STV as soon as viral genomes enter the nucleus, DI RNAs with an advantage in either regulation or packaging do not show a strong parasitic behavior. In contrast, they seem to co-replicate with the FL segments instead of out-growing them, which also results in higher DIP progeny numbers (Figure 4.11 B).

Testing different strengths of interference   So far, we simulated co-infections by a defined DIP carrying a DI S1, similar to DI 244, a known antiviral candidate [145]. However, in a real scenario, multiple DI RNAs arise during replication, which provide different lengths and/or ability to interfere with STV growth (reviewed in [13, 115]). To test whether our models can reproduce those experimental observations, we simulated co-infections by DIPs carrying DI S1 with different lengths and evaluated virus yield and intracellular levels of viral genomes and proteins (Figure 4.13). For this, we used our simplified model assumption that the DI RNA's length translates directly into its advantage over the FL segment, expressed by the parameter F_{Adv} in the model (Equation (3.2.25), Section 3.2.2), and systematically analyzed the impact of changes in F_{Adv} on model output. Independent of mode of interference, co-infected cells release equal amounts of STVs and DIP in case the DI RNA does not exert any growth advantage (upper panel, compare to control simulations with DI-like S1 RNA, Figure 4.11). Then, with increasing F_{Adv} two distinct regimen can be observed for DI RNAs with an advantage in either replication or regulation. Firstly, the DIP-to-STV ratio increases until DIP release is maximal, while the number of total virus particles released remains unaffected (Figure 4.13, upper panel). In the second regimen, where F_{Adv} increases beyond its optimum, the number of DIPs as well as the total amount of released viral progeny are significantly decreasing. Those two regimen are directly linked to the abundance of free viral NP and polymerases (Figure 4.13, middle panel). In the first regimen, NP and polymerases are highly abundant such that comparable amounts of replication-competent DI and FL vRNPs are formed. Hence, while the FL segment keeps
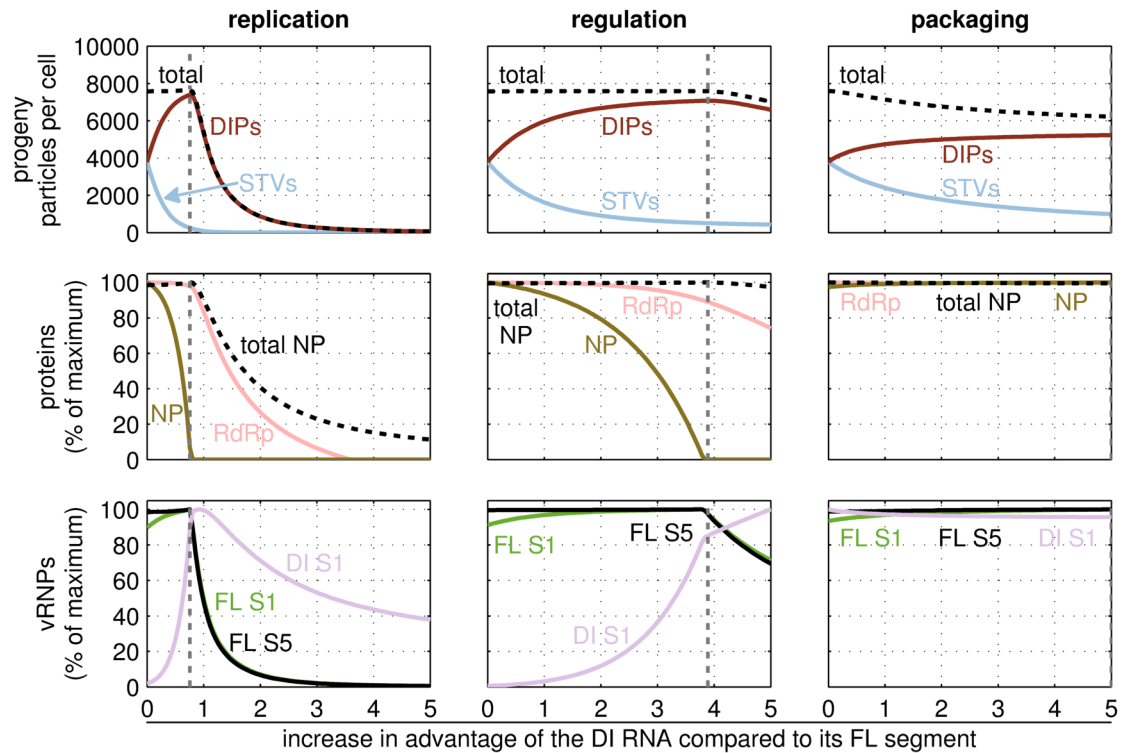
Figure 4.13.: Impact of the DI RNAs' mode and strength of interference on virus growth. Shown are changes in particle release and intracellular viral replication in a cell co-infection by one STV and one DIP. The DIP carries a DI RNA of segment 1 (S1, encoding PB2) which exerts an advantage over its full-length (FL) segment at one of the particular steps of the viral life cycle indicated at the top of each column (bold letters). The DI RNAs vary in length depending on their strength of interference, i.e., their advantage factor F_{Adv} (Equation (3.2.25), Section 3.2.2), indicated on the abscissa of each plot. Co-infection occurs simultaneously at 0 h p.i. and model output is recorded at 12 h p.i. The vertical gray dashed lines indicate the optimal DI RNAs' F_{Adv} at which the maximum number of DIP progeny is achieved. (Upper panel) Number of progeny DIPs and STVs. (Middle panel) Levels of unbound nucleoprotein (NP), total NP synthesized and unbound viral polymerase complexes (RdRp) normalized to their corresponding maximum values achieved within the tested range of F_{Adv}. (Lower panel) Normalized levels of viral ribonucleoprotein complexes (vRNPs) of S1 and FL segment 5 (S5, encoding NP). Model assumptions used to simulate an advantage in DI RNA replication (first column) according to Laske and Heldt *et al.* [309].

replicating to a sufficient extent, the DI segment benefits from an increase in F_{Adv} and can take advantage of the excess functional viral proteins. Consequently, with an increase in F_{Adv}, increasing amounts of DI vRNPs are formed (Figure 4.13, bottom panel), which leads to an increase in the number of progeny DIPs. In addition, not only FL S1 genomes are sufficiently available but also other FL segments, for instance FL S5, needed to form a complete set of eight vRNPs, that is packaged into progeny of both DIPs and STVs. In the first regimen, a slight increase in FL S1 became evident, which is related to the continuously decreasing demand of FL S1 for the formation of progeny STVs. Thus, with an increase in F_{Adv}, fewer FL S1 are packaged into budding particles and the excess FL S1 reside in the cytoplasm. Despite this small difference, FL S1 and FL S5 show a similar behavior for the majority of the tested range of F_{Adv}. The transition from the first to the second regimen is marked by the depletion of the pool of unbound NP, which represents a bottleneck if the strength of interference exceeds its optimum (Figure 4.13, middle panel). As explained in the previous section, multiple molecules of NP per RNA are needed for RNA encapsidation. Consequently, NP becomes limiting while polymerases (RdRp) are still available even if the DI RNA is strongly interfering. However, due to the lack of NP, the levels of both, FL and DI vRNPs decrease (Figure 4.13, bottom panel). Hence, the second regimen is very disadvantageous for virus replication since the decrease in vRNPs of FL S5, i.e., the NP segment, causes a reduction in the overall amount of NP produced (Figure 4.13, middle panel, black dashed line). This further impairs the availability of NP for RNA encapsidation. In summary, our modeling study suggests that DI RNAs with an advantage in either replication or regulation have an optimal F_{Adv} at which a balance between FL and DI RNA synthesis is established. This optimum is characterized by a minimal impact of DI RNA replication on viral protein synthesis, which allows maximum release of progeny DIPs. DI RNAs that strongly interfere with STV growth, i.e., DI RNAs with a very short length, are mediocre competitors since they impair their own replication. Such self-interference is more pronounced for the DI RNAs with an advantage in RNA replication and becomes evident as soon as $F_{Adv} \geq 0.8$. In contrast, DI RNAs with an advantage in regulation continue to accumulate inside the host cell even beyond their optimal F_{Adv}. However, despite high abundance of DI vRNPs, the number of DIP progeny is decreasing due the shortage in FL vRNPs needed to from progeny particles (Figure 4.13, bottom panel). In contrast to the two types of DI RNA described above, a DI RNA with an advantage in vRNP packaging does not interfere with STV growth at the level of RNA and protein synthesis (Figure 4.13, right hand column). Thus, there is no significant impact on the level of viral components, even if F_{Adv} is very high (Figure 4.13, middle and bottom panel). Counter-intuitively, we can observe a slight - however, continuous - decrease in total number of virus progeny as soon as $F_{Adv} > 0$. This is related to the

competitive inhibition of S1 vRNPs during viral progeny assembly, where the DI S1 vRNP is more efficient in suppressing the FL S1 vRNP's incorporation into budding particles. In turn, the accumulation of cytoplasmic FL S1 vRNPs provides a negative feedback to DI S1 vRNP packaging. Thus, with an increasing packaging advantage, the overall packaging process becomes less efficient. Still, we observe a moderate increase in DIP progeny numbers and a corresponding decrease in STV progeny numbers towards higher F_{Adv}. Although those changes appear to be small, the DIP-to-STV ratio is increasing accordingly (Figure B.7 in the appendix).

Impact of delayed DIP co-infection on virus yield In the previous simulations we analyzed model outputs in the ideal case of simultaneous co-infection. However, in a real-world scenario, STVs and DIPs might infect a cell successively, which may influence the outcome of the co-infection. To also analyze such infection events, we simulated infections accounting for a delay in either DIP or STV infection (Figure 4.14). In case STV infection occurs first, FL genomes can replicate without interference such that FL genomes and viral proteins accumulate inside the cell. As soon as a DIP co-infects the cell, it can take advantage of those already available resources and promote its own replication. In particular, delayed co-infections by DIPs with an advantage in RNA replication yield significantly more progeny compared to a simultaneous co-infection (Figure 4.14 C). However, successful DIP replication is challenged by the advancement of STV growth. While the number of progeny DIPs is decreasing as soon as DIP co-infection occurs later than 3 h p.i., STV numbers are recovering correspondingly, reaching virus yields comparable to an STV-only infected cell. Here, DIPs with an advantage in replication show a distinct optimum in co-infection timing around 3 h p.i., whereas progeny numbers of DIPs with an advantage in either regulation or packaging are highest only in case of a simultaneous co-infection (Figure 4.14 E, G). Then, with increasing delays in DIP co-infection, numbers of DIP progeny are decreasing and STV progeny numbers recover rapidly. Those differences in virus production in response to different co-infection timings are related to how DIP propagation is affected by regulatory mechanisms of virus replication. The longer DIP co-infection is delayed, the higher are the intracellular levels of regulatory proteins, i.e., M1 and NEP (see also Figure 4.15 G), which mediate the nuclear export of vRNPs. As explained before, upon nuclear export, vRNPs cannot serve as template for replication any longer. DI vRNPs with an advantage in regulation directly escape M1-binding and, thus, prevent pre-mature shutdown of DI RNA replication. Likewise, DIPs with an advantage in replication can partially escape this mechanisms since they strongly interfere with FL protein expression (see before, Figure 4.13) and also counteract M1 accumulation. Thus, the co-infection time window that allows DIP
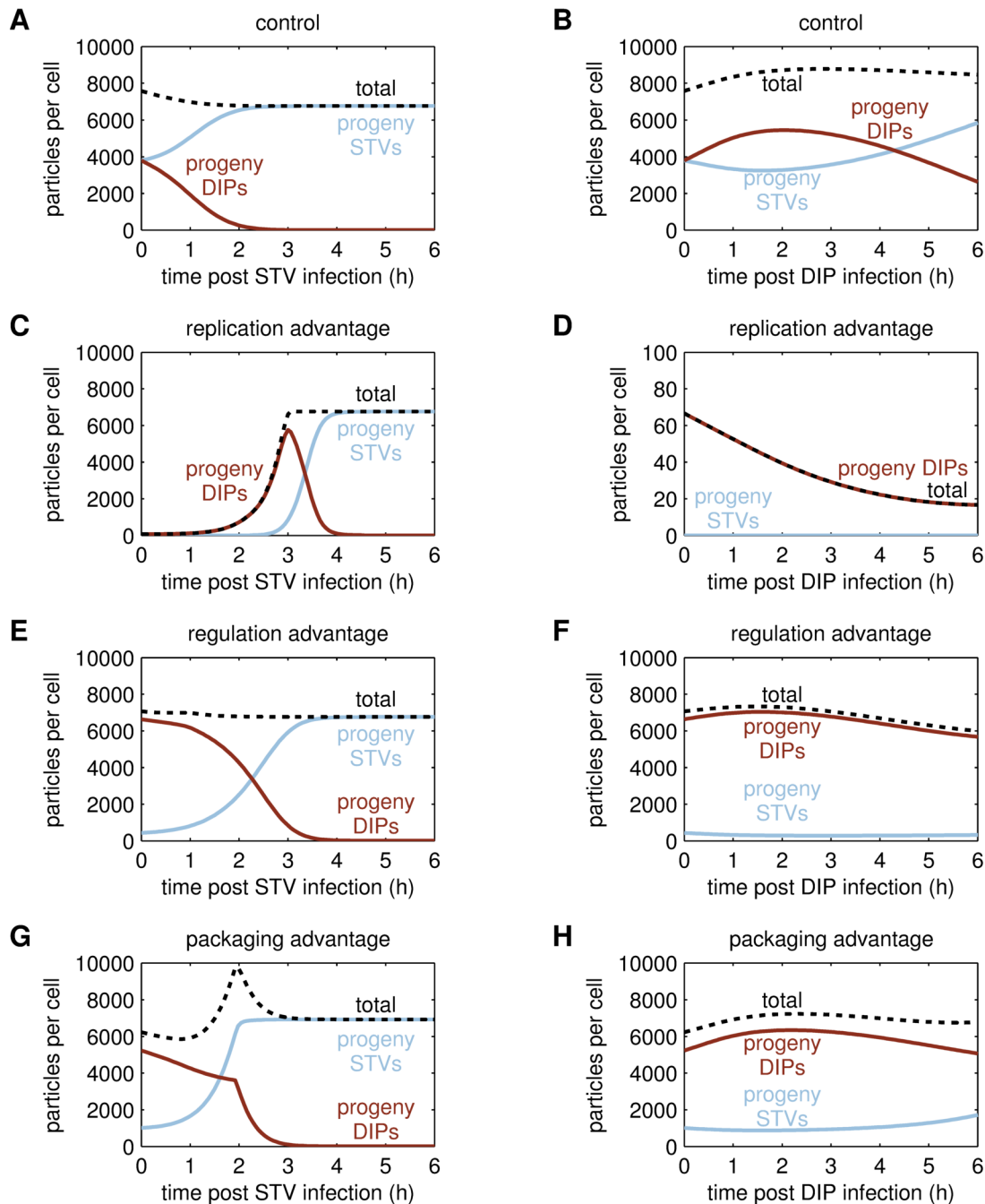
Figure 4.14.: Influence of the DI RNA's mode of interference on virus yield in different scenarios of co-infection timing. Simulated number of viral progeny released by a cell co-infected by one DIP and one STV at 12 h post STV infection. The DIP carries a defective segment 1 (S1, encoding PB2) which is 395 nt long ($F_{\mathrm{Adv}} = 4.93$) and exerts different advantages over its cognate FL segment at particular steps of the viral life cycle, as indicated in the figure titles. Simulations are compared to those of a FL DI-like S1 (2341 nt) that has no propagation advantage (control). (A, C, E, G) STV infection occurs first and DIP infection with the indicated delay. (B, D, F, H) DIP infection occurs first and STV infection with the indicated delay. (C, D) The model used to simulate an advantage in DI RNA replication follows the approach by Laske and Heldt *et al.* [309]. Note different ordinate scale in (D).

release is similar for DIPs with an advantage in either replication or regulation. On the contrary, DIPs with a packaging advantage do neither interfere with M1 expression nor escape regulatory mechanisms. Hence, their co-infection time window is shorter and their progeny DIP count decreases more rapidly with an increasing delay in DIP co-infection. Counter-intuitively, we observed an abrupt drop of DIP progeny when DIP co-infection occurs later than 2 h. Moreover, this drop is accompanied by a peak-like maximum of the total virus progeny number (Figure 4.14 G, black dashed line). We hypothesize that this unexpected model output is related to an advantageous cytoplasmic FL-to-DI vRNP ratio. First, up to a delay in DIP infection of 2 h, FL vRNPs are retained in the cytoplasm and, thus, they provide a negative feedback to DI vRNP packaging (explained before). However, the longer DIP co-infection is delayed, the fewer DI vRNPs accumulate in the cytoplasm, decreasing the impact of DI vRNP-mediated blockage of FL vRNP release (details on nuclear and cytoplasmic retention of FL and DI vRNPs are visualized in Figure B.8 in the appendix). In addition, DIPs with an advantage in packaging do not interfere with viral protein expression. Therefore viral capsid components are highly abundant. Together, sufficient levels of proteins needed to form progeny particles and a decreased negative feedback by FL vRNPs on DI vRNP packaging allow DIP release even at low levels of DI vRNPs in the cytoplasm. However, if DIP co-infection occurs later than 2 h, DI vRNP levels become too low to form DIP progeny, such that total number of virus particles decreases as well, reaching levels of a DIP-free infection. Overall, the increased number of total virus particles provides an interesting feature of co-infections by DIPs with a packaging advantage, whose biological relevance is, however, elusive.

Impact of delayed STV co-infection on virus yield In addition to the analysis of delayed DIP co-infection, we also investigated the impact of delays in STV co-infection on virus growth (Figure 4.14). In theory, this scenario is disadvantageous for DIP propagation since DIPs cannot replicate in absence of the missing viral proteins. Nonetheless, primary mRNA synthesis of FL segments, except of FL S1, takes place, mediated by the resident polymerases of the incoming FL vRNPs [53]. As a consequence, successful virus propagation is challenged by the pre-mature expression of regulatory proteins, i.e., M1 and NEP, whose levels are increasing with an increasing delay in STV co-infection (see also Figure 4.15 H). Thus, as soon as STV infection occurs, virus growth is influenced by both, an initial level of regulatory proteins and a DI RNA already in place to hamper FL vRNP propagation. Still, the DI RNA can take advantage of other pre-expressed viral proteins, e.g. NP and viral surface proteins, and, thus, mainly DIPs are released. Even in case the DI RNA has no advantage in virus growth, more DIP than STV progeny are released for the majority of the tested co-infection

time window (Figure 4.14 B). Similar to the control, cells infected by DIPs with an advantage in either regulation or packaging show the same qualitative trend in progeny release. However, the progeny DIP-to-STV ratio is higher compared to the control simulation (Figure 4.14 F, H). In contrast, the DIP with an advantage in replication strongly interferes with FL vRNP growth and, thus, also with its own replication. Due to this self-interference, the number of progeny DIPs is constantly decreasing with an increasing delay of STV co-infection (Figure 4.14 D). In contrast, DIPs with an advantage in either regulation or packaging do not significantly impact FL RNA and protein synthesis. Thus, cells previously infected by one of those DIPs are able to release significantly more progeny compared to cells previously infected by a DIP with an advantage in replication (Figure 4.14 D, F, H).

Testing strength of interference in combination with co-infection timing In the previous paragraphs we analyzed the impact of either strength of interference or co-infection timing on model output depending on the mode of interference of a DI S1. To complement those analyses, we additionally investigated DIP yields in response to various combinations of the DI RNAs' strength of interference and co-infection timings (Figure 4.15). Firstly, when DIP infection is delayed, cells co-infected by DIPs with an advantage in either replication or regulation show different qualitative features in their release profiles compared to cells co-infected by DIPs with an advantage in packaging. In particular, for DIPs with an advantage in either replication or regulation, an increase in strength of interference results in a shift of the co-infection time window toward later time points. As observed before, cells co-infected by DIPs with an advantage in replication show a distinct optimum of co-infection timing where DIP release is maximal (Figure 4.15 A). With increasing F_{Adv} this maximum is not only shifted in time, but also its peak becomes smaller and narrower. This is related to a trade-off, where rapidly replicating DI RNAs hamper M1 accumulation and prolong M1-mediated nuclear export but interfere too strongly with FL protein expression resulting in self-interference (see before, Figure 4.13). Likewise, cells co-infected by DIPs with an advantage in regulation show DIP release for extended co-infection time windows in response to increasing F_{Adv} (Figure 4.15 C). Although, those DIPs can escape M1-mediated nuclear export, the number of progeny DIPs decreases when DIP co-infection is delayed by 3 h and levels of pre-expressed M1 are too high (Figure 4.15 G). In contrast, cells co-infected by DIPs with an advantage in packaging show an abrupt drop in DIP release when DIP co-infection is delayed about 2 h, independent of F_{Adv} (Figure 4.15 E). This is expected, since those DIPs cannot counteract M1-mediated shutdown of RNA replication. Thus, a further increase in F_{Adv} will neither result in an extended co-infection time window nor in a significant increase in the number
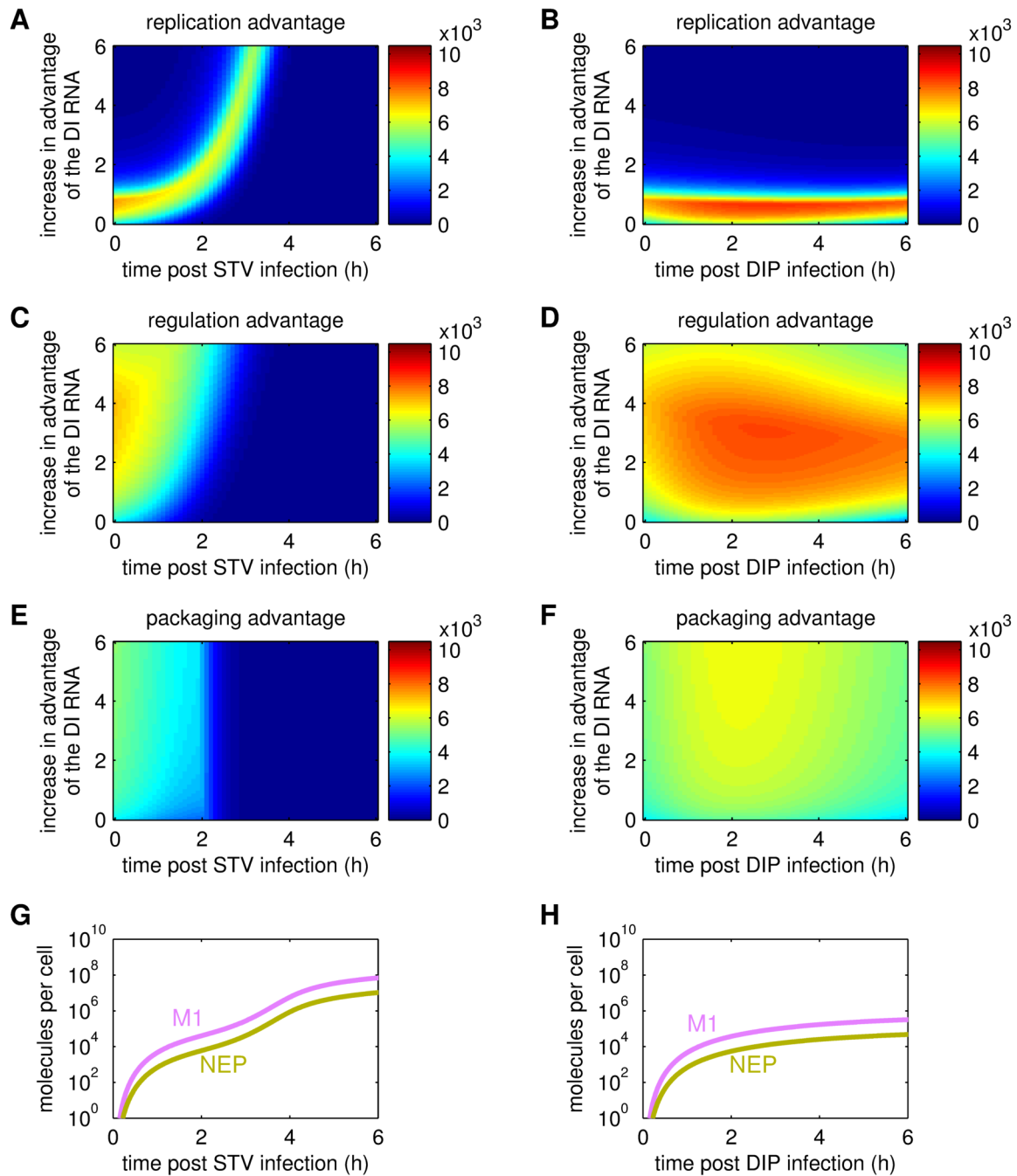
Figure 4.15.: Impact of the DI RNAs' mode of interference on virus growth in response to various combinations of strength of interference and co-infection timings. Simulated infections of a cell by one STV and one DIP. The DIP carries a defective segment 1 (S1, encoding PB2) which exerts different advantages over its cognate FL segment, indicated in the figure titles. (A–F) Number of progeny DIPs at 12 h post STV infection considering the indicated advantage and that either DIP infection (A, C, E) or STV infection (B, D, F) occurs with the indicated delay, respectively. (G, H) Number of unbound M1 and NEP in either an STV-only (G) or a DIP-only (H) infected cell. For (H) the DI S1 has an advantage of 0.5 and the corresponding length compared to its parental FL RNA (Equation (3.2.25), Section 3.2.2). The model used to simulate an advantage in DI RNA replication (A, B) follows the approach by Laske and Heldt *et al.* [309]. Corresponding STV yields are given in Figure B.6 in the appendix.

of progeny DIPs. In case that STV infection is delayed, DIP progeny release profiles are governed by the impact of F_{Adv}. Strikingly, cells co-infected by DIPs with an advantage in either regulation or packaging can release high numbers of DIP progeny over a wide range of both F_{Adv} and STV co-infection timing. In contrast, DI S1 with an advantage in replication cannot exert advantages that are too high compared to their FL segment since this leads to a significant decrease in numbers of progeny DIPs if $F_{Adv} \geq 0.8$, mostly governed by the phenomenon of self-interference (see before, Figure 4.13).

In summary, this combined evaluation of strength of interference and co-infection timings underlines the main characteristics of the DI RNAs' mode of interference. While DIPs with an advantage in replication interfere too strongly with STV growth and thereby hamper their own replication, the other two types of DI RNAs allow co-infected cells to release overall more virus progeny even in disadvantageous infection scenarios with large delays in STV co-infection.

Growth of DI RNAs with an advantage in replication that originate from different genome segments Up to now, we have focused our *in silico* studies on co-infections by a DI S1, a representative of the polymerase-encoding segments. While most DI RNAs described in literature originate from one of the three polmyerase-encoding segments, sub-genomic RNAs can also arise from one of the other influenza virus genome segments [84, 120, 121, 356]. Thus, we were wondering whether defects in certain segments may support DIP growth, while others propagate less efficiently and are, therefore, lost from the virus population in subsequent replication rounds. To elucidate this hypothesis, we compared simulated infections by DIPs carrying DI RNAs from either of the eight viral genome segments. In particular, we analyzed changes in DIP yield in response to various combinations of the DI RNAs' strength of interference and delays in STV co-infection. In case the DI RNAs exert an advantage in replication, two groups of release profiles became evident in response to co-infection timing (Figure 4.16). First, cells co-infected by DIPs with a deletion in either S1, segment 5 (S5) or segment 7 (S7) release DIP progeny even for long delays in STV co-infection. Second, if the DI RNA originates from either segment 4 (S4), segment 6 (S6) or S8 a significant drop in DIP release becomes evident for delays in STV co-infection longer than 3 h. As described before, those differences stem from differential accumulation of regulatory proteins, i.e., M1 and NEP (Figure 4.16 G, H), and the corresponding timing in shutdown of DI RNA replication by nuclear export of DI vRNPs. In particular, in cells infected by DI S4, S6 or S8, all viral proteins except for HA, NA and NEP will be expressed. Thus, M1 accumulates inside the cell and causes pre-mature shutdown of FL segment replication and transcription if STV co-infection is delayed by more than 3 h. In contrast, in DI S1-only infected cells
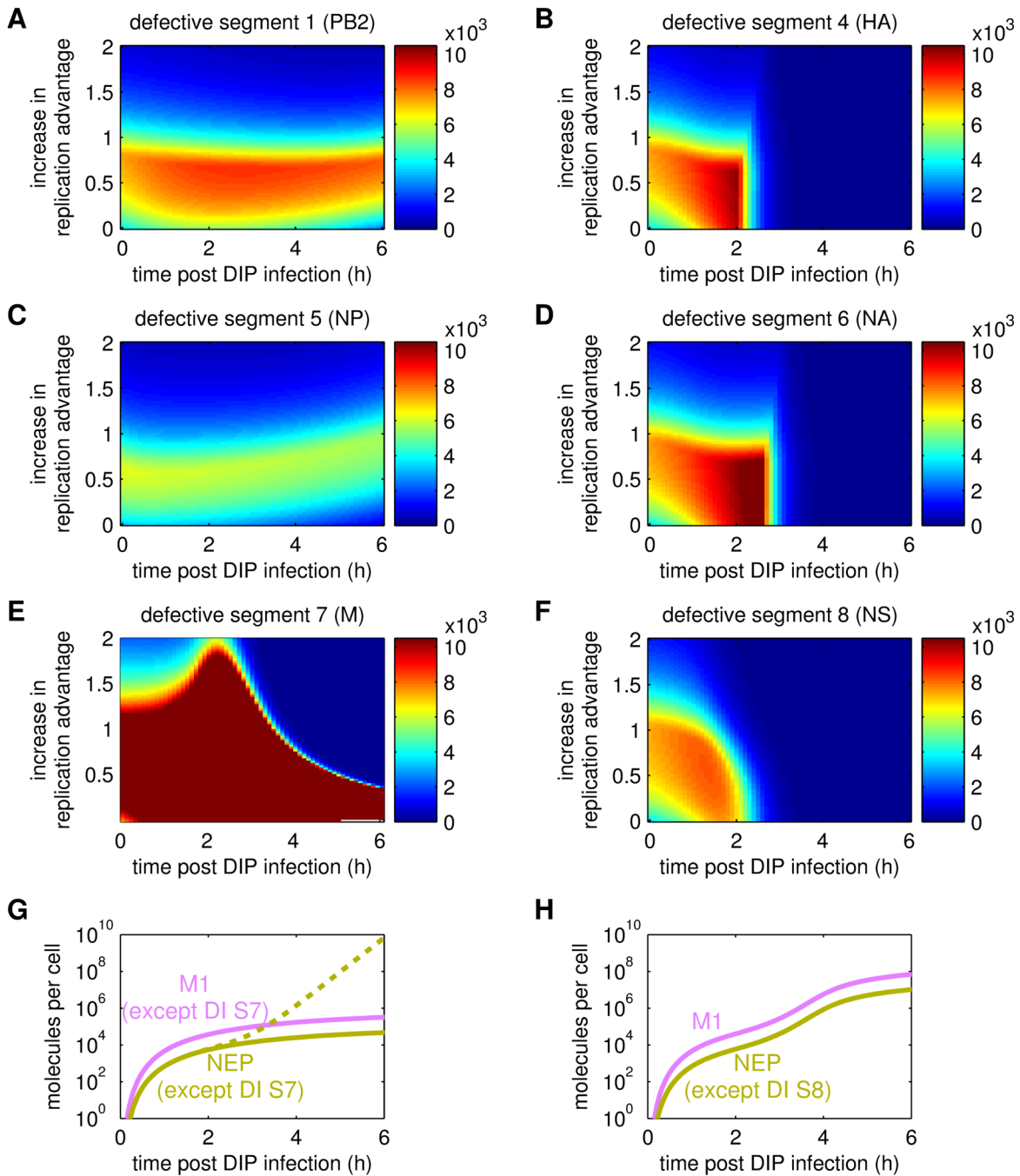
Figure 4.16.: Growth of DI RNAs with an advantage in replication that originate from different genome segments. Simulated infection of a cell by one DIP and one STV. (A–F) Number of progeny DIPs at 12 h post STV infection considering the indicated replication advantage and delay in STV co-infection. The DI RNA's segment origin is indicated in the figure titles. (E) Conditions for which no simulations were obtained are highlighted in gray. (G, H) Dynamics of unbound M1 and NEP numbers in a cell infected by one DIP with $F_{\mathrm{Adv}} = 0.5$. (G) The DI RNAs originate from either S1 or S5 (solid lines), or S7 (dashed line). (H) The DI RNAs originate from either S4, S6 or S8 (solid lines). Models used to simulate an advantage in DI RNA replication follow the approach by Laske and Heldt *et al.* [309].

no functional polymerases can be formed such that only primary transcription mediated by the vRNP-resident polymerases takes place. Likewise, RNA replication is hampered as well in cells co-infected by DI S5 since NP, needed to form replication-competent vRNPs, is only synthesized in insufficient amounts. Even though a cell co-infected by DI S5 can release DIP progeny for extended delays in STV co-infection, the number of progeny is significantly lower compared to similar infections by a DI S1. This is expected considering that NP is already a limiting factor in the presence of rapidly replicating DI RNAs (Figure 4.13) and that a defective NP-encoding segment is further shortening its supply.

Opposed to that, co-infections by DI S7, encoding M1 and M2, were the most productive among those that allow DIP release for extended delays in STV co-infection. This is related to the absence of M1 in DIP-only infected cells and, thus, a lack of regulatory mechanisms. On one hand, the model predicts that lack of M1 is advantageous, since replication and transcription are not regulated by M1-mediated export of viral genomes, allowing exceptionally high intracellular concentrations of both viral genomes and proteins with up to 10^{20} molecules per cell (Figure 4.16 G yellow dashed line, and Figure B.9 in the appendix). On the other hand, export of viral genomes is a crucial prerequisite for virus release. Hence, if STV co-infection is delayed too long, too few M1 molecules are synthesized, and, despite high levels of vRNPs, the number of DIP progeny decrease significantly if STV co-infection is delayed by more than 3 h. Besides, 3000 M1 molecules are required to form the envelope of the progeny particles [30]. Thus, the more M1 molecules are used up for vRNP export, the fewer are available for particle formation, providing a further disadvantage in DI S7 infections. The correlation between M1, formation of M1-vRNPs and corresponding progeny numbers is visualized in the appendix (Figure B.9).

Growth of DI RNAs with an advantage in either regulation or packaging that originate from different genome segments In addition, we conducted the same analysis for the cases that DI RNAs derived from different segments have an advantage in either regulation or packaging, shown in the appendix (Figure B.10, Figure B.11). Here, it became evident that the impact of segment origin on DIP progeny release results in similar qualitative features independent of the mode of interference. In particular, defective S4, S6, or S8 show a limited co-infection time window while defective S1 and S5 allow DIP progeny release even for long delays in STV co-infection with the fewest progeny released for co-infections by DI S5. However, a major difference is that DIPs with an advantage in either regulation or packaging allow a broader range in strength of interference, a characteristic described before (Figure 4.13). Furthermore, we observed unexpected

differences for DI S7 simulations, which are explained in the following.

DI S7 with an advantage in regulation escape M1-mediated shutdown of replication via two mechanisms. First, we explicitly modeled a reduced M1-binding rate to mimic an advantage in regulation. Second, there is a lack of M1-mediated regulation due to the defective M1-encoding segment. Hence, intracellular numbers of vRNPs and proteins accumulate to much higher levels compared to conventional infections, with more than 10^{10} molecules per cell (Figure B.9 in the appendix). While those high molecule numbers did not allow to obtain simulation results for delays in STV infection longer than 2.3 h, a noticeable recovery of STV yields became evident (Figure B.12 B in the appendix). We may hypothesize that FL segments can take advantage of the highly abundant viral resources to form STV progeny, however, overall virus release is challenged by a simultaneous drop in both NP and M1 molecule numbers (Figure B.9 in the appendix). Since M1 is highly relevant for both mediation of nuclear export as well as viral particle formation, a shortage of M1 related to high intracellular vRNP levels becomes indeed disadvantageous. In particular, here, the reduced binding rate of M1 to DI S7 vRNPs might even provide an additional disadvantage for the DI RNA, further delaying its nuclear export.

Also for a DI S7 with a packaging advantage, M1 supply becomes limiting with increasing delays in STV infection. However, the release of DI S7 progeny was restricted to a similar co-infection time window as for DI S4, S6 and S8 with the only difference that significantly more DI S7 could be released with up to 10^4 DIPs per cell (see Figure B.11 E and Figure B.9 in the appendix). The latter is due to the lack of regulatory mechanisms mediated by M1 as explained before.

Summary Using a single-cell model of IAV replication, we investigated the impact of DIPs on virus growth assuming three different modes of DI RNA interference and various infection conditions. In literature, it is commonly proposed that the growth advantage of DI RNAs is based on their length since they are usually significantly shorter compared to FL segments. Based on the analysis of intracellular viral RNA dynamics of FL segments we concluded that a length-dependent growth advantage might, however, only apply to DI RNAs and not to short FL segments. In our model, we accounted for this by an advantage factor F_{Adv} based the FL-to-DI RNA length ratio. We found, that DIPs with an advantage in regulation seem to be successful in releasing high numbers of DIP progeny in the majority of the tested scenarios. This is, in particular, related to the reduced M1-binding kinetics for such DI RNAs, which allows them to reside longer in the nucleus and replicate to higher levels compared to the FL segments. However, those DI RNAs do not strongly interfere with FL RNA replication and viral protein synthesis, such that

they guarantee a continuous basal level of STV growth. Furthermore, DIPs with an advantage in vRNP packaging show similar features, however, overall fewer DIP progeny are released. In some scenarios, reduced progeny numbers were related to the negative feedback during virus particle formation provided by FL vRNPs that accumulate in the cytoplasm. In contrast, DIPs with an advantage in replication are highly interfering and replicate almost at total expense of the STV. While the latter provides a disadvantage in a real-world scenario, where the DIP quickly extincts its STV and limits spreading of the virus, this characteristic is the key feature of an interfering antiviral RNA with the ability to rapidly clear acute infections.

4.2.2. Discussion of intracellular replication of RNA deletion mutants

To obtain a deeper understanding of how DI RNAs interfere with virus replication, we implemented three single-cell models accounting for either faster DI RNA synthesis or differential regulation of DI RNA replication or preferential packaging of DI vRNPs into progeny particles. Results of the three models will be discussed and compared to literature where applicable. Since the advantage of DI RNAs is mainly associated with their reduced length, we are also discussing length-dependent aspects of viral RNA accumulation using a data set on intracellular virus replication and, additionally, discuss which further properties of DI RNAs might be relevant with respect to their growth advantage and/or parasitic behavior.

Length-dependency of influenza A virus RNA replication According to literature, DI RNAs have a growth advantage due to their reduced length. As a consequence, more copies of sub-genomic than FL RNAs can be synthesized by the viral polymerase. While the majority of experimental results points, indeed, to a preferential amplification of sub-genomic RNAs (reviewed in [105, 115]), proof for the underlying assumption is missing, which conveys that the viral RNA synthesis rate is length-dependent and that the polymerase synthesizes a constant number of nucleotides per unit of time. Since the FL genome segments of IAV differ significantly in length, we expected that the shortest of them, S8, would replicate significantly faster than one of the longest segments, i.e., one of the polymerase-encoding segments, S3. However, a simple analysis of IAV cRNA synthesis, previously described as the major source of the DI RNAs' growth advantage [125], only provided weak support for a length-dependent replication mechanism. Nonetheless, the cRNA synthesis rate determined for S5 is in agreement to previous estimations [18]. Furthermore, our findings on the FL RNA synthesis rates are supported by other studies which investigated intracellular replication of all eight viral genome segments. While those studies observed indeed higher levels of short FL mRNAs and/or FL cRNAs [296, 299], they found only insignificant differences in the synthesis of FL vRNAs. The latter observation is in favor of other findings by our group, which conveyed that despite changes in mRNA and/or cRNA replication, vRNA levels were unchanged in genetically engineered host cells (Section 4.1). In addition, a single-cell study of IAV-infected MDCK cells showed that release of high progeny number is linked to intracellular equimolarity of FL segments [277]. Together, those observations suggest that there are overarching mechanisms that balance RNA synthesis to allow optimal usage of resources and generation of high virus progeny numbers. Consequently, only if DI RNAs acquire properties that allow them to escape those mechanisms, they can replicate to levels higher than FL RNAs and, thus, disturb virus replication and progeny formation.

However, it is still unclear whether those properties are primarily related to DI RNA length. Likewise, they might be also linked to other properties of the DI RNA, such as RNA sequence or secondary structure of the RNA. A finding in favor of this argumentation comes from a study comparing the growth of three DI RNAs of VSV. Here, the longest of the three DI RNAs accumulated to a higher level than the shorter ones, even when cells were co-infected by all three DI RNAs [130]. In contrast, more recent work using IAV-like reporter systems provide experimental evidence that support a length-dependent replication mechanism [126, 357]. Here, Widjaja and colleagues assessed competition between two influenza virus-like RNAs in a dual luciferase reporter assay and found that the shorter of them showed a stronger inhibition of luciferase expression than the longer one. Moreover, they also evaluated the competition between natural FL segments and the reporter RNA in co-transfected cells and found a noticeable trend toward stronger inhibition of luciferase expression by short FL segments [126]. Nonetheless, the authors also stated that other RNA properties, such as the parts of the coding region and polymerase-binding site that were retained in the DI RNA sequence, influenced the outcome of the assay. Another mini-replicon study, conducted by S. Pöhlmann's group, analyzed competition between a luciferase-expressing IAV-like reporter segment and ten different deletion mutants of S1, whose internal deletion were systematically increased [357]. In those experiments, a decrease in length directly correlated with a decrease in luciferase expression. In particular, luciferase expression in cells co-transfected with the shortest RNA construct of 418 nt length, harboring the sequence of DI 244, was decreased by three orders of magnitude. In contrast, luciferase expression in cells co-transfected with the longest construct, comprising a length of 2254 nt, was decreased by only one order of magnitude. However, no further decrease in expression was observed when constructs shorter than the DI 244-harboring one were co-transfected.

In conclusion, we and others have shown that during conventional *in vitro* infection experiments, the synthesis rates of viral RNAs are not dependent on their length. So far, support in favor of length-dependent replication comes mainly from mini-replicon systems, where the replication of single vRNPs is evaluated in absence of regulatory mechanisms that usually control RNA replication. Together, this points to the fact that the polymerase can synthesize a constant number of nucleotides per unit time but maximum RNA levels are controlled by overarching regulatory mechanisms. Likely, DI RNAs can escape those mechanisms, which allows them to outnumber their FL counterparts. However, reduced length might not be the only determinant for this advantage. Several lines of evidence convey that also other properties, such as RNA sequence or secondary structure of DI RNAs play a role for their growth advantage, as noted for IAV [115, 126] and also for some positive-strand viruses, such as dengue virus [358], plant viruses [359, 360] and

mouse corona virus [361].

Please note, that our single-cell model cannot directly integrate information on DI RNA sequence or secondary structure. Instead, we express such properties using the parameter F_{Adv}. While we chose the simplest assumption and related F_{Adv} to the FL-to-DI RNA length ratio, it can also be adjusted independently of the DI RNA length, which allows to tune model output to experimental data that point to a different strength of interference.

Yield reduction analyses depending on the mode of interference Conflicting experimental results lead us to challenge the conventional hypothesis that the growth advantage of DI RNAs is mainly based on length-dependent RNA replication. At a first glance, the step of RNA replication seems very promising to be hijacked by DI RNAs, which is in accordance to the sensitivity study of our single-cell model (Section 4.1). Intriguingly, other highly sensitive steps of the viral life cycle, previously identified to be an option to improve virus yields for vaccine production, are also those that are potentially targeted by the DI RNAs, i.e., the regulation of RNA replication and assembly of viral progeny (reviewed in [115]). To implement those modes of interference into our single-cell model, we accounted for either a reduced binding rate of M1 to DI vRNAs or an advantage of the DI segment during incorporation into budding particles.

As a first step, we compared virus yields from simulated co-infections of a representative DI S1 with available experimental data. Since data on *in vitro* virus dynamics in the context of DIP co-infection have been scarce until the mid 2010s, we were unable to perform in-depth model (in)validation. Nonetheless, relevant experiments performed before by various research groups served to perform at least qualitative model comparisons. With respect to virus yield, we identified two distinct phenomena caused by DIP co-infection: (i) exclusive DIP release, i.e., abolishment of STV release, and a significant reduction of total virus yield, (ii) the majority of virus progeny are DIPs, however, also noticeable amounts of STVs are released and total virus yield is only insignificantly reduced. The first observation is a characteristic of DI RNAs with an advantage in RNA replication and is well in agreement to reports in literature [95, 129, 355]. In particular, the model that accounts for enhanced DI RNA synthesis reproduced the normalized data on reversal of DIP-mediated interference (Figure 4.11 C) without parameter fitting. In contrast, models accounting for an advantage in either regulation or packaging can only capture the overall trend of those data. This is due to the higher amount of STVs and total virus yield predicted by those models, described in (ii). However, please note, that the extent of yield reduction in experiments may also depend on differences in experimental conditions, differences in virus-host cell systems and varying

compositions of seed virus material [95, 121, 355, 362]. Furthermore, we systematically analyzed the impact of various combinations of initial number of infecting STVs (MOI) and infecting DIPs (MODIP). Here, only the model with a replication advantage can reproduce the data series of Nayak and colleagues [363], who found that with increasing MODIP the overall virus yield is decreasing significantly. In addition, we observed self-interference, which is a further reduction in DIP yield for increasing MODIP. The models we built to account for either an advantage in regulation or packaging of the DI segment cannot reproduce this phenomenon. Interestingly, Bellett and Cooper [364] made use of this experimental observation and developed a yield reduction assay to assess the amount of "interfering units" contained in a virus sample. When Liao and colleagues [365] modeled the assay, one of the main principles to be followed was that co-infected cells release less than one STV per 1000 DIPs. This finding is well in agreement to DI RNAs with a replication advantage in our study and supports that this might be the mode of interference employed by the most relevant DI RNAs described, i.e., such that originate from the polymerase-encoding IAV genes. However, the same study also revealed that the Bellett-and-Cooper assay can fail to correctly estimate the content of DIPs in virus samples. The authors speculate that one of the reasons for this failure might be the mode of DI RNA interference, which is so far neglected during evaluation of the Bellett-and-Cooper assay [365]. Thus, DI RNAs exerting other mechanisms of interference and do not directly hijack RNA replication might have been overlooked due to their insignificant impact on virus yields. Following the terminology of ecology, DIPs that cause a stark reduction of STV and total yield and show self-interference can be referred to as parasitic causing quick extinction of their helper virus and, thus, itself. On the other hand, DIPs that only weakly interfere with STV replication while promoting their own progeny numbers, can be referred to as symbiotic. To further investigate the molecular mechanisms behind these two principles, we took a deeper look into the differences of intracellular protein and RNA levels related to the mode of interference.

Impact of the DI RNA's mode of interference on viral protein levels During co-infection, DIPs act as molecular parasites of their FL virus and sequester joint viral or cellular resources [105]. In particular, simulations show that viral NP and polymerases become limiting in case a cell is co-infected by a DI RNA with an advantage in RNA replication. Hence, the key aspect of interference by those DI RNAs is the competition for proteins needed to form replication-competent genomes and replication intermediates, i.e., vRNPs and cRNPs. In agreement to our model findings, Widjaja and colleagues described a shortage of viral polymerases in cells co-transfected by short IAV-like reporter RNAs [126]. In contrast our model predicts that first viral NP and then

polymerases are depleted, while they did not see a bottleneck in supply of viral NP. On one hand, the mini-replicon assay used in that study might not reflect all mechanisms present in an authentic infection scenario. On the other hand, the estimated number of NP molecules required per RNA for encapsidation is based on the average number of nucleotides bound by one NP molecule (reviewed in [57]) and the assumption that NP molecules are homogeneously distributed along the entire length of the RNPs. In contrast, more recent studies convey that the NP distribution is rather uneven and that there are parts in every vRNP with a low density of NP, which significantly influences the secondary structure of the genome segments (reviewed in [366]). Thus, if we adopted the actual number of NP molecules needed for genome encapsidation, polymerases instead of NP might become limiting during co-infection. This could be accounted for in future models given that quantitative data on protein synthesis and consumption during co-infection become available. Moreover, we observed a similar interfering phenotype for DI RNAs with an advantage in regulation of RNA replication. However, for this mode of interference, limitations in NP and viral polymerases only became relevant for very high F_{Adv} (Figure 4.13). While for DI RNAs with an advantage in either replication or regulation competition for viral resources is a main characteristic of their interference mechanisms, DI RNAs with an advantage in packaging do not impact intracellular viral protein levels. Due to their minor impact on virus growth, we may hypothesize that such DIPs cannot be easily identified in a real-world scenario.

Impact of the DI RNA's mode of interference on viral RNA levels　When we analyzed the impact of the mode of interference on intracellular vRNA levels we observed three phenomena during co-infection by a DI S1: (i) DI RNA levels were elevated and vRNA levels of both, FL S1 and other FL segments were significantly reduced, (ii) DI vRNA levels were elevated, however, FL vRNA levels were not significantly affected, and (iii) neither DI nor FL RNA levels were affected.

In agreement to our modeling results, reduction of FL segment levels were also observed in experiments. However, the majority of studies shows that, in particular, levels of those FL segments are reduced for which a DI RNA is present, pointing to a segment-specific mechanism of interference [14, 121, 124, 367]. Moreover, it was also found that intracellular FL RNA and DI RNA levels do not differ significantly during DIP co-infection and that there is an increase in the DI-to-FL RNA ratio from the intracellular to the extracellular level [124, 128, 129, 367]. Such increase is reproduced well by the model accounting for an advantage in DI vRNP packaging. However, the predicted extracellular DI-to-FL RNA ratio is significantly lower compared to those predicted by the models accounting for either an advantage in DI RNA synthesis or its regulation (Figure B.5

in the appendix). Clearly, this is related to the number of STVs still released during co-infection, which is highest in case the DI RNA exerts an advantage in packaging. In contrast, experiments show an almost exclusive release of DI vRNPs [124, 128, 129] and DIP-to-STV ratios up to 10^5 (see Figure 4.26, Section 4.3.2). Those findings are reproduced best by the model accounting for an advantage in DI RNA replication. For this, intracellular numbers of DI vRNA significantly outnumber their FL counterparts, which directly translates to high extracellular DIP-to-STV ratios.

Nonetheless, we did not find a clear agreement between model predictions and the available experimental data. Likely, DI RNAs have acquired advantages at multiple steps of the replication cycle and only a combination of the mechanisms presented in this study will allow model simulations to capture the data. Thus far, the model accounting for an advantage in DI RNA synthesis seems best at reproducing the majority of features associated with DIP-induced interference.

DI RNAs with different modes and strength of interference In virus preparations, multiple DI RNAs can arise which provide different lengths and/or modes of interference. In our models, we linked the strength of interference directly to the DI-to-FL RNA length ratio, which is accounted for by the parameter F_{Adv}. The systematic analysis of the impact of F_{Adv} on simulation results revealed that DI RNAs with either a replication or regulation advantage have an optimal length, i.e., an optimal F_{Adv}, for which DIP release is maximal. This optimum is linked to a minimal impact of the DI RNA on FL RNA and viral protein synthesis. However, beyond this optimum, DI RNAs interfere too strongly with virus replication and virus progeny numbers decrease significantly. In accordance, it was also proposed in literature that DI RNAs have an optimal length and that very large deletions are most advantageous. However, the advantage of very short DI RNAs is limited since too large deletions might disrupt the terminal packaging signals required for successful virus propagation [105]. In that case, very short DI RNAs might replicate to very high intracellular copy numbers but fail to be incorporated into progeny particles. This particular phenomenon was reproduced by our models accounting for an advantage in either RNA replication or regulation and was most pronounced for the DI RNA with a regulation advantage when $F_{\text{Adv}} > 4$ (Figure 4.13). Note, that our model cannot account for particular functions of sequence elements but still succeeds in reproducing this experimental observations mechanistically. Consequently, the model prediction is based on the fact that a too high F_{Adv} causes an imbalance of DI and FL RNA replication, reducing the overall availability of viral proteins and, thus, hampers virus growth in general. While such DI RNAs show a strong parasitic phenotype hampering their own progeny release, an optimal DI RNA replicates efficiently without affecting FL RNA levels, which agrees

to experimental findings described before [124, 128]. Moreover, the transcription and translation of DI genomes may represent an additional burden for the host cell further compromising virus release in co-infected cells. Considering that some viral proteins are already in short supply, competition of DI mRNAs with their FL counterparts for active translation sites could decrease viral protein levels even further. Such a self-limiting replication due to the exhaustion of the host cell's translational machinery has been proposed before for HCV infections in highly permissive host cells [269].

In contrast to the models accounting for an advantage in either DI RNA replication or regulation, the model describing the DI vRNP packaging advantage does not clearly reproduce the phenomenon of self-interference for very short DI RNAs, i.e., DI RNAs with a high F_{Adv}. Instead, self-interference is only provided indirectly through the negative feedback of FL vRNPs. Due to this less parasitic behavior of DI RNAs with a packaging advantage, we may hypothesize that their minimal length is only limited by the loss of the packaging signal in case too large parts of the sequence are deleted. Since DI RNAs are preferential formed close to the terminal ends of the genome segments [117] and the conservation of the packaging signal is highly relevant regardless of the mode of interference, future models could consider additional constraints to explicitly describe the behavior of packaging-incompetent DI RNAs.

Impact of co-infection timing on virus growth   To capture at least a part of the various co-infection scenarios possible in a cell population, we also analyzed the impact of delayed DIP and STV co-infection using our single-cell models (Figure 4.14). If STV infection occurs first, we observed a limited co-infection time window for DIP co-infection of about 3 h post STV infection independent of the mode of interference. If DIP infection occurs later, the model predicts that DIP-mediated interference is blocked by the pre-mature shutdown of DI RNA synthesis due to pre-expressed M1 and NEP. This finding agrees well with an experimental observation by Nayak and colleagues, who observed a reversal of DIP-related interference when DIP co-infection was delayed longer than 3 h post STV infection [363]. In addition, further model-based studies by Liao and colleagues revealed that the co-infection time window for which DIP release is possible represents half the length of the eclipse phase of the corresponding STV [365]. The eclipse phase is defined as the time span from the time point of infection until virus release becomes evident and can be up to 7 h for IAV [37, 254], a value that agrees well with our co-infection timing study. Thus, we may conclude, that DIPs can only impact virus growth as long as STV infection has not progressed too far, which is mainly related to the intracellular accumulation of M1 hampering DI RNA replication. This finding is supported by experiments of Bui and colleagues, who found that vRNPs were unable to enter the nucleus and replicate in the

presence of pre-expressed M1 [49]. In case STV infection is delayed, M1 is also expressed through primary transcription, however, at significantly lower levels. Thus, DIP release is still possible over an extended co-infection time window. Here, only cells co-infected by the DIP with an advantage in replication showed a continuous drop in DIP progeny release if STV infection occurred too late (Figure 4.14 D). This may indicate that those DIPs are more sensitive to disadvantageous co-infection scenarios, which is also in line with their self-interfering and parasitic phenotype. In addition, the predicted length of the co-infection time windows tolerated by DI RNAs of S1 was largely independent of the mode of interference. To test whether this observation holds true for the remaining segments, we also analyzed virus release in response to F_{Adv} and co-infection timing if the DI RNA originated from one of the other genome segments.

DI RNAs from different genome segments　Sub-genomic RNAs that originate from one of the polymerase-encoding segments are the most abundantly found in virus preparations [120, 122]. However, there is also evidence that sub-genomic RNAs are formed by other segments [84, 120, 121, 356]. To elucidate why only certain defects manifest in virus populations, we compared simulated co-infections by DIPs carrying DI RNAs in either one of the eight genome segments. In agreement to the results obtained for DI S1, those simulations have shown that qualitative features of DIP production in response to delays in STV infection were independent of the mode of interference. In particular, we found that a defective polymerase-encoding segment is more beneficial for progeny DIP release than a defective segment encoding a protein that is non-essential for viral RNA synthesis, i.e., that is not needed to form replication-competent RNPs. Accordingly, simulations suggest that also a defective S5, encoding NP, can lead to the release of progeny DIPs even if STV infection is delayed longer than 3 h. In contrast, DIP progeny release by HA-, NA- or NS-derived DIPs only occurs in a limited time window for delays in STV infection, which is related to the differential accumulation of M1 (discussed before). Nonetheless, the maximum progeny numbers achieved in co-infections by HA-, NA- or NS-derived DIPs are higher compared to those by NP-derived DIPs. Considering the relevance of NP as an encapsidation factor, a defect in the NP-encoding segment is clearly detrimental for the virus and would cause its extinction. This is also in agreement with the fact that for the NP segment only a few DI RNA sequences were described [84]. In addition, we did not find DI RNAs of the NP segment in a highly DIP-contaminated seed virus stock which, however, contained defective NA- and polymerase-encoding segments [121]. Likewise, no sub-genomic NP RNAs were formed within three weeks of continuous IAV cultures [14]. Together, we can conclude that defects in polymerase-encoding segments (segments 1–3, encoding PB2, PB1, PA, respectively)

are more likely to manifest in virus populations, whereas other defects may die out when STV infection is delayed.

DI RNAs originating from segment 7 Simulated co-infections with a defective S7, encoding M1 and M2, showed ambiguous results. In general, high DIP progeny numbers were predicted for co-infections by DIPs carrying a defective M segment independent of the mode of interference. However, only defective M segments with a replication advantage tolerated delays in STV infection longer than $3\,\mathrm{h}$ (Figure 4.16 E). On one hand, the lack of regulatory mechanisms, normally exerted by the M1 protein, can provide a growth advantage and allow unusually high progeny numbers with up to 10^{10} DIPs per cell. On the other hand, the benefit of a shortage in M1 is limited due to its important role in nuclear export of vRNPs and for the formation of progeny particles. Consequently, progeny numbers are decreasing significantly with decreasing intracellular levels of M1 (Figure B.9 in the appendix). While, thus far, no sub-genomic RNAs were described for the M segment in experiments [84], it might exert interference through other mechanisms. For instance, Tobita and colleagues [368] described a defective M segment in influenza B virus infections, which showed features of a DIP during co-infection, e.g. reduction of the infectious virus titer. However, they did not observe deleted M segments and, thus, speculated that the M segment might have acquired other defects leading to a DI-like phenotype. In line with this, our group discovered a novel DI-like S7 in an A/PR/8/34 seed virus strain, called OP7 [123]. Opposed to conventional DIPs, OP7 contains a FL S7 that has acquired multiple point mutations in the coding and non-coding parts of its genome sequence. Those allow interference with STV replication comparable to what has been described for DIPs carrying deleted genome segments, for instance, cells co-infected by OP7 show reduced virus yields and elevated levels of S7 RNA compared to other FL segments. However, up to now, it is unclear whether proteins encoded by the M segment of OP7 are functional and might even contribute to the interference mechanisms. Thus, in the future, the modeling of DI S7 as a deletion mutant might be dropped in favor of more complex assumptions. In particular, the modeling of the aberrant M1 functionality may help to elucidate the mode of interference exerted by DI-like M segments.

Please note, that our IAV single-cell model accounts for the so-called "daisy chain" model of nuclear export. For this, first, M1 binds to the nuclear vRNPs, inactivates the replication and transcription of the vRNP, and then NEP binds to the M1-vRNP complex to mediate nuclear export via interaction with relevant host cell proteins. In contrast, Brunotte and colleagues [78] proposed an alternative mechanisms, where NEP-vRNP association is a prerequisite for the formation of the M1-NEP-vRNP complex and its

export. In addition, they describe, that sole binding of M1 is not sufficient for the shut down of vRNP replication and, instead, co-expression of NEP and M1 is required to efficiently diminish polymerase activity. Thus, if we adopted the Brunotte-model, the simulated co-infections by DI S7 and DI S8 might yield similar results due to their joint importance for the regulation of RNA synthesis and nuclear trafficking.

Summary   By analyzing different models of DI RNA replication, we can conclude that the majority of features described for DIP co-infections was reproduced best by our model accounting for an advantage in DI RNA synthesis. Although it is still not evident why length-dependency of RNA replication is limited to DI RNAs and does not extend to FL segments, this assumption served well to elucidate experimental observations of DIP co-infections with respect to varying strength of interference, MOI-to-MODIP ratios, co-infection timing and DI segment origin.

Still, these findings do not allow to finally rule out that DI RNAs might hijack other steps of the viral life cycle. As our simulations suggest, DIPs that exert an advantage in either regulation of RNA synthesis or vRNP packaging influence overall virus growth to a lesser extent. Hence, those types of DIPs might have been overlooked in experiments and were not investigated in detail in the past, e.g. because the differences caused in virus titers were within the error range of the applied assays. This might have shaped an incomplete picture of how DIPs are capable of influencing the viral life cycle.

Clearly, DIPs that do not interfere noticeably with STV replication and are simply dragged along during multiple replication cycles will not serve as an antiviral candidate. While antiviral DIPs act parasitic and quickly extinct virus growth, others co-replicate with their STV and are potentially long-lived and impact the outcome of infections on a larger scale. For instance, by influencing the heterogeneity of the viral population [369] or by attenuating disease symptoms of the host, which supports viral spread as shown for dengue virus [358] (see also recent review by Genoyer and López [118]). Our modeling results provide guidance to discriminate DIPs with different modes of interference by analyzing their impact on intracellular concentrations of viral components and on virus yields under controlled infection conditions.

4.3. Modeling continuous production of influenza A virus

A previous study on the continuous production of IAV by Frensing and Heldt *et al.* (2013) showed that the presence of DIPs causes oscillations in virus titers [14]. For instance, those oscillations lead to a drop in TCID$_{50}$ titers by up to six orders of magnitude. Here, we show that those oscillations can be successfully influenced by the operator of such continuous virus production systems using both *in silico* and experimental studies. However, results presented here raise questions on whether continuous production is suited for influenza vaccine manufacturing. For the *in silico* study we employed the model by Frensing and Heldt *et al.* (2013) [14]. Furthermore, we used the extended version of that model to capture experimental data obtained from continuous cultures of IAV performed at different process conditions. The latter was previously presented in the original *Frontiers in Biotechnology and Bioengineering* publication by Tapia and Laske *et al.* (2019) [314]. A preliminary implementation of the modeling approaches presented in this section was developed as part of the Master thesis by Markus Rammhold [370].

4.3.1. Model-based optimization of continuous virus production

To avoid periodic drops in virus titers during continuous IAV production, one would have to eliminate the cause of oscillations in the system, namely DIPs. Using a mathematical analysis, Frensing and Heldt *et al.* (2013) [14] have already shown that in the absence of DIPs no oscillations in virus titers would occur. However, their study also provided experimental evidence that DI RNAs accumulate quickly in such continuous cultures, which is due to amplification of the DI RNAs present in the seed virus as well as *de novo* generation of DI RNAs.

Influence of residence time on oscillations Ideally, operators of continuous virus production systems would be able to directly downregulate the interfering potential of DIPs or their *de novo* generation. However, the molecular mechanisms behind those phenoma are still largely elusive and to date no measures are available that would allow such downregulation. Nevertheless, it is also known that the propagation of DIPs is favored especially in scenarios at high MOI [101]. Hence, one possible way to manipulate the influence of DIPs in such continuous systems would be to run it constantly at a low MOI regimen. This will decrease the co-infection probability for the target cells. In consequence, less co-infected cells will be present in the production system and less DIPs will be produced. The most immediate possibility to establish low MOI conditions in the production vessel, referred to as virus bioreactor, is to increase its dilution rate. Like this, the residence time of DIPs, i.e., the time that DIPs spend on average in the virus
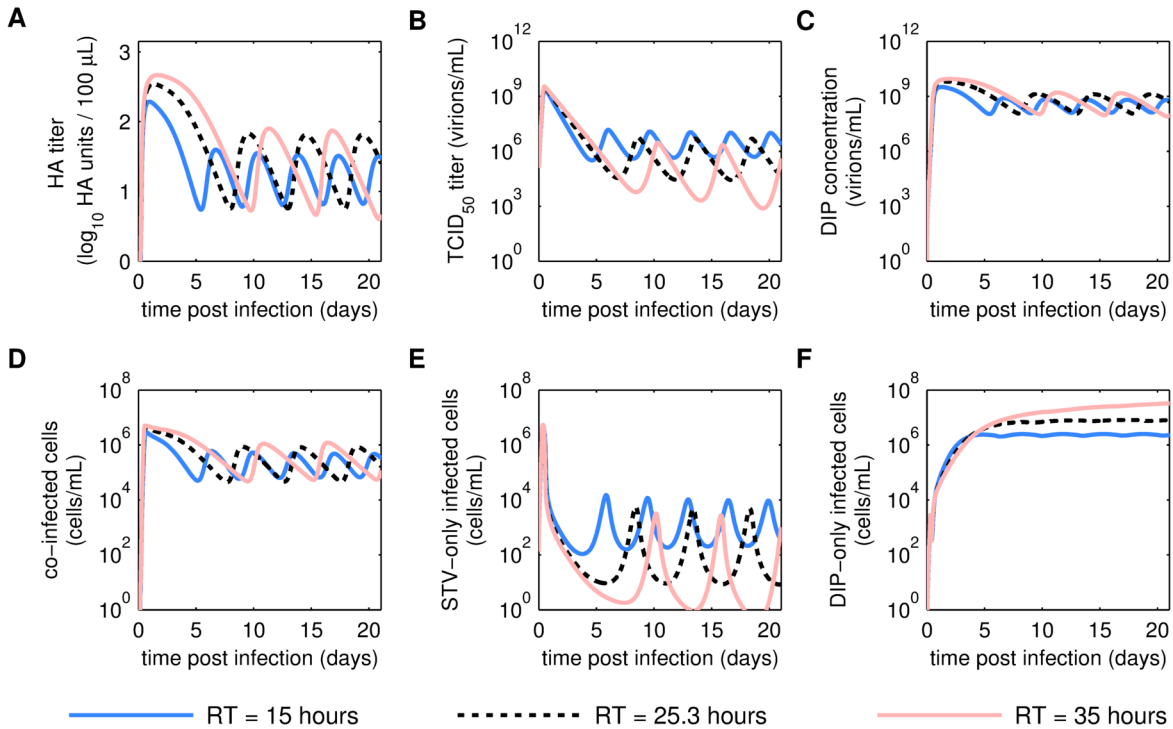
Figure 4.17.: Simulation of continuous influenza A virus production at three different residence times (RTs). Dynamics of total and infectious virus titers, expressed as HA titer (A) and $TCID_{50}$ titer (B), respectively, as well as concentration of defective interfering particles (DIPs) (C), and concentrations of sub-populations of infected cells, namely co-infected (D), STV-only infected (E) and DIP-only infected (D) cells for a simulated infection at MOI 0.025. Parameters were set according to Table 4.2. Dependent on the RT, the flow rate of fresh medium from the medium reservoir to the virus bioreactor F_{FM} and the cell concentration in the feed T_{in} were adjusted according to Equation (3.3.11) and Equation (3.3.4), respectively (see Section 3.3.1). Colors according to legend.

bioreactor until they are harvested, is also decreased.

To elucidate this approach in more detail, we first simulated the model of Frensing and Heldt *et al.* (2013) [14] at three different RTs (Figure 4.17). The RT was adjusted by changing the flow rate from the fresh medium reservoir to the virus bioreactor (explained in Models and Methods, Section 3.3.1). As a benchmark, the RT of the original study (RT = 25.3 h) was used.

We observed that a decrease in the RT caused a decrease in the amplitude and an increase in the frequency of oscillations for the majority of the state variables of the model (Figure 4.17 A–E). *Vice versa*, an increase in the RT caused an increase in amplitude and decrease in frequency of oscillations. Independent of the RT, the initial maxima of the state variables were reached within 1 to 2 days p.i. and were always higher than the subsequent maxima of the oscillations. In particular, the longer the RT, the higher was the first maximum of the state variables. As a proof of concept, these

Table 4.2.: Parameters and non-zero initial conditions for the simulation of continuous influenza A virus production as in Frensing and Heldt *et al.* (2013) [14].

Parameter		Description	Value
μ	(h^{-1})	specific cell growth rate	0.027
D^{a}	(h^{-1})	dilution rate of VB	0.0396
F_{CB}	(ml/h)	flow rate from CB to VB	13.2
$F_{\text{FM}}{}^{\text{a}}$	(ml/h)	flow rate from medium reservoir to VB	6.6
V_{VB}	(ml)	working volume of VB	500
f	(−)	*de novo* DIP production	10^{-3}
F_{Inf}	(cells/virion)	infection efficiency	1
k^{Apo}	(h^{-1})	apoptosis rate of infected cells	7.13×10^{-3}
$k_{\text{V}}^{\text{Deg}}$	(h^{-1})	virus degradation rate	0.035
k^{Inf}	(ml/(virion · h))	virus infection rate	2.12×10^{-9}
k^{Prod}	(virions/(cell · h))	virus production rate	168
T_{CB}	(cells/ml)	average target cell concentration in CB	4.50×10^6
$T_{\text{in}}{}^{\text{a}}$	(cells/ml)	cell concentration in feed	3.00×10^6
T_0	(cells/ml)	initial target cell concentration in VB	5.00×10^6
$V_{\text{s0}}{}^{\text{b}}$	(virions/ml)	initial STV concentration	1.25×10^5

[a] Depending on the RT ought to be tested during simulations, the dilution rate D, flow rate F_{FM} and cell concentration T_{in} are adjusted according to Equation (3.3.2), Equation (3.3.11) and Equation (3.3.4), respectively (see Section 3.3.1).
[b] Concentration of infectious virions equivalent to MOI 0.025 based on TCID$_{50}$ titer.
VB - virus bioreactor, CB - cell bioreactor

simulations showed that the TCID$_{50}$ titer is highest for short RTs, i.e., for high dilution rates, at which DIPs are out-diluted faster and the probability of a co-infection is lowest. Accordingly, this also results in a low concentration of co-infected cells (Figure 4.17 D). However, due to the increased dilution of the virus broth, the total number of virions present in the virus bioreactor is also decreased as can be seen by the lower maxima of the HA titer at the shorter RTs (Figure 4.17 A). On the contrary, the maxima of the HA titer are highest for the long RT but show an overall decreasing trend over process time, a trend that is also evident for the TCID$_{50}$ titer (Figure 4.17 A, B). Intuitively, one would assume that this decreasing trend is related to virus degradation that has a higher impact on virus titers at longer RTs. However, when we set $k_{\text{V}}^{\text{Deg}}$ to zero, we still observed this decreasing trend (Figure C.1 in the appendix). Interestingly, we observed that the concentration of DIP-only infected cells showed only minor oscillations, reaching a steady state for the two shorter RTs. Even more surprisingly, the number of DIP-only infected cells increased at the longest RT (Figure 4.17 F). The latter is caused

by the model assumption that DIP-only infected cells grow and give rise to DIP-infected daughter cells. However, in case we exclude growth of DIP-only infected cells, they reach a steady state at the longest RT, with a value similar to that observed for the other RTs tested (Figure C.2 in the appendix). Moreover, the previously mentioned downward trend of viral titers is also reverted in that scenario and, instead, HA titer and $TCID_{50}$ titer show dampened oscillations. Hence, it seems that growth of DIP-only infected cells can provide an additional feature of interference at long RTs. Although interference can only take place in co-infected cells, the high number of DIP-only infected cells will take up a significant amount of the few available STVs, hampering the formation of STV-only infected cells. As a consequence, the number of STV-only infected cells is decreasing on average over process time (Figure 4.17 E) while co-infected cells do not change in their average concentration (Figure 4.17 D).

Oscillations are diminished at short residence times   Secondly, we investigated the influence of the RT on virus titers and cell concentrations in a systematic way and simulated continuous IAV production at multiple RTs (Figure 4.18). We found that at a residence time of 3.5 h ($D = 0.2856$ 1/h) the $TCID_{50}$ titer was maximal at steady state showing no oscillations (Figure 4.18 B). Likewise, all state variables showed a steady state, proving that oscillations can be diminished completely by manipulating the RT of the virus bioreactor. However, while at this short RT, the steady state of the $TCID_{50}$ titer is maximal, the HA titer is minimal with only 0.62 log_{10} HA units. This is in line with our initial observations, where the elimination of oscillations was accompanied by a decrease in the total number of virions present in the virus bioreactor (Figure 4.17).

Influence of residence time on space-time yield   To understand how the reduced virus concentration during the run is affecting the productivity of the process we, next, evaluated the STY of the process comparing an oscillating to a non-oscillating process regimen (Figure 4.19). In brief, the STY is a measure for the productivity of the process, representing the total amount of virions harvested per production time and cultivation volume. Here, we consider that the production time is the time elapsed since the time point of infection and the cultivation volume is equivalent to the volume of cell culture medium spent by running the virus bioreactor continuously (see Equation (3.3.12), Section 3.3.1). We found that the cumulative amount of total virus particles in the harvest after 21 days is 1.54×10^{13} virions at RT 25.3 h and 5.84×10^{12} virions at RT 3.5 h (Figure 4.19 A, B). Despite the comparable output of total virus particles, the STY of the non-oscillating process is up to two orders of magnitude lower than that of the oscillating process (Figure 4.19 C, D). This significant drop in productivity can be explained by the increased use in cell culture medium for the non-oscillating process. Here,
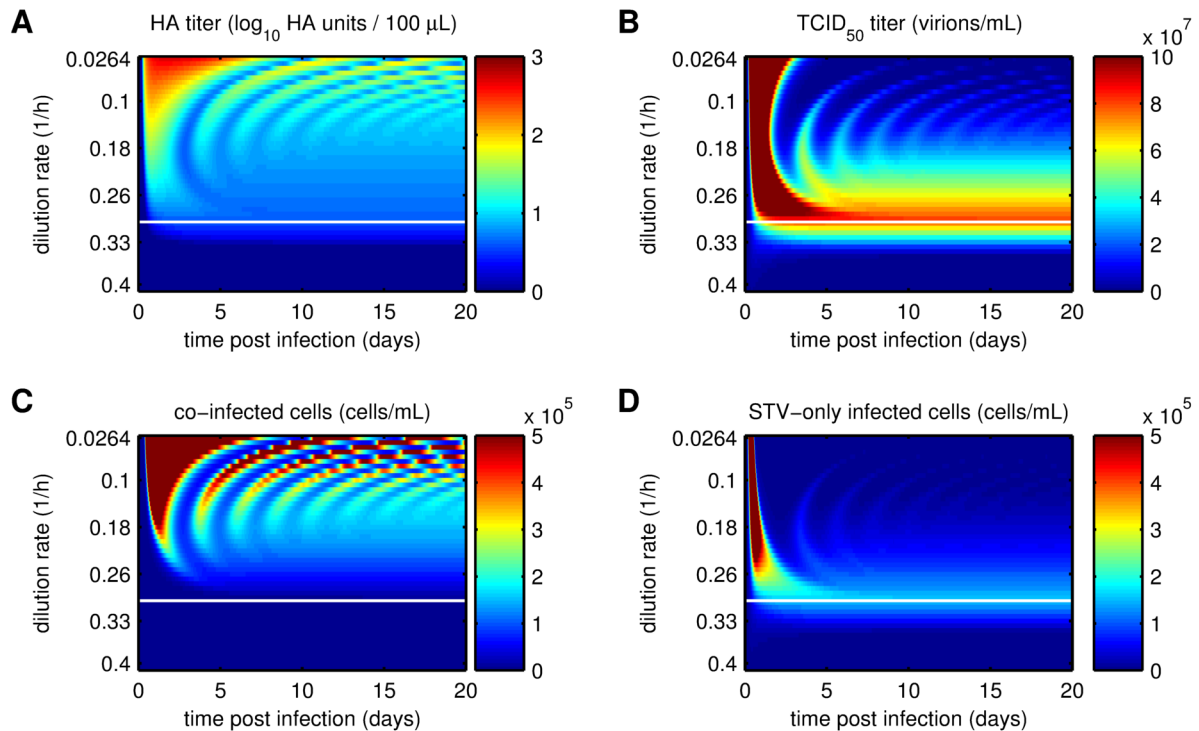
Figure 4.18.: Influence of dilution rate on oscillations in virus titers and cell concentrations during continuous influenza A virus production. Multiple simulated infections were evaluated for HA titer (A), TCID$_{50}$ titer (B) as well as the concentration of co-infected cells (C) and STV-only infected cells (D) over process time. Simulations were performed using the parameters in Table 4.2, where the flow rate of fresh medium from the medium reservoir to the virus bioreactor F_{FM} and the cell concentration in the feed T_{in} were adjusted according to Equation (3.3.11) and Equation (3.3.4), respectively (see Section 3.3.1) to agree with the dilution rates indicated on the y-axes. The horizontal white line marks the dilution rate $D = 0.2856$ 1/h at which the highest TCID$_{50}$ titer of 7.94×10^7 virions/mL was achieved in a non-oscillating steady state.

an almost ten times higher volume of medium has to be spent compared to the oscillating process to establish the steady state of the virus concentration. This is accompanied by an increased wash-out of virions and cells from the virus bioreactor. In particular, cell bleeding will be critical since doubling times of animal cells are usually much longer than 3.5 h, e.g. 23 h in case of AGE.CR cells [200]. In addition, one has to bear in mind that in the model of Frensing and Heldt *et al.* (2013) [14] cells start to release virus immediately after infection. In a real scenario, however, the influenza virus has an eclipse phase of up to 7 h [37, 254]. Hence, we can expect that in the experimental implementation of the continuous production system with a residence time of 3.5 h, the majority of infected cells will be harvested before virus release starts. This would result in an even lower STY than predicted. Nevertheless, we clearly showed that in the non-oscillating process regimen DIPs accumulate slowly and comprise only a small fraction ($\leq 3.2\,\%$) of the overall amount
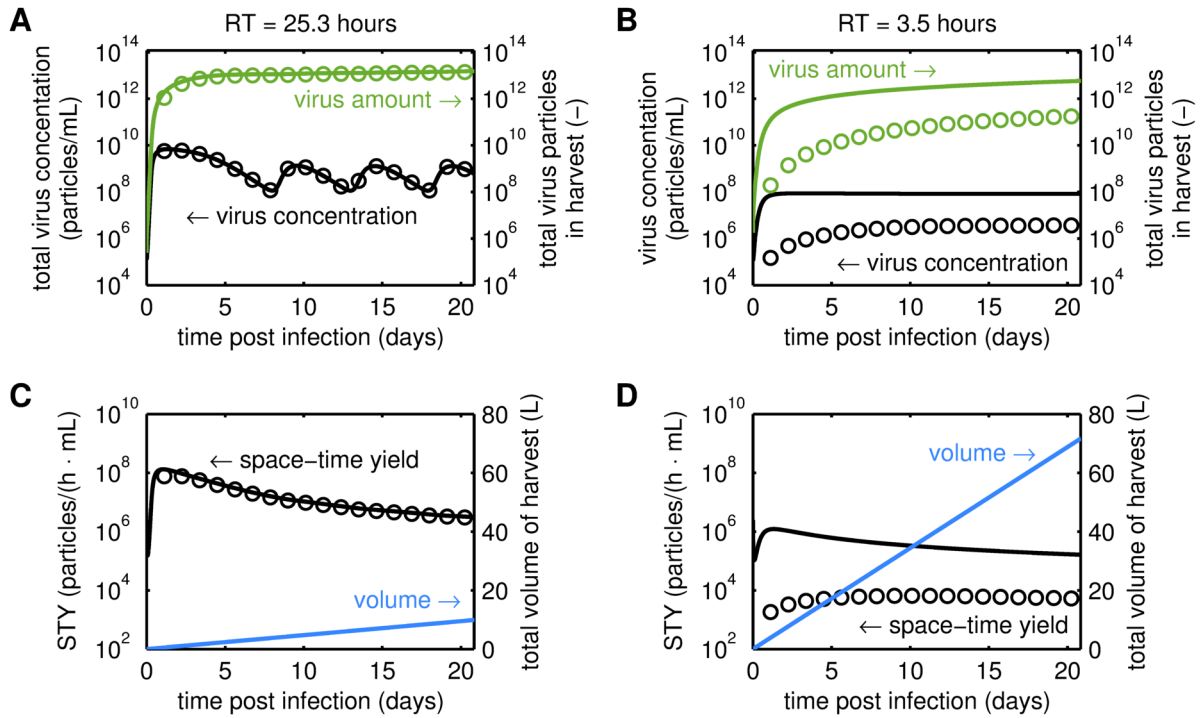
Figure 4.19.: Influence of oscillating and non-oscillating process regimen on virus harvest and space-time yield (STY). Concentration of virus particles and cumulative amount of virus particles harvested over process time (A, B) as well as STY and total volume of the harvest (C, D) for simulated infections at MOI 0.025. Shown are values related to either total virus particles (solid lines) or DIPs (open circles). Here, the number of total virus particles is equivalent to the HA titer according to Equation (3.3.23). For the oscillating regimen at RT 25.3 h (A, C) parameters were set as in Table 4.2, while for the non-oscillating regimen (B, D) the flow rate of fresh medium from the medium reservoir to the virus bioreactor F_{FM} and the cell concentration in the feed T_{in} were adjusted according to Equation (3.3.11) and Equation (3.3.4), respectively (see Section 3.3.1), to simulate RT 3.5 h. The short RT corresponds to the optimal dilution rate necessary to establish a non-oscillating steady state in accordance to the analysis in Figure 4.18.

of virus harvested. In contrast, in the oscillating process regimen, DIPs accumulate quickly and comprise the majority ($\leq 93.2\,\%$) of the harvested virus particles (Figure 4.19 A, B).

In summary, we provided proof of concept that oscillations in continuous production systems related to DIPs can be diminished by a reduction in the RT, i.e., an increase in the dilution rate of the virus bioreactor. On one hand, the continuous process benefits from a short RT since DIPs are out-diluted faster from the system and less cells are co-infected, resulting in a steady state of all process variables and a high $TCID_{50}$ titer. On the other hand, the high amount of medium spent decreases the process yield, rendering it infeasible for the application to vaccine manufacturing. However, due to the high number of DIPs achieved in the oscillating regimen, this continuous process might rather be applied for the purpose of DIP production instead.

4.3.2. Continuous production of DIPs at defined residence times

Since DIPs interfere with virus replication of infectious standard virus, they can potentially serve as a novel antiviral. While the two-stage bioreactor system might not be applicable for conventional vaccine manufacturing, it might well serve for the production of high DIP amounts, sufficient for tests in animal trials. In the following, we present results of a mathematical model describing the production of a promising antiviral candidate carrying a deletion in S1. In experiments, two RTs were tested for the production of this antiviral candidate. While we did not observe a significant impact of the RT on the amount of DIPs produced, model-based evaluation of the data revealed novel insights into mechanisms of DIP growth. The majority of this subsection was published in the original *Frontiers in Bioengineering and Biotechnology* article of Tapia and Laske *et al.* (2019) [314].

Parallel continuous infection system To allow a head-to-head comparison of virus dynamics at different RTs, our group established a continuous system with two bioreactors operated in parallel for IAV production [314]. This system is based on the previously published two-stage bioreactor setup of Frensing and Heldt *et al.* [14] with the modification that two bioreactors used for virus production are simultaneously fed from one bioreactor where producer cells are grown (Figure 4.20). The different RTs of 22 h and 36 h were achieved by operating the two virus bioreactors at different working volumes with the same feeding and harvesting flow rates (Equation (3.3.2), Section 3.3.1). During virus production of A/PR/8/34-delS1(1), we followed virus titers (Figure 4.21) and cell concentration (Figure 4.23 A, B). Like in previous continuous cultures of IAV, we distinguished between infectious virions, measured by $TCID_{50}$ assay, and total count of virus particles, measured by HA assay (Figure 4.21 A, B). In addition, a recently developed qPCR method allowed to assess copy numbers of the known DI RNA contained in the A/PR/8/34-delS1(1) seed virus with a deletion in S1 (DI S1) as well as its corresponding FL segment (FL S1) (Figure 4.21 C, D). As expected, viral titers showed oscillations for both RTs, which spanned four orders of magnitude in $TCID_{50}$ titers, two orders of magnitude in FL S1 particle concentrations and one order of magnitude in HA titers and DI S1 particle concentrations. In agreement to the simulation studies on different RTs (see Section 4.3.1), we also observed a slightly higher frequency of oscillations for the shorter RT. In contrast, the differences in amplitude of the oscillations were not as pronounced as in the simulation study. In particular, maxima and minima of the $TCID_{50}$ titer seem independent of the RT. The amplitude of the HA titer was larger for the shorter RT, immediately evident by the lower HA minima at RT 22 h compared to the minima at RT 36 h (Figure 4.21 A, B). In contrast, previous simulations predicted
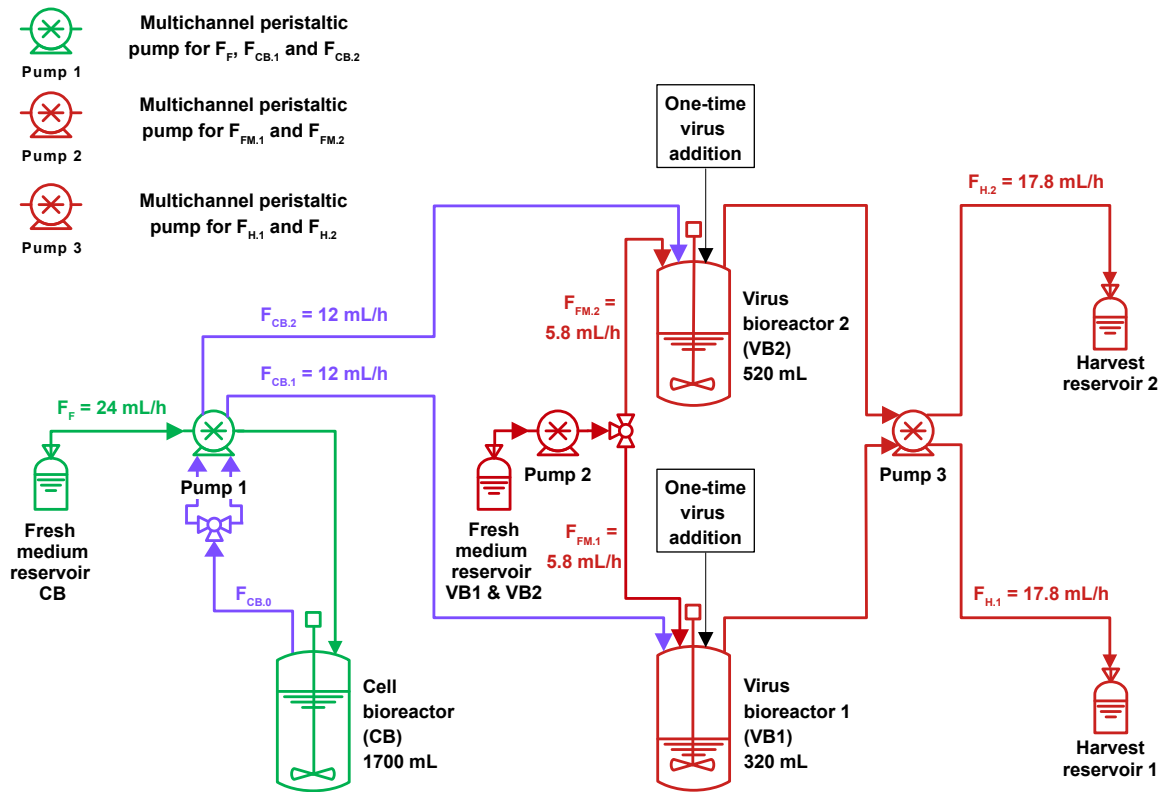
Figure 4.20.: Two-stage bioreactor system for parallel continuous production of influenza A virus in two cultivation vessels. MDCK suspension cells (MDCK.SUS2) were grown in the cell bioreactor (CB, green highlighting) and fed to the two virus bioreactors (VB1 and VB2, red highlighting) operated in parallel at residence times of 22 h and 36 h, respectively. In the VBs, cells were infected by A/PR/8/34-delS1(1) at MOI 0.1. VBs were cultivated in batch mode for another 23.4 h post infection before the system was switched to continuous mode for which cell broth from the CB as well as fresh medium from additional reservoirs were constantly fed to the two VBs using the nominal flow rates indicated in the schematic. Figure from Tapia and Laske *et al.* (2019) [314] was adapted to the nomenclature of this thesis.

a higher amplitude for longer RTs (Figure 4.17). Discrepancies between previous model predictions and the experimental data of A/PR/8/34-delS1(1) production might be due to the use of a different seed virus, cell line and cultivation medium. Still, we hereby provide proof that oscillations can be successfully influenced by the operator of such continuous systems.

Mathematical model for delS1(1) growth   To further elucidate differences in the experiments that might be dependent on the RT and extract crucial infection parameters from the available quantitative data, we integrated cell numbers and the different virus titers into a mathematical model for continuous influenza virus production (Figure 4.22). Since the numbers of viral genome copies determined by qPCR do not directly translate into numbers of viral particles, we converted DI S1 and FL S1 vRNA measurements to
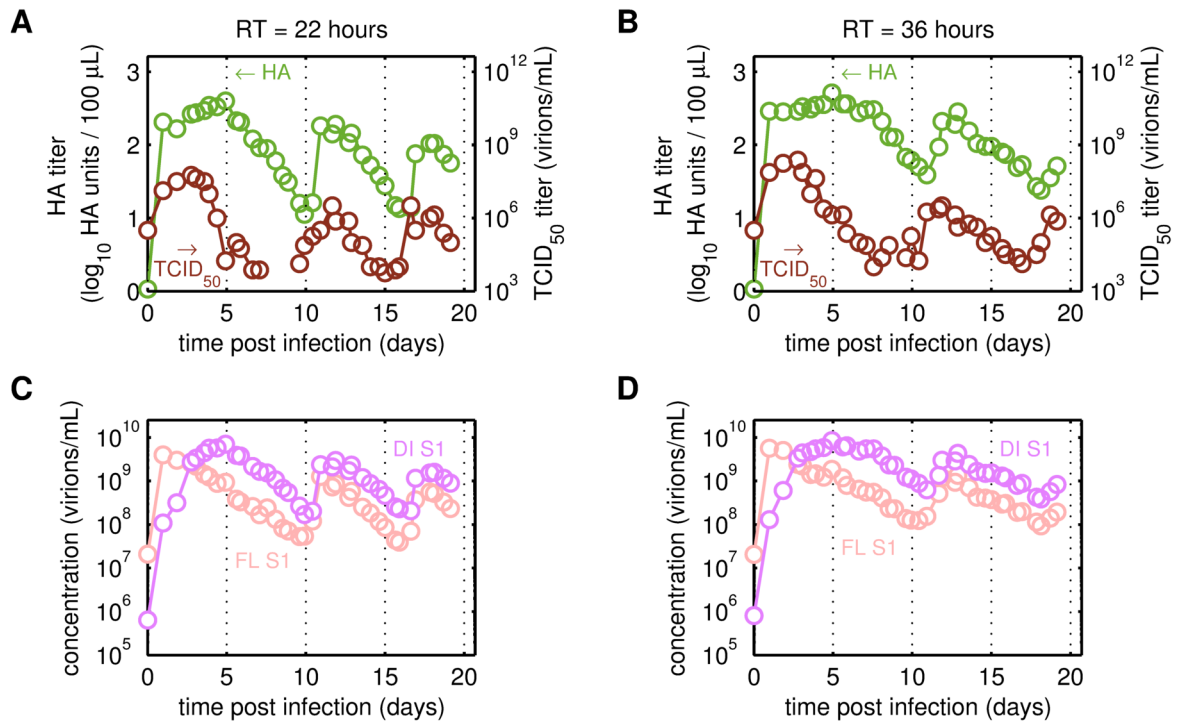
Figure 4.21.: Virus dynamics of A/PR/8/34-delS1(1) produced in MDCK.SUS2 cells in a parallel continuous bioreactor system at residence times (RTs) of 22 h and 36 h. Measurements (open circles) of (A, B) $TCID_{50}$ and HA titer, and (C, D) concentration of virions containing either defective interfering (DI) segment 1 (S1) or full-length (FL) S1 determined based on reverse transcription-qPCR measurements and the corresponding HA titer, according to Equation (3.3.24) and Equation (3.3.25). The continuous culture was started at 23.4 h p.i. Data as presented in Tapia and Laske *et al.* (2019) [314].

an equivalent virus particle concentration using the maximal number of virus particles determined by HA assay as a reference value (Equation (3.3.23) – Equation (3.3.25)). Besides, we could further divide the FL S1-containing particles into fully infectious virions, equivalent to STVs measured by $TCID_{50}$ assay, and those that carry a FL S1 but are non-infectious (NIPs, see Equation (3.3.25)). To describe the dynamics of the viral sub-populations including infectious STVs, NIPs and replication-incompetent DIPs during continuous virus production, we proposed a simple mathematical model that is based on the Frensing-and-Heldt model [14]. It describes the growth of uninfected cells, their infection as well as virus release from the STV-infected and co-infected sub-populations of infected cells. All infected cell sub-populations undergo virus-induced apoptosis while infectious STVs lose infectivity over time and finally degrade together with the other viral sub-populations. Moreover, the model accounts for the continuous feed of uninfected cells from the cell bioreactor as well as continuous harvest of cells and viruses from the virus bioreactor (Figure 4.22).
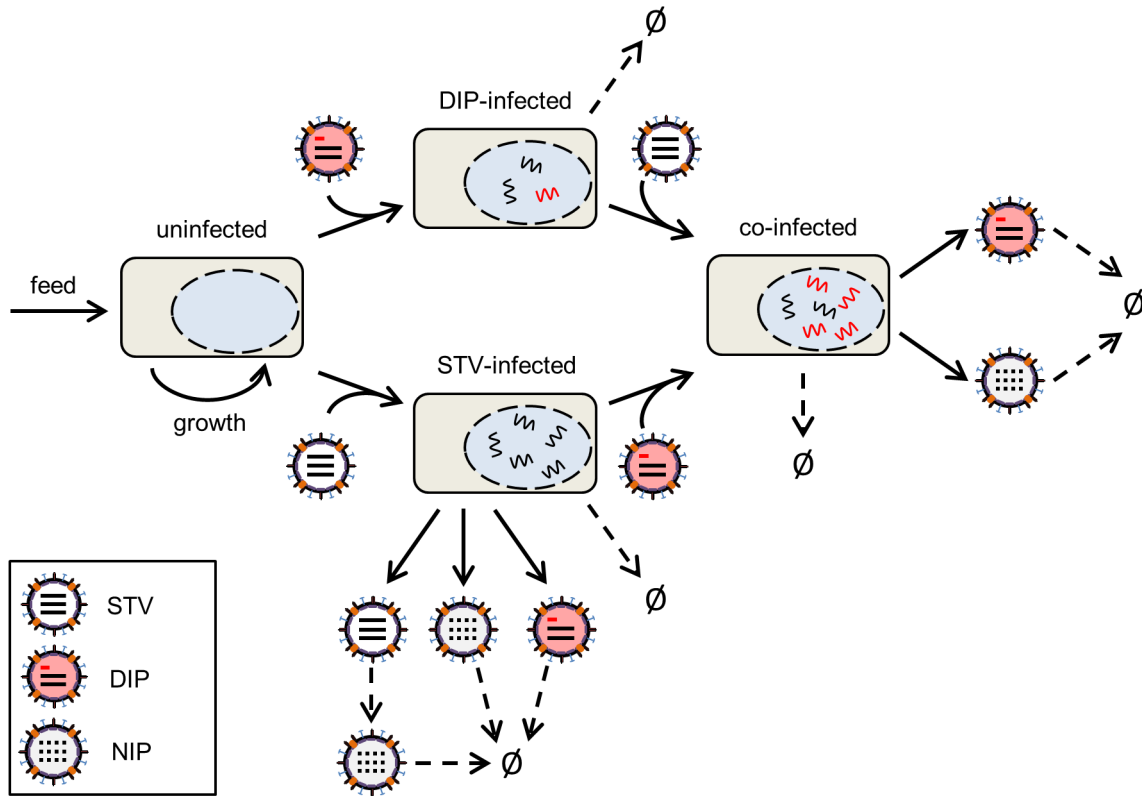
Figure 4.22.: Schematic of the model for continuous production of influenza A/PR/8/34-delS1(1). In brief, uninfected cells are fed from the cell bioreactor and can grow until they get infected by either DIPs or STVs. STV-infected cells release virus, including STVs, *de novo* generated DIPs and non-infectious STVs (NIPs). DIP-only infected cells and STV-only infected cells can be co-infected by either STVs or DIPs, respectively. Due to the interference by DIPs with virus replication, co-infected cells release no STVs but mainly DIPs and a few non-infectious STVs. Dashed arrows indicate apoptosis of infected cells or virus inactivation and degradation. See Section 3.3.2 for detailed model description and equations. Figure is based on the model scheme by Frensing and Heldt *et al.* (2013) [14].

Cell population dynamics   Overall, the total cell concentration in the virus bioreactors remained relatively stable with an average of 1.12×10^6 cells/mL (standard deviation $\pm\, 0.30 \times 10^6$ cells/mL) and 1.17×10^6 cells/mL (standard deviation $\pm\, 0.22 \times 10^6$ cells/mL) for RT 22 h and RT 36 h, respectively (Figure 4.23 A, B). Although the cell measurements seem to show rather random fluctuations, the slight cycling trend of the model fit is linked to the dynamics of the underlying cell sub-populations driven by virus propagation. As expected, addition of the seed virus causes a fast increase in STV-only infected cells, followed by a significant drop in their concentration and a simultaneous increase of the co-infected cell population through superinfection by DIPs (Figure 4.23 C, D). The co-infected cell population reaches its maximum at approximately 2 days p.i. and 4 days p.i., for RT 22 h and RT 36 h, respectively. Since co-infected cells mainly
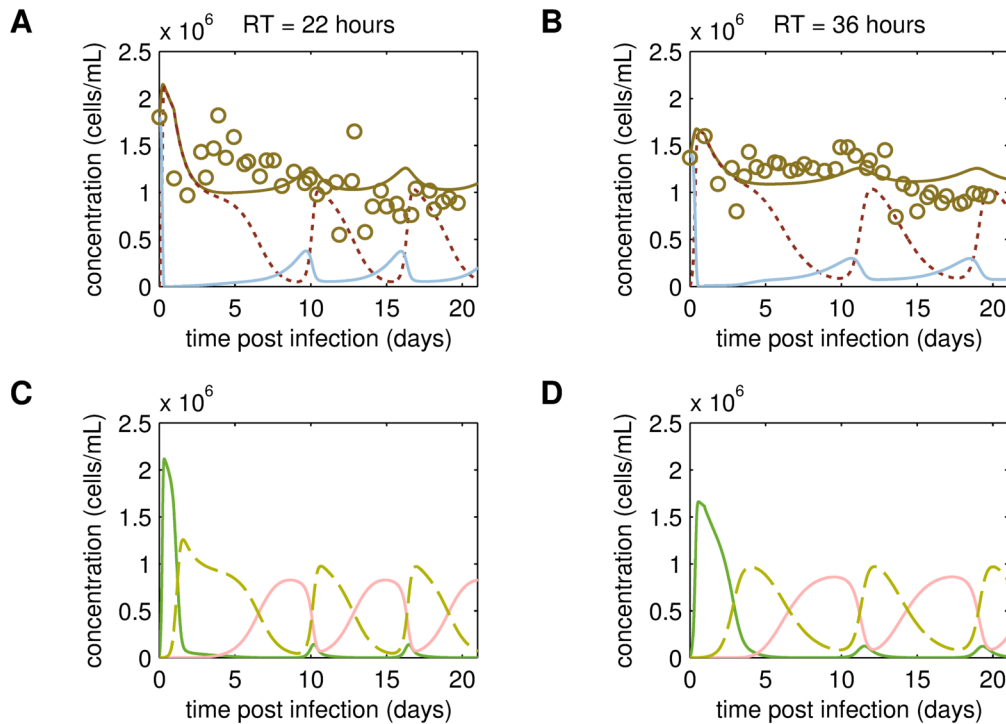
Figure 4.23.: Cell population dynamics of MDCK.SUS2 cells infected by A/PR/8/34-delS1(1) in a parallel continuous bioreactor system at residence times (RTs) of 22 h and 36 h. Upper panel: Measurements (open circles) and model fit (brown solid lines) of the total viable cell concentration, and the simulated number of productively infected cells, i.e., the sum of STV-only infected and co-infected cells (dotted dark red line), and uninfected cells (blue solid line) in the virus bioreactors operated at RTs of 22 h (A) and 36 h (B), respectively. Lower panel: Model predictions for the different infected cell populations, i.e., cells infected by infectious STV only (green solid line), cells infected by DIP only (red solid line), and co-infected cells (dashed yellow line) in the virus bioreactors operated at RTs of 22 h (C) and 36 h (D), respectively. Simulations were performed using the parameters in Table 4.3. For both, experiment and model simulations, the continuous culture was started at 23.4 h p.i. Figure taken from Tapia and Laske *et al.* (2019) [314].

release DIPs, uninfected target cells fed into the virus bioreactors will be mostly infected by DIPs only. Consequently the DIP-only infected cell population reaches its peak concentration at approximately 8 days p.i. (RT 22 h) and 10 days p.i. (RT 36 h). Meanwhile, the population of co-infected cells undergoes virus-induced apoptosis and ceases to a minimum (Figure 4.23 C, D). However, the number of co-infected cells rises again quickly, since previously DIP-only infected cells are now superinfected by STVs produced by the small sub-population of STV-only infected cells. This behavior is repeated for another 1 to 1.5 cycles within the cultivation time. Thereby, all sub-populations of cells reach their peak concentration repeatedly, which are similar in both virus bioreactors and, thus, seem independent of the RT.

Table 4.3.: Parameters and non-zero initial conditions for continuous production of A/PR/8/34-delS1(1) at residence times (RTs) of 22 h and 36 h, as in Tapia and Laske *et al.* (2019) [314].

Parameter		Description	RT 22 h	RT 36 h
μ^{a}	(h^{-1})	specific cell growth rate	0.0454	0.0278
D^{a}	(h^{-1})	dilution rate of VB	0.0454	0.0278
$F_{\mathrm{CB}}{}^{\mathrm{a}}$	$(\mathrm{ml/h})$	flow rate from CB to VB	12	12
$F_{\mathrm{FM}}{}^{\mathrm{a}}$	$(\mathrm{ml/h})$	flow rate from FM to VB	5.8	5.8
$V_{\mathrm{VB}}{}^{\mathrm{a}}$	(ml)	working volume of VB	320	520
$k_{\mathrm{S}}^{\mathrm{Inf}}$	$(\mathrm{ml/(virion \cdot h)})$	STV infection rate	1.59×10^{-7}	5.38×10^{-8}
$k_{\mathrm{D}}^{\mathrm{Inf}}$	$(\mathrm{ml/(virion \cdot h)})$	DIP infection rate	2.32×10^{-10}	7.96×10^{-11}
k^{Apo}	(h^{-1})	apoptosis rate	0.008	0.003
$k_{\mathrm{Vs}}^{\mathrm{Prod}}$	$(\mathrm{virions/(cell \cdot h)})$	STV production by I_{s}	2.51	4.12
$k_{\mathrm{Vd}}^{\mathrm{Prod,Ic}}$	$(\mathrm{virions/(cell \cdot h)})$	DIP production by I_{c}	203	177
$k_{\mathrm{Vd}}^{\mathrm{Prod,Is}}$	$(\mathrm{virions/(cell \cdot h)})$	*de novo* DIP production	10^{-5}	1.13×10^{-9}
$k_{\mathrm{V_{Ni}}}^{\mathrm{Prod,Ic}}$	$(\mathrm{virions/(cell \cdot h)})$	NIP production by I_{c}	4.91×10^{-16}	1.41×10^{-8}
$k_{\mathrm{V_{Ni}}}^{\mathrm{Prod,Is}}$	$(\mathrm{virions/(cell \cdot h)})$	NIP production by I_{s}	120	173
$k_{\mathrm{Vs}}^{\mathrm{Deg}}$	(h^{-1})	STV inactivation rate	1.58×10^{-7}	0.07
$k_{\mathrm{V}}^{\mathrm{Deg}}$	(h^{-1})	virus degradation rate	3.82×10^{-27}	2.02×10^{-9}
T_{CB}	$(\mathrm{cells/ml})$	cell concentration CB	1.68×10^{6}	1.68×10^{6}
$T_{\mathrm{in}}{}^{\mathrm{b}}$	$(\mathrm{cells/ml})$	cell concentration in feed	1.13×10^{6}	1.13×10^{6}
T_0	$(\mathrm{cells/ml})$	initial cell concentration VB	1.80×10^{6}	1.37×10^{6}
$V_{\mathrm{s0}}{}^{\mathrm{c}}$	$(\mathrm{virions/ml})$	initial STV concentration	3.16×10^{5}	3.16×10^{5}
$V_{\mathrm{d0}}{}^{\mathrm{c}}$	$(\mathrm{virions/ml})$	initial DIP concentration	6.41×10^{5}	8.06×10^{5}
$V_{\mathrm{Ni0}}{}^{\mathrm{c}}$	$(\mathrm{virions/ml})$	initial NIP concentration	2.05×10^{7}	2.03×10^{7}

[a] Mean dilution rate D was estimated from measurements of the harvest volume, for continuous cultivations we assume $\mu = D$, excluded from model fitting. Flow rates and reactor volumes are given as nominal values.

[b] T_{in} is calculated according to Equation (3.3.4) (see Section 3.3.1).

[c] Concentration of infectious virions according to TCID$_{50}$ titer. Initial concentrations of DIPs and NIPs were calculated using Equation (3.3.23) – Equation (3.3.25). The seed virus preparation was characterized with an HA titer of 2.36 log$_{10}$ HA units/100 μL, TCID$_{50}$ titer of 6.76×10^{7} virions/mL, DI S1 content of 1.33×10^{8} virions/mL and FL S1 content of 4.45×10^{9} virions/mL.

VB - virus bioreactor, CB - cell bioreactor, FM - fresh medium reservoir, NIP - non-infectious FL S1-containing particle, I_{s} - STV-only infected cell, I_{c} - co-infected cell
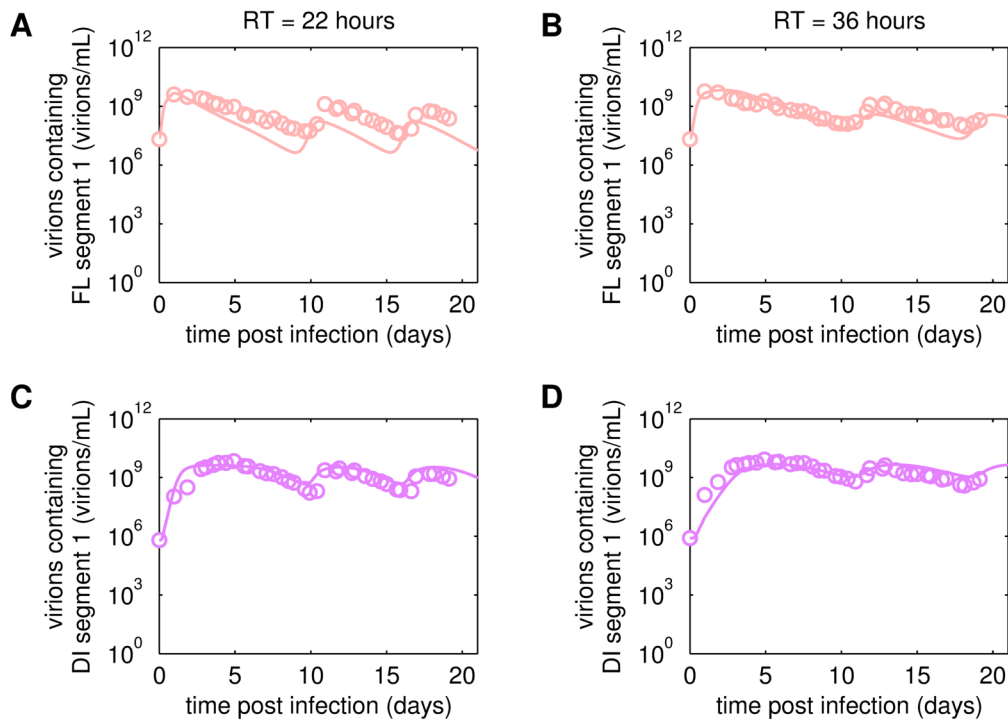
Figure 4.24.: Dynamics of full-length (FL) and defective interfering (DI) segment 1 (S1)-containing virions of A/PR/8/34-delS1(1) produced in MDCK.SUS2 cells in a parallel continuous bioreactor system at residence times (RTs) of 22 h and 36 h. Measurements (open circles) based on reverse transcription-qPCR and model fit (solid lines) are shown for (A, B) all virions containing FL S1 and (C, D) virions containing DI S1. Model fits correspond to the parameters in Table 4.3. For both, experiment and model simulations, the continuous culture was started at 23.4 h p.i. Figure taken from Tapia and Laske *et al.* (2019) [314].

Virus dynamics   The dynamics of the DI S1- and FL S1-containing particles were similar for the two RTs (Figure 4.24). While the FL S1-containing particles already reached their maximum at approximately 1 day p.i., the DI S1-containing particles showed an initial delay in growth and peaked at about 5 days p.i. (Figure 4.24). For both RTs, maximal concentrations of DI S1- and FL S1-containing particles were in the range of 10^9 virions/mL. For RT 36 h, the frequency of oscillations in qPCR-based virus titers was slightly reduced, resulting in a delay of cycles in the range of one to two days compared to RT 22 h. Correspondingly, infectious virus titer, measured by TCID$_{50}$ assay, and number of total virus particles, assessed by HA assay, also showed pronounced oscillations with the previously mentioned shift in minima and maxima for the longer RT (Figure 4.25). Interestingly, the HA data indicate a trend for an overall decrease in the amplitude of titers toward later cultivation time points for both RTs (Figure 4.25 C, D). According to our previous simulation study (Section 4.3.1), this overall decrease was, however, only anticipated for the longer RTs (Figure 4.17) and is not reproduced by the current
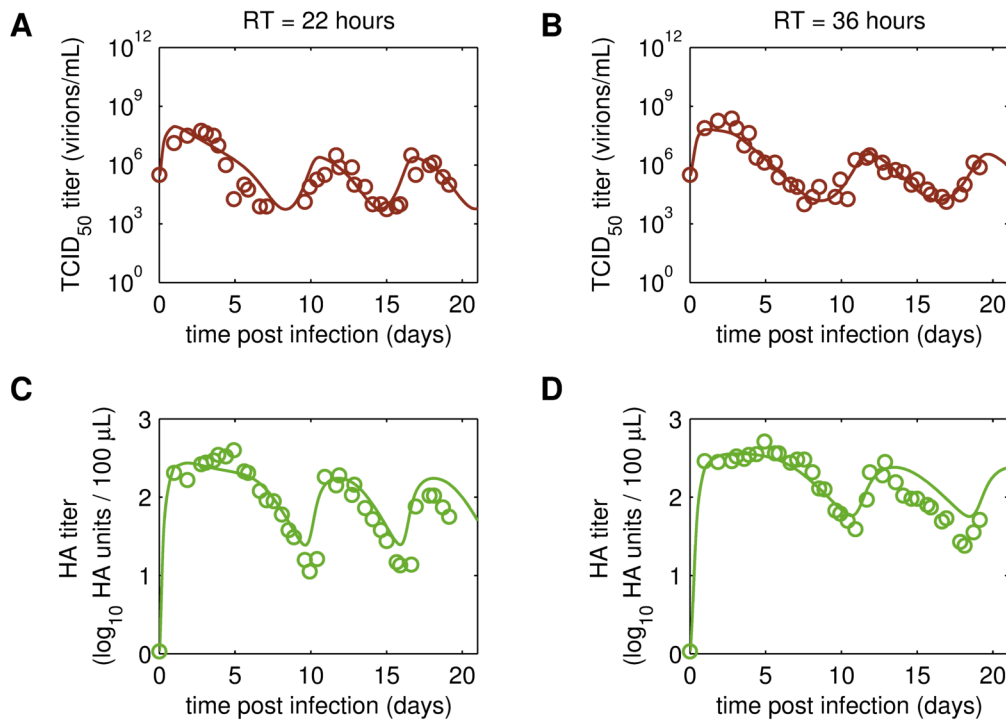
Figure 4.25.: Dynamics of infectious virions and total number of virions produced in MDCK.SUS2 cells infected by A/PR/8/34-delS1(1) in a parallel continuous bioreactor system at residence times (RTs) of 22 h and 36 h. Measurements (open circles) and model fit (solid lines) are shown for (A, B) $TCID_{50}$ titer, representing the fully infectious viral sub-population of virions containing FL S1, and (C, D) HA titer which is the sum of all viral sub-populations containing FL S1 and DI S1. Model fits correspond to the parameters in Table 4.3. For both, experiment and model simulations, the continuous culture was started at 23.4 h p.i. Figure taken from Tapia and Laske *et al.* (2019) [314].

model fit. Moreover, the virus titers show neither a downward trend nor a trend toward dampened oscillations even if simulated for a period of 90 days (Figure C.3 in the appendix). In contrast, dynamics of the $TCID_{50}$ titer, representing the viral sub-populations of STVs, are captured well both qualitatively and quantitatively. In particular, the difference of one order of magnitude between initial $TCID_{50}$ peak titer and its subsequent peak titers is reproduced well. However, in contrast to the HA titer, no overall decrease in peak infectious titers was observed (Figure 4.25 A, B). Despite the delays in oscillations, the amplitude of the $TCID_{50}$ titer was independent of the RT, ranging on average between 10^3 and 10^6 virions/mL.

DIP-to-STV ratio   As expected, oscillations were also observed in the dynamics of the DIP-to-STV ratios (Figure 4.26). In both cultivations, the ratio reached a maximum of about 10^5 around 7 days p.i. This value is similar for both RTs and correlates with the lowest $TCID_{50}$ titer. We may hypothesize that one infectious STV per 10^5 DIPs is a critical
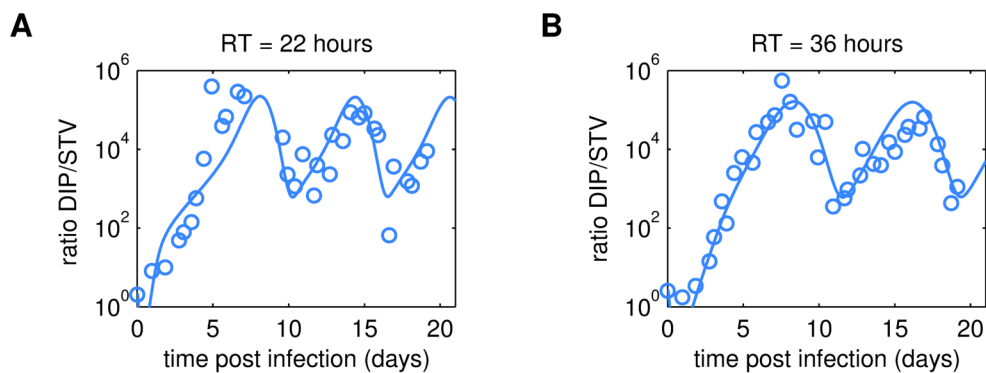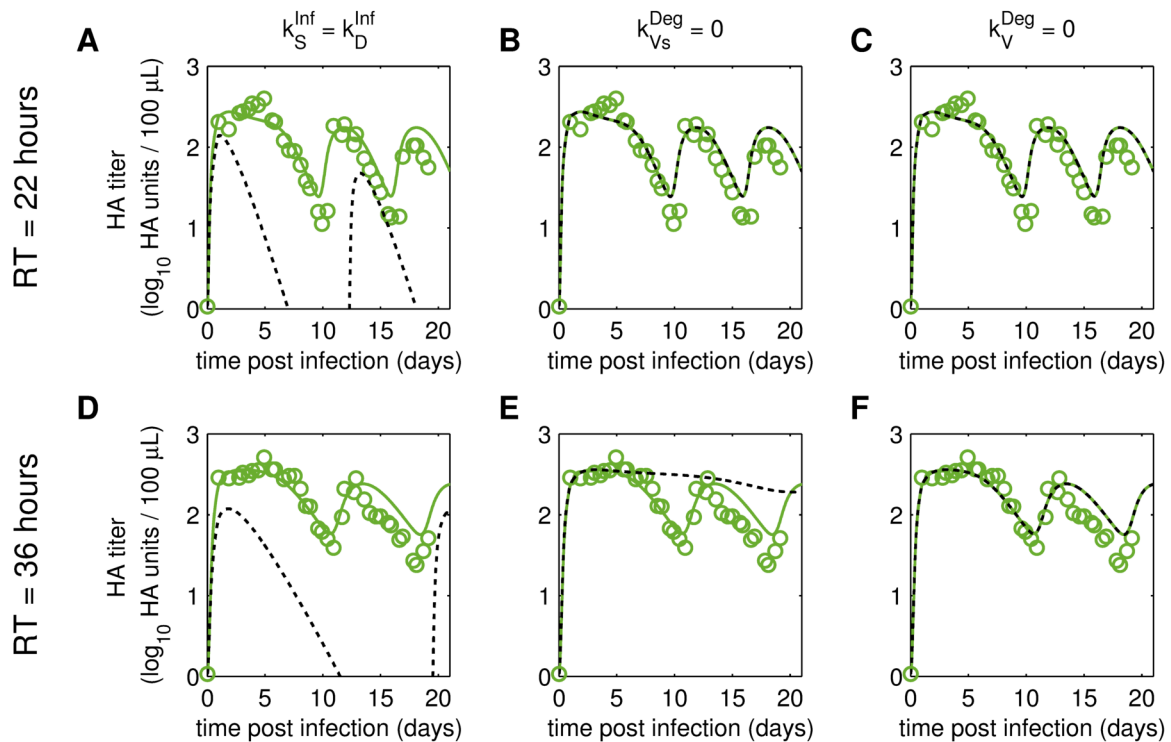
Figure 4.26.: Dynamics of the DIP-to-STV ratio in parallel continuous cultures of MDCK.SUS2 cells infected by A/PR/8/34-delS1(1) at residence times (RTs) of 22 h and 36 h. The experimental DIP-to-STV ratio (open circles) was determined by dividing the number of DI S1-containing virions by the corresponding $TCID_{50}$ titer and compared to the simulated DIP-to-STV ratio (according to Equation (3.3.20)) at RTs of 22 h (A) and 36 h (B), respectively. Simulations were performed using the parameters in Table 4.3. For both, experiment and model simulations, the continuous culture was started at 23.4 h p.i. Figure taken from Tapia and Laske *et al.* (2019) [314].

ratio at which DIPs cause self-interference and start to hamper overall virus replication significantly. The impact of too high DIP-to-STV ratios and related self-interference is supported by modeling studies on influenza virus (Section 4.2.1, [309]) and VSV [371]. As a consequence of self-interference, DIP concentrations decrease, reaching a minimum around 11 days p.i., and numbers of infectious STVs are rising again, initiating a new cycle (see also Figure 4.24 and Figure 4.25). It would be interesting to test whether this critical ratio can be reproduced in other experiments of continuous influenza virus production.

Sensitivity analysis Sensitivity analyses reveal how accurate parameter estimates from experimental data are and how the model output is influenced by perturbations in the initial conditions. Furthermore high sensitivities may highlight the importance of certain mechanisms in the model, which might be different with respect to the RT. In general, the majority of parameters was estimated well from the experimental data (Figure 4.27). In case of the specific infection rates, the estimation of the DIP infection rate k_D^{Inf} was better compared to the STV infection rate k_S^{Inf} for both RTs. Moreover, it became evident that infection rates estimated from the RT 36 h data set were slightly better compared to those of RT 22 h. The high sensitivity of both infection rates underlines the importance of assuming that DIPs and STVs infect cells at different specific rates. In case only one joint infection rate is used in the model, the simulations are not able to capture the experimental data any more (Figure 4.28 A, D). Furthermore, the specific rate for virus-induced apoptosis k^{Apo} shows a lower sensitivity compared to those of the infection
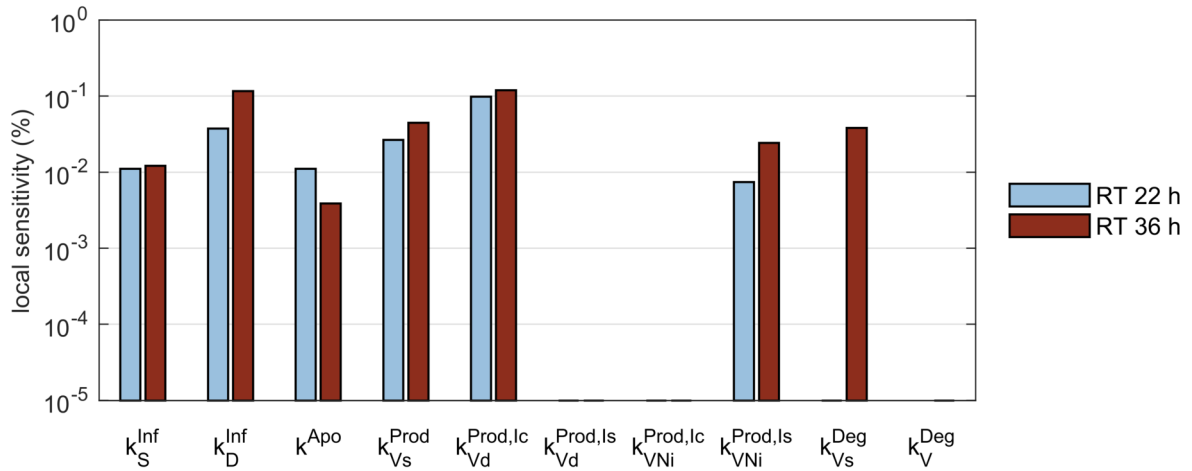
Figure 4.27.: Local sensitivity of parameter values estimated from experimental data of continuous cultures of MDCK.SUS2 cells infected by A/PR/8/34-delS1(1) at residence times (RTs) of 22 h and 36 h. Shown are the local sensitivities of the parameter estimates listed in Table 4.3. The sensitivities represent the normalized change in the model output in response to a parameter perturbation by $+1\%$ (see Equation (2.3.4) and Equation (2.3.5)). Sensitivity values of all parameters and initial conditions are listed in Table C.1 in the appendix. Colors according to legend.

rates, and is, however, the only parameter that yielded a slightly better estimate for the shorter RT. In addition, we got very good estimates for the specific production rates of the different viral sub-populations. In particular, the estimates of the rates for the production of STVs and NIPs by STV-infected cells, $k_{\mathrm{Vs}}^{\mathrm{Prod}}$ and $k_{\mathrm{V_{Ni}}}^{\mathrm{Prod,Is}}$, as well as the DIP production rate of co-infected cells, $k_{\mathrm{Vd}}^{\mathrm{Prod,Ic}}$, were highly sensitive. Here, once more, the estimates based on the RT 36 h data were slightly better compared to those of RT 22 h. The remaining parameters related to virus release yielded less good estimates. In particular, the specific *de novo* generation of DIPs from STV-infected cells, $k_{\mathrm{Vd}}^{\mathrm{Prod,Is}}$, showed a low sensitivity. For the two RTs tested, this *de novo* generation rate is estimated close to zero (Table 4.3) and, even if excluded from the model, the simulations still yield oscillations due to the amplification of DIPs present in the seed virus (Figure C.4 A, D in the appendix). Moreover, the specific production rate of NIPs by co-infected cells, $k_{\mathrm{V_{Ni}}}^{\mathrm{Prod,Ic}}$, is also close the zero and might therefore be neglected as well with no influence on the goodness of fit (Figure C.4 B, E in the appendix). Hence, it seems that NIPs are mainly released from STV-infected cells, which is supported by both, a reasonable value and sensitivity of $k_{\mathrm{V_{Ni}}}^{\mathrm{Prod,Is}}$ (see also Figure C.4 C, F in the appendix). Finally, the low sensitivity of virus inactivation, i.e., the decay of previously infectious STVs to NIPs expressed by rate $k_{\mathrm{Vs}}^{\mathrm{Deg}}$, and lysis rate of virions $k_{\mathrm{V}}^{\mathrm{Deg}}$ show that these mechanisms do not have a significant influence on the model simulations (Figure 4.28 B, C, F). The

Figure 4.28.: Dynamics of the HA titer produced in parallel continuous cultures of MDCK.SUS2 cells infected by A/PR/8/34-delS1(1) at residence times (RTs) of 22 h and 36 h in response to changes in infection rates and virus degradation. HA titer measurements (open circles), original model fit (solid line) and model simulations (dashed lines) are shown in case of (A, D) the DIP infection rate $k_{\mathrm{D}}^{\mathrm{Inf}}$ equals the STV infection rate $k_{\mathrm{S}}^{\mathrm{Inf}}$, (B, E) the rate for STV inactivation $k_{\mathrm{Vs}}^{\mathrm{Deg}}$ is zero and (C, F) the lysis rate of virions $k_{\mathrm{V}}^{\mathrm{Deg}}$ is zero, for RT 22 h (upper panel) and 36 h (lower panel), respectively. For the different simulation scenarios the remaining parameters were fixed according to the values in Table 4.3. For both, experiment and model simulations, the continuous culture was started at 23.4 h p.i.

latter is, however, different in case of the longer RT, for which $k_{\mathrm{Vs}}^{\mathrm{Deg}}$ shows a high local sensitivity and, if set to zero in a simulation, prevents the model from capturing the experimental data (Figure 4.28 E). Although we found that some mechanisms, such as *de novo* generation of DIPs, virus inactivation and degradation, were not necessarily needed to reproduce the given data sets, we suggest to keep those included in the model. Hence, we can propose a model that covers more general cases, e.g. in case that a DIP-free seed virus is used for infection or the RT is varied such that virus inactivation becomes relevant. Most intriguingly was that we needed to account for virus-specific infection rates, $k_{\mathrm{S}}^{\mathrm{Inf}}$ and $k_{\mathrm{D}}^{\mathrm{Inf}}$, which has never been proposed before.

Concerning the influence of the initial conditions on model output, we found that the starting cell concentration in the virus bioreactors as well as the cell concentration in the feed are more crucial than the seed virus composition (Table C.1 in the appendix).

Summary   Using the Frensing-and-Heldt model, we have shown that DIP-induced oscillations in continuous cultures of IAV can be influenced by manipulating the RT, i.e., the dilution rate, of the virus bioreactor. While it is economically unfeasible to completely out-dilute DIPs, our *in silico* study showed that a short RT, i.e., a high dilution rate, can reduce the amplitude and increase frequency of oscillations in virus titers. Indeed, we also found in experiments that the frequency of oscillations was increased for the shorter of two RTs in cultures infected by A/PR/8/34-delS1(1). However, the amplitude of the different viral sub-populations was either increased or unaffected. Using the two delS1(1) data sets obtained at defined RTs, we extended and parameterized a new within-host model for DIP co-infection. Simulations and model analysis revealed that the relevance of some mechanisms, such as *de novo* generation of DIPs and virus degradation, depend on the initial and operating conditions of the process. In addition, we have learned that, independent of the RT, it is necessary to account for DIP- and STV-specific infection rates to describe the data. Thus, the mechanisms of infection that had to be accounted for in the delS1(1) model might be the reason why predictions by the Frensing-and-Heldt model were not fully in agreement to the new experimental data.

4.3.3. Discussion of continuous influenza A virus production

A recent study of our group showed that the presence of DIPs causes periodic oscillations in viral titers during continuous production of IAV [14]. Using the simple mathematical model presented in that study we could demonstrate *in silico* that oscillations can be successfully influenced by adjusting the RT of the virus bioreactor. To test this hypothesis, our group performed an experiment using a novel continuous production system that allows long-term head-to-head comparison of virus dynamics at two RTs. We integrated those experimental data into an extended version of the previously published model [14]. Like this, we did not only extract crucial infection parameters from oscillating measurement data, but also revealed interesting features of DIP co-infection that have not been reported before.

Possibilities to reduce oscillations   Performing simulations we have shown that the RT has a significant impact on frequency and amplitude of oscillations in both, virus titers and cell concentrations (Figure 4.17). In particular, oscillations in virus titers are diminished at short RTs due to reduced accumulation of DIPs. Initially, we expected an improved productivity in case periodic drops in virus titers are avoided. Instead, it became evident that the overall productivity was significantly reduced in a non-oscillating process regimen, which was caused by the increase in spent medium (Figure 4.19). Thus, Rammhold *et al.* performed further model-based studies testing options to maintain productivity while diminishing oscillations [370]. Indeed, it was possible to reach a steady state in virus titers, e.g. by using a discontinuous feed of fresh medium to the virus bioreactor. The technical implementation of such a control strategy would, however, significantly increase the complexity of the two-stage bioreactor setup. Furthermore, this control strategy would require the online measurement of the HA titer or, if only offline HA values are available, a determination of the HA titer as often as every hour during the entire run. Thus, an even closer supervision of the process would be required. Nonetheless, the amount of spent medium was reduced while the STY was comparable to the conventional two-stage bioreactor process, not taking into account costs for equipment and personnel. Finally, Rammhold *et al.* also implemented and simulated a two-stage bioreactor with a re-circulation loop. This setup allowed to infect cells constantly at a low MOI by re-circulating small volumes of the virus bioreactor to a tubular reactor where infection took place. With that, a relatively stable virus titer was achieved in simulations. While a first experimental implementation suffered from the complex setup of this system [372], its experimental validation is yet to be accomplished. Note that even though stable titers were predicted by those different approaches, the majority of the virus harvest was, once more, comprised by DIPs [370]. While stable product titers may facilitate downstream

processing of the harvest, one would have to assure that the high amount of DIPs does not hamper the product quality. In addition, multiple replication rounds during long cultivation times affect the genetic stability of the virus, which is incompatible with the high quality standards required for human vaccine production. Thus, the bench-marking and regulatory approval of such process might be complicated, if not impossible. Recently, it was shown that continuous production of IAV can be realized successfully with a tubular bioreactor, where the impact of DIP formation on virus titers can be reduced to a minimum [373]. Nevertheless, it seems that as soon as DIPs are present in a continuous production process, elaborate measures have to be considered to avoid their formation and propagation. For instance, in case of baculovirus, it took over 15 years of research on different bioreactor setups [374–376] as well as genetic engineering [377, 378] to investigate the impact of DIPs and finally prevent DIP-related losses in product yield. On the other hand, the option to produce virus-based biopharmaceuticals using continuous cultivation systems is more feasible in case no DIPs are formed, e.g. in case of modified Vaccinia virus Ankara (MVA) [379].

Impact of residence time on oscillations   The use of the two-stage bioreactor system might not be feasible for conventional influenza vaccine manufacturing when operated in oscillating process regimen. Instead, it allows to produce DIPs in high amounts and to analyze the impact of certain process parameters, e.g. the RT, on the system's response. In simulations, the decrease in the RT reduced the amplitude of oscillations to a minimum, while an increase in the RT caused an increase in amplitude, holding the promise of even higher peak HA titers (Figure 4.17). On the contrary, in experiments, the amplitude of oscillations was higher for the shorter RT with no significant difference in peak HA titers (Figure 4.21). Furthermore, peak values of the different viral sub-populations as well as the DIP-to-STV ratio did not seem to depend on the RT (Figure 4.24 – Figure 4.26). Likely, even though the RTs tested had a difference of 14 h, both were sufficiently long to achieve similar peak titers. This was also evident in our *in silico* studies evaluating IAV production at RT 25.3 h and RT 35 h (Figure 4.17), which are similar to the RTs tested in experiments. Eventually, the experimental data showed that the peak values were reached twice and three times for RT 36 h and RT 22 h, respectively. This is in agreement to model simulations that predicted a reduced frequency of oscillations for longer RTs. Since the model we used for predictions was based upon a data set from AGE1.CR cells we can anticipate that model simulations will agree only partially with the experimental data from MDCK.SUS2 cells. The two cell lines show very distinct properties in propagating the virus, which leads to, e.g. different frequency and amplitude of the HA titer observed previously in small-scale two-stage bioreactor

experiments [372]. Moreover, differences in virus dynamics may also be related to the use of different seed viruses. While a conventional influenza A/PR/8/34 seed virus was used for the AGE1.CR cultivation, a particular seed virus engineered by reverse genetics, A/PR/8/34-delS1(1), was used to test growth of a specific DI RNA of S1 in MDCK.SUS2 cells. Nevertheless, the AGE1.CR-based model was able to predict the overall impact of the RT on oscillations well, which supports the basic model assumptions and mechanisms of the model. However, to be finally able to describe production of A/PR/8/34-delS1(1) in MDCK.SUS2 cells at two distinct RTs, we had to augment the model and fit it individually to the two data set.

Modeling virus production at defined residence times To model continuous A/PR/8/34-delS1(1) production, we mainly followed the principles of the model by Frensing and Heldt *et al.* [14]. While we introduced new aspects based on the available experimental data, e.g. an additional viral sub-population and various virus production rates for the different infected cell sub-populations, we also excluded some of the previous model assumptions. In particular, we neglected the growth of DIP-only infected cells and assumed, instead, that those cells can undergo virus-induced apoptosis. Note, that Cane and co-workers found that DIP-only infected MDCK cells can continue to grow and give rise to DIP-infected daughter cells [380]. However, the experimental conditions applied in their study, i.e., the use of UV-irradiated seed virus, passaging of cells in a virus-free culture and a culture time of 5–10 days between passages, cannot be compared to the cultivation conditions during continuous production. Furthermore, due to the high DIP concentrations achieved in the experiment, uninfected cells take up a high number of DIPs, which results in a high number of intracellular viral RNAs (10^3 to 10^4 DIPs per uninfected cell), comparable to RNA levels reached during a conventional infection (see, e.g. Frensing and Pflugmacher *et al.* [121]). Since intracellular viral RNAs trigger antiviral mechanisms, such as the IFN-mediated innate immune response and virus-induced cell death [33, 34, 121], it was reasonable to assume cell death of DIP-only infected cells. An additional justification for this was also given by simulations using the Frensing-and-Heldt model [14]. Those showed that the population of DIP-only infected cells was the only state variable in steady state and even accumulated in case the RT was sufficiently long (Figure 4.17). In that case, we observed not only oscillations but an overall decreasing trend of the $TCID_{50}$ titers in simulations. Due to this additional reduction of the infectious titer, we hypothesized that growth of DIP-only infected cells might, thus, provide another feature of interference by DIPs. However, in our experiments, the $TCID_{50}$ titer showed regular oscillations supporting to exclude growth of DIP-only infected cells. Note, that since this additional layer of interference might also be dependent

on individual characteristics of the predominant DI RNA in the system, more experimental as well as model-based investigations are required to elucidate this phenomenon even further.

Evaluation of model fits and predictions   Overall, the cyclic behavior of the virus titers is described clearly by the model fits. However, note, that some quantitative discrepancies remain, such as the underestimation of the FL S1-containing virus titers for some time points (Figure 4.24) and the unability of the model to reproduce the minima of the total virus particle count measured by HA assay (Figure 4.25). Still, model simulations are mainly within the error range of the assays for HA (about $\pm$ 0.15 log) and $TCID_{50}$ (about $\pm$ 0.3 log). Regarding the error for the number of virions containing either FL S1 or DI S1, it has to be considered that those are derived from both qPCR measurements with a relative standard deviation of 25 % as well as HA titers (Equation (3.3.23) – Equation (3.3.25)). Furthermore, a good agreement with the data could only be achieved upon fitting the model individually to each of the two data sets. Attempts to find a joint parameterization by fitting both data sets simultaneously failed (not shown) and we were also unable to predict virus dynamics for RT 36 h using the parameterization of the RT 22 h data set and *vice versa* (Figure C.5 and Figure C.6 in the appendix). Thus, the model's predictive power needs improvement before it can be applied to further applications, such as model-based process optimization. We think that only the comparison of multiple continuous runs at different RTs can reveal whether those discrepancies can be cured by further model extensions or if the model needs to be informed by more experimental data including all state variable, e.g. also measurements of the infected cell sub-populations as well as apoptotic cells. To still draw conclusions from the currently available data-model-pairs we performed local sensitivity analysis and parameter perturbation studies. The biological relevance of those results will be discussed in the following.

Virus release of STV-infected cells   In our extended model we assume that STV-only infected cells and co-infected cells can release three different virus species. Their total release rates are similar ranging from 123–203 virions/(cell · h), which is in the same order of magnitude as determined previously for IAV replication models proposed for adherent MDCK cells [37, 253, 254]. With about 99 %, the majority of released virions by STV-only infected cells are NIPs while only a minority are fully infectious STVs. With respect to the data, those values were estimated well and agree to previous findings [121, 381]. However, the amount of DIPs generated *de novo* by STV-only infected cells was not estimated well from the experimental data. This insensitivity of the *de novo* generation rate is supported by a parameter study of Frensing and Heldt *et al.* [14] who demonstrated

that perturbations of the *de novo* generation rate had only a minor impact on model output. In case of the specific DI S1 candidate evaluated in our study, a negligible *de novo* generation rate is, however, reasonable. Since it is unlikely that the same DI RNA sequence is emerging repeatedly by *de novo* generation, its dominance stems solely from the amplification of the DI S1 RNA introduced with the seed virus. Nonetheless, we observed that various sub-genomic RNAs from other segments were generated *de novo* during the run (see original publication [314]). Likely, some of them are also interfering and have an impact on STV replication. Hence, future models might also consider additional classes of DIPs, given that experimental methods allow to identify and quantify them.

Virus release of co-infected cells   For co-infected cells, virus release rates were similar to those of STV-infected cells or slightly higher in case of RT 22 h. In general, little is known about release rates of co-infected cells and even controversial data can be found in literature. For instance, our single-cell model of DIP co-infection suggest that co-infected cells release in total less virus particles than STV-only infected cells (Section 4.2, [309]). In addition, some experimental and modeling studies for IAV [123, 309, 355] and VSV [371] convey that the total virus output of a co-infected cell depends on the infecting DIP-to-STV ratio. As we have seen in our study, the DIP-to-STV ratio spans multiple orders of magnitude during the run (Figure 4.26). Our co-infection model does, however, not account for the infecting DIP-to-STV ratio but assumes that a single DIP is sufficient to cause interference and, thus, to cause a complete suppression of the STV production in a co-infected cells. This single-hit mechanism was assumed before by Frensing and Heldt *et al.* [14] as well as in other modeling studies by Kirkwood and Bangham [315, 382] and others [383]. In addition, we have indications from both our single-cell model (Section 4.2, [309]) and experiments by Nayak and colleagues [363] that DIPs cannot interfere anymore in case STV replication is already well advanced. The delS1(1) model, as well as the Frensing-and-Heldt model [14] do, however, not account for this effect. To account for both, the infecting DIP-to-STV ratio as well as the limited time window for DIP interference, a multi-scale model with cell age-segregation is required. Such model is currently under development based on previous works by our group on IAV replication [37, 278]. However, preliminary investigations have shown that despite the increased model complexity and numerical cost, no significant improvement was achieved in describing the experimental data (unpublished). We may hypothesize that, due to the well-mixed conditions and the constantly high virus concentrations in the virus bioreactors, the distribution of the co-infection timing is narrow. Thus, on average, we can assume that cells are co-infected simultaneously such that the simple within-host

model is sufficient to describe virus dynamics in such cultivation system. Instead, when describing co-infection in experimental scenarios where less virions are present, mixing might be a limiting factor and broader distributions of co-infection timing can occur. Accordingly, the use of more complex multi-scale approaches might be beneficial.

Relevance of two separate infection rates   Most surprisingly, we had to assume that DIPs and STVs infect cells at different specific rates. In general, the parameter estimates for the infection rates agree with previous findings [14, 254] and are supported by relatively high local sensitivities (Figure 4.27). In case only one joint infection rate was used in the model, we were not able to capture the dynamics of the experimental data, neither by prediction (Figure 4.28), nor by repeated model fitting (see original publication [314]). This seems counter-intuitive since both particle species are antigenically identical and, therefore, we do not expect distinct virus entry kinetics. However, the finding that the DIP infection rate is three orders of magnitude lower than the STV infection rate might also be a modeling artifact related to mass action kinetics. Since the number of DIPs in the system is, on average, three orders of magnitude higher than the STV numbers, the model estimates a lower DIP infection rate to yield a reasonable number of co-infected cells. Likewise, the lower DIP infection rate might be also related to the general infectiousness of DIPs. Certainly, we can determine that FL S1-containing particles are present as infectious and non-infectious forms, i.e., as STVs and NIPs, respectively. Thus, very likely, also DIPs form non-infectious viral sub-populations. In case the fraction of infectious DIPs is as small as the fraction of STVs of the FL S1-containing particles, the specific DIP infection rate of the model would be in the order of 10^{-8} ml/(virion · h), which is equivalent to the STV infection rate in the RT 36 h cultivation. However, to elucidate this even further, assays have to be performed that allow to relate the DI RNA measurements of virus preparation to their infectivity, i.e., their interfering potential, which can be assessed by yield reduction assays, such as the Bellett and Cooper assay [364].

DIP-to-STV ratio in cell culture and antiviral treatment   In our study we found that DIPs accumulate in the system until a critical DIP-to-STV ratio of 10^5 is achieved. We hypothesized that when this ratio is reached, cells are overloaded by DIPs which eventually interfere with their own replication. Please note, that this DIP-to-STV ratio is based on DI RNA qPCR measurements, taking into account also the non-infectious DIP population. Thus, the DIP-to-STV ratio based on fully infectious particles is probably lower. The DIP-to-STV ratio is not only a characteristic value in cell culture but also an essential key parameter in trials evaluating DIPs as antiviral agent. Interestingly, Dimmock and Easton found that mice challenged with different mixtures of DIPs and STVs of an influenza A/WSN strain showed only a mild disease and rapid recovery in case they were infected

at a DIP-to-STV ratio of 10^3, and full protection with no signs of illness at ratios of 10^4 and 10^5 [136]. Thus, at those ratios DIPs were able to replicate and interfere successfully with STV replication in the lung when both viruses were administered simultaneously.

Summary The presence of DIPs poses a major challenge to continuous production of influenza vaccines. Using mathematical models of within-host dynamics we have elucidated strategies to reduce DIP accumulation in such systems. However, the experimental implementation of these approaches is either not suitable or, yet, too complex while regulatory issues with respect to genetic stability of the virus are still the most significant concern. Nonetheless, the two-stage bioreactor system has served well in studying DIP propagation under controlled conditions over extended periods of time, which might also support future studies evaluating *de novo* generation of DIPs and other aspects of virus evolution. While for a long time DIPs were seen as an unwanted byproduct of virus replication, the option to produce DIPs as antiviral can be realized well in continuous cultivations. However, since infectious STVs are contaminating the antiviral DIPs, they have to be inactivated, e.g. by UV irradiation, to supply safe clinical-grade material. Recently, a transcomplementing MDCK cell line was developed that allows to produce DIPs in the absence of infectious STVs [153–155]. Together with appropriate assaying procedures for DIP quantification, pure DIP preparations allow to control important infection parameters in clinical trials, such as the DIP-to-STV ratio.

CHAPTER 5

Conclusions

In this thesis, mathematical models of IAV growth were employed to explore options to overcome bottlenecks in virus replication at the intracellular and the cell population level to improve cell culture-based virus production. To achieve this goal, we focused on investigating the impact of two inevitable constraints of virus growth: host cell factors and DIPs.

Impact of selected host cell factors on virus growth   With the aim to increase virus yields in influenza vaccine production, we applied a single-cell model of IAV replication to suggest targets for cell line engineering. For this, we performed parameter perturbation studies assuming that particular steps of the viral life cycle can be directly manipulated by changing the expression level of a putative host cell factor. As a result, we found that steps of viral RNA synthesis, their regulation, and particle assembly and virus budding would be promising steps to be targeted by cell line engineering. The importance of those steps was confirmed when we analyzed intracellular measurements of virus growth obtained from infected cell lines overexpressing selected host cell genes. However, modeling results suggested that those genetic modifications had a negative impact on RNA synthesis rates. As a result, engineered cell lines only released similar or slightly higher numbers of progeny virions compared to the parental cell line. According to our parameter estimates, this was only possible by an increase in the virus release rate, which rescued viral titers. Furthermore, we presented a simulation approach that allowed to predict the production phenotype of cell lines with multiple gene modifications, which were validated qualitatively in experiments. However, an increase in cell-specific virus yield by less than two-fold is not expected to benefit vaccine production. Nonetheless, those research efforts highlight that it is not immediately possible to manipulate virus replication mechanisms via genetic engineering of the host cell. In particular, the intracellular concentration of viral genomes (vRNA) seemed robust in response to host cell manipulation, even though changes in cRNA and mRNA levels were observed. Thus, overarching mechanisms might regulate the maximal possible number of vRNAs, and, thus, the maximum number of released virions. For now, it remains elusive whether those control mechanisms are governed by the viral or the cellular system, or both. While we and others have struggled in optimizing vaccine production by cell line engineering, we have shown that detailed mathematical models of the intracellular viral life cycle are indispensable for the evaluation

and meaningful interpretation of infection data from engineered cell lines.

Intracellular DIP replication   Since DIPs have a negative impact on virus production, we aimed to gain a deeper understanding of the mechanisms by which they interfere with virus replication. For this, we investigated three hypotheses on the mode of DI RNA interference. According to literature, it is assumed that DI RNAs are able to out-compete their FL counterparts at the cellular level by either an advantage in RNA synthesis, regulation of RNA replication or during progeny vRNP packaging into budding particles. To account for those, we implemented a length-dependent factor for DI RNAs at the corresponding steps into the intracellular IAV model. Analysis of simulated co-infections suggests, that DI RNAs which exert an advantage in RNA synthesis are most successful in hampering virus growth. They rapidly deplete the pool of viral resources and even limit their own growth through self-interference when too many DIPs infect a cell or their strength of interference is too high. In contrast, DI RNAs with an advantage in regulation of RNA replication act less parasitic and release high numbers of DIP progeny during the majority of the tested scenarios, while a basal level of STV release is still guaranteed. This tendency was also observed for DI RNAs with an advantage in vRNP packaging, however, overall fewer of those DIP progeny were released. We also tested the different modes of interference in case that DI RNAs originate from different parental segments. Interestingly, the qualitative behavior of different DI RNAs with respect to strength of interference and co-infection timing was independent of the mode of interference. For instance, DI RNAs originating from segments essential for viral RNA synthesis have an additional growth advantage when STV infection is delayed. This was particularly evident for DI RNAs derived from polymerase-encoding genes, which may provide an explanation as to why they are the most abundant DI RNAs found in virus preparations. In contrast, for some IAV genome segments, there are only a few or even no deleted RNA sequences reported in literature, such as for segment 7 which encodes M1 and M2. Modeling suggests that deletion mutants of segment 7 are less competitive in certain infection scenarios due to the important role of M1 in the regulation of the viral life cycle and as a structural component of virus particles. Yet, recent experiments showed that a hyper-mutated DI RNA of segment 7 can strongly interfere with virus growth. Thus, to reveal how mutated DI RNAs can overcome the drawbacks of deleted DI RNAs will be an interesting question for future studies.

According to our detailed *in silico* investigations on different DI RNAs, we characterized those that interfere most successfully with virus growth as well as those that probably go unseen in experiments due to their negligible impact on virus yields. Furthermore, our results represent a road map that can be used to discriminate DIPs with different

modes of interference by analyzing their impact on intracellular concentrations of viral components and on virus yields under controlled infection conditions.

DIP growth during continuous cultivation During continuous production of IAV, DIPs cause periodic drops in viral titers leading to losses in productivity. Using a simple within-host model of DIP co-infection, we predicted that oscillations can be avoided by running the process at a short residence time. Although this process mode resulted in a reduced DIP accumulation, it was also characterized by a significant decrease in productivity. Hence, manipulating the process mode is an economically unfeasible strategy to diminish DIP-mediated interference. Nonetheless, analyzing the impact of perturbations on complex systems can lead to valuable mechanistic insights. Thus, we performed further continuous IAV cultivations at defined residence times. Based on experimental observations, we derived an augmented within-host model of DIP co-infection that allowed to reproduce the measurement data. Most importantly, the frequency of oscillations is reduced for the longer of the two residence times, which was also clearly evident in model fits. According to parameter estimates, co-infected cells exclusively release DIPs, which is well in agreement to our findings obtained with the single-cell DIP model that accounts for an advantage in RNA replication. In contrast, we had to implement DIP- and STV-specific infection rates to describe the data reasonably well. Thus, the combination of studying DIP propagation under controlled experimental conditions over extended periods of time allows to define new hypothesis on cell-to-cell spread of DIPs and STVs that can be addressed in future experiments.

Summary Using several mathematical models of IAV replication, we analyzed virus dynamics with the aim to improve our understanding of how selected host cell factors and DIPs influence the production of virus-based biopharmaceuticals. In that context, the application of single-cell models allowed to (i) evaluate the suitability of cell line engineering for improved vaccine production and (ii) to discriminate hypotheses on possible mechanism by which DIPs interfere with virus replication. Furthermore, within-host models that describe virus production in the presence of DIPs uncovered new features of DIP co-infection that have not been reported before. Together, modeling played an important role in data analysis and interpretation as well as in proposing new research avenues that can be followed-up in the future with the help of well-informed models such as presented in this thesis.

Chapter 6

Outlook

Using various modeling and simulation approaches, this thesis allowed detailed insights into IAV growth kinetics in cell culture under the influence of selected host cell factors and DIPs. Those investigations have not only contributed to an improved quantitative understanding of IAV dynamics, but also uncovered significant challenges, yet to be addressed in future studies.

To further improve the description of virus-host cell interactions, future models may account more explicitly for the function of specific host cell factors and the dynamics of their intracellular expression levels. However, due to the limited effects of host cell factors investigated in this study, further investigations on those is unreasonable. One option to identify more relevant factors is the bioinformatical re-evaluation of host cell factor screenings, which recently lead to the identification and validation of IAV-host cell factors that were unnoticed before. For instance, UBR4 is an interaction partner of the viral protein M2 [346] that is important for membrane bending during budding of progeny particles. Without UBR4, M2 is degraded in specific cellular compartments, such that virus release is blocked. To transfer such findings from virus-host cell interaction maps to a kinetic model, which provides the underlying dynamic and mechanistic principles, calls for new modeling and computational approaches. Thus, the classical systems biology cycle has to be extended to combine bioinformatical tools for the analysis of high-throughput screens and mathematical models that describe virus dynamics data to draw a clearer picture of specific virus-host cell interactions. While more and more data and mechanistic knowledge of virus replication become available, artificial intelligence methods will play an increasingly important role in such research studies [208, 210]. Besides the optimization of the bioinformatical analysis, we have also discussed that the screening approaches themselves have to be re-taylored to account for parameters relevant in vaccine production. This re-tayloring should include the adaptation of initial infection conditions and a frequent sampling up to the time point of harvest when the maximum number of viral progeny is released.

With respect to different modes of DI RNA interference, our *in silico* studies gave detailed insights into DIP replication mechanisms and allowed to derive novel explanations for historic experimental findings. However, we still struggle to find a coherent modeling frame work able to reproduce all quantitative and qualitative features together. Thus,

additional mechanisms potentially relevant for DIP growth should be investigated that might be also included in future models. For instance, it has been shown that DI polypeptides can influence the host response to infection [36], and, thus, may also affect virus replication. Accordingly, it should be scrutinized whether candidate DI RNAs form translation-competent transcripts, i.e., DI mRNAs. In addition, the translation of highly abundant DI mRNAs can further impact overall virus growth by competing for components of the biosynthetic machinery of the cell. In case this cannot be ruled out, a more comprehensive sub-model of DI and FL mRNA synthesis and translation should be included, provided that experimental measurements allow to discriminate and quantify the corresponding proteins. Furthermore, we discussed the impact of specific sequence elements retained in DI RNAs and the potential impact of the DI vRNP's secondary structure that could impact their interfering potential. For instance, it is known that certain sequence elements are responsible for polymerase-binding or for the successful packaging of vRNPs into progeny particles. To incorporate such knowlegde, our intracellular model would have to be extended to allow a genotype-phenotype prediction for such DI RNA features. However, given that various DI RNAs are usually present in authentic virus samples, it can be computationally costly to account for each one of them individually. Nonetheless, such an approach could also help to reveal characteristics inherent to the different DI RNA sequences and might provide insights into biological principles related to their *de novo* generation. Furthermore, we have shown both on the intracellular and on the within-host level that self-interference is a characteristic of potent antiviral candidates. While we cannot immediately predict DIP co-infection at the tissue level of the lung, there are at least indications that the DIP-to-STV ratio needed to clear infections is similar to that of an animal model. Whether this also holds true for infected humans is yet to be clarified.

Our investigations have shown that the analysis of host cell screens is not mature enough yet to derive robust knowledge on virus-host cell interactions that support increased cell-specific virus yields. Still, it seems tempting to ask if certain host cell factors could potentially support or hamper DI RNA synthesis. With that, DI RNA synthesis could be kept at levels that might allow the continuous production of IAV in steady state. Likewise, approaches that aim to produce DIPs as antiviral could also benefit from such knowledge by avoiding the emergence of unwanted DI RNA sub-populations and guarantee the manufacturing of homogeneous DIP preparations for (pre)-clinical trials. Another link between host cell factors and DIPs might be represented by resource limitations. For instance, it has been shown that some deletion mutants of bacteriophages show strong interference in resource-rich environments, but interfere to a lesser extent in resource-poor scenarios [209]. While standard cell culture media are optimized to support maximal

growth performance of producer cells, a future question could be whether cell culture media can be fine-tuned to manipulate emergence and growth of DIPs during virus production. Here, modeling can also help to link and predict media composition with respect to changes in DIP replication. Please note, that we focused our modeling efforts on *in vitro* systems with a resource-rich environment and saturated infection conditions. Likewise, the role of the immune system as well as of stochastic effects during virus replication have been neglected. Both can be highly important in a real-world scenario where, for instance, the antiviral response of certain producer cell lines may further inhibit virus growth, or DIP-induced changes in virus replication affect viral clearance by the host immune system. Furthermore, stochastic effects may influence the emergence of dominant DI RNAs when potentially competitive *de novo* DI RNAs are spontaneously degraded early during infection. To account for such competition of DI RNAs, the usage of population balance or multi-scale approaches is required since this cannot be described reasonably by simple within-host models. Competition of different types of DIPs might be also addressed by the presented two-stage bioreactor setup. Hence, in the future, multi-scale DIP models for continuous production of IAV are relevant for both bioprocess engineering as well as for fundamental infection research.

Thus, mathematical modeling has been and will be playing a vital part in the fight against infectious diseases, such as influenza, that pose an ongoing socio-economic threat to our societies. Since progress made in virus dynamics modeling applied to one disease has been shown to be greatly translatable to another, every new insight on influenza infections will be valuable for our preparedness in counteracting the next viral pandemic.

List of Figures

List of Tables

List of Publications

Parts of the following publications and supervised theses were included in this work.

Publications

Duvigneau S*, Dürr R*, **Laske T***, Bachmann M, Dostert M, Kienle A (2020) Model-based approach for predicting the impact of genetic modifications on product yield in biopharmaceutical manufacturing — Application to influenza vaccine production. PLoS Comput Biol 16 (6): e1007810.

Contribution: conceptualization, data curation, formal analysis, investigation, methodology, software, validation, visualization, writing (review, editing, proofs)

Laske T*, Bachmann M*, Dostert M, Karlas A, Wirth D, Frensing T, Meyer TF, Hauser H, Reichl U (2019) Model-based analysis of influenza A virus replication in genetically engineered cell lines elucidates the impact of host cell factors on key kinetic parameters of virus growth. PLoS Comput Biol 15 (4): e1006944.

Contribution: conceptualization, data curation, formal analysis, investigation, methodology, software, validation, visualization, writing (original draft, review, editing, proofs)

Rüdiger D*, Kupke SY, **Laske T**, Zmora P, Reichl U (2019) Multiscale modeling of influenza A virus replication in cell cultures predicts infection dynamics for highly different infection conditions. PLoS Comput Biol 15 (2): e1006819.

Contribution: formal analysis, writing (review, editing)

Tapia F*, **Laske T***, Wasik MA, Rammhold M, Genzel Y, Reichl U (2019) Production of defective interfering particles of influenza A virus in parallel continuous cultures at two residence times — Insights from qPCR measurements and viral dynamics modeling. Front Bioeng Biotechnol 7: 275.

Contribution: conceptualization, data curation, formal analysis, investigation, methodology, software, validation, visualization, writing (original draft, review, editing, proofs)

Laske T*, Heldt FS*, Hoffmann H, Frensing T, Reichl U (2016) Reprint of "Modeling the intracellular replication of influenza A virus in the presence of defective interfering RNAs". Virus Res 218: 86–95.

Contribution: conceptualization, data curation, formal analysis, investigation, methodology, software, validation, visualization, writing (original draft, review, editing, proofs)

Conference paper

Duvigneau S*, Dürr R, **Laske T**, Bachmann M, Dostert M, Reichl U, Kienle A (2018) Mathematical modeling as a tool to improve influenza vaccine production processes. Foundations of Systems Biology in Engineering (FOSBE), Chicago, Illinois, USA, August 05–08, 2018. IFAC-PapersOnLine 51 (19): 1–4.

Contribution: conceptualization, data curation, formal analysis, investigation, methodology, software, validation, writing (review, editing, proofs)

Dürr R*, Duvigneau S, **Laske T**, Bachmann M, Kienle A (2016) Analyzing the impact of heterogeneity in genetically engineered cell lines for influenza vaccine production using population balance modeling. Foundations of Systems Biology in Engineering (FOSBE), Magdeburg, Germany, October 09–12, 2016. IFAC-PapersOnLine 49 (26): 225–230.

Contribution: conceptualization, writing (review, editing, proofs)

*first author

Supervised theses

Geilert B (2015) Stochastische Multiskalen-Modellierung der Replikation von Influenzaviren während der Impfstoffproduktion. Bachelor thesis, Faculty of Process and Systems Engineering, Otto von Guericke University, Magdeburg.

Rammhold M (2017) Model-based optimization of continuous influenza vaccine production processes. Master thesis, Faculty of Process and Systems Engineering, Otto von Guericke University, Magdeburg.

Nortmann L (2020) Modeling de novo generation of defective interfering RNAs during influenza A virus replication. Master thesis, Faculty of Process and Systems Engineering, Otto von Guericke University, Magdeburg.

Talks

Laske T, Tapia F, Wasik M, Rammhold M, Genzel Y, Reichl U (2019) Production of defective interfering particles of influenza A virus in continuously cultured bioreactors at two residence times — insights from within-host virus dynamics. 4th Workshop on Virus Dynamics, Paris, France, October 21–23, 2019.

Rüdiger D, **Laske T**, Kupke SY, Reichl U (2019) Multiscale model of DIP interference and production during influenza A virus infection in animal cell culture. 4th Workshop on Virus Dynamics, Paris, France, October 21–23, 2019.

Laske T, Bernhauerová V, Carruthers J, Molina-París C, Liao LE (2018) Parameter estimation from oscillating experimental data using approximate Bayesian computation. Hackathon at DARPA INTERCEPT Review Meeting, New York City, New York, USA, October 15–17, 2018.

Dürr R, Duvigneau S, **Laske T**, Bachmann M, Dostert M, Reichl U, Kienle A (2018) Mathematical modeling as a tool to improve influenza vaccine production processes. Foundations of Systems Biology in Engineering (FOSBE), Chicago, Illinois, USA, August 05–08, 2018.

Laske T, Bachmann M, Dostert M, Karlas A, Wirth D, Frensing T, Reichl U (2017) Model-based characterization of influenza A virus production in genetically engineered cell lines elucidates changes in virus replication. 3rd Workshop on Virus Dynamics, Heidelberg, Germany, October 6–7, 2017.

Laske T, Bachmann M, Frensing T, Reichl U (2016) Model-based analysis of influenza A virus replication in genetically modified cell lines elucidates virus-host cell interactions. 1st European Society for Animal Cell Technology (ESACT) Frontiers Retreat, Lyon, France, October 20–22, 2016.

Laske T, Heldt FS, Frensing T, Reichl U (2015) Analyzing the dynamics of influenza A virus replication in the presence of defective interfering RNAs. 2nd Workshop on Virus Dynamics, Toronto, Ontario, Canada, July 17–18, 2015.

Laske T, Heldt FS, Frensing T, Reichl U (2014) Mathematical modeling of virus-host cell interactions during influenza virus replication supports cell line development for vaccine production. Workshop on Virus Dynamics and Evolution at *Centre De Recerca Matemàtica* (CRM), Bellaterra, Spain, June 30–July 4, 2014.

Posters

Rüdiger D, **Laske T**, Kupke SY, Reichl U (2019) A multiscale model of defective interfering particle replication. Foundations of Systems Biology in Engineering (FOSBE), Valencia, Spain, October 15–18, 2019.

Laske T, Bachmann M, Dostert M, Frensing T, Karlas A, Wirth D, Reichl U (2018) Modeling reveals changes in key parameters of influenza A virus replication in engineered cell lines. 11th Annual International Conference on Systems Biology of Human Diseases (SBHD), Los Angeles, USA, June 04-06, 2018.

Dürr R, Duvigneau S, **Laske T**, Bachmann M, Kienle A (2016) Analyzing the impact of heterogeneity in genetically engineered cell lines for influenza vaccine production using population balance modeling. 6th IFAC Conference on Foundations of Systems Biology in Engineering (FOSBE), Magdeburg, Germany, October 09–12, 2016.

Laske T, Bachmann M, Frensing T, Reichl U (2016) Model-based analysis of influenza A virus replication in genetically modified cell lines elucidates virus-host cell interactions. 17th International Conference on Systems Biology (ICSB), Barcelona, Spain, September 16–20, 2016.

Laske T, Heldt FS, Hoffmann H, Frensing T, Reichl U (2016) Modeling the intracellular replication of influenza A virus in the presence of defective interfering RNAs. 26th Annual Meeting of the Society for Virology, Münster, Germany, April 06–09, 2016.

Laske T, Heldt FS, Frensing T, Reichl U (2015) Analyzing the intracellular replication of influenza A virus in the presence of defective interfering RNAs. International Conference on Systems Biology of Human Disease (SBHD), Heidelberg, Germany, July 06–08, 2015.

Laske T, Heldt FS, Frensing T, Reichl U (2014) Mathematical modeling of virus-host cell interactions during influenza A virus replication supports cell line development for vaccine production. 4th International Influenza Meeting, Münster, Germany, September 21-23, 2014.

Bibliography

1. World Health Organization (2021). Influenza update - No. 390. online. URL `https://www.who.int/influenza/surveillance_monitoring/updates/latest_update_GIP_surveillance/en/`. Accessed April 01, 2021.

2. Iuliano AD, Roguski KM, Chang HH, Muscatello DJ, Palekar R, et al. (2018) Estimates of global seasonal influenza-associated respiratory mortality: a modelling study. The Lancet 391: 1285–1300.

3. Krammer F, Smith GJD, Fouchier RAM, Peiris M, Kedzierska K, et al. (2018) Influenza. Nat Rev Dis Primers 4: 3.

4. Wright PF, Neumann G, Kawaoka Y (2013) Orthomyxoviruses. In: Fields BN, Knipe DM, editors, Fields Virology, Philadelphia, PA: Wolters Kluwer Lippincott Williams & Wilkins, chapter 41. 6th edition, pp. 1186–1243.

5. Taubenberger JK, Morens DM (2006) 1918 influenza: the mother of all pandemics. Emerg Infect Dis 12: 15–22.

6. LePan N (2021). Visualizing the history of pandemics. online. URL `https://www.visualcapitalist.com/history-of-pandemics-deadliest/`. Accessed April 01, 2021.

7. Potter CW (2001) A history of influenza. J Appl Microbiol 91: 572–579.

8. Watanabe T, Watanabe S, Kawaoka Y (2010) Cellular networks involved in the influenza virus life cycle. Cell Host Microbe 7: 427–439.

9. Shaw ML, Stertz S (2017) Role of host genes in influenza virus replication. In: Tripp RA, Tompkins SM, editors, Roles of Host Gene and Non-coding RNA Expression in Virus Infection, Springer International Publishing, volume 419 of *Current Topics in Microbiology and Immunology*. pp. 151–189.

10. Shaw ML (2011) The host interactome of influenza virus presents new potential targets for antiviral drugs. Rev Med Virol 21: 358–369.

11. Sidorenko Y, Reichl U (2004) Structured model of influenza virus replication in MDCK cells. Biotechnol Bioeng 88: 1–14.

12. Frensing T, Kupke SY, Bachmann M, Fritzsche S, Gallo-Ramirez LE, et al. (2016) Influenza virus intracellular replication dynamics, release kinetics, and particle morphology during propagation in MDCK cells. Appl Microbiol Biotechnol 100: 7181–7192.

13. Frensing T (2015) Defective interfering viruses and their impact on vaccines and viral vectors. Biotechnol J 10: 681-689.

14. Frensing T, Heldt FS, Pflugmacher A, Behrendt I, Jordan I, et al. (2013) Continuous influenza virus production in cell culture shows a periodic accumulation of defective interfering particles. PLoS One 8: e72288.

15. Dimmock NJ, Easton AJ (2014) Defective interfering influenza virus RNAs: Time to reevaluate their clinical potential as broad-spectrum antivirals? J Virol 88: 5217–5227.

16. Beauchemin CAA, Handel A (2011) A review of mathematical models of influenza A infections within a host or cell culture: lessons learned and challenges ahead. BMC Public Health 11 Suppl 1: S7.

17. Murillo LN, Murillo MS, Perelson AS (2013) Towards multiscale modeling of influenza infection. J Theor Biol 332: 267–290.

18. Heldt FS, Frensing T, Reichl U (2012) Modeling the intracellular dynamics of influenza virus replication to understand the control of viral RNA synthesis. J Virol 86: 7806–7817.

19. Shaw ML, Palese P (2013) Orthomyxoviridae. In: Fields BN, Knipe DM, editors, Fields Virology, Philadelphia, PA: Wolters Kluwer Lippincott Williams & Wilkins, volume I, chapter 40. 6th edition, pp. 1151–1185.

20. Dou D, Revol R, Östbye H, Wang H, Daniels R (2018) Influenza A virus cell entry, replication, virion assembly and movement. Front Immunol 9: 1581.

21. Badham MD, Rossman JS (2016) Filamentous influenza viruses. Current Clinical Microbiology Reports 3: 155–161.

22. Dadonaite B, Vijayakrishnan S, Fodor E, Bhella D, Hutchinson EC (2016) Filamentous influenza viruses. J Gen Virol 97: 1755–1764.

23. Fodor E (2013) The RNA polymerase of influenza A virus: mechanisms of viral transcription and replication. Acta Virol 57: 113–122.

24. Hutchinson EC, Fodor E (2013) Transport of the influenza virus genome from nucleus to nucleus. Viruses 5: 2424–2446.

25. Fodor E, te Velthuis AJW (2019) Structure and function of the influenza virus transcription and replication machinery. Cold Spring Harbor Perspectives in Medicine 10: a038398.

26. Heldt FS (2015) Mathematical Models of Influenza A Virus Infection: From Intracellular Replication to Virus Growth in Cell Populations. Ph.D. thesis, Faculty of Process and Systems Engineering, Otto von Guericke University Magdeburg.

27. Noda T, Sagara H, Yen A, Takada A, Kida H, et al. (2006) Architecture of ribonucleoprotein complexes in influenza A virus particles. Nature 439: 490–492.

28. Noda T, Murakami S, Nakatsu S, Imai H, Muramoto Y, et al. (2018) Importance of the 1+7 configuration of ribonucleoprotein complexes for influenza A virus genome packaging. Nat Commun 9: 54.

29. Nakatsu S, Murakami S, Shindo K, Horimoto T, Sagara H, et al. (2018) Influenza C and D viruses package eight organized ribonucleoprotein complexes. J Virol 92.

30. Lamb RA, Krug RM (2001) Orthomyxoviridae: the viruses and their replication. In: Knipe DM, Howley PM, editors, Fields Virology, Lippincott Williams & Wilkins. 4th edition, pp. 1487–1531.

31. Vasin AV, Temkina OA, Egorov VV, Klotchenko SA, Plotnikova MA, et al. (2014) Molecular mechanisms enhancing the proteome of influenza A viruses: an overview of recently discovered proteins. Virus Res 185: 53–63.

32. Dawson WK, Lazniewski M, Plewczynski D (2017) RNA structure interactions and ribonucleoprotein processes of the influenza A virus. Briefings in Functional Genomics 17: 402–414.

33. Killip MJ, Fodor E, Randall RE (2015) Influenza virus activation of the interferon system. Virus Res 209: 11–22.

34. Chen X, Liu S, Goraya MU, Maarouf M, Huang S, et al. (2018) Host immune response to influenza A virus infection. Front Immunol 9.

35. Klemm C, Boergeling Y, Ludwig S, Ehrhardt C (2018) Immunomodulatory nonstructural proteins of influenza A viruses. Trends Microbiol 26: 624–636.

36. Boergeling Y, Rozhdestvensky TS, Schmolke M, Resa-Infante P, Robeck T, et al. (2015) Evidence for a novel mechanism of influenza virus-induced type I interferon expression by a defective RNA-encoded protein. PLoS Pathog 11: e1004924.

37. Heldt FS, Frensing T, Pflugmacher A, Gröpler R, Peschel B, et al. (2013) Multiscale modeling of influenza A virus infection supports the development of direct-acting antivirals. PLoS Comput Biol 9: e1003372.

38. Luo M (2012) Influenza virus entry. In: Rossmann MG, Rao VB, editors, Viral Molecular Machines, Boston, MA: Springer US. pp. 201–221.

39. Edinger TO, Pohl MO, Stertz S (2014) Entry of influenza A virus: host factors and antiviral targets. J Gen Virol 95: 263–277.

40. Lamb RA (2020) The structure, function, and pathobiology of the influenza A and B virus ion channels. Cold Spring Harbor Perspectives in Medicine 10: a038505.

41. Yamauchi Y (2020) Chapter one - Influenza A virus uncoating. In: Kielian M, Mettenleiter TC, Roossinck MJ, editors, Advances in Virus Research, Academic Press, volume 106. pp. 1–38.

42. Chou YY, Heaton NS, Gao Q, Palese P, Singer RH, et al. (2013) Colocalization of different influenza viral RNA segments in the cytoplasm before viral budding as shown by single-molecule sensitivity FISH analysis. PLoS Pathog 9: e1003358.

43. Eisfeld AJ, Neumann G, Kawaoka Y (2014) At the centre: influenza A virus ribonucleoproteins. Nat Rev Microbiol 13: 28–41.

44. Cros JF, Palese P (2003) Trafficking of viral genomic RNA into and out of the nucleus: influenza, thogoto and borna disease viruses. Virus Res 95: 3–12.

45. Boulo S, Akarsu H, Ruigrok RWH, Baudin F (2007) Nuclear traffic of influenza virus proteins and ribonucleoprotein complexes. Virus Res 124: 12–21.

46. Hutchinson EC, Fodor E (2012) Nuclear import of the influenza A virus transcriptional machinery. Vaccine 30: 7353–7358.

47. O'Neill RE, Jaskunas R, Blobel G, Palese P, Moroianu J (1995) Nuclear import of influenza virus RNA can be mediated by viral nucleoprotein and transport factors required for protein import. J Biol Chem 270: 22701–22704.

48. Cros JF, García-Sastre A, Palese P (2005) An unconventional NLS is critical for the nuclear import of the influenza a virus nucleoprotein and ribonucleoprotein. Traffic 6: 205–213.

49. Bui M, Whittaker G, Helenius A (1996) Effect of M1 protein and low pH on nuclear transport of influenza virus ribonucleoproteins. J Virol 70: 8391–8401.

50. Martin K, Helenius A (1991) Nuclear transport of influenza virus ribonucleoproteins: the viral matrix protein (M1) promotes export and inhibits import. Cell 67: 117–130.

51. Whittaker G, Bui M, Helenius A (1996) Nuclear trafficking of influenza virus ribonuleoproteins in heterokaryons. J Virol 70: 2743–2756.

52. Martin K, Helenius A (1991) Transport of incoming influenza virus nucleocapsids into the nucleus. J Virol 65: 232–244.

53. Jorba N, Coloma R, Ortín J (2009) Genetic trans-complementation establishes a new model for influenza virus RNA transcription and replication. PLoS Pathog 5: e1000462.

54. York A, Fodor E (2013) Biogenesis, assembly, and export of viral messenger ribonucleoproteins in the influenza A virus infected cell. RNA Biol 10: 1274–1282.

55. Yángüez E, Nieto A (2011) So similar, yet so different: selective translation of capped and polyadenylated viral mRNAs in the influenza virus infected cell. Virus Res 156: 1–12.

56. Resa-Infante P, Jorba N, Coloma R, Ortín J (2011) The influenza virus RNA synthesis machine: Advances in its structure and function. RNA Biol 8: 207-215.

57. Portela A, Digard P (2002) The influenza virus nucleoprotein: a multifunctional RNA-binding protein pivotal to virus replication. J Gen Virol 83: 723–734.

58. Vreede FT, Jung TE, Brownlee GG (2004) Model suggesting that replication of influenza virus is regulated by stabilization of replicative intermediates. J Virol 78: 9568–9572.

59. Vreede FT, Brownlee GG (2007) Influenza virion-derived viral ribonucleoproteins synthesize both mRNA and cRNA in vitro. J Virol 81: 2196–2204.

60. Moeller A, Kirchdoerfer RN, Potter CS, Carragher B, Wilson IA (2012) Organization of the influenza virus replication machinery. Science 338: 1631–1634.

61. Kawaguchi A, Nagata K (2007) De novo replication of the influenza virus RNA genome is regulated by DNA replicative helicase, MCM. EMBO J 26: 4566–4575.

62. Kawaguchi A, Momose F, Nagata K (2011) Replication-coupled and host factor-mediated encapsidation of the influenza virus genome by viral nucleoprotein. J Virol 85: 6197-6204.

63. Bullido R, Gómez-Puertas P, Saiz MJ, Portela A (2001) Influenza A virus NEP (NS2 protein) downregulates RNA synthesis of model template RNAs. J Virol 75: 4912–4917.

64. Robb NC, Smith M, Vreede FT, Fodor E (2009) NS2/NEP protein regulates transcription and replication of the influenza virus RNA genome. J Gen Virol 90: 1398–1407.

65. Paterson D, Fodor E (2012) Emerging roles for the influenza A virus nuclear export protein (NEP). PLoS Pathog 8: e1003019.

66. Reuther P, Giese S, Götz V, Kilb N, Mänz B, et al. (2014) Adaptive mutations in the nuclear export protein of human-derived H5N1 strains facilitate a polymerase activity-enhancing conformation. J Virol 88: 263–271.

67. Perez JT, Varble A, Sachidanandam R, Zlatev I, Manoharan M, et al. (2010) Influenza A virus-generated small RNAs regulate the switch from transcription to replication. Proc Natl Acad Sci U S A 107: 11525–11530.

68. Perez JT, Zlatev I, Aggarwal S, Subramanian S, Sachidanandam R, et al. (2012) A small-RNA enhancer of viral polymerase activity. J Virol 86: 13475–13485.

69. Neumann G, Hughes MT, Kawaoka Y (2000) Influenza A virus NS2 protein mediates vRNP nuclear export through NES-independent interaction with hCRM1. EMBO J 19: 6751–6758.

70. Akarsu H, Burmeister WP, Petosa C, Petit I, Müller CW, et al. (2003) Crystal structure of the M1 protein-binding domain of the influenza A virus nuclear export protein (NEP/NS2). EMBO J 22: 4646–4655.

71. Zvonarjev AY, Ghendon YZ (1980) Influence of membrane (M) protein on influenza A virus virion transcriptase activity in vitro and its susceptibility to rimantadine. J Virol 33: 583–586.

72. Hankins RW, Nagata K, Kato A, Ishihama A (1990) Mechanism of influenza virus transcription inhibition by matrix (M1) protein. Res Virol 141: 305–314.

73. Watanabe K, Handa H, Mizumoto K, Nagata K (1996) Mechanism for inhibition of influenza virus RNA polymerase activity by matrix protein. J Virol 70: 241–247.

74. Nasser EH, Judd AK, Sanchez A, Anastasiou D, Bucher DJ (1996) Antiviral activity of influenza virus M1 zinc finger peptides. J Virol 70: 8639–8644.

75. Perez DR, Donis RO (1998) The matrix 1 protein of influenza A virus inhibits the transcriptase activity of a model influenza reporter genome in vivo. Virology 249: 52–61.

76. Baudin F, Petit I, Weissenhorn W, Ruigrok RW (2001) In vitro dissection of the membrane and RNP binding activities of influenza virus M1 protein. Virology 281: 102–108.

77. Mänz B, Brunotte L, Reuther P, Schwemmle M (2012) Adaptive mutations in NEP compensate for defective H5N1 RNA replication in cultured human cells. Nat Commun 3: 802.

78. Brunotte L, Flies J, Bolte H, Reuther P, Vreede F, et al. (2014) The nuclear export protein of H5N1 Influenza A viruses recruits matrix 1 (M1) protein to the viral ribonucleoprotein to mediate nuclear export. J Biol Chem 289: 20067–20077.

79. Chua MA, Schmid S, Perez JT, Langlois RA, Tenoever BR (2013) Influenza A virus utilizes suboptimal splicing to coordinate the timing of infection. Cell Rep 3: 23–29.

80. Rossman JS, Lamb RA (2011) Influenza virus assembly and budding. Virology 411: 229–236.

81. Gerl MJ, Sampaio JL, Urban S, Kalvodova L, Verbavatz JM, et al. (2012) Quantitative analysis of the lipidomes of the influenza virus envelope and MDCK cell apical membrane. J Cell Biol 196: 213–221.

82. Rossman JS, Lamb RA (2013) Viral membrane scission. Annu Rev Cell Dev Biol 29: 551–569.

83. Eisfeld AJ, Kawakami E, Watanabe T, Neumann G, Kawaoka Y (2011) RAB11A is essential for influenza genome transport to the plasma membrane. J Virol 85: 6117-6126.

84. Hutchinson EC, von Kirchbach JC, Gog JR, Digard P (2010) Genome packaging in influenza A virus. J Gen Virol 91: 313–328.

85. Noda T, Kawaoka Y (2010) Structure of influenza virus ribonucleoprotein complexes and their packaging into virions. Rev Med Virol 20: 380–391.

86. Fournier E, Moules V, Essere B, Paillart JC, Sirbat JD, et al. (2012) A supramolecular assembly formed by influenza A virus genomic RNA segments. Nucleic Acids Res 40: 2197–2209.

87. Fournier E, Moules V, Essere B, Paillart JC, Sirbat JD, et al. (2012) Interaction network linking the human H3N2 influenza A virus genomic RNA segments. Vaccine 30: 7359–7367.

88. Noda T, Sugita Y, Aoyama K, Hirase A, Kawakami E, et al. (2012) Three-dimensional analysis of ribonucleoprotein complexes in influenza A virus. Nat Commun 3: 639.

89. Gavazzi C, Yver M, Isel C, Smyth RP, Rosa-Calatrava M, et al. (2013) A functional sequence-specific interaction between influenza A virus genomic RNA segments. Proc Natl Acad Sci U S A 110: 16604–16609.

90. Goto H, Muramoto Y, Noda T, Kawaoka Y (2013) The genome-packaging signal of the influenza A virus genome comprises a genome incorporation signal and a genome-bundling signal. J Virol 87: 11316–11322.

91. Dadonaite B, Gilbertson B, Knight ML, Trifkovic S, Rockman S, et al. (2019) The structure of the influenza A virus genome. Nat Microbiol 4: 1781–1789.

92. Inagaki A, Goto H, Kakugawa S, Ozawa M, Kawaoka Y (2012) Competitive incorporation of homologous gene segments of influenza A virus into virions. J Virol 86: 10200–10202.

93. Nakatsu S, Sagara H, Sakai-Tagawa Y, Sugaya N, Noda T, et al. (2016) Complete and incomplete genome packaging of Influenza A and B viruses. mBio 7.

94. Carter MJ, Mahy BW (1982) Incomplete avian influenza virus contains a defective non-interfering component. Arch Virol 71: 13–25.

95. Marcus PI, Ngunjiri JM, Sekellick MJ (2009) Dynamics of biologically active subpopulations of influenza virus: plaque-forming, noninfectious cell-killing, and defective interfering particles. J Virol 83: 8122–8130.

96. Lauring AS, Andino R (2010) Quasispecies theory and the behavior of RNA viruses. PLoS Pathog 6: e1001005.

97. Brooke CB (2017) Population diversity and collective interactions during influenza virus infection. J Virol 91.

98. Diefenbacher M, Sun J, Brooke CB (2018) The parts are greater than the whole: the role of semi-infectious particles in influenza A virus biology. Current Opinion in Virology 33: 42–46.

99. Rezelj VV, Levi LI, Vignuzzi M (2018) The defective component of viral populations. Current Opinion in Virology 33: 74–80.

100. Henle W, Henle G (1943) Interference of inactive virus with the propagation of virus of influenza. Science 98: 87–89.

101. von Magnus P (1951) Propagation of the PR8 strain of influenza A virus in chick embryos. II. The formation of incomplete virus following inoculation of large doses of seed virus. Acta Pathol Microbiol Scand 28: 278-293.

102. von Magnus P (1954) Incomplete forms of influenza virus. Adv Virus Res 2: 59–79.

103. Huang AS, Baltimore D (1970) Defective viral particles and viral disease processes. Nature 226: 325–327.

104. Rast LI, Rouzine IM, Rozhnova G, Bishop L, Weinberger AD, et al. (2016) Conflicting selection pressures will constrain viral escape from interfering particles: Principles for designing resistance-proof antivirals. PLoS Comput Biol 12: e1004799.

105. Marriott AC, Dimmock NJ (2010) Defective interfering viruses and their potential as antiviral agents. Rev Med Virol 20: 51–62.

106. Huang AS, Baltimore D (1977) Defective interfering animal viruses. In: Fraenkel-Conrat H, Wagner RR, editors, Comprehensive Virology 10, Boston, MA: Springer US. pp. 73–116.

107. Vignuzzi M, López CB (2019) Defective viral genomes are key drivers of the virus–host interaction. Nat Microbiol 4: 1075–1087.

108. Yang Y, Lyu T, Zhou R, He X, Ye K, et al. (2019) The antiviral and antitumor effects of defective interfering particles/genomes and their mechanisms. Front Microbiol 10.

109. Holland JJ, Villarreal LP (1975) Purification of defective interfering T particles of vesicular stomatitis and rabies viruses generated in vivo in brains of newborn mice. Virology 67: 438–449.

110. Saira K, Lin X, DePasse JV, Halpin R, Twaddle A, et al. (2013) Sequence analysis of in vivo defective interfering-like RNA of influenza a H1N1 pandemic virus. J Virol 87: 8064–8074.

111. Tapia K, Kim WK, Sun Y, Mercado-López X, Dunay E, et al. (2013) Defective viral genomes arising in vivo provide critical danger signals for the triggering of lung antiviral immunity. PLoS Pathog 9: e1003703.

112. Gould PS, Easton AJ, Dimmock NJ (2017) Live attenuated influenza vaccine contains substantial and unexpected amounts of defective viral genomic RNA. Viruses 9: 296.

113. Lazzarini RA, Keene JD, Schubert M (1981) The origins of defective interfering particles of the negative-strand RNA viruses. Cell 26: 145–154.

114. Perrault J (1981) Origin and replication of defective interfering particles. In: Current Topics in Microbiology and Immunology, Springer Berlin Heidelberg. pp. 151–207.

115. Nayak DP, Chambers TM, Akkina RK (1985) Defective-interfering (DI) RNAs of influenza viruses: origin, structure, expression, and interference. Curr Top Microbiol Immunol 114: 103–151.

116. Alnaji FG, Brooke CB (2020) Influenza virus DI particles: Defective interfering or delightfully interesting? PLoS Pathog 16: e1008436.

117. Alnaji FG, Holmes JR, Rendon G, Vera JC, Fields CJ, et al. (2019) Sequencing framework for the sensitive detection and precise mapping of defective interfering particle-associated deletions across influenza A and B viruses. J Virol 93.

118. Genoyer E, López CB (2019) The impact of defective viruses on infection and immunity. Annu Rev Virol 6: 547–566.

119. Akkina RK, Chambers TM, Nayak DP (1984) Expression of defective-interfering influenza virus-specific transcripts and polypeptides in infected cells. J Virol 51: 395–403.

120. Jennings PA, Finch JT, Winter G, Robertson JS (1983) Does the higher order structure of the influenza virus ribonucleoprotein guide sequence rearrangements in influenza viral RNA? Cell 34: 619–627.

121. Frensing T, Pflugmacher A, Bachmann M, Peschel B, Reichl U (2014) Impact of defective interfering particles on virus replication and antiviral host response in cell culture-based influenza vaccine production. Appl Microbiol Biotechnol 98: 8999–9008.

122. Davis AR, Nayak DP (1979) Sequence relationships among defective interfering influenza viral RNAs. Proc Natl Acad Sci U S A 76: 3092–3096.

123. Kupke SY, Riedel D, Frensing T, Zmora P, Reichl U (2019) A novel type of influenza A virus-derived defective interfering particle with nucleotide substitutions in its genome. J Virol 93: e01786-18.

124. Duhaut SD, McCauley JW (1996) Defective RNAs inhibit the assembly of influenza virus genome segments in a segment-specific manner. Virology 216: 326–337.

125. Odagiri T, Tominaga K, Tobita K, Ohta S (1994) An amino acid change in the non-structural NS2 protein of an influenza a virus mutant is responsible for the generation of defective interfering (DI) particles by amplifying DI RNAs and suppressing complementary RNA synthesis. J Gen Virol 75 (Pt 1): 43–53.

126. Widjaja I, de Vries E, Rottier PJM, de Haan CAM (2012) Competition between Influenza A virus genome segments. PLoS One 7: e47529.

127. Giachetti C, Holland JJ (1989) Vesicular stomatitis virus and its defective interfering particles exhibit in vitro transcriptional and replicative competition for purified L-NS polymerase molecules. Virology 170: 264–267.

128. Odagiri T, Tashiro M (1997) Segment-specific noncoding sequences of the influenza virus genome RNA are involved in the specific competition between defective interfering RNA and its progenitor RNA segment at the virion assembly step. J Virol 71: 2138–2145.

129. Duhaut SD, Dimmock NJ (2002) Defective segment 1 RNAs that interfere with production of infectious influenza A virus require at least 150 nucleotides of 5' sequence: evidence from a plasmid-driven system. J Gen Virol 83: 403–411.

130. Rao DD, Huang AS (1982) Interference among defective interfering particles of vesicular stomatitis virus. J Virol 41: 210–221.

131. Chanda PK, Chambers TM, Nayak DP (1983) In vitro transcription of defective interfering particles of influenza virus produces polyadenylic acid-containing complementary RNAs. J Virol 45: 55–61.

132. Ke R, Aaskov J, Holmes EC, Lloyd-Smith JO (2013) Phylodynamic analysis of the emergence and epidemiological impact of transmissible defective dengue viruses. PLoS Pathog 9: e1003193.

133. Vasilijevic J, Zamarreño N, Oliveros JC, Rodriguez-Frandsen A, Gómez G, et al. (2017) Reduced accumulation of defective viral genomes contributes to severe outcome in influenza virus infected patients. PLoS Pathog 13: e1006650.

134. Barrett ADT, Dimmock NJ (1986) Defective interfering viruses and infections of animals. In: Current Topics in Microbiology and Immunology, Springer Berlin Heidelberg. pp. 55–84.

135. Dimmock NJ, Beck S, McLain L (1986) Protection of mice from lethal influenza: evidence that defective interfering virus modulates the immune response and not virus multiplication. J Gen Virol 67 (Pt 5): 839–850.

136. Dimmock N, Easton A (2015) Cloned defective interfering influenza RNA and a possible pan-specific treatment of respiratory virus diseases. Viruses 7: 3768–3788.

137. Notton T, Sardanyés J, Weinberger AD, Weinberger LS (2014) The case for transmissible antivirals to control population-wide infectious disease. Trends Biotechnol 32: 400–405.

138. Zhao H, To KKW, Chu H, Ding Q, Zhao X, et al. (2018) Dual-functional peptide with defective interfering genes effectively protects mice against avian and seasonal influenza. Nat Commun 9.

139. Moss RB, Davey RT, Steigbigel RT, Fang F (2010) Targeting pandemic influenza: a primer on influenza antivirals and drug resistance. J Antimicrob Chemother 65: 1086–1093.

140. McKimm-Breschkin JL (2013) Influenza neuraminidase inhibitors: antiviral action and mechanisms of resistance. Influenza Other Respi Viruses 7 Suppl 1: 25–36.

141. Samson M, Pizzorno A, Abed Y, Boivin G (2013) Influenza virus resistance to neuraminidase inhibitors. Antiviral Res 98: 174–185.

142. Shin WJ, Seong BL (2018) Novel antiviral drug discovery strategies to tackle drug-resistant mutants of influenza virus strains. Expert Opin Drug Discovery 14: 153–168.

143. Lackenby A, Besselaar TG, Daniels RS, Fry A, Gregory V, et al. (2018) Global update on the susceptibility of human influenza viruses to neuraminidase inhibitors and status of novel antivirals, 2016–2017. Antiviral Res 157: 38–46.

144. Noble S, McLain L, Dimmock NJ (2004) Interfering vaccine: a novel antiviral that converts a potentially virulent infection into one that is subclinical and immunizing. Vaccine 22: 3018–3025.

145. Dimmock NJ, Rainsford EW, Scott PD, Marriott AC (2008) Influenza virus protecting RNA: an effective prophylactic and therapeutic antiviral. J Virol 82: 8570–8578.

146. Scott PD, Meng B, Marriott AC, Easton AJ, Dimmock NJ (2011) Defective interfering influenza A virus protects in vivo against disease caused by a heterologous influenza B virus. J Gen Virol 92: 2122–2132.

147. Dimmock NJ, Dove BK, Scott PD, Meng B, Taylor I, et al. (2012) Cloned defective interfering influenza virus protects ferrets from pandemic 2009 influenza A virus and allows protective immunity to be established. PLoS One 7: e49394.

148. Dimmock NJ, Dove BK, Meng B, Scott PD, Taylor I, et al. (2012) Comparison of the protection of ferrets against pandemic 2009 influenza A virus (H1N1) by 244 DI influenza virus and oseltamivir. Antiviral Res 96: 376–385.

149. López CB (2014) Defective viral genomes: critical danger signals of viral infections. J Virol 88: 8720–8723.

150. Baum A, García-Sastre A (2011) Differential recognition of viral RNA by RIG-I. Virulence 2: 166–169.

151. Easton AJ, Scott PD, Edworthy NL, Meng B, Marriott AC, et al. (2011) A novel broad-spectrum treatment for respiratory virus infections: Influenza-based defective interfering virus provides protection against pneumovirus infection in vivo. Vaccine 29: 2777–2784.

152. te Velthuis AJW, Long JC, Bauer DLV, Fan RLY, Yen HL, et al. (2018) Mini viral RNAs act as innate immune agonists during influenza virus infection. Nat Microbiol 3: 1234–1242.

153. Ozawa M, Victor ST, Taft AS, Yamada S, Li C, et al. (2011) Replication-incompetent influenza a viruses that stably express a foreign gene. J Gen Virol 92: 2879–2888.

154. Bdeir N, Arora P, Gärtner S, Hoffmann M, Reichl U, et al. (2019) A system for production of defective interfering particles in the absence of infectious influenza A virus. PLoS One 14: e0212757.

155. Yamagata Y, Muramoto Y, Miyamoto S, Shindo K, Nakano M, et al. (2019) Generation of a purely clonal defective interfering influenza virus. Microbiol Immunol 63: 164–171.

156. Harding AT, Haas GD, Chambers BS, Heaton NS (2019) Influenza viruses that require 10 genomic segments as antiviral therapeutics. PLoS Pathog 15: e1008098.

157. Wille M, Holmes EC (2019) The ecology and evolution of influenza viruses. Cold Spring Harbor Perspectives in Medicine 10: a038489.

158. Plotkin S (2014) History of vaccination. Proc Natl Acad Sci U S A 111: 12283–12287.

159. Soema PC, Kompier R, Amorij JP, Kersten GFA (2015) Current and next generation influenza vaccines: Formulation and production strategies. Eur J Pharm Biopharm 94: 251–263.

160. Yamayoshi S, Kawaoka Y (2019) Current and future influenza vaccines. Nature Medicine 25: 212–220.

161. Lee MS, Hu AYC (2012) A cell-based backup to speed up pandemic influenza vaccine production. Trends Microbiol 20: 103–105.

162. Thomas F, Magill TP (1936) Vaccination of human subjects with virus of human influenza. Exp Biol Med 33: 604–606.

163. Cox MMJ, Patriarca PA, Treanor J (2008) FluBlok, a recombinant hemagglutinin influenza vaccine. Influenza Other Respir Viruses 2: 211–219.

164. Treanor JJ, Campbell JD, Brady RC, Keitel WA, Drame M, et al. (2005) Rapid licensure of a new, inactivated influenza vaccine in the United States. Human Vaccines 1: 239–244.

165. Doroshenko A, Halperin SA (2009) Trivalent MDCK cell culture-derived influenza vaccine Optaflu® (novartis vaccines). Expert Rev Vaccines 8: 679–688.

166. Amorij JP, Kersten GFA, Saluja V, Tonnis WF, Hinrichs WLJ, et al. (2012) Towards tailored vaccine delivery: Needs, challenges and perspectives. J Controlled Release 161: 363–376.

167. Carter NJ, Curran MP (2011) Live attenuated influenza vaccine (FluMist®; Fluenz™). Drugs 71: 1591–1622.

168. Skowronski DM, Janjua NZ, Serres GD, Sabaiduc S, Eshaghi A, et al. (2014) Low 2012–13 influenza vaccine effectiveness associated with mutation in the egg-adapted H3N2 vaccine strain not antigenic drift in circulating viruses. PLoS One 9: e92153.

169. Gulati U, Wu W, Gulati S, Kumari K, Waner JL, et al. (2005) Mismatched hemagglutinin and neuraminidase specificities in recent human H3N2 influenza viruses. Virology 339: 12–20.

170. Zost SJ, Parkhouse K, Gumina ME, Kim K, Perez SD, et al. (2017) Contemporary H3N2 influenza viruses have a glycosylation site that alters binding of antibodies elicited by egg-adapted vaccine strains. Proc Natl Acad Sci U S A 114: 12578–12583.

171. Trucchi C, Paganino C, Amicizia D, Orsi A, Tisa V, et al. (2019) Universal influenza virus vaccines: what needs to happen next? Expert Opin Biol Ther 19: 671–683.

172. Lee LYY, Izzard L, Hurt AC (2018) A review of DNA vaccines against influenza. Front Immunol 9.

173. Scorza F, Pardi N (2018) New kids on the block: RNA-based influenza virus vaccines. Vaccines 6: 20.

174. Lundstrom K (2018) Latest development on RNA-based drugs and vaccines. Future Sci OA 4: FSO300.

175. Perdue ML, Arnold F, Li S, Donabedian A, Cioce V, et al. (2011) The future of cell culture-based influenza vaccine production. Expert Rev Vaccines 10: 1183–1194.

176. Hegde NR (2015) Cell culture-based influenza vaccines: A necessary and indispensable investment for the future. Human Vaccines & Immunotherapeutics 11: 1223–1234.

177. Tree JA, Richardson C, Fooks AR, Clegg JC, Looby D (2001) Comparison of large-scale mammalian cell culture systems with egg culture for the production of influenza virus A vaccine strains. Vaccine 19: 3444–3450.

178. Blume S (2000) A brief history of polio vaccines. Science 288: 1593–1594.

179. Zahoor MA, Khurshid M, Qureshi R, Naz A, Shahid M (2016) Cell culture-based viral vaccines: current status and future prospects. Future Virology 11: 549–562.

180. Genzel Y, Reichl U (2009) Continuous cell lines as a production system for influenza vaccines. Expert Rev Vaccines 8: 1681–1692.

181. Le Ru A, Jacob D, Transfiguracion J, Ansorge S, Henry O, et al. (2010) Scalable production of influenza virus in HEK-293 cells for efficient vaccine manufacturing. Vaccine 28: 3661–3671.

182. Pau MG, Ophorst C, Koldijk MH, Schouten G, Mehtali M, et al. (2001) The human cell line PER.C6 provides a new manufacturing system for the production of influenza vaccines. Vaccine 19: 2716–2721.

183. Genzel Y, Behrendt I, Rödig J, Rapp E, Kueppers C, et al. (2012) CAP, a new human suspension cell line for influenza virus production. Appl Microbiol Biotechnol 97: 111–122.

184. Tsai HC, Lehman CW, Lin CC, Tsai SW, Chen CM (2019) Functional evaluation for adequacy of MDCK-lineage cells in influenza research. BMC Research Notes 12.

185. Onions D, Egan W, Jarrett R, Novicki D, Gregersen JP (2010) Validation of the safety of MDCK cells as a substrate for the production of a cell-derived influenza vaccine. Biologicals 38: 544–551.

186. Liu J, Mani S, Schwartz R, Richman L, Tabor DE (2010) Cloning and assessment of tumorigenicity and oncogenicity of a Madin–Darby canine kidney (MDCK) cell line for influenza vaccine production. Vaccine 28: 1285–1293.

187. Gregersen JP, Schmitt HJ, Trusheim H, Bröker M (2011) Safety of MDCK cell culture-based influenza vaccines. Future Microbiology 6: 143–152.

188. Brands R, Visser J, Medema J, Palache AM, van Scharrenburg GJ (1999) Influvac: a safe Madin Darby Canine Kidney (MDCK) cell culture-based influenza vaccine. Dev Biol Stand 98: 93–100.

189. Gröner A, Vorlop J (1997). Patent WO 1997/037000: Animal cells and processes for the replication of influenza viruses (Chiron Behring GmbH & Co).

190. Rubio AP, Eiros JM (2018) Cell culture-derived flu vaccine: Present and future. Human Vaccines & Immunotherapeutics 14: 1874–1882.

191. Chu C, Lugovtsev V, Golding H, Betenbaugh M, Shiloach J (2009) Conversion of MDCK cell line to suspension culture by transfecting with human siat7e gene and its application for influenza virus production. Proc Natl Acad Sci U S A 106: 14802–14807.

192. van Wielink R, Kant-Eenbergen HCM, Harmsen MM, Martens DE, Wijffels RH, et al. (2011) Adaptation of a Madin–Darby canine kidney cell line to suspension growth in serum-free media and comparison of its ability to produce avian influenza virus to Vero and BHK21 cell lines. J Virol Methods 171: 53–60.

193. Lohr V, Genzel Y, Behrendt I, Scharfenberg K, Reichl U (2010) A new MDCK suspension line cultivated in a fully defined medium in stirred-tank and wave bioreactor. Vaccine 28: 6256–6264.

194. Castro R, Fernandes P, Laske T, Sousa MFQ, Genzel Y, et al. (2015) Production of canine adenovirus type 2 in serum-free suspension cultures of MDCK cells. Appl Microbiol Biotechnol 99: 7059–7068.

195. Peschel B, Frentzel S, Laske T, Genzel Y, Reichl U (2013) Comparison of influenza virus yields and apoptosis-induction in an adherent and a suspension MDCK cell line. Vaccine 31: 5693–5699.

196. Tapia F, Vogel T, Genzel Y, Behrendt I, Hirschel M, et al. (2014) Production of high-titer human influenza A virus with adherent and suspension MDCK cells cultured in a single-use hollow fiber bioreactor. Vaccine 32: 1003–1011.

197. Kluge S, Benndorf D, Genzel Y, Scharfenberg K, Rapp E, et al. (2015) Monitoring changes in proteome during stepwise adaptation of a MDCK cell line from adherence to growth in suspension. Vaccine 33: 4269–4280.

198. Nerome K, Kumihashi H, Nerome R, Hiromoto Y, Yokota Y, et al. (1999) Evaluation of immune responses to inactivated influenza vaccines prepared in embryonated chicken eggs and MDCK cells in a mouse model. Dev Biol Stand 98: 53–63.

199. Fineberg HV (2014) Pandemic preparedness and response — lessons from the H1N1 influenza of 2009. New England Journal of Medicine 370: 1335–1342.

200. Lohr V, Rath A, Genzel Y, Jordan I, Sandig V, et al. (2009) New avian suspension cell lines provide production of influenza virus and MVA in serum-free media: Studies on growth, metabolism and virus propagation. Vaccine 27: 4975–4982.

201. Genzel Y, Vogel T, Buck J, Behrendt I, Ramirez DV, et al. (2014) High cell density cultivations by alternating tangential flow (ATF) perfusion for influenza A virus production using suspension cells. Vaccine 32: 2770–2781.

202. Coronel J, Behrendt I, Bürgin T, Anderlei T, Sandig V, et al. (2019) Influenza A virus production in a single-use orbital shaken bioreactor with ATF or TFF perfusion systems. Vaccine 37: 7011–7018.

203. Gränicher G, Coronel J, Pralow A, Marichal-Gallardo P, Wolff M, et al. (2019) Efficient influenza A virus production in high cell density using the novel porcine suspension cell line PBG.PK2.1. Vaccine 37: 7019–7028.

204. Hamamoto I, Takaku H, Tashiro M, Yamamoto N (2013) High yield production of influenza virus in Madin Darby canine kidney (MDCK) cells with stable knockdown of IRF7. PLoS One 8: e59892.

205. van der Sanden SMG, Wu W, Dybdahl-Sissoko N, Weldon WC, Brooks P, et al. (2015) Engineering enhanced vaccine cell lines to eradicate vaccine-preventable diseases: the polio end game. J Virol 90: 1694–1704.

206. Matrosovich M, Matrosovich T, Carr J, Roberts NA, Klenk HD (2003) Overexpression of the alpha-2,6-sialyltransferase in MDCK cells increases influenza virus sensitivity to neuraminidase inhibitors. J Virol 77: 8418–8425.

207. Hatakeyama S, Sakai-Tagawa Y, Kiso M, Goto H, Kawakami C, et al. (2005) Enhanced expression of an alpha2,6-linked sialic acid on MDCK cells improves isolation of human influenza viruses and evaluation of their sensitivity to a neuraminidase inhibitor. J Clin Microbiol 43: 4139–4146.

208. Smith AM (2018) Host-pathogen kinetics during influenza infection and coinfection: insights from predictive modeling. Immunol Rev 285: 97–112.

209. Yin J, Redovich J (2018) Kinetic modeling of virus growth in cells. Microbiol Mol Biol Rev 82.

210. Jenner AL, Aogo RA, Davis CL, Smith AM, Craig M (2020) Leveraging computational modeling to understand infectious diseases. Current Pathobiol Rep 8: 149–161.

211. Schlosser F, Maier BF, Jack O, Hinrichs D, Zachariae A, et al. (2020) COVID-19 lockdown induces disease-mitigating structural changes in mobility networks. Proc Natl Acad Sci U S A 117: 32883–32890.

212. Madrahimov A, Helikar T, Kowal B, Lu G, Rogers J (2013) Dynamics of influenza virus and human host interactions during infection and replication cycle. Bull Math Biol 75: 988–1011.

213. Beauchemin C, Samuel J, Tuszynski J (2005) A simple cellular automaton model for influenza A viral infections. J Theor Biol 232: 223–234.

214. Beauchemin C (2006) Probing the effects of the well-mixed assumption on viral infection dynamics. J Theor Biol 242: 464–477.

215. Lin H, Shuai JW (2010) A stochastic spatial model of HIV dynamics with an asymmetric battle between the virus and the immune system. New J Phys 12: 043051.

216. Mitchell H, Levin D, Forrest S, Beauchemin CAA, Tipper J, et al. (2011) Higher level of replication efficiency of 2009 (H1N1) pandemic influenza virus than those of seasonal and avian strains: kinetics from epithelial cell culture and computational modeling. J Virol 85: 1125–1135.

217. Akpinar F, Inankur B, Yin J (2016) Spatial-temporal patterns of viral amplification and interference initiated by a single infected cell. J Virol 90: 7552–7566.

218. Haseltine E, Rawlings J, Yin J (2005) Dynamics of viral infections: incorporating both the intracellular and extracellular levels. Comput Chem Eng 29: 675-686.

219. Müller T, Dürr R, Isken B, Schulze-Horsel J, Reichl U, et al. (2013) Distributed modeling of human influenza A virus-host cell interactions during vaccine production. Biotechnol Bioeng 110: 2252–2266.

220. Bauer AL, Beauchemin CAA, Perelson AS (2009) Agent-based modeling of host-pathogen systems: The successes and challenges. Inf Sci 179: 1379–1389.

221. Narang V, Decraene J, Wong SY, Aiswarya BS, Wasem AR, et al. (2012) Systems immunology: a survey of modeling formalisms, applications and simulation tools. Immunol Res 53: 251–265.

222. Smith AM (2018) Validated models of immune response to virus infection. Curr Opin Syst Biol 12: 46–52.

223. Zitzmann C, Kaderali L (2018) Mathematical analysis of viral replication dynamics and antiviral treatment strategies: From basic models to age-based multi-scale modeling. Front Microbiol 9.

224. Nowak MA, May RM (2004) Virus Dynamics: Mathematical Principles of Immunology and Virology. Oxford, UK: Oxford University Press.

225. Perelson AS (2002) Modelling viral and immune system dynamics. Nat Rev Immunol 2: 28–36.

226. Iwami S, Koizumi Y, Ikeda H, Kakizoe Y (2013) Quantification of viral infection dynamics in animal experiments. Front Microbiol 4: 264.

227. Heffernan JM, Keeling MJ (2009) Implications of vaccination and waning immunity. Proc Biol Sci 276: 2071–2080.

228. Smith AM, Perelson AS (2011) Influenza A virus infection kinetics: quantitative data and models. Wiley Interdiscip Rev Syst Biol Med 3: 429–445.

229. Rong L, Perelson AS (2009) Modeling HIV persistence, the latent reservoir, and viral blips. J Theor Biol 260: 308–331.

230. Alizon S, Magnus C (2012) Modelling the course of an HIV infection: Insights from ecology and evolution. Viruses 4: 1984–2013.

231. Perelson AS, Ribeiro RM (2013) Modeling the within-host dynamics of HIV infection. BMC Biol 11: 96.

232. Bernhauerová V, Rezelj VV, Vignuzzi M (2020) Modelling degradation and replication kinetics of the Zika virus in vitro infection. Viruses 12: 547.

233. Liao LE, Carruthers J, Smither SJ, CL4 Virology Team, Weller SA, et al. (2020) Quantification of Ebola virus replication kinetics in vitro. PLoS Comput Biol 16: e1008375.

234. Perelson AS, Neumann AU, Markowitz M, Leonard JM, Ho DD (1996) HIV-1 dynamics in vivo: virion clearance rate, infected cell life-span, and viral generation time. Science 271: 1582–1586.

235. Perelson A, Nelson P (1999) Mathematical analysis of HIV-1 dynamics in vivo. SIAM Rev 41: 3-44.

236. Chatterjee A, Guedj J, Perelson AS (2012) Mathematical modelling of HCV infection: what can it teach us in the era of direct-acting antiviral agents? Antivir Ther 17: 1171–1182.

237. Chatterjee A, Smith PF, Perelson AS (2013) Hepatitis C viral kinetics: the past, present, and future. Clin Liver Dis 17: 13–26.

238. Holder BP, Beauchemin CAA (2011) Exploring the effect of biological delays in kinetic models of influenza within a host or cell culture. BMC Public Health 11 Suppl 1: S10.

239. Lloyd AL (2001) The dependence of viral parameter estimates on the assumed viral life cycle: limitations of studies of viral load data. Proc Biol Sci 268: 847–854.

240. Baccam P, Beauchemin C, Macken CA, Hayden FG, Perelson AS (2006) Kinetics of influenza A virus infection in humans. J Virol 80: 7590–7599.

241. Beauchemin CAA, McSharry JJ, Drusano GL, Nguyen JT, Went GT, et al. (2008) Modeling amantadine treatment of influenza A virus in vitro. J Theor Biol 254: 439–451.

242. Handel A, Longini IM, Antia R (2007) Neuraminidase inhibitor resistance in influenza: assessing the danger of its generation and spread. PLoS Comput Biol 3: e240.

243. Dobrovolny HM, Gieschke R, Davies BE, Jumbe NL, Beauchemin CAA (2011) Neuraminidase inhibitors for treatment of human and avian strain influenza: A comparative modeling study. J Theor Biol 269: 234–244.

244. Perelson AS, Rong L, Hayden FG (2012) Combination antiviral therapy for influenza: predictions from modeling of human infections. J Infect Dis 205: 1642–1645.

245. Kamal MA, Gieschke R, Lemenuel-Diot A, Beauchemin CAA, Smith PF, et al. (2015) A drug-disease model describing the effect of oseltamivir neuraminidase inhibition on influenza virus progression. Antimicrob Agents Chemother 59: 5388–5395.

246. Larson EW, Dominik JW, Rowberg AH, Higbee GA (1976) Influenza virus population dynamics in the respiratory tract of experimentally infected mice. Infect Immun 13: 438–447.

247. Bocharov GA, Romanyukha AA (1994) Mathematical model of antiviral immune response. III. Influenza A virus infection. J Theor Biol 167: 323–360.

248. Saenz RA, Quinlivan M, Elton D, Macrae S, Blunden AS, et al. (2010) Dynamics of influenza virus infection and pathology. J Virol 84: 3974–3983.

249. Handel A, Longini IM, Antia R (2010) Towards a quantitative understanding of the within-host dynamics of influenza A infections. J R Soc Interface 7: 35–47.

250. Dobrovolny HM, Reddy MB, Kamal MA, Rayner CR, Beauchemin CAA (2013) Assessing mathematical models of influenza infections using features of the immune response. PLoS One 8: e57088.

251. Myers MA, Smith AP, Lane LC, Moquin DJ, Aogo R, et al. (2021) Dynamically linking influenza virus infection kinetics, lung injury, inflammation, and disease severity. eLife 10: e68864.

252. Pinilla LT, Holder BP, Abed Y, Boivin G, Beauchemin CAA (2012) The H275Y neuraminidase mutation of the pandemic A/H1N1 influenza virus lengthens the eclipse phase and reduces viral output of infected cells, potentially compromising fitness in ferrets. J Virol 86: 10651–10660.

253. Möhler L, Flockerzi D, Sann H, Reichl U (2005) Mathematical model of influenza A virus production in large-scale microcarrier culture. Biotechnol Bioeng 90: 46–58.

254. Schulze-Horsel J, Schulze M, Agalaridis G, Genzel Y, Reichl U (2009) Infection dynamics and virus-induced apoptosis in cell culture-based influenza vaccine production-Flow cytometry and mathematical modeling. Vaccine 27: 2712-22.

255. Sidorenko Y, Schulze-Horsel J, Voigt A, Reichl U, Kienle A (2008) Stochastic population balance modeling of influenza virus replication in vaccine production processes. Chem Eng Sci 63: 157-169.

256. Sidorenko Y, Voigt A, Schulze-Horsel J, Reichl U, Kienle A (2008) Stochastic population balance modeling of influenza virus replication in vaccine production processes. II. detailed description of the replication mechanism. Chem Eng Sci 63: 2299-2304.

257. Endy D, Kong D, Yin J (1997) Intracellular kinetics of a growing virus: A genetically structured simulation for bacteriophage T7. Biotechnol Bioeng 55: 375–389.

258. Reddy B, Yin J (1999) Quantitative intracellular kinetics of HIV type 1. AIDS Res Hum Retroviruses 15: 273–283.

259. Dee KU, Hammer DA, Shuler ML (1995) A model of the binding, entry, uncoating, and RNA synthesis of semliki forest virus in baby hamster kidney (BHK-21) cells. Biotechnol Bioeng 46: 485–496.

260. Regoes RR, Crotty S, Antia R, Tanaka MM (2005) Optimal replication of poliovirus within cells. Am Nat 165: 364–373.

261. Lim KI, Lang T, Lam V, Yin J (2006) Model-based design of growth-attenuated viruses. PLoS Comput Biol 2: e116.

262. Hensel SC, Rawlings JB, Yin J (2009) Stochastic kinetic modeling of vesicular stomatitis virus intracellular growth. Bull Math Biol 71: 1671–1692.

263. Dee KU, Shuler ML (1997) A mathematical model of the trafficking of acid-dependent enveloped viruses: application to the binding, uptake, and nuclear accumulation of baculovirus. Biotechnol Bioeng 54: 468–490.

264. Jang JD, Sanderson CS, Chan LC, Barford JP, Reid S (2000) Structured modeling of recombinant protein production in batch and fed-batch culture of baculovirus-infected insect cells. Cytotechnology 34: 71–82.

265. Nakabayashi J, Sasaki A (2011) A mathematical model of the intracellular replication and within host evolution of hepatitis type B virus: Understanding the long time course of chronic hepatitis. J Theor Biol 269: 318–329.

266. Dahari H, Ribeiro RM, Rice CM, Perelson AS (2007) Mathematical modeling of subgenomic hepatitis C virus replication in Huh-7 cells. J Virol 81: 750–760.

267. McLean AK, Luciani F, Tanaka MM (2010) Trade-offs in resource allocation in the intracellular life-cycle of hepatitis C virus. J Theor Biol 267: 565–572.

268. Nakabayashi J (2012) A compartmentalization model of hepatitis C virus replication: an appropriate distribution of HCV RNA for the effective replication. J Theor Biol 300: 110–117.

269. Binder M, Sulaimanov N, Clausznitzer D, Schulze M, Hüber CM, et al. (2013) Replication vesicles are load- and choke-points in the hepatitis C virus lifecycle. PLoS Pathog 9: e1003561.

270. Zitzmann C, Kaderali L, Perelson AS (2020) Mathematical modeling of hepatitis C RNA replication, exosome secretion and virus release. PLoS Comput Biol 16: e1008421.

271. Nakabayashi J, Sasaki A (2009) The function of temporally ordered viral gene expression in the intracellular replication of herpes simplex virus type 1 (HSV-1). J Theor Biol 261: 156–164.

272. Nunes-Correia I, Ramalho-Santos J, Nir S, de Lima MCP (1999) Interactions of influenza virus with cultured cells: detailed kinetic modeling of binding and endocytosis. Biochemistry 38: 1095–1101.

273. Schelker M, Mair CM, Jolmes F, Welke RW, Klipp E, et al. (2016) Viral RNA degradation and diffusion act as a bottleneck for the influenza A virus infection efficiency. PLoS Comput Biol 12: e1005075.

274. Zitzmann C, Schmid B, Ruggieri A, Perelson AS, Binder M, et al. (2020) A coupled mathematical model of the intracellular replication of dengue virus and the host cell immune response to infection. Front Microbiol 11.

275. Mittal A, Bentz J (2001) Comprehensive kinetic analysis of influenza hemagglutinin-mediated membrane fusion: role of sialate binding. Biophys J 81: 1521–1535.

276. Bazhan SI, Kashevarova NA, Khlebodarova TM, Likhoshvaĭ VA, Kolchanov NA (2009) A mathematical model of the intracellular reproduction of the influenza virus. (in Russian). Biofizika 54: 1066–1080.

277. Heldt FS, Kupke SY, Dorl S, Reichl U, Frensing T (2015) Single-cell analysis and stochastic modelling unveil large cell-to-cell variability in influenza A virus infection. Nat Commun 6: 8938–8938.

278. Rüdiger D, Kupke SY, Laske T, Zmora P, Reichl U (2019) Multiscale modeling of influenza A virus replication in cell cultures predicts infection dynamics for highly different infection conditions. PLoS Comput Biol 15: 1-22.

279. Haseltine EL, Yin J, Rawlings JB (2008) Implications of decoupling the intracellular and extracellular levels in multi-level models of virus growth. Biotechnol Bioeng 101: 811–820.

280. Guedj J, Neumann AU (2010) Understanding hepatitis C viral dynamics with direct-acting antiviral agents due to the interplay between intracellular replication and cellular infection dynamics. J Theor Biol 267: 330–340.

281. Guedj J, Dahari H, Rong L, Sansone ND, Nettles RE, et al. (2013) Modeling shows that the NS5A inhibitor daclatasvir has two modes of action and yields a shorter estimate of the hepatitis C virus half-life. Proc Natl Acad Sci U S A 110: 3991–3996.

282. Rong L, Guedj J, Dahari H, Coffield DJ Jr, Levi M, et al. (2013) Analysis of hepatitis C virus decline during treatment with the protease inhibitor danoprevir using a multiscale model. PLoS Comput Biol 9: e1002959.

283. Rong L, Perelson AS (2013) Mathematical analysis of multiscale models for hepatitis C virus dynamics under therapy with direct-acting antiviral agents. Math Biosci 245: 22–30.

284. Clausznitzer D, Harnisch J, Kaderali L (2016) Multi-scale model for hepatitis C viral load kinetics under treatment with direct acting antivirals. Virus Res 218: 96 - 101.

285. Kumberger P, Frey F, Schwarz US, Graw F (2016) Multiscale modeling of virus replication and spread. FEBS Lett 590: 1972–1986.

286. Sattenspiel L, Dimka J, Orbann C (2019) Using cultural, historical, and epidemiological data to inform, calibrate, and verify model structures in agent-based simulations. Math Biosci Eng 16: 3071–3093.

287. Ho BS, Chao KM (2020) On the influenza vaccination policy through mathematical modeling. Int J Inf Dis 98: 71–79.

288. Brockmann D (2017) Human mobility, networks and disease dynamics on a global scale. In: Diffusive Spreading in Nature, Technology and Society, Springer International Publishing. pp. 375–396.

289. Raue A, Kreutz C, Maiwald T, Bachmann J, Schilling M, et al. (2009) Structural and practical identifiability analysis of partially observed dynamical models by exploiting the profile likelihood. Bioinformatics 25: 1923-9.

290. van Riel NAW (2006) Dynamic modelling and analysis of biochemical networks: mechanism-based models and model-based experiments. Brief Bioinform 7: 364–374.

291. Gutenkunst RN, Waterfall JJ, Casey FP, Brown KS, Myers CR, et al. (2007) Universally sloppy parameter sensitivities in systems biology models. PLoS Comput Biol 3: 1871–1878.

292. Joshi M, Seidel-Morgenstern A, Kremling A (2006) Exploiting the bootstrap method for quantifying parameter confidence intervals in dynamical systems. Metab Eng 8: 447–455.

293. Efron B, Tibshirani R (1986) Bootstrap methods for standard errors, confidence intervals, and other measures of statistical accuracy. Statistical Science 1: pp. 54-75.

294. Laske T, Bachmann M, Dostert M, Karlas A, Wirth D, et al. (2019) Model-based analysis of influenza A virus replication in genetically engineered cell lines elucidates the impact of host cell factors on key kinetic parameters of virus growth. PLoS Comput Biol 15: 1-30.

295. Koff WC, Knight V (1979) Inhibition of influenza virus uncoating by rimantadine hydrochloride. J Virol 31: 261–263.

296. Hatada E, Hasegawa M, Mukaigawa J, Shimizu K, Fukuda R (1989) Control of influenza virus gene expression: quantitative analysis of each viral RNA species in infected cells. J Biochem 105: 537–546.

297. Kawakami E, Watanabe T, Fujii K, Goto H, Watanabe S, et al. (2011) Strand-specific real-time RT-PCR for distinguishing influenza vRNA, cRNA, and mRNA. J Virol Methods 173: 1–6.

298. Duesberg PH (1969) Distinct subunits of the ribonucleoprotein of influenza virus. J Mol Biol 42: 485–499.

299. Enami M, Fukuda R, Ishihama A (1985) Transcription and replication of eight RNA segments of influenza virus. Virology 142: 68–77.

300. Inglis SC, Mahy BW (1979) Polypeptides specified by the influenza virus genome. 3. control of synthesis in infected cells. Virology 95: 154–164.

301. Arava Y, Wang Y, Storey JD, Liu CL, Brown PO, et al. (2003) Genome-wide analysis of mRNA translation profiles in Saccharomyces cerevisiae. Proc Natl Acad Sci U S A 100: 3889–3894.

302. Huang IC, Li W, Sui J, Marasco W, Choe H, et al. (2008) Influenza A virus neuraminidase limits viral superinfection. J Virol 82: 4834–4843.

303. Bushman F, Lewinski M, Ciuffi A, Barr S, Leipzig J, et al. (2005) Genome-wide analysis of retroviral DNA integration. Nat Rev Microbiol 3: 848-858.

304. Kvaratskhelia M, Sharma A, Larue RC, Serrao E, Engelman A (2014) Molecular mechanisms of retroviral integration site selection. Nucleic Acids Res 42: 10209–10225.

305. Cohen S, Hindmarsh A (1996) CVODE, a stiff/nonstiff ODE solver in C. Computers in Physics 10: 138-43.

306. Schmidt H, Jirstrand M (2006) Systems biology toolbox for matlab: a computational platform for research in systems biology. Bioinformatics 22: 514–515.

307. Egea JA, Rodriguez-Fernandez M, Banga JR, Marti R (2007) Scatter search for chemical and bio-process optimization. J Global Optim 37: 481-503.

308. Kaffka H (2013) Model-based analysis of the influence of defective interfering particles on influenza virus replication. Bachelor thesis, Faculty for Process and Systems Engineering, Otto von Guericke University, Magdeburg.

309. Laske T, Heldt FS, Hoffmann H, Frensing T, Reichl U (2016) Modeling the intracellular replication of influenza A virus in the presence of defective interfering RNAs. Virus Res 213: 90 - 99.

310. Wakefield L, Brownlee GG (1989) RNA-binding properties of influenza A virus matrix protein M1. Nucleic Acids Res 17: 8569–8580.

311. Klipp E, Liebermeister W, Wierling C, Kowald A, Herwig R, editors (2016) Systems Biology, Wiley-VCH GmbH, chapter Kinetic Models of Biochemical Networks. pp. 39–62.

312. Castiglione K (2018) Enzymkinetik. In: Chmiel H, Takors R, Weuster-Botz D, editors, Bioprozesstechnik, Springer Berlin Heidelberg. pp. 1–44.

313. Wasik MA, Eichwald L, Genzel Y, Reichl U (2017) Cell culture-based production of defective interfering particles for influenza antiviral therapy. Appl Microbiol Biotechnol 102: 1167–1177.

314. Tapia F, Laske T, Wasik MA, Rammhold M, Genzel Y, et al. (2019) Production of defective interfering particles of influenza A virus in parallel continuous cultures at two residence times - insights from qPCR measurements and viral dynamics modeling. Front Bioeng Biotechnol 7: 275.

315. Kirkwood TB, Bangham CR (1994) Cycles, chaos, and evolution in virus cultures: a model of defective interfering particles. Proc Natl Acad Sci U S A 91: 8685–8689.

316. Kalbfuss B, Knöchlein A, Kröber T, Reichl U (2008) Monitoring influenza virus content in vaccine production: precise assays for the quantitation of hemagglutination and neuraminidase activity. Biologicals 36: 145–161.

317. Genzel Y, Reichl U (2007) Vaccine production – state of the art and future needs in upstream processing. In: Poertner R, editor, Animal Cell Biotechnology: Methods and Protocols, Humana Press. pp. 457–473.

318. Genzel Y, Rödig J, Rapp E, Reichl U (2014) Vaccine production: upstream processing with adherent or suspension cell lines. Methods Mol Biol 1104: 371–393.

319. Bachmann M (2019) Charakterisierung der Influenzavirus-Vermehrung in genetisch veränderten humanen Zelllinien zur Optimierung der Impfstoffproduktion. Ph.D. thesis, Faculty of Process and Systems Engineering, Otto von Guericke University Magdeburg.

320. Stegmann T, Schoen P, Bron R, Wey J, Bartoldus I, et al. (1993) Evaluation of viral membrane fusion assays. comparison of the octadecylrhodamine dequenching assay with the pyrene excimer assay. Biochemistry 32: 11330–11337.

321. Karlas A, Machuy N, Shin Y, Pleissner KP, Artarini A, et al. (2010) Genome-wide RNAi screen identifies human host factors crucial for influenza virus replication. Nature 463: 818–822.

322. Hao L, Sakurai A, Watanabe T, Sorensen E, Nidom C, et al. (2008) Drosophila RNAi screen identifies host genes important for influenza virus replication. Nature 454(7206): 890-893.

323. Shapira SD, Gat-Viks I, Shum BOV, Dricot A, de Grace MM, et al. (2009) A physical and regulatory map of host-influenza interactions reveals pathways in H1N1 infection. Cell 139: 1255–1267.

324. Brass A, Huang I, Benita Y, John S, Krishnan M, et al. (2009) The IFITM proteins mediate cellular resistance to influenza A H1N1 virus, west nile virus, and dengue virus. Cell 139(7): 1243-1254.

325. Tafforeau L, Chantier T, Pradezynski F, Pellet J, Mangeot PE, et al. (2011) Generation and comprehensive analysis of an influenza virus polymerase cellular interaction network. J Virol 85: 13010–13018.

326. Gaur P, Ranjan P, Sharma S, Patel JR, Bowzard JB, et al. (2012) Influenza A virus neuraminidase protein enhances cell survival through interaction with carcinoembryonic antigen-related cell adhesion molecule 6 (CEACAM6) protein. J Biol Chem 287: 15109-15117.

327. Ueda M, Yamate M, Du A, Daidoji T, Okuno Y, et al. (2008) Maturation efficiency of viral glycoproteins in the ER impacts the production of influenza A virus. Virus Res 136: 91 - 97.

328. Larsen S, Bui S, Perez V, Mohammad A, Ramirez HM, et al. (2014) Influenza polymerase encoding mRNAs utilize atypical mRNA nuclear export. Virol J 11: 154.

329. Oguin TH, Sharma S, Stuart AD, Duan S, Scott SA, et al. (2014) Phospholipase D facilitates efficient entry of influenza virus, allowing escape from innate immune inhibition. J Biol Chem 289: 25405-25417.

330. Sikora D, Rocheleau L, Brown EG, Pelchat M (2017) Influenza A virus cap-snatches host RNAs based on their abundance early after infection. Virology 509: 167 - 177.

331. Vitenshtein A, Weisblum Y, Hauka S, Halenius A, Oiknine-Djian E, et al. (2016) CEACAM1-mediated inhibition of virus production. Cell Reports 15: 2331 - 2339.

332. Li N, Parrish M, Chan TK, Yin L, Rai P, et al. (2015) Influenza infection induces host DNA damage and dynamic DNA damage responses during tissue regeneration. Cell Mol Life Sci 72: 2973–2988.

333. Kuraoka I, Ito S, Wada T, Hayashida M, Lee L, et al. (2008) Isolation of XAB2 complex involved in pre-mRNA splicing, transcription, and transcription-coupled repair. J Biol Chem 283: 940-950.

334. Thakur A, Qureshi A, Kumar M (2017) vhfRNAi: a web-platform for analysis of host genes involved in viral infections discovered by genome wide RNAi screens. Mol Biosyst 13: 1377-1387.

335. Dürr R, Duvigneau S, Laske T, Bachmann M, Kienle A (2016) Analyzing the impact of heterogeneity in genetically engineered cell lines for influenza vaccine production using population balance modeling. IFAC-PapersOnLine 49: 225–230.

336. Duvigneau S, Dürr R, Laske T, Bachmann M, Dostert M, et al. (2018) Mathematical modeling as a tool to improve influenza vaccine production processes. IFAC-PapersOnLine 51: 1–4.

337. Duvigneau S, Dürr R, Laske T, Bachmann M, Dostert M, et al. (2020) Model-based approach for predicting the impact of genetic modifications on product yield in biopharmaceutical manufacturing—application to influenza vaccine production. PLoS Comput Biol 16: e1007810.

338. Simon PF, de La Vega MA, Paradis É, Mendoza E, Coombs KM, et al. (2016) Avian influenza viruses that cause highly virulent infections in humans exhibit distinct replicative properties in contrast to human H1N1 viruses. Sci Rep 6: 24154–24154.

339. González-Parra G, De Ridder F, Huntjens D, Roymans D, Ispas G, et al. (2018) A comparison of RSV and influenza in vitro kinetic parameters reveals differences in infecting time. PLoS One 13: e0192645.

340. Hirsch AJ (2010) The use of RNAi-based screens to identify host proteins involved in viral replication. Future Microbiology 5: 303-311.

341. Stertz S, Shaw ML (2011) Uncovering the global host cell requirements for influenza virus replication via RNAi screening. Microbes Infect 13: 516 - 525.

342. König R, Stertz S (2015) Recent strategies and progress in identifying host factors involved in virus replication. Curr Opin Microbiol 26: 79 - 88.

343. König R, Stertz S, Zhou Y, Inoue A, Hoffmann HH, et al. (2010) Human host factors required for influenza virus replication. Nature 463: 813–817.

344. Zhou Z, Cao M, Guo Y, Zhao L, Wang J, et al. (2014) Fragile X mental retardation protein stimulates ribonucleoprotein assembly of influenza A virus. Nat Commun 5: 3259.

345. Chasman D, Walters KB, Lopes TJS, Eisfeld AJ, Kawaoka Y, et al. (2016) Integrating transcriptomic and proteomic data using predictive regulatory network models of host response to pathogens. PLoS Comput Biol 12: 1-42.

346. Tripathi S, Pohl M, Zhou Y, Rodriguez-Frandsen A, Wang G, et al. (2015) Meta- and orthogonal integration of influenza OMICs data defines a role for UBR4 in virus budding. Cell Host & Microbe 18: 723 - 735.

347. Forst CV, Zhou B, Wang M, Chou TW, Mason G, et al. (2017) Integrative gene network analysis identifies key signatures, intrinsic networks and host factors for influenza virus A infections. NPJ Syst Biol Appl 3: 35.

348. Mahmoudabadi G, Milo R, Phillips R (2017) Energetic cost of building a virus. Proc Natl Acad Sci U S A 114: E4324–E4333.

349. Wirth D, Gama-Norton L, Riemer P, Sandhu U, Schucht R, et al. (2007) Road to precision: recombinase-based targeting technologies for genome engineering. Curr Opin Biotechnol 18: 411 - 419.

350. Wang H, La Russa M, Qi LS (2016) CRISPR/Cas9 in genome editing and beyond. Annu Rev Biochem 85: 227-264.

351. Gossen M, Bujard H (1992) Tight control of gene expression in mammalian cells by tetracycline-responsive promoters. Proc Natl Acad Sci U S A 89: 5547–5551.

352. Weber W, Fussenegger M (2004) Inducible gene expression in mammalian cells and mice. In: Balbás P, Lorence A, editors, Recombinant Gene Expression: Reviews and Protocols, Totowa, NJ: Humana Press, Methods in Molecular Biology. 2nd edition, pp. 451–466.

353. Hoeksema F, Karpilow J, Luitjens A, Lagerwerf F, Havenga M, et al. (2018) Enhancing viral vaccine production using engineered knockout vero cell lines – A second look. Vaccine 36: 2093–2103.

354. Devkota P, Wuchty S (2020) Controllability analysis of molecular pathways points to proteins that control the entire interaction network. Sci Rep 10: 2943.

355. Akkina RK, Chambers TM, Nayak DP (1984) Mechanism of interference by defective-interfering particles of influenza virus: Differential reduction of intracellular synthesis of specific polymerase proteins. Virus Res 1: 687 - 702.

356. Schwartz SL, Lowen AC (2016) Droplet digital PCR: A novel method for detection of influenza virus defective interfering particles. J Virol Methods 237: 159 - 165.

357. Arora P (2020) Novel Production System for Influenza A Virus-derived Defective Interfering Particles and Analysis of Antiviral ctivity. Ph.D. thesis, Faculty of Biology and Psychology, Georg August University Göttingen.

358. Li D, Aaskov J (2014) Sub-genomic RNA of defective interfering (D.I.) dengue viral particles is replicated in the same manner as full length genomes. Virology 468-470: 248–255.

359. Chang YC, Borja M, Scholthof HB, Jackson AO, Morris TJ (1995) Host effects and sequences essential for accumulation of defective interfering RNAs of cucumber necrosis and tomato bushy stunt tombusviruses. Virology 210: 41–53.

360. He L, Wang Q, Gu Z, Liao Q, Palukaitis P, et al. (2019) A conserved RNA structure is essential for a satellite RNA-mediated inhibition of helper virus accumulation. Nucleic Acids Res 47: 8255-8271.

361. Repass JF, Makino S (1998) Importance of the positive-strand RNA secondary structure of a murine coronavirus defective interfering RNA internal replication signal in positive-strand RNA synthesis. J Virol 72: 7926–7933.

362. Odagiri T, Tobita K (1990) Mutation in NS2, a nonstructural protein of influenza A virus, extragenically causes aberrant replication and expression of the PA gene and leads to generation of defective interfering particles. Proc Natl Acad Sci U S A 87: 5988–5992.

363. Nayak DP, Tobita K, Janda JM, Davis AR, De BK (1978) Homologous interference mediated by defective interfering influenza virus derived from a temperature-sensitive mutant of influenza virus. J Virol 28: 375–386.

364. Bellett AJD, Cooper PD (1959) Some properties of the transmissible interfering component of vesicular stomatitis virus preparations. Microbiology 21: 498-509.

365. Liao LE, Iwami S, Beauchemin CAA (2016) (In)validating experimentally derived knowledge about influenza A defective interfering particles. J R Soc Interface 13: 20160412.

366. Ferhadian D, Contrant M, Printz-Schweigert A, Smyth RP, Paillart JC, et al. (2018) Structural and functional motifs in influenza virus RNAs. Front Microbiol 9: 559.

367. Meng B, Bentley K, Marriott AC, Scott PD, Dimmock NJ, et al. (2017) Unexpected complexity in the interference activity of a cloned influenza defective interfering RNA. Virol J 14.

368. Tobita K, Odagiri T, Tanaka T (1986) Isolation of a novel type of interfering influenza B virus defective in the function of M gene. Arch Virol 90: 223–236.

369. Fonville JM, Marshall N, Tao H, Steel J, Lowen AC (2015) Influenza virus reassortment is enhanced by semi-infectious particles but can be suppressed by defective interfering particles. PLoS Pathog 11: 1–30.

370. Rammhold M (2017) Model-based optimization of continuous influenza vaccine production processes. Master thesis, Faculty of Process and Systems Engineering, Otto von Guericke University, Magdeburg.

371. Stauffer-Thompson KA, Rempala GA, Yin J (2009) Multiple-hit inhibition of infection by defective interfering particles. J Gen Virol 90: 888–899.

372. Tapia-Delgado FI (2019) Continuous upstream processing for cell culture-derived virus production. Ph.D. thesis, Faculty of Process and Systems Engineering, Otto von Guericke University Magdeburg.

373. Tapia F, Wohlfarth D, Sandig V, Jordan I, Genzel Y, et al. (2019) Continuous influenza virus production in a tubular bioreactor system provides stable titers and avoids the "von Magnus effect". PLoS One 14: 1-21.

374. Kompier R, Tramper J, Vlak J (1988) A continuous process for the production of baculovirus using insect-cell cultures. Biotechnol Lett 10: 849-854.

375. van Lier FLJ, van den End EJ, de Gooijer CD, Vlak JM, Tramper J (1990) Continuous production of baculovirus in a cascade of insect-cell reactors. Appl Microbiol Biotechnol 33: 43–47.

376. van Lier FLJ, van den Hombergh JPTW, de Gooijer CD, den Boer MM, Vlak JM, et al. (1996) Long-term semi-continuous production of recombinant baculovirus protein in a repeated (fed-)batch two-stage reactor system. Enzyme Microb Technol 18: 460–466.

377. van Lier FLJ, van Duijnhoven GCF, de Vaan MMJACM, Vlak JM, Tramper J (1994) Continuous beta-galactosidase production in insect cells with a p10 gene based baculovirus vector in a two-stage bioreactor system. Biotechnol Progr 10: 60–64.

378. Pijlman GP, de Vrij J, van den End FJ, Vlak JM, Martens DE (2004) Evaluation of baculovirus expression vectors with enhanced stability in continuous cascaded insect-cell bioreactors. Biotechnol Bioeng 87: 743–753.

379. Tapia F, Jordan I, Genzel Y, Reichl U (2017) Efficient and stable production of Modified Vaccinia Ankara virus in two-stage semi-continuous and in continuous stirred tank cultivation systems. PLoS One 12: 1-17.

380. Cane C, McLain L, Dimmock NJ (1987) Intracellular stability of the interfering activity of a defective interfering influenza virus in the absence of virus multiplication. Virology 159: 259 - 264.

381. Isken B, Genzel Y, Reichl U (2012) Productivity, apoptosis, and infection dynamics of influenza A/PR/8 strains and A/PR/8-based reassortants. Vaccine 30: 5253–5261.

382. Bangham CR, Kirkwood TB (1990) Defective interfering particles: effects in modulating virus growth and persistence. Virology 179: 821–826.

383. Nelson GW, Perelson AS (1995) Modeling defective interfering virus therapy for aids: conditions for div survival. Math Biosci 125: 127–153.

384. Robb NC, Jackson D, Vreede FT, Fodor E (2010) Splicing of influenza A virus NS1 mRNA is independent of the viral NS1 protein. J Gen Virol 91: 2331–2340.

385. Amorim MJ, Bruce EA, Read EKC, Foeglein A, Mahen R, et al. (2011) A Rab11 and microtubule dependent mechanism for cytoplasmic transport of influenza A virus vRNA. J Virol 85: 4143-4156.

386. Babcock HP, Chen C, Zhuang X (2004) Using single-particle tracking to study nuclear trafficking of viral genes. Biophys J 87: 2749–2758.

387. Spirin AS (1986) Ribosome structure and protein biosynthesis. Benjamin/Cummings Pub. Co., Advanced Book Program, Menlo Park, CA.

APPENDIX A

Single-cell model and virus-host cell interactions

This chapter provides additional information on simulations of the model of intracellular influenza A virus replication and its application to analyze virus-host cell interactions in genetically modified A549 cell lines.

A.1. Model of intracellular virus replication

Table A.1.: List of parameters for the intracellular model.

Parameter		Value	Source, Reference, Comment
$B_{\text{hi}}^{\text{tot}}$	(sites)	150	[272]
$B_{\text{lo}}^{\text{tot}}$	(sites)	1 000	[272]
D_{Rib}	(nucleotides)	160	[301]
F_{Fus}	(−)	0.51	[18]
F_{Spl_7}	(−)	0.02	Ratio of M2 to M1 in virion
F_{Spl_8}	(−)	0.125	[384]
K_{VRel}	(virions)	10	Adjusted
$k_{\text{hi}}^{\text{Att}}$	(site · h)$^{-1}$	8.09×10^{-2}	Adjusted to data in [272]
$k_{\text{lo}}^{\text{Att}}$	(site · h)$^{-1}$	4.55×10^{-4}	Adjusted to data in [272]
$k_{\text{M1}}^{\text{Bind}}$	(molecule · h)$^{-1}$	1.39×10^{-6}	[18]
$k_{\text{NP}}^{\text{Bind}}$	(molecule · h)$^{-1}$	3.01×10^{-4}	[18]
$k_{\text{RdRp}}^{\text{Bind}}$	(molecule · h)$^{-1}$	1	[18]
$k_{\text{M}}^{\text{Deg}}$	(h^{-1})	0.33	[18]
$k_{\text{R}}^{\text{Deg}}$	(h^{-1})	36.36	[18]
$k_{\text{Rnp}}^{\text{Deg}}$	(h^{-1})	0.09	[18]
$k_{\text{RRdRp}}^{\text{Deg}}$	(h^{-1})	4.25	[18]
k^{En}	(h^{-1})	4.8	[18]
$k_{\text{hi}}^{\text{Eq}}$	(site^{-1})	1.13×10^{-2}	[272]

Parameter		Value	Source
$k_{\text{lo}}^{\text{Eq}}$	(site^{-1})	8.33×10^{-5}	[272]
k^{Exp}	(molecule $\cdot$ h)$^{-1}$	1×10^{-6}	Adjusted to data in [385]
k^{Fus}	(h^{-1})	3.21	[18]
k^{Imp}	(h^{-1})	6	[386]
k^{RdRp}	(molecule$^{-2} \cdot$ h^{-1})	1	Rapid complex formation assumed
k^{Rel}	(virions/(molecule $\cdot$ h))	3.7×10^{-3}	Cell releases 10^4 virions in 12 h
$k_{\text{C}}^{\text{Syn}}$	(h^{-1})	1.38	[18]
$k_{\text{M}}^{\text{Syn}}$	(nucleotides/h)	2.5×10^5	[18]
$k_{\text{P}}^{\text{Syn}}$	(nucleotides/h)	64 800	[387]
$k_{\text{V}}^{\text{Syn}}$	(h^{-1})	13.86	[18]
L_1	(nucleotides)	2 320	[30]
L_2	(nucleotides)	2 320	[30]
L_3	(nucleotides)	2 211	[30]
L_4	(nucleotides)	1 757	[30]
L_5	(nucleotides)	1 540	[30]
L_6	(nucleotides)	1 392	[30]
L_7	(nucleotides)	1 005	[30]
L_8	(nucleotides)	868	[30]
L^{V}	(nucleotides)	1 700	Based on [30]
$N_{\text{P}_{\text{HA}}}$	(molecules/virion)	500	[30]
$N_{\text{P}_{\text{M1}}}$	(molecules/virion)	3 000	[30]
$N_{\text{P}_{\text{M2}}}$	(molecules/virion)	40	[30]
$N_{\text{P}_{\text{NA}}}$	(molecules/virion)	100	[30]
$N_{\text{P}_{\text{NP}}}$	(molecules/virion)	1 000	[30]
$N_{\text{P}_{\text{NEP}}}$	(molecules/virion)	165	[30]
$N_{\text{P}_{\text{RdRp}}}$	(molecules/virion)	45	[30]
$N_{\text{M1}}^{\text{Nuc}}$	(nucleotides)	200	[310]
$N_{\text{NEP}}^{\text{Nuc}}$	(nucleotides)	1 700	Adjusted to [57]
$N_{\text{NP}}^{\text{Nuc}}$	(nucleotides)	24	[57]

A.2. Model for infected A549 and MDCK cells

Table A.2.: Summary of *in silico* optimized kinetic parameters and corresponding model response according to the analysis shown in Figure 4.2, Section 4.1.1.

Parameter		p_0[a]	p_{opt}[b]	$V^{\text{Rel}}(p_{\text{opt}})$[c]	$\frac{p_{\text{opt}}}{p_0}$	$\frac{V^{\text{Rel}}(p_{\text{opt}})}{V^{\text{Rel}}(p_0)}$
F_{Spl_8}	-	0.125	0.625	1.01×10^3	5.00	1.04
$k_{\text{hi}}^{\text{Att}}$	$(\text{site} \cdot \text{h})^{-1}$	0.081	0.405	9.72×10^2	5.00	1.00
k^{En}	h^{-1}	4.800	23.998	9.74×10^2	5.00	1.00
k^{Fus}	h^{-1}	3.210	16.050	9.73×10^2	5.00	1.00
k^{Imp}	h^{-1}	0.296	1.480	9.81×10^2	5.00	1.01
k^{Exp}	$(\text{molecule} \cdot \text{h})^{-1}$	1.00×10^{-6}	5.00×10^{-6}	1.01×10^3	5.00	1.04
$k_{\text{P}}^{\text{Syn}}$	nucleotides/h	6.48×10^4	3.24×10^5	1.27×10^4	5.00	13.03
$k_{\text{V}}^{\text{Syn}}$	h^{-1}	100.93	20.19	1.98×10^3	0.20	2.04
$k_{\text{C}}^{\text{Syn}}$	(h^{-1})	1.53	0.31	2.12×10^3	0.20	2.18
$k_{\text{M}}^{\text{Syn}}$	nucleotides/h	3.06×10^4	1.53×10^5	1.27×10^4	5.00	13.03
$k_{\text{RdRp}}^{\text{Bind}}$	$(\text{molecule} \cdot \text{h})^{-1}$	1.00	4.94	9.72×10^2	4.94	1.00
$k_{\text{NP}}^{\text{Bind}}$	$(\text{molecule} \cdot \text{h})^{-1}$	3.01×10^{-4}	6.02×10^{-5}	2.87×10^3	0.20	2.95
$k_{\text{M1}}^{\text{Bind}}$	$(\text{molecule} \cdot \text{h})^{-1}$	1.82×10^{-6}	3.64×10^{-7}	5.05×10^3	0.20	5.20
k^{Rel}	virions/(molecule $\cdot$ h)	1.10×10^{-3}	5.50×10^{-3}	4.66×10^3	5.00	4.79

[a] Initial parameter values for k^{Imp}, $k_{\text{V}}^{\text{Syn}}$, $k_{\text{C}}^{\text{Syn}}$, $k_{\text{M}}^{\text{Syn}}$, $k_{\text{M1}}^{\text{Bind}}$, k^{Rel} estimated from the available data on infected A549 cells (Figure 4.1, Table 4.1 in Section 4.1.1), others taken from the original model (Table A.1 in the appendix, [18]).
[b] Optimized parameter value, determined using the procedure described in Section 3.1.2.
[c] Cell-specific virus yield obtained with the optimal parameter value p_{opt}.
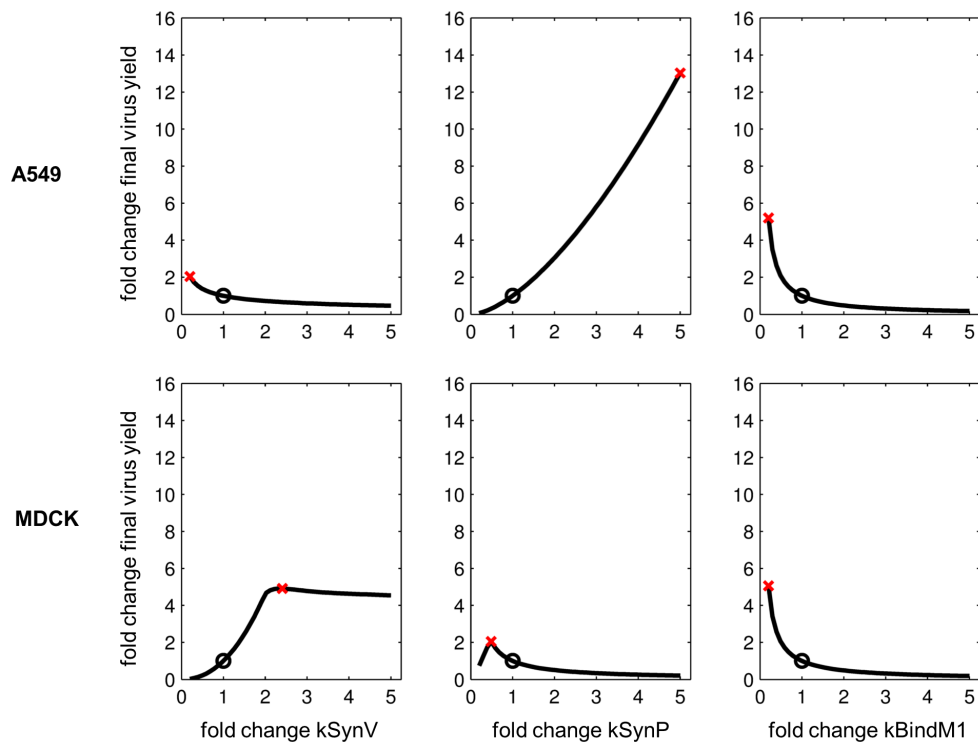
Figure A.1.: Fold change in final virus yield in response to parameter perturbations. We simulated manipulation of vRNA synthesis (column 1), viral protein synthesis (column 2) and the binding of the matrix protein 1 (M1) to nuclear vRNPs (column 3) by perturbing the corresponding kinetic parameters in the IAV replication model for both A549 cells established in the present study (upper panel) and for MDCK cells established previously by our group [18] (bottom panel). Shown are the fold changes of the virus yield at 24 h p.i. in response to the fold changes in the corresponding parameters (black solid lines) with respect to the simulation of the parental cell lines. For every parameter analysis the simulation read out for the parental cell line (black open circle) and the optimal cell line (red cross) is marked.
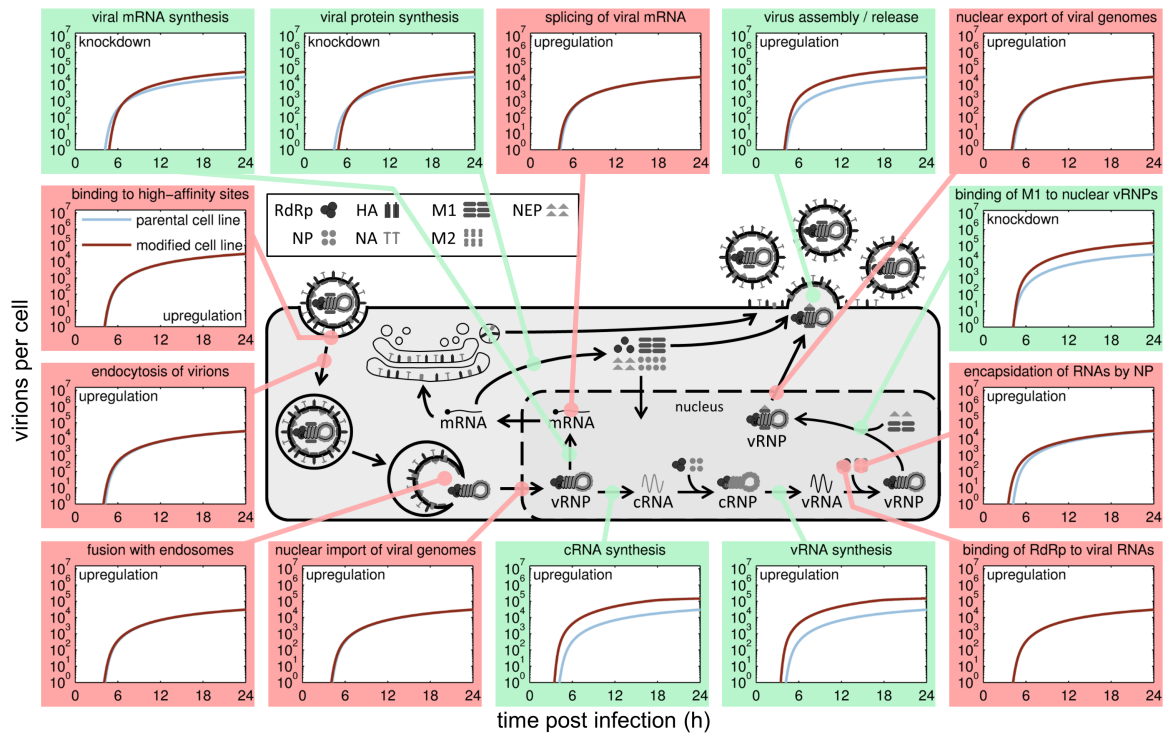
Figure A.2.: Virus release dynamics in response to *in silico* manipulation of gene expression of host cell factors in MDCK cells. We assume that efficiency of individual steps in the virus life cycle is directly dependent on host cell factors and that their influence is changed upon knockdown or overexpression of the corresponding gene. We simulated manipulation of gene expression by perturbing the corresponding kinetic parameters in the IAV replication model for MDCK cells established previously by our group (Section 3.1.1, [18]) according to the approach presented for A549 cells (Figure 4.2, Section 4.1.1). For the most important steps, virus release of parental MDCK cells (blue solid line) and the engineered cell line (brown solid line) are shown for a simulated infection at MOI 1. Colors indicate whether perturbation of the indicated step improved final virus yield at 24 h p.i. by at least two-fold (green), or had no impact (red). Scheme of IAV replication adapted from [37].

A.3. Cell lines overexpressing a single gene

Table A.3.: Comparison of key kinetic parameters of influenza A virus replication in parental A549 cells and A549 cells overexpressing selected host cell factors.

Parameter[a] → Cell line ↓	k^{Imp}	$k_{\mathrm{V}}^{\mathrm{Syn}}$	$k_{\mathrm{C}}^{\mathrm{Syn}}$	$k_{\mathrm{M}}^{\mathrm{Syn}}$	$k_{\mathrm{M1}}^{\mathrm{Bind}}$	k^{Rel}
A549 cells	0.296	100.93	1.53	3.06×10^4	1.82×10^{-6}	1.10×10^{-3}
control	0.281	93.66	1.48	3.62×10^4	2.14×10^{-6}	0.98×10^{-3}
CEACAM6	0.199	142.56	1.65	2.34×10^4	1.73×10^{-6}	2.20×10^{-3}
FANCG	0.258	137.45	0.88	1.91×10^4	1.81×10^{-6}	2.60×10^{-3}
NXF1	0.209	151.89	1.48	1.97×10^4	1.34×10^{-6}	3.10×10^{-3}
PLD2	0.287	156.26	0.80	2.15×10^4	1.54×10^{-6}	1.70×10^{-3}
XAB2	0.295	95.07	1.10	2.71×10^4	1.58×10^{-6}	1.20×10^{-3}

[a] Nuclear import rate k^{Imp} (h^{-1}), vRNA synthesis rate $k_{\mathrm{V}}^{\mathrm{Syn}}$ (h^{-1}), cRNA synthesis rate $k_{\mathrm{C}}^{\mathrm{Syn}}$ (h^{-1}), viral mRNA synthesis rate $k_{\mathrm{M}}^{\mathrm{Syn}}$ (nucleotides/h), M1 binding rate $k_{\mathrm{M1}}^{\mathrm{Bind}}$ (molecule · h)$^{-1}$, virus release rate k^{Rel} (virions/(molecule · h)).

Median values of the corresponding parameter distributions, see also Figure 4.7, Section 4.1.2 and Figure A.3 in the appendix.
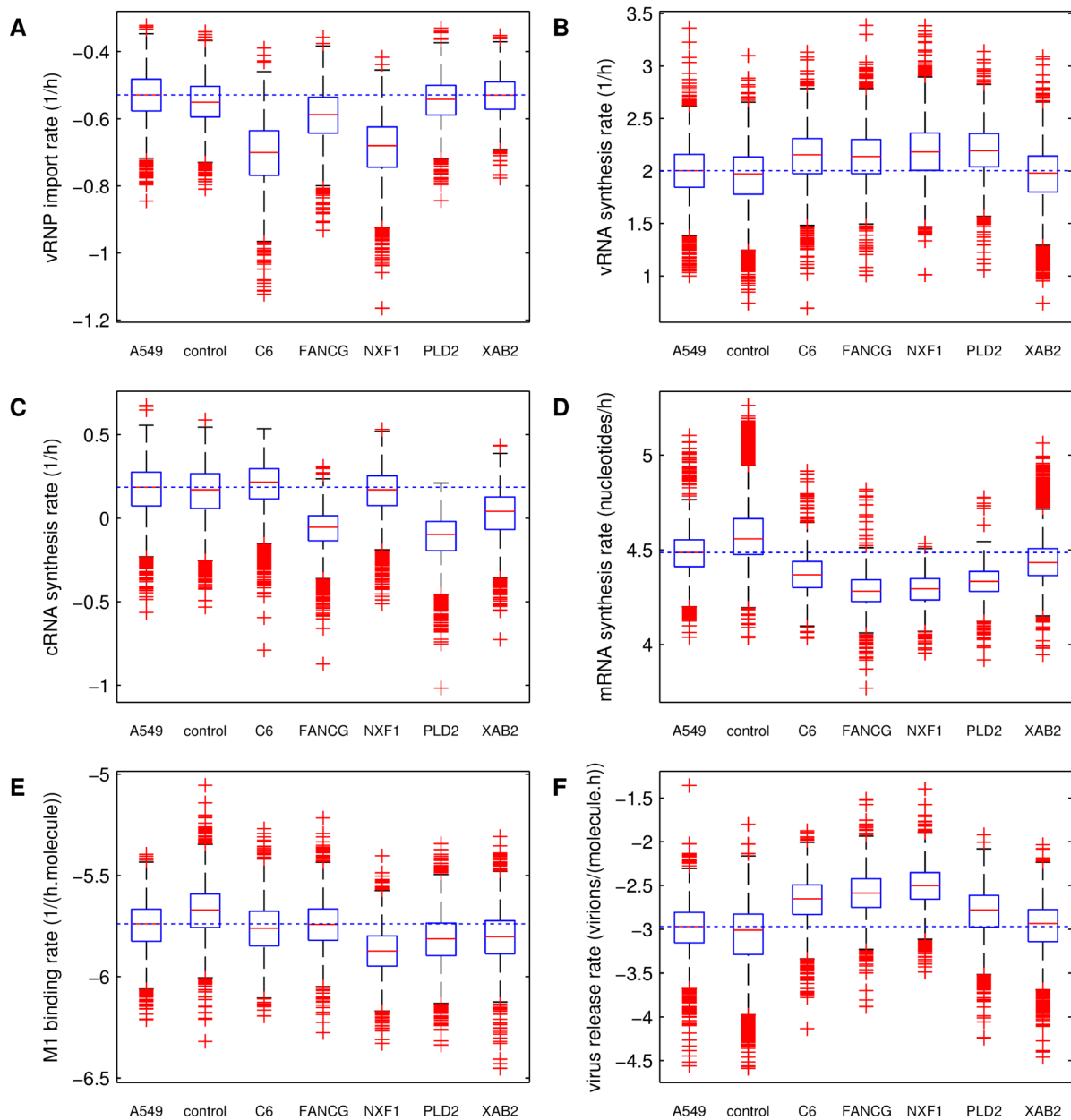
Figure A.3.: Comparison of parameter distributions for different A549 cell lines.
Decadic logarithm of parameter values obtained by fitting 3000 re-samples of the available experimental data acquired from infected SGOs. Shown are median (red solid line), first and third quartile (blue box), maximum values (whiskers) and outliers (red crosses). Blue dashed lines represent the median of the respective parameter value for parental A549 cells. Experimental data used for estimating the nuclear vRNP import rate in cycloheximide-treated cells (A) were re-sampled separately from those used for simultaneous estimation of the vRNA (B), cRNA (C), mRNA (D), M1 binding (E) and virus release rate (F) in conventional infection experiments (without cycloheximide treatment). C6 indicates parameter values obtained from infected cells overexpressing CEACAM6. Results from statistical testing are given in Figure 4.7 (Section 4.1.2).

Table A.4.: Uniprot identifier, names and functions of selected host cell genes.

| Entry (Entry name)	Protein names	Gene names	Functions
P40199 (CEAM6_HUMAN)	Carcinoembryonic antigen-related cell adhesion molecule 6 (Non-specific cross-reacting antigen) (Normal cross-reacting antigen) (CD antigen CD66c)	CEACAM6, NCA	Direct interaction with viral NA, activates the Src/Akt survival pathway [326]
O15287 (FANCG_HUMAN)	Fanconi anemia group G protein (Protein FACG) (DNA repair protein XRCC9)	FANCG, XRCC9	DNA repair, direct interaction with the viral polymerase, knockdown results in reduced virus replication, overexpression increases virus replication (minigenome replicon assay) [325]
Q9UBU9 (NXF1_HUMAN)	Nuclear RNA export factor 1 (Tip-associated protein) (Tip-associating protein) (mRNA export factor TAP)	NXF1, TAP	Inhibition of NXF1 results in less nuclear export of influenza virus mRNA for HA and NA in both HEK293T and A549 cells [328]
O14939 (PLD2_HUMAN)	Phospholipase D2 (PLD 2) (hPLD2) (EC 3.1.4.4) (Choline phosphatase 2) (PLD1C) (Phosphatidylcholine-hydrolyzing phospholipase D2)	PLD2	RNAi of PLD delays influenza virus entry and reduced viral titers *in vitro*; *in vivo*, PLD2 inhibition reduces virus titer and correlates with significant increase in transcription of innate antiviral effectors [329]
Q9HCS7 (SYF1_HUMAN)	Pre-mRNA-splicing factor SYF1 (Protein HCNP) (XPA-binding protein 2)	XAB2, HCNP, KIAA1177, SYF1, PP3898	DNA repair mechanism, transcription and transcription-coupled repair [333], host restriction factor for various viruses [334]
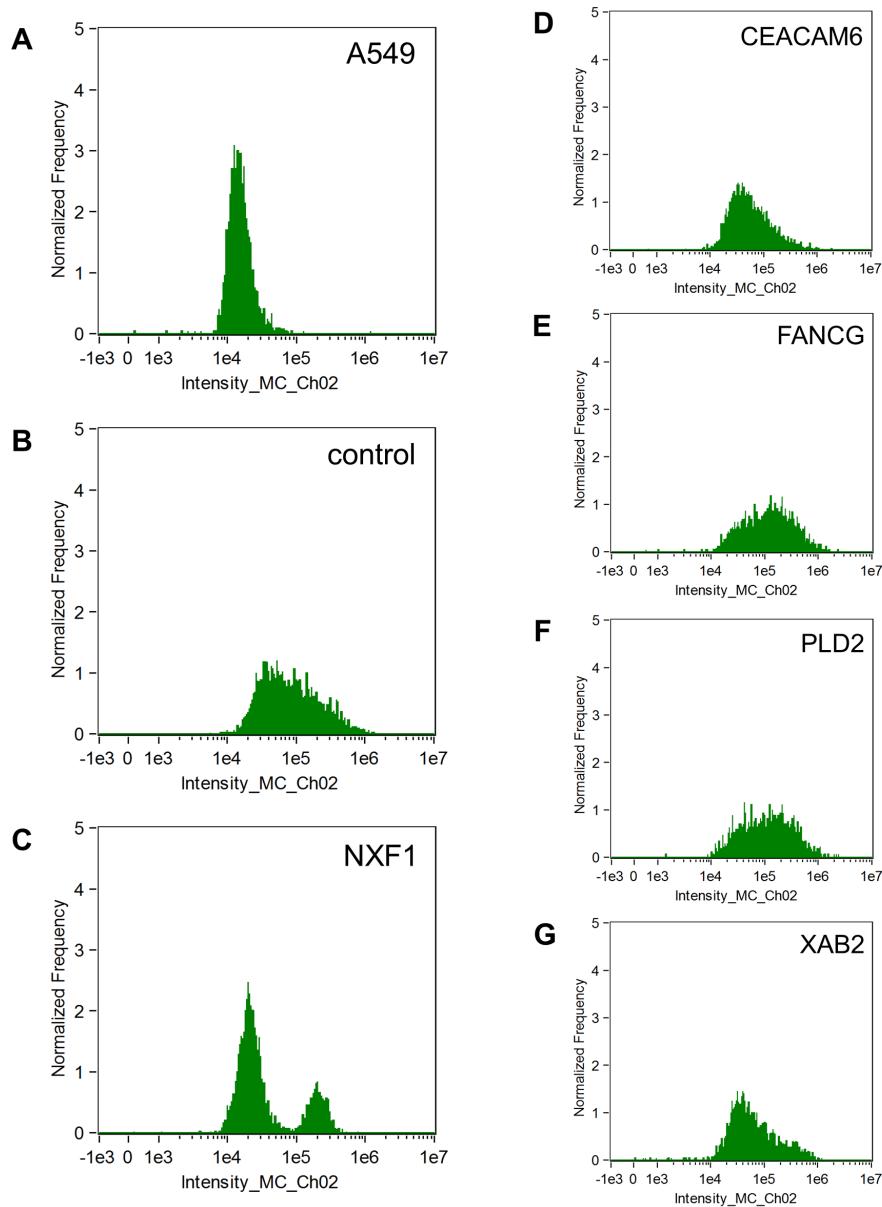
Figure A.4.: Flow cytometry measurement of eGFP from parental and transduced A549 cell lines during cell culture maintenance. PFA-fixated cells were measured by imaging flow cytometry using the 488 nm laser. The eGFP signal of single cells in focus was evaluated using the mean FI (mean pixel feature) of channel 2 (CH02) and visualized as histograms for parental A549 cells (A), the transduction control (B) and A549 cells overexpressing one of the following host cell factors: NXF1 (C), CEACAM6 (D), FANCG (E), PLD2 (F), XAB2 (G).

Table A.5.: HA titers and ranking results of cell lines overexpressing single host cell genes and infected by A/PR/8/34 (H1N1) at MOI 10^{-4}.

time p.i. (h)	HA titer[a]				Ranking value[b]			
	36	42	72	96	36	42	72	96
A549	1.05	1.44	1.85	1.97	0	0	0	0
control	0.97	1.39	1.60	1.87	0	0	0	0
CEACAM6	1.13	1.40	1.80	1.78	1	0	0	0
FANCG	1.27	1.55	1.76	1.85	3	1	0	0
NXF1	1.37	1.65	1.90	1.91	5	3	0	0
PLD2	1.16	1.49	1.91	1.88	1	0	0	0
XAB2	1.12	1.48	1.73	1.79	2	0	0	0

[a]HA titer given in $\log_{10}$ HA units/100 µl.
[b]Zero, 1, 2, 3, 4, 5 for increase in HA titer by $< 20\,\%$, $\geq 20\,\%$, $\geq 40\,\%$, $\geq 60\,\%$, $\geq 80\,\%$, $\geq 100\,\%$, respectively.
See Table A.6 in the appendix for the level of overexpression of the corresponding genes.

Table A.6.: Overexpression level of host cell genes in cell lines overexpressing one of the indicated genes as determined by $2^{-\Delta\Delta C_T}$ method.

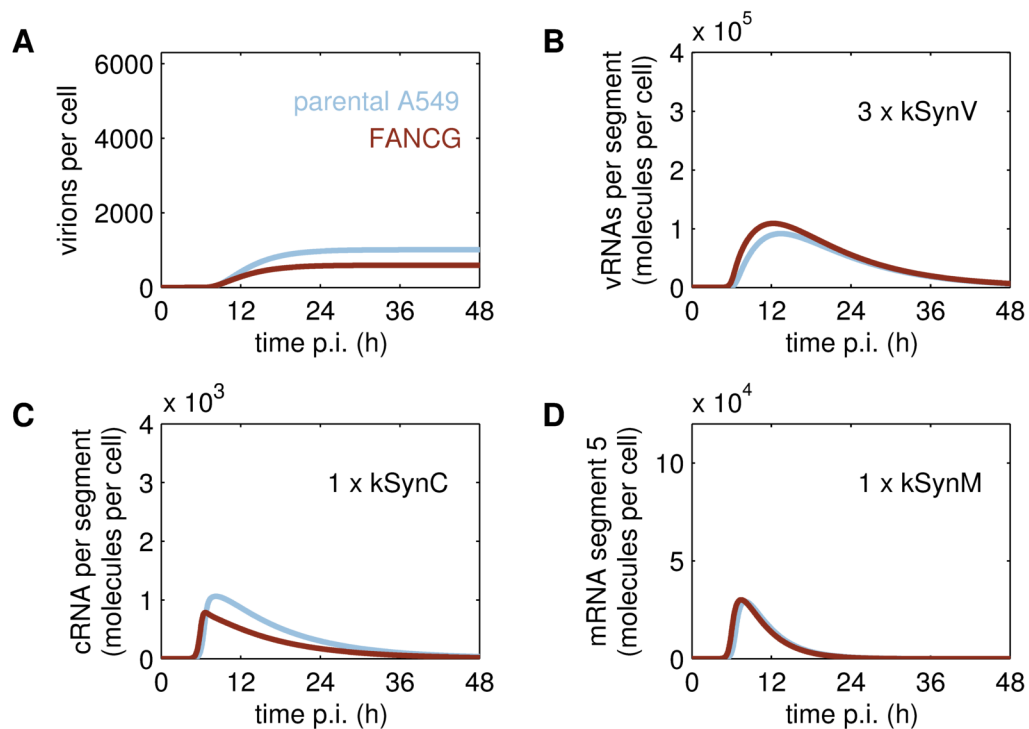| Gene overexpressed in corresponding SGO	Fold overexpression compared to parental A549 cells
CEACAM6	19
FANCG	7
NXF1	1.5
PLD2	14
XAB2	3

Figure A.5.: Simulating the impact of FANCG on the vRNA synthesis rate in A549 cells. Simulation of viral components in parental A549 cells and in an *in silico* A549 cell line with changed parameters according to findings for the impact of FANCG on viral polymerase activity, proposed by Tafforeau and colleagues [325]. Virus particle release (A) and dynamics of intracellular vRNA (B), cRNA (C) and mRNA (D) if overexpression of FANCG causes a three-fold increase in the vRNA synthesis rate.
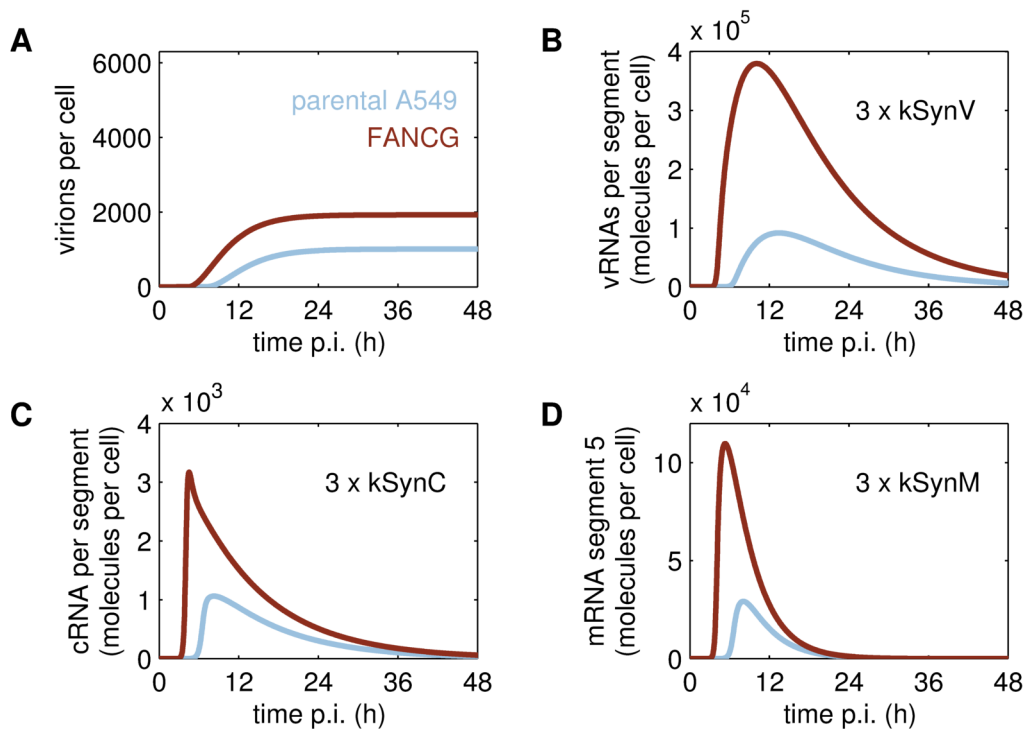
Figure A.6.: Simulating the impact of FANCG on the synthesis rate of vRNA, cRNA and mRNA synthesis in A549 cells. Simulation of viral components in parental A549 cells and in an *in silico* A549 cell line with changed parameters according to findings for the impact of FANCG on viral polymerase activity, proposed by Tafforeau and colleagues [325]. Virus particle release (A) and dynamics of intracellular vRNA (B), cRNA (C) and mRNA (D) if overexpression of FANCG causes a three-fold increase in the vRNA, cRNA and mRNA synthesis rate.

Figure A.7.: Simulating the impact of FANCG on the mRNA synthesis rate in A549 cells. Simulation of viral components in parental A549 cells and in an *in silico* A549 cell line with changed parameters according to findings for the impact of FANCG on viral polymerase activity, proposed by Tafforeau and colleagues [325]. Virus particle release (A) and dynamics of intracellular vRNA (B), cRNA (C) and mRNA (D) if overexpression of FANCG causes a three-fold increase in the mRNA synthesis rate.

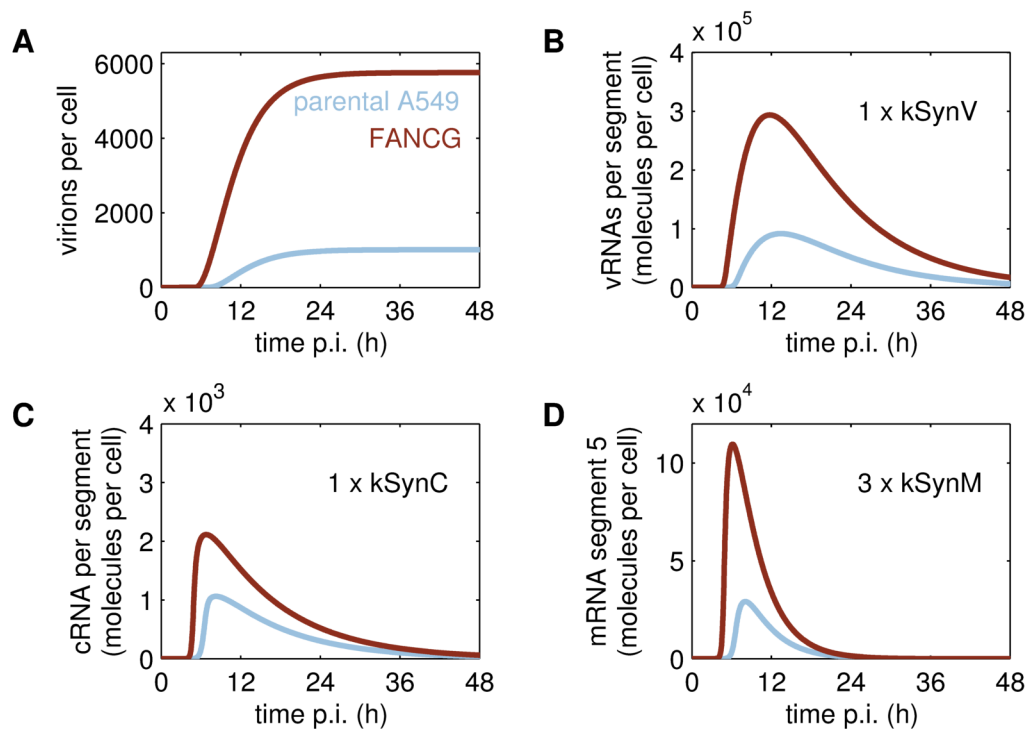## A.4. Cell lines overexpressing multiple genes

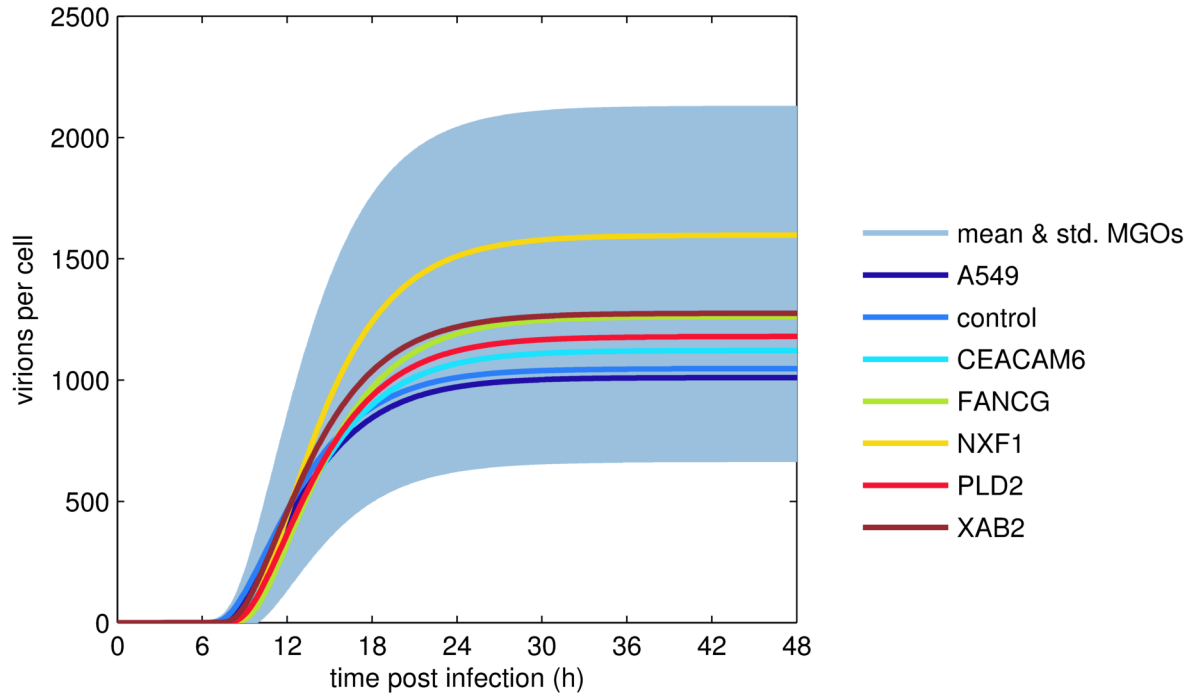**Figure A.8.: Simulated virus release dynamics of MGO CFNPX and A549 cells.**
Light blue area shows the mean and standard deviation of released virions from approximately
2×10^4 simulations with randomized parameter sets, for a simulated infection at MOI 1. Infection
of parental A549 cells, the transduction control and SGOs were simulated with parameter sets
according to Table A.3 (colors according to legend).

Table A.7.: HA titers and ranking results of cell lines overexpressing multiple host cell genes and infected by A/PR/8/34 (H1N1) at MOI 10^{-4}.

time p.i. (h)	HA titer[a]				Ranking value[b]			
	36	42	72	96	36	42	72	96
A549	1.05	1.44	1.85	1.97	0	0	0	0
control	0.97	1.39	1.60	1.87	0	0	0	0
MGO 1	1.49	1.67	1.96	1.92	5	3	0	0
MGO 2	1.56	1.69	2.01	2.02	5	3	2	0
MGO 3	1.55	1.67	2.01	1.95	5	3	2	0
MGO 4	1.38	1.56	1.89	1.79	5	1	0	0

[a]HA titer given in $\log_{10}$ HA units/100 µl.
[b]Zero, 1, 2, 3, 4, 5 for increase in HA titer by $< 20\,\%$, $\geq 20\,\%$, $\geq 40\,\%$, $\geq 60\,\%$, $\geq 80\,\%$, $\geq 100\,\%$, respectively.
MGO 1–3 overexpress all five host cell genes, MGO 4 overexpresses three host cell genes (FANCG, PLD2, XAB2). See Table A.8 in the appendix for the level of overexpression of the corresponding genes.

Table A.8.: Overexpression level of host cell genes in cell lines overexpressing multiple genes (MGOs) as determined by $2^{-\Delta\Delta C_T}$ method.

	Fold overexpression compared to parental A549 cells				
Gene name ↓	control	MGO 1	MGO 2	MGO 3	MGO 4
CEACAM6	3	12	57	25	n.o.
FANCG	1	10	1	20	15
NXF1	1	2	3	2	n.o.
PLD2	1	1	1	2.5	4
XAB2	1	1.5	7	4	11

n.o. - gene was not overexpressed.

$$\text{—— APPENDIX B ——}$$

Intracellular replication of DI RNAs

Here, we provide additional information on the models describing intracellular DI RNA replication and simulations thereof. This includes a list of parameters and model equations for growth of DI RNAs that originate from segment 1 (encoding PB2) or from segments 4–8, encoding HA, NP, NA, M1 and M2, and NS1 and NEP, respectively.

Table B.1.: List of parameters for the intracellular model of DI RNA replication.[a]

Parameter		Value	Source, Reference, Comment
F_{Adv}	$(-)$	4.93^{b}	Assumption (see Equation (3.2.25), Section 3.2.2)
k^{Cplx}	$(\text{molecules}^{-7} \cdot \text{h}^{-1})$	1	Rapid complex formation assumed
K_{i}	(molecules)	5.65×10^3	Adjusted[c]
$k_{\max}^{\text{Rel}}$	$(\text{virions}/(\text{cell} \cdot \text{h}))$	249.59	Adjusted[c]
K_{VRel}	(virions)	2800	Adjusted[c]
L_1^{V}	(nucleotides)	$2\,341$	[30]
L_2^{V}	(nucleotides)	$2\,341$	[30]
L_3^{V}	(nucleotides)	$2\,233$	[30]
L_4^{V}	(nucleotides)	$1\,778$	[30]
L_5^{V}	(nucleotides)	$1\,565$	[30]
L_6^{V}	(nucleotides)	$1\,413$	[30]
L_7^{V}	(nucleotides)	$1\,027$	[30]
L_8^{V}	(nucleotides)	890	[30]
L_9^{V}	(nucleotides)	395^{b}	[145]

[a]In addition to the parameters shown, here the model uses the values from Table A.1.
[b]If not otherwise indicated, we simulate growth of a model DI RNA originating from segment 1 with the corresponding length and F_{Adv}.
[c]Parameters used to simulate preferential packaging of DI vRNPs. See Equations (3.2.30)–(3.2.31), Section 3.2.2 for explanations.

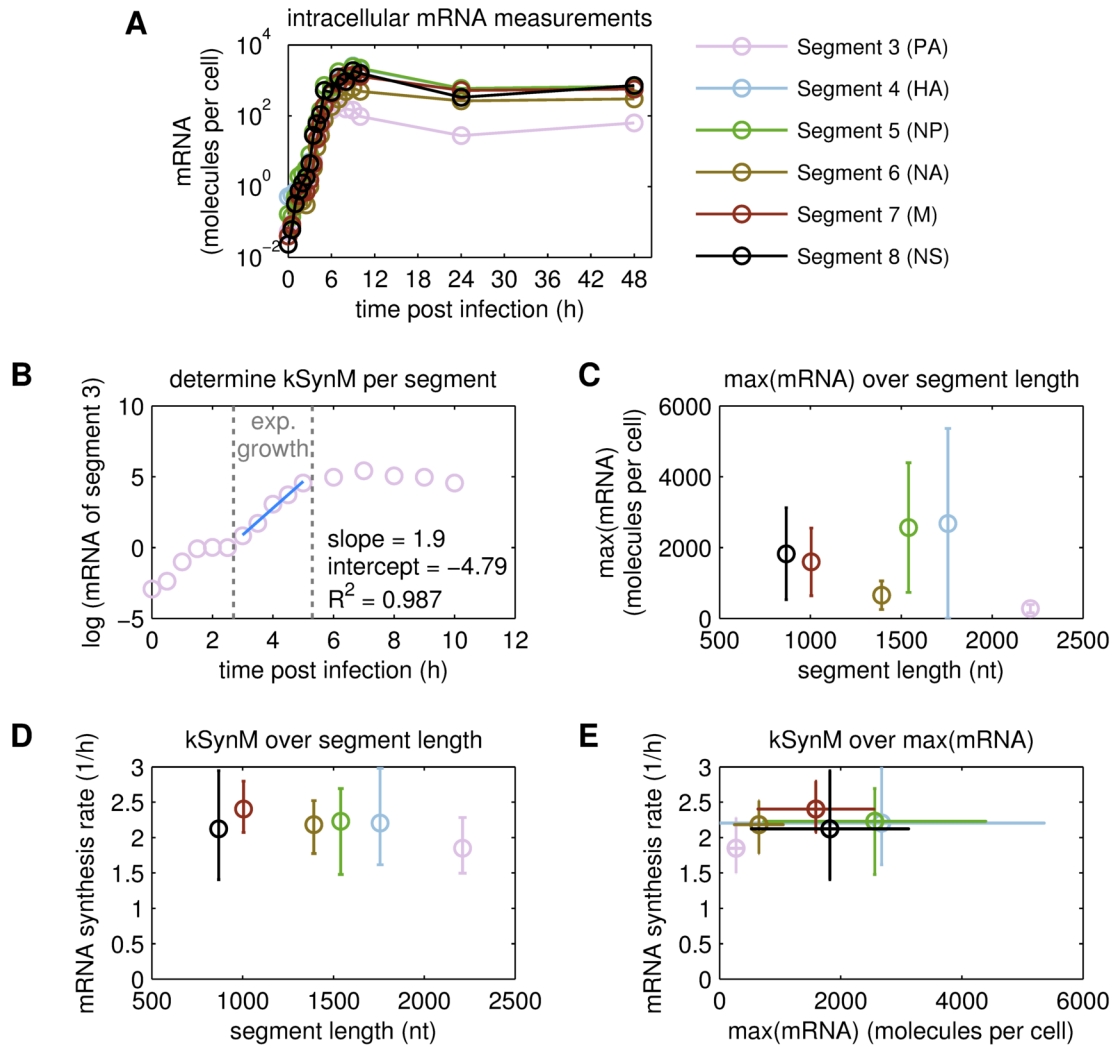# B.1. Length-dependency of RNA synthesis rates

Figure B.1.: Length-dependency of synthesis rates and maximum intracellular levels of influenza A virus full-length segments' mRNA. Adherent MDCK cells were infected by the influenza virus strain A/PR/8/34 (H1N1) at MOI 6 and intracellular viral mRNA levels were assessed by segment-specific RT-qPCR ($n = 3$). (A) Median mRNA values of the viral genome segments 3–8 (open circle, error bars were omitted for sake of simplicity). (B) Log-transformation (open circles) and linear regression (blue solid line) of median mRNA values were performed to determine the mRNA synthesis rate (kSynM) of each segment during the exponential growth phase (vertical gray dotted lines), exemplified using the mRNA measurements of segment 3. (C) Correlation of maximal intracellular mRNA levels and segment length (open circles, average ± standard deviation). (D) Correlation of kSynM and segment length (open circles). Error bars represent the 95 % confidence interval of the slope determined by linear regression, described in (B). (E) Correlation of kSynM and the maximal intracellular mRNA levels of each segment (open circles, horizontal and vertical error bars as in (C) and (D), respectively). Experiments conducted by Antje Pflugmacher, measurements of segment 5 published in [37]. Similar analyses were conducted for the viral cRNA and vRNA measurements of this study (Figure 4.9 in Section 4.2.1 and Figure B.2 in the appendix).
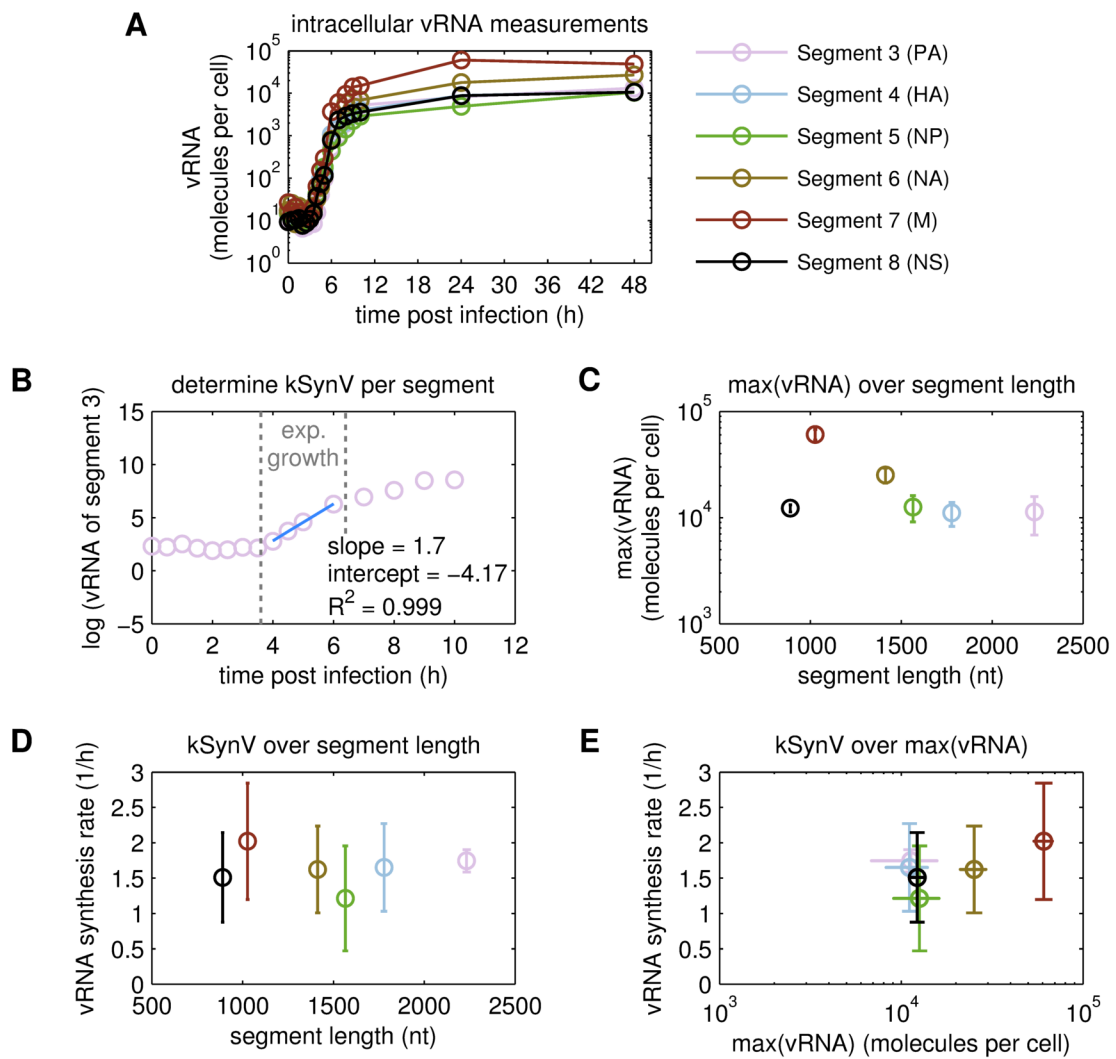
Figure B.2.: Length-dependency of synthesis rates and maximum intracellular levels of influenza A virus full-length segments' vRNA. For further details refer to the caption of Figure B.1.

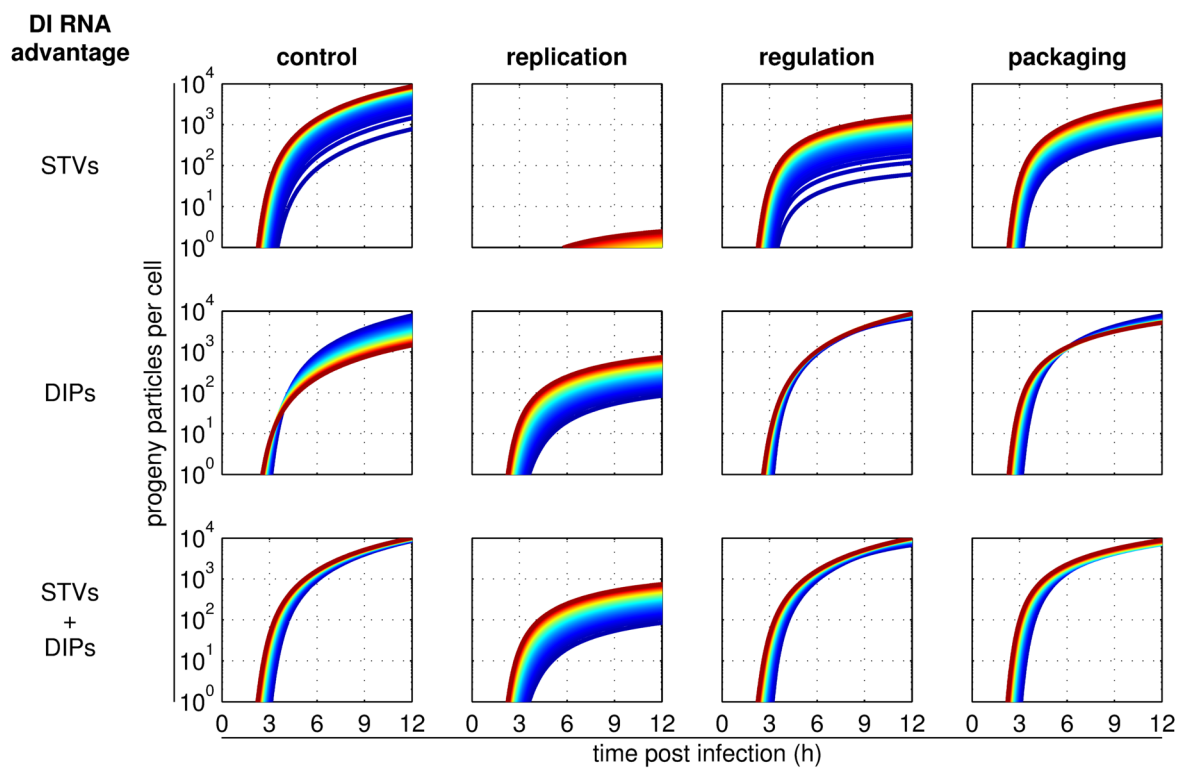## B.2. Different modes of DI RNA interference

Figure B.3.: Impact of DIP co-infection on virus release dynamics and virus yield for different interfering hypotheses. Virus release dynamics of progeny STVs (upper panel), DIPs (middle panel) and total virus particles (sum of STVs and DIPs, lower panel) for various simulated infections at a fixed initial amount of infecting DIPs (MODIP 5) in combination with increasing numbers of infecting STVs (MOI 0–30). Co-infection occurs simultaneously at 0 h p.i. The DIP carries a defective segment 1 (encoding PB2) with a length of 395 nt and exerts one of three different advantages over its STV at particular stages of the viral life cycle as indicated at the top of each column (bold letters). The gradual increase in color from dark blue to dark red used to visualize the simulation results (solid lines) corresponds to the increase in MOI, where dark blue denotes MOI zero and dark red MOI 30, respectively. The MOI was gradually increased with an increment of 0.5 STV/cell.
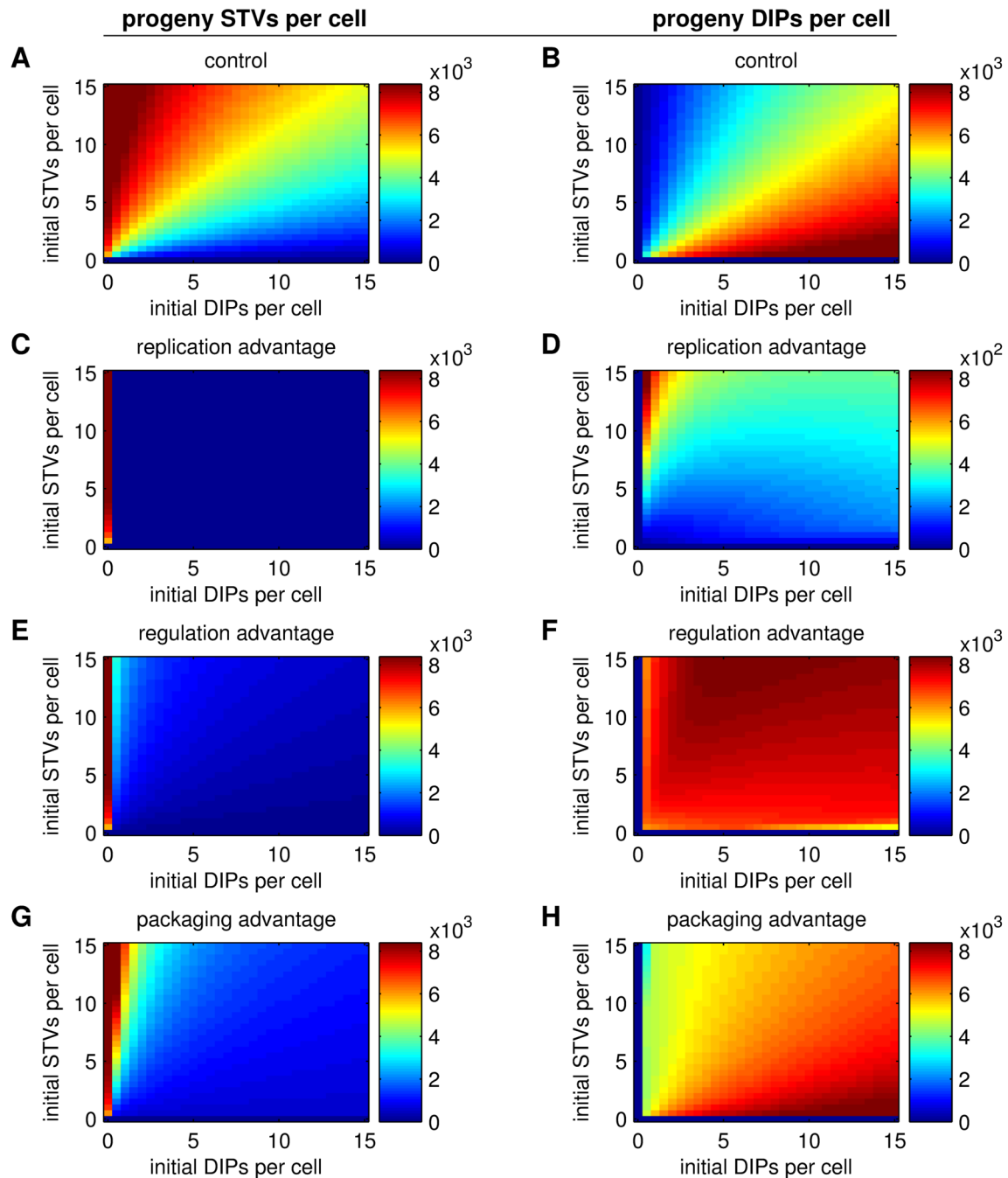
Figure B.4.: Influence of the MOI-to-MODIP ratio on cell-specific virus release.
Simulated number of progeny STVs (A, C, E, G) and DIPs (B, D, F, H) at $12\,\mathrm{h\,p.i.}$ considering
co-infections at various combinations of MOI and MODIP. Co-infection occurs simultaneously
at $0\,\mathrm{h\,p.i.}$ The DIP carries a defective segment 1 (S1, encoding PB2) with a length of $395\,\mathrm{nt}$
and exerts one of three different advantages over its STV at particular stages of the viral life
cycle as indicated in the title of each subfigure. Simulations of DI S1 are compared to those
of a full-length DI-like S1 ($2341\,\mathrm{nt}$) that has no propagation advantage (A, B). Please note
the different scaling of the color bar for (D). Results in (C, D) represent a validation of the
study by Laske and Heldt *et al.* [309], who simulated co-infections by DIPs with a DI RNA of
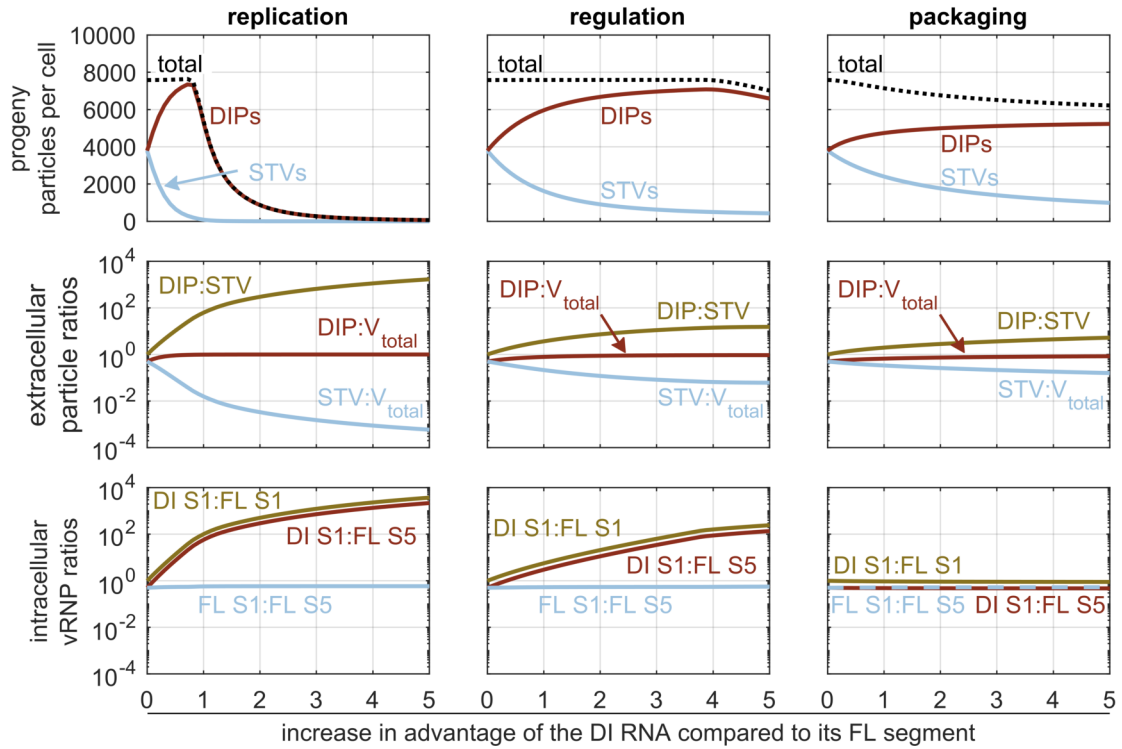segment 3 (encoding PA).

Figure B.5.: Impact of the DI RNAs' mode and strength of interference on DIP-to-STV ratios. Shown are changes in particle release and ratios of virus particles and intracellular vRNPs in a cell co-infection by one STV and one DIP. The DIP carries a DI RNA of segment 1 (S1, encoding PB2) which exerts an advantage over its full-length (FL) segment at one of the particular steps of the viral life cycle indicated at the top of each column (bold letters). The DI RNAs vary in length depending on their strength of interference, i.e., their advantage factor F_{Adv} (see Equation (3.2.25), Section 3.2.2), indicated on the abscissa of each plot. Co-infection occurs simultaneously at 0 h p.i. and model output is recorded at 12 h p.i. (Upper panel) Number of progeny DIPs and STVs. (Middle panel) Ratios of extracellular virus particles, where total number of virus particles V_{total} is the sum of DIPs and STVs. (Bottom panel) Intracellular vRNP ratios of DI S1, FL S1 and FL segment 5 (S5, encoding NP). Numbers of particle release and intracellular vRNPs correspond to results shown in Figure 4.13, Section 4.2.1.
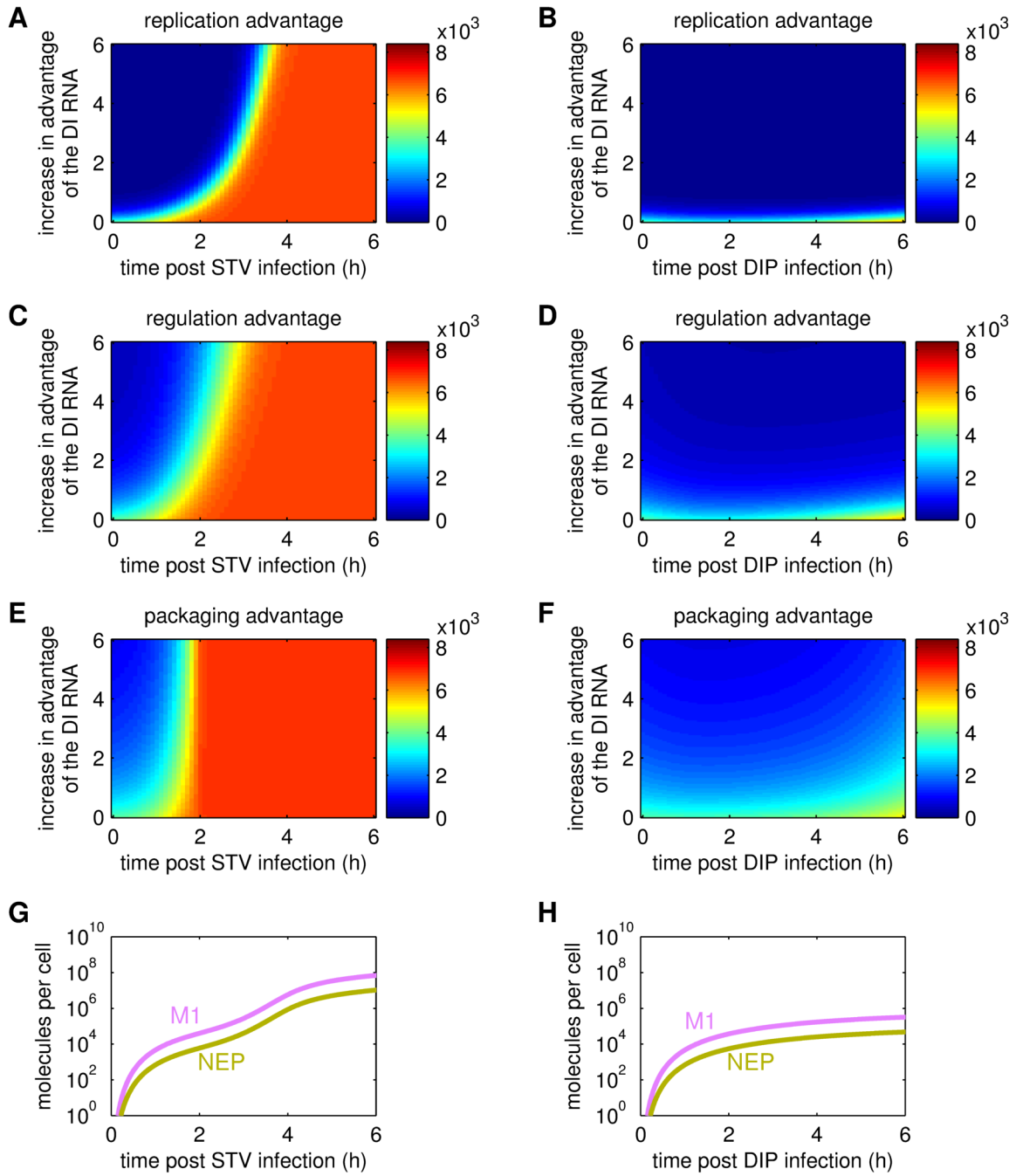
Figure B.6.: Impact of the DI RNAs' mode of interference on virus growth in response to various combinations of strength of interference and co-infection timings. Simulated infections of a cell by one STV and one DIP. The DIP carries a defective segment 1 (S1, encoding PB2) which exerts different advantages over its cognate FL segment, indicated in the figure titles. (A–F) Number of progeny STVs at 12 h post STV infection considering the indicated advantage and that either DIP infection (A, C, E) or STV infection (B, D, F) occurs with the indicated delay, respectively. (G, H) Number of unbound M1 and NEP in either an STV-only (G) or a DIP-only (H) infected cell. For (H) the DI S1 has an advantage of 0.5 and the corresponding length compared to its parental FL RNA (Equation (3.2.25), Section 3.2.2). The model used to simulate an advantage in DI RNA replication (A, B) follows the approach by Laske and Heldt *et al.* [309]. Corresponding DIP yields are given in Figure 4.15.

B.3. DI RNAs with a packaging advantage
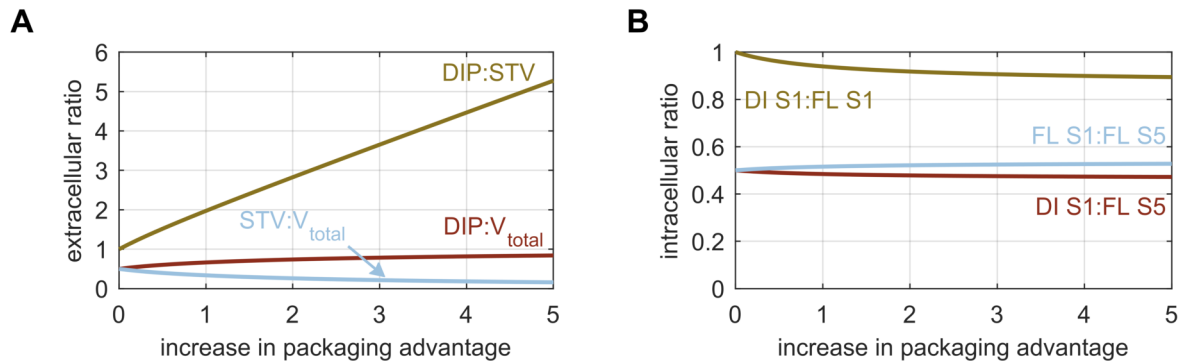
Figure B.7.: Impact of the strength of interference on DIP-to-STV ratios during co-infection by a DIP with an advantage in vRNP packaging. Shown are simulated ratios of virus particles and intracellular vRNPs in a cell co-infected by one DIP and one STV. The DIP carries a defective segment 1 (S1, encoding PB2) which varies in length depending on its strength of interference, i.e., its packaging advantage F_{Adv} (see Equation (3.2.25), Section 3.2.2). Co-infection occurs simultaneously at 0 h p.i. and model output is recorded at 12 h p.i. (A) Ratios of extracellular virus particles, where total number of virus particles V_{total} is the sum of DIPs and STVs. (B) Intracellular vRNP ratios of DI S1, full-length (FL) S1 and FL segment 5 (S5, encoding NP). Numbers of particle release and intracellular vRNPs correspond to results shown in Figure 4.13, Section 4.2.1.
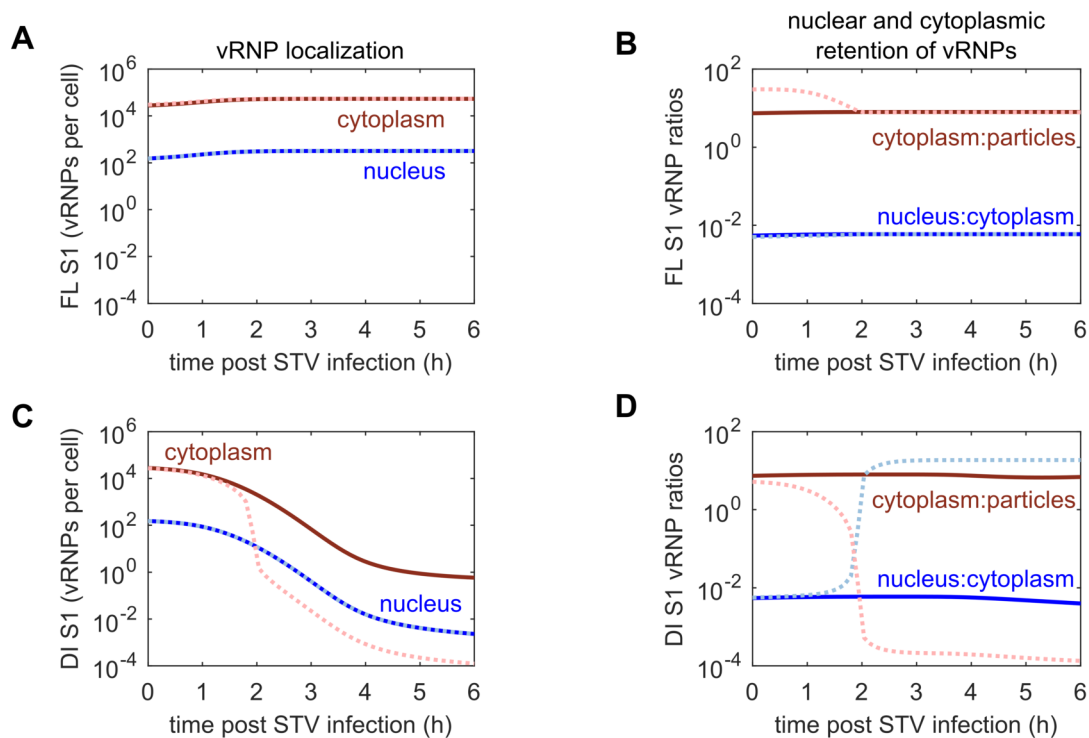
Figure B.8.: Localization of S1 vRNPs in response to delays in co-infection by a DIP with an advantage in vRNP packaging. Simulated numbers of S1 vRNPs in cells co-infected by one DIP and one STV. Model readouts were recorded at 12 h post STV infection. The DIP carries a defective segment 1 (S1, encoding PB2) which is 395 nt long ($F_{\mathrm{Adv}} = 4.93$). Simulations of DI S1 co-infections (light-colored dashed lines) are compared to those of a FL DI-like S1 (2341 nt) that has no propagation advantage (dark-colored solid lines). (A, C) Concentration of S1 vRNPs in the cytoplasm (brown) and in the nucleus (blue) of FL S1 and DI S1, respectively. (B, D) Cytoplasmic (brown) and nuclear (blue) retention of FL S1 and DI S1 vRNPs, respectively. Numbers of corresponding DIP and STV progeny release are shown in Figure 4.14 G, Section 4.2.1.

B.4. DI RNAs originating from different genome segments
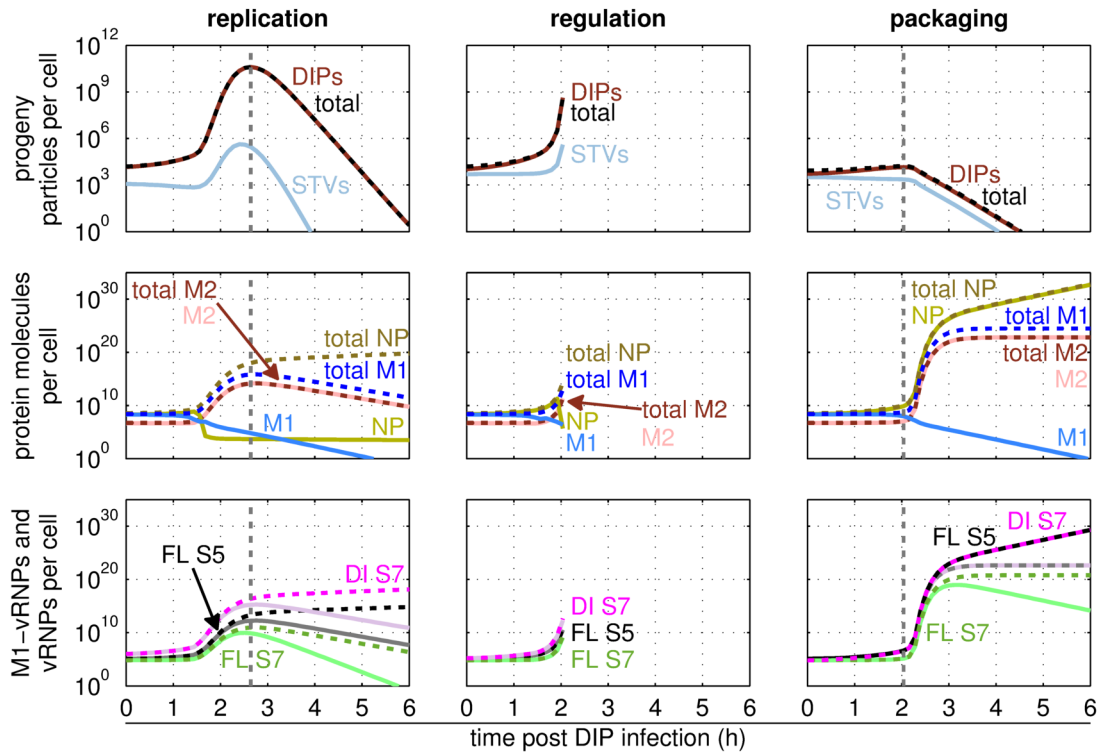
Figure B.9.: Impact of segment 7 DI RNAs' mode of interference and STV co-infection timing on virus growth. Simulated infection of a cell by one DIP and one STV. The DIP carries a DI RNA of segment 7 (S7, encoding M1 and M2) with $F_{\text{Adv}} = 0.5$. The DI RNA's mode of interference is indicated at the top of each column (bold letters). DIP infection occurs first and STV infection occurs with the indicated delay. Model output is recorded 12 h post STV infection. The vertical gray dashed lines indicate the optimal delay in STV co-infection for which DIP yield is maximal. (Upper panel) Number of progeny viruses. (Middle panel) Levels of total (dashed, dark-colored lines) and unbound (solid, light-colored lines) NP, M1 and M2. (Lower panel) Levels of total viral ribonucleoprotein complexes (vRNPs; dashed, dark-colored lines) and M1-vRNP complexes (solid, light-colored lines) of S7 and FL segment 5 (S5, encoding NP). For DI S7 with an advantage in regulation, simulations were obtained only when STV co-infection occurred no later than 2.3 h.
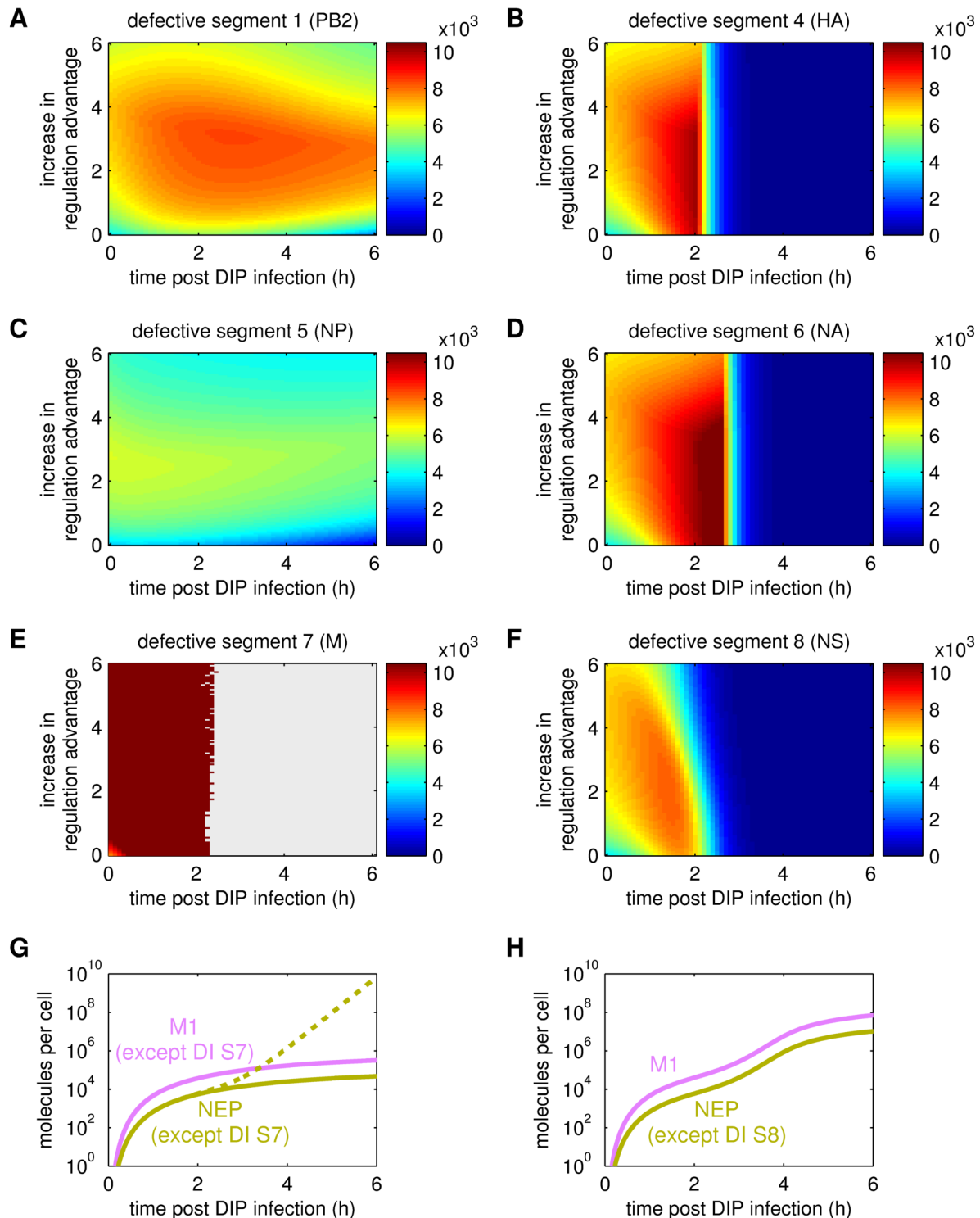
Figure B.10.: Growth of DI RNAs with an advantage in regulation that originate from different genome segments. Simulated infection of a cell by one DIP and one STV. (A–F) Number of progeny DIPs at 12 h post STV infection considering the indicated regulation advantage and delay in STV co-infection. The DI RNA's segment origin is indicated in the figure titles. (E) Conditions for which no simulations were obtained are highlighted in gray. (G, H) Dynamics of unbound M1 and NEP numbers in a cell infected by one DIP with $F_{\text{Adv}} = 0.5$. (G) The DI RNAs originate from either S1 or S5 (solid lines), or S7 (dashed line). (H) The DI RNAs originate from either S4, S6 or S8 (solid lines).
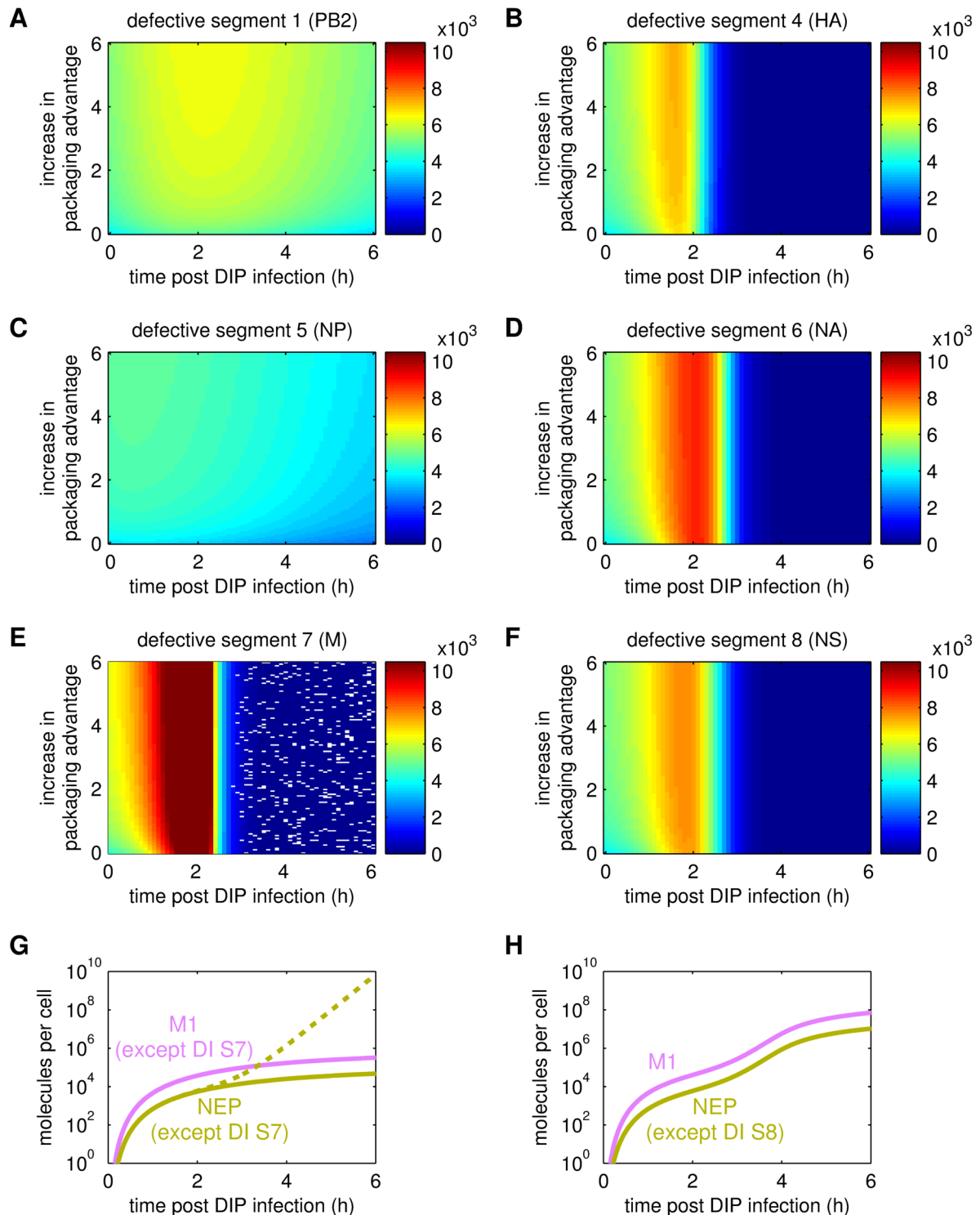
Figure B.11.: Growth of DI RNAs with an advantage in packaging that originate from different genome segments. Simulated infection of a cell by one DIP and one STV. (A–F) Number of progeny DIPs at 12 h post STV infection considering the indicated packaging advantage and delay in STV co-infection. The DI RNA's segment origin is indicated in the figure titles. (E) Conditions for which no simulations were obtained are highlighted in gray. (G, H) Dynamics of unbound M1 and NEP numbers in a cell infected by one DIP with $F_{Adv} = 0.5$. (G) The DI RNAs originate from either S1 or S5 (solid lines), or S7 (dashed line). (H) The DI RNAs originate from either S4, S6 or S8 (solid lines).
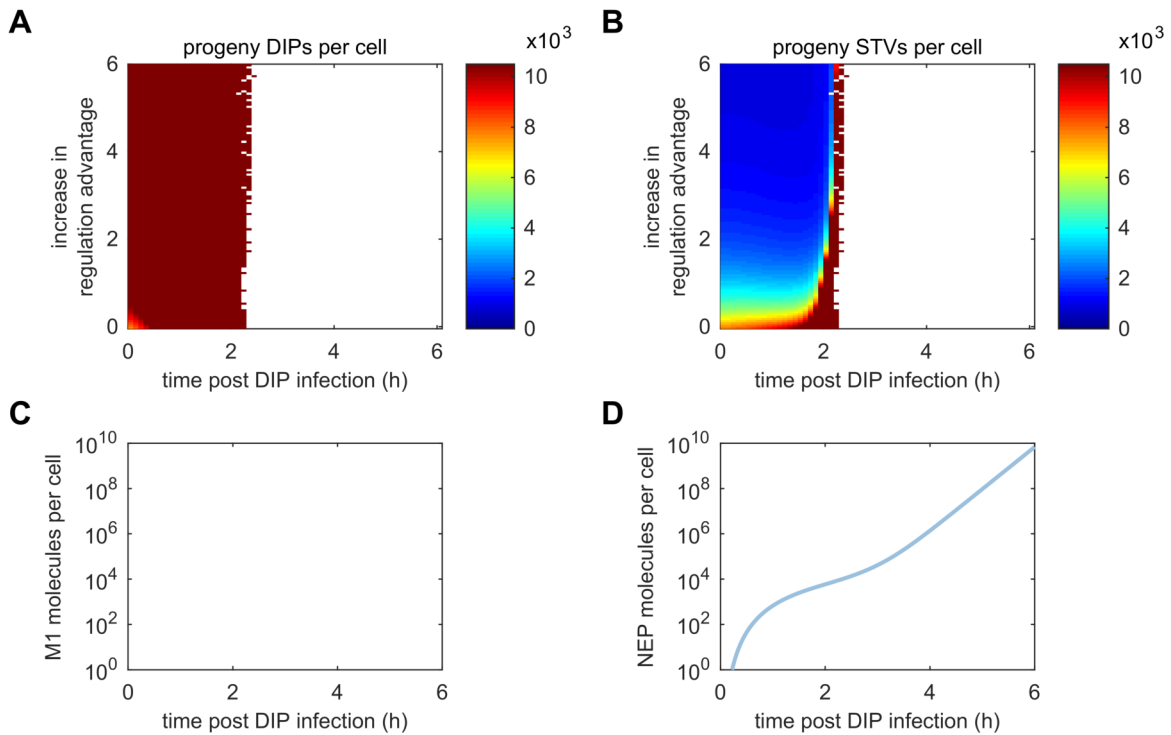
Figure B.12.: Virus growth in co-infections by DI RNAs with an advantage in regulation that originate from segment 7. Simulated infection of a cell by one DIP and one STV. The DIP carries DI RNA of segment 7 (encoding M1 and M2). (A, B) Number of progeny DIPs and STVs at 12 h post STV infection considering the indicated regulation advantage and delay in STV co-infection. Conditions for which no simulations were obtained are highlighted in gray. (C, D) Dynamics of unbound M1 and NEP numbers in a cell infected by one DIP with $F_{\mathrm{Adv}} = 0.5$.

B.5. Model for a DI RNA of segment 1

In addition to Section 3.2, we, here, list the complete set of equations used to describe intracellular virus replication upon co-infection by STVs and DIPs that carry a DI RNA of segment 1 (DI S1, encoding PB2). Since STVs and DIPs are antigenically identical, we assume that uptake of STVs and DIPs is similar. For entry of STVs, we used Equations (3.1.1)–(3.1.4) as before (Section 3.1.1, [18]) and added the corresponding equations for DIPs.

$$\frac{\mathrm{d}D^{\mathrm{Ex}}}{\mathrm{d}t} = k_{\mathrm{hi}}^{\mathrm{Dis}} D_{\mathrm{hi}}^{\mathrm{Att}} + k_{\mathrm{lo}}^{\mathrm{Dis}} D_{\mathrm{lo}}^{\mathrm{Att}} - \left(k_{\mathrm{hi}}^{\mathrm{Att}} B_{\mathrm{hi}} + k_{\mathrm{lo}}^{\mathrm{Att}} B_{\mathrm{lo}} \right) D^{\mathrm{Ex}},$$

$$\text{for} \quad B_{\mathrm{n}} = B_{\mathrm{n}}^{\mathrm{tot}} - V_{\mathrm{n}}^{\mathrm{Att}} - D_{\mathrm{n}}^{\mathrm{Att}}, \quad n \in \{\mathrm{hi}, \mathrm{lo}\},$$

$$\frac{\mathrm{d}D_{\mathrm{n}}^{\mathrm{Att}}}{\mathrm{d}t} = k_{\mathrm{n}}^{\mathrm{Att}} B_{\mathrm{n}} D^{\mathrm{Ex}} - \left(k_{\mathrm{n}}^{\mathrm{Dis}} + k^{\mathrm{En}} \right) D_{\mathrm{n}}^{\mathrm{Att}},$$

$$\frac{\mathrm{d}D^{\mathrm{En}}}{\mathrm{d}t} = k^{\mathrm{En}} \left(D_{\mathrm{hi}}^{\mathrm{Att}} + D_{\mathrm{lo}}^{\mathrm{Att}} \right) - \left(k^{\mathrm{Fus}} + k_{\mathrm{En}}^{\mathrm{Deg}} \right) D^{\mathrm{En}},$$

where D denotes the DIP. Then, viruses in endosomes (V^{En}, D^{En}) fuse and release a complex of eight genome segments to the cytoplasm.

$$\frac{\mathrm{d}V^{\mathrm{cyt}}}{\mathrm{d}t} = k^{\mathrm{Fus}} V^{\mathrm{En}} - k^{\mathrm{Imp}} V^{\mathrm{cyt}},$$

$$\frac{\mathrm{d}D^{\mathrm{cyt}}}{\mathrm{d}t} = k^{\mathrm{Fus}} D^{\mathrm{En}} - k^{\mathrm{Imp}} D^{\mathrm{cyt}},$$

where V^{cyt} and D^{cyt} contain FL vRNAs of segments 2–8, and one copy of a FL S1 or a DI S1, respectively. Upon nuclear import, those complexes dissociate and the individual vRNA segments are transcribed and replicated separately.

$$\frac{\mathrm{d}Vp_{\mathrm{k}}^{\mathrm{nuc}}}{\mathrm{d}t} = k^{\mathrm{Imp}} V^{\mathrm{cyt}} + k^{\mathrm{Imp}} D^{\mathrm{cyt}} + k_{\mathrm{NP}}^{\mathrm{Bind}} P_{\mathrm{NP}} R_{\mathrm{RdRp,k}}^{\mathrm{V}} - \left(k_{\mathrm{M1}}^{\mathrm{Bind}} P_{\mathrm{M1}} + k_{\mathrm{Rnp}}^{\mathrm{Deg}} \right) Vp_{\mathrm{k}}^{\mathrm{nuc}},$$

$$\text{for} \quad k = 2, \dots, 8 \quad \text{and}$$

$$\frac{\mathrm{d}Vp_{1}^{\mathrm{nuc}}}{\mathrm{d}t} = k^{\mathrm{Imp}} V^{\mathrm{cyt}} + k_{\mathrm{NP}}^{\mathrm{Bind}} P_{\mathrm{NP}} R_{\mathrm{RdRp,1}}^{\mathrm{V}} - \left(k_{\mathrm{M1}}^{\mathrm{Bind}} P_{\mathrm{M1}} + k_{\mathrm{Rnp}}^{\mathrm{Deg}} \right) Vp_{1}^{\mathrm{nuc}},$$

$$\frac{\mathrm{d}Vp_{9}^{\mathrm{nuc}}}{\mathrm{d}t} = k^{\mathrm{Imp}} D^{\mathrm{cyt}} + k_{\mathrm{NP}}^{\mathrm{Bind}} P_{\mathrm{NP}} R_{\mathrm{RdRp,9}}^{\mathrm{V}} - \left(k_{\mathrm{M1}}^{\mathrm{Bind}} P_{\mathrm{M1}} + k_{\mathrm{Rnp}}^{\mathrm{Deg}} \right) Vp_{9}^{\mathrm{nuc}},$$

$$\frac{\mathrm{d}R_{\mathrm{k}}^{\mathrm{C}}}{\mathrm{d}t} = k_{\mathrm{C}}^{\mathrm{Syn}} Vp_{\mathrm{k}}^{\mathrm{nuc}} - k_{\mathrm{RdRp}}^{\mathrm{Bind}} P_{\mathrm{RdRp}} R_{\mathrm{k}}^{\mathrm{C}} - k_{\mathrm{R}}^{\mathrm{Deg}} R_{\mathrm{k}}^{\mathrm{C}}, \quad k = 1, \dots, 9,$$

$$\frac{\mathrm{d}R_{\mathrm{k}}^{\mathrm{V}}}{\mathrm{d}t} = k_{\mathrm{V}}^{\mathrm{Syn}} Cp_{\mathrm{k}} - k_{\mathrm{RdRp}}^{\mathrm{Bind}} P_{\mathrm{RdRp}} R_{\mathrm{k}}^{\mathrm{V}} - k_{\mathrm{R}}^{\mathrm{Deg}} R_{\mathrm{k}}^{\mathrm{V}},$$

$$\frac{\mathrm{d}R_{\mathrm{RdRp,k}}^{\mathrm{C}}}{\mathrm{d}t} = k_{\mathrm{RdRp}}^{\mathrm{Bind}} P_{\mathrm{RdRp}} R_{\mathrm{k}}^{\mathrm{C}} - k_{\mathrm{NP}}^{\mathrm{Bind}} P_{\mathrm{NP}} R_{\mathrm{RdRp,k}}^{\mathrm{C}} - k_{\mathrm{RRdRp}}^{\mathrm{Deg}} R_{\mathrm{RdRp,k}}^{\mathrm{C}},$$

$$\frac{\mathrm{d}R_{\mathrm{RdRp,k}}^{\mathrm{V}}}{\mathrm{d}t} = k_{\mathrm{RdRp}}^{\mathrm{Bind}} P_{\mathrm{RdRp}} R_{\mathrm{k}}^{\mathrm{V}} - k_{\mathrm{NP}}^{\mathrm{Bind}} P_{\mathrm{NP}} R_{\mathrm{RdRp,k}}^{\mathrm{V}} - k_{\mathrm{RRdRp}}^{\mathrm{Deg}} R_{\mathrm{RdRp,k}}^{\mathrm{V}},$$

$$\frac{\mathrm{d}Cp_{\mathrm{k}}}{\mathrm{d}t} = k_{\mathrm{NP}}^{\mathrm{Bind}} P_{\mathrm{NP}} R_{\mathrm{RdRp,k}}^{\mathrm{C}} - k_{\mathrm{Rnp}}^{\mathrm{Deg}} Cp_{\mathrm{,k}},$$

$$\frac{\mathrm{d}Vp_{\mathrm{M1,k}}^{\mathrm{nuc}}}{\mathrm{d}t} = k_{\mathrm{M1}}^{\mathrm{Bind}} P_{\mathrm{M1}} Vp_{\mathrm{k}}^{\mathrm{nuc}} - \left(k^{\mathrm{Exp}} P_{\mathrm{NEP}} + k_{\mathrm{Rnp}}^{\mathrm{Deg}} \right) Vp_{\mathrm{M1,k}}^{\mathrm{nuc}}.$$

where $k = 1, \ldots, 8$ are the FL segments and $k = 9$ denotes the DI S1. Once M1 binds to vRNPs, they become inactive and are no further template for viral replication and transcription. Then, nuclear export of M1-vRNP complexes is initiated upon binding of NEP.

$$\frac{\mathrm{d}Vp_{\mathrm{M1,k}}^{\mathrm{cyt}}}{\mathrm{d}t} = k^{\mathrm{Exp}} P_{\mathrm{NEP}} Vp_{\mathrm{M1,k}}^{\mathrm{nuc}} - k^{\mathrm{Cplx}} Vp_{\mathrm{M1,1}}^{\mathrm{cyt}} \prod_{k} Vp_{\mathrm{M1,k}}^{\mathrm{cyt}}$$
$$- k^{\mathrm{Cplx}} Vp_{\mathrm{M1,9}}^{\mathrm{cyt}} \prod_{k} Vp_{\mathrm{M1,k}}^{\mathrm{cyt}} - k_{\mathrm{Rnp}}^{\mathrm{Deg}} Vp_{\mathrm{M1,k}}^{\mathrm{cyt}},$$

$$\text{for} \quad k = 2, \ldots, 8 \quad \text{and}$$

$$\frac{\mathrm{d}Vp_{\mathrm{M1,1}}^{\mathrm{cyt}}}{\mathrm{d}t} = k^{\mathrm{Exp}} P_{\mathrm{NEP}} Vp_{\mathrm{M1,1}}^{\mathrm{nuc}} - k^{\mathrm{Cplx}} Vp_{\mathrm{M1,1}}^{\mathrm{cyt}} \prod_{k} Vp_{\mathrm{M1,k}}^{\mathrm{cyt}} - k_{\mathrm{Rnp}}^{\mathrm{Deg}} Vp_{\mathrm{M1,1}}^{\mathrm{cyt}},$$

$$\frac{\mathrm{d}Vp_{\mathrm{M1,9}}^{\mathrm{cyt}}}{\mathrm{d}t} = k^{\mathrm{Exp}} P_{\mathrm{NEP}} Vp_{\mathrm{M1,9}}^{\mathrm{nuc}} - k^{\mathrm{Cplx}} Vp_{\mathrm{M1,9}}^{\mathrm{cyt}} \prod_{k} Vp_{\mathrm{M1,k}}^{\mathrm{cyt}} - k_{\mathrm{Rnp}}^{\mathrm{Deg}} Vp_{\mathrm{M1,9}}^{\mathrm{cyt}},$$

where k^{Cplx} denotes the formation rate for cytoplasmic complexes that consists of eight progeny vRNPs, i.e., vRNPs of segments 2–8 and either the FL S1 or the DI S1. Viral mRNA and protein synthesis was described by the following equations.

$$\frac{\mathrm{d}R_{\mathrm{k}}^{\mathrm{M}}}{\mathrm{d}t} = \frac{k_{\mathrm{M}}^{\mathrm{Syn}}}{L_{\mathrm{k}}} Vp_{\mathrm{k}}^{\mathrm{nuc}} - k_{\mathrm{M}}^{\mathrm{Deg}} R_{\mathrm{k}}^{\mathrm{M}}, \quad k = 1, \ldots, 8,$$

$$\frac{\mathrm{d}P_{\mathrm{PB1}}}{\mathrm{d}t} = \frac{k_{\mathrm{P}}^{\mathrm{Syn}}}{D_{\mathrm{Rib}}} R_{2}^{\mathrm{M}} - k^{\mathrm{RdRp}} P_{\mathrm{PB1}} P_{\mathrm{PB2}} P_{\mathrm{PA}},$$

$$\frac{\mathrm{d}P_{\mathrm{PB2}}}{\mathrm{d}t} = \frac{k_{\mathrm{P}}^{\mathrm{Syn}}}{D_{\mathrm{Rib}}} R_{1}^{\mathrm{M}} - k^{\mathrm{RdRp}} P_{\mathrm{PB1}} P_{\mathrm{PB2}} P_{\mathrm{PA}},$$

$$\frac{\mathrm{d}P_{\mathrm{PA}}}{\mathrm{d}t} = \frac{k_{\mathrm{P}}^{\mathrm{Syn}}}{D_{\mathrm{Rib}}} R_{3}^{\mathrm{M}} - k^{\mathrm{RdRp}} P_{\mathrm{PB1}} P_{\mathrm{PB2}} P_{\mathrm{PA}},$$

$$\frac{\mathrm{d}P_{\mathrm{RdRp}}}{\mathrm{d}t} = k^{\mathrm{RdRp}} P_{\mathrm{PB1}} P_{\mathrm{PB2}} P_{\mathrm{PA}} - k_{\mathrm{RdRp}}^{\mathrm{Bind}} P_{\mathrm{RdRp}} \sum_{k} \left[R_{\mathrm{k}}^{\mathrm{V}} + R_{\mathrm{k}}^{\mathrm{C}} \right], \quad k = 1, \ldots, 9,$$

$$\frac{\mathrm{d}P_{\mathrm{NP}}}{\mathrm{d}t} = \frac{k_{\mathrm{P}}^{\mathrm{Syn}}}{D_{\mathrm{Rib}}} R_5^{\mathrm{M}} - k_{\mathrm{NP}}^{\mathrm{Bind}} P_{\mathrm{NP}} \sum_k \frac{L_k^{\mathrm{V}}}{N_{\mathrm{NP}}^{\mathrm{Nuc}}} \left(R_{\mathrm{RdRp},k}^{\mathrm{V}} + R_{\mathrm{RdRp},k}^{\mathrm{C}} \right),$$

$$\frac{\mathrm{d}P_{\mathrm{M1}}}{\mathrm{d}t} = \frac{k_{\mathrm{P}}^{\mathrm{Syn}}}{D_{\mathrm{Rib}}} \left(1 - F_{\mathrm{Spl7}} \right) R_7^{\mathrm{M}} - k_{\mathrm{M1}}^{\mathrm{Bind}} P_{\mathrm{M1}} \sum_k \frac{L_k^{\mathrm{V}}}{N_{\mathrm{M1}}^{\mathrm{Nuc}}} Vp_k^{\mathrm{nuc}}$$
$$- (N_{\mathrm{P_{M1}}} - \sum_{p=1,\ldots,8} \frac{L_p^{\mathrm{V}}}{N_{\mathrm{M1}}^{\mathrm{Nuc}}}) r^{\mathrm{Rel}} - (N_{\mathrm{P_{M1}}} - \sum_{p=2,\ldots,9} \frac{L_p^{\mathrm{V}}}{N_{\mathrm{M1}}^{\mathrm{Nuc}}}) r_{\mathrm{D}}^{\mathrm{Rel}},$$

$$\frac{\mathrm{d}P_{\mathrm{NEP}}}{\mathrm{d}t} = \frac{k_{\mathrm{P}}^{\mathrm{Syn}}}{D_{\mathrm{Rib}}} F_{\mathrm{Spl8}} R_8^{\mathrm{M}} - k^{\mathrm{Exp}} P_{\mathrm{NEP}} \sum_k Vp_{\mathrm{M1},k}^{\mathrm{nuc}},$$

$$\frac{\mathrm{d}P_{\mathrm{HA}}}{\mathrm{d}t} = \frac{k_{\mathrm{P}}^{\mathrm{Syn}}}{D_{\mathrm{Rib}}} R_4^{\mathrm{M}} - N_{\mathrm{P_{HA}}} \left(r^{\mathrm{Rel}} + r_{\mathrm{D}}^{\mathrm{Rel}} \right),$$

$$\frac{\mathrm{d}P_{\mathrm{NA}}}{\mathrm{d}t} = \frac{k_{\mathrm{P}}^{\mathrm{Syn}}}{D_{\mathrm{Rib}}} R_6^{\mathrm{M}} - N_{\mathrm{P_{NA}}} \left(r^{\mathrm{Rel}} + r_{\mathrm{D}}^{\mathrm{Rel}} \right),$$

$$\frac{\mathrm{d}P_{\mathrm{M2}}}{\mathrm{d}t} = \frac{k_{\mathrm{P}}^{\mathrm{Syn}}}{D_{\mathrm{Rib}}} F_{\mathrm{Spl7}} R_7^{\mathrm{M}} - N_{\mathrm{P_{M2}}} \left(r^{\mathrm{Rel}} + r_{\mathrm{D}}^{\mathrm{Rel}} \right),$$

where $r_{\mathrm{D}}^{\mathrm{Rel}}$ is the release rate of DIPs. For assembly and budding of progeny viruses, complexes of eight progeny vRNPs are formed.

$$\frac{\mathrm{d}V_{\mathrm{Cplx}}^{\mathrm{cyt}}}{\mathrm{d}t} = k^{\mathrm{Cplx}} Vp_{\mathrm{M1},1}^{\mathrm{cyt}} \prod_k Vp_{\mathrm{M1},k}^{\mathrm{cyt}} - r^{\mathrm{Rel}} - k_{\mathrm{Rnp}}^{\mathrm{Deg}} V_{\mathrm{Cplx}}^{\mathrm{cyt}}, \quad k = 2, \ldots, 8,$$

$$\frac{\mathrm{d}D_{\mathrm{Cplx}}^{\mathrm{cyt}}}{\mathrm{d}t} = k^{\mathrm{Cplx}} Vp_{\mathrm{M1},9}^{\mathrm{cyt}} \prod_k Vp_{\mathrm{M1},k}^{\mathrm{cyt}} - r_{\mathrm{D}}^{\mathrm{Rel}} - k_{\mathrm{Rnp}}^{\mathrm{Deg}} D_{\mathrm{Cplx}}^{\mathrm{cyt}},$$

where $V_{\mathrm{Cplx}}^{\mathrm{cyt}}$ and $D_{\mathrm{Cplx}}^{\mathrm{cyt}}$ denote the complexes that contain vRNPs of segments 2–8 and either the FL S1 or the DI S1, respectively. For virus release, we adjusted Equation (3.1.26) by assuming that unbound polymerases, NP and NEP are not required for virus budding (see Section 3.2.1 for further explanations).

$$\frac{\mathrm{d}V^{\mathrm{Rel}}}{\mathrm{d}t} = r^{\mathrm{Rel}} = 8 k^{\mathrm{Rel}} V_{\mathrm{Cplx}}^{\mathrm{cyt}} \prod_j \frac{P_j}{P_j + K_{V^{\mathrm{Rel}}} N_{\mathrm{P_j}}},$$

$$\frac{\mathrm{d}D^{\mathrm{Rel}}}{\mathrm{d}t} = r_{\mathrm{D}}^{\mathrm{Rel}} = 8 k^{\mathrm{Rel}} D_{\mathrm{Cplx}}^{\mathrm{cyt}} \prod_j \frac{P_j}{P_j + K_{V^{\mathrm{Rel}}} N_{\mathrm{P_j}}},$$

$$\text{with} \quad j \in \{ \mathrm{HA}, \mathrm{NA}, \mathrm{M1}, \mathrm{M2} \},$$

where V^{Rel} and D^{Rel} are the STVs and DIPs, respectively, that are released from the cell.

B.6. Models for DI RNAs of different genome segments

To simulate co-infections by DI RNAs that originate from segments 4–8, we used the same equations as presented in Section B.5. In the following, we highlight those equations that have to be adjusted accordingly. Equation (3.2.9) remains unaffected.

$$\frac{\mathrm{d}Vp_{\mathrm{k}}^{\mathrm{nuc}}}{\mathrm{d}t} = k^{\mathrm{Imp}}V^{\mathrm{cyt}} + k^{\mathrm{Imp}}D^{\mathrm{cyt}} + k_{\mathrm{NP}}^{\mathrm{Bind}}P_{\mathrm{NP}}R_{\mathrm{RdRp,k}}^{\mathrm{V}} - \left(k_{\mathrm{M1}}^{\mathrm{Bind}}P_{\mathrm{M1}} + k_{\mathrm{Rnp}}^{\mathrm{Deg}}\right)Vp_{\mathrm{k}}^{\mathrm{nuc}},$$

with $k = 1, 2, 3, 5, \ldots, 8$ for DI S4,

with $k = 1, 2, 3, 4, 6 \ldots, 8$ for DI S5,

with $k = 1, 2, 3, 4, 5, 7, 8$ for DI S6,

with $k = 1, \ldots, 6, 8$ for DI S7,

with $k = 1, \ldots, 7$ for DI S8,

$$\frac{\mathrm{d}Vp_{\mathrm{i}}^{\mathrm{nuc}}}{\mathrm{d}t} = k^{\mathrm{Imp}}V^{\mathrm{cyt}} + k_{\mathrm{NP}}^{\mathrm{Bind}}P_{\mathrm{NP}}R_{\mathrm{RdRp,i}}^{\mathrm{V}} - \left(k_{\mathrm{M1}}^{\mathrm{Bind}}P_{\mathrm{M1}} + k_{\mathrm{Rnp}}^{\mathrm{Deg}}\right)Vp_{\mathrm{i}}^{\mathrm{nuc}},$$

with $i = 4$ for DI S4,

with $i = 5$ for DI S5,

with $i = 6$ for DI S6,

with $i = 7$ for DI S7,

with $i = 8$ for DI S8,

$$\frac{\mathrm{d}Vp_{\mathrm{M1,k}}^{\mathrm{cyt}}}{\mathrm{d}t} = k^{\mathrm{Exp}}P_{\mathrm{NEP}}Vp_{\mathrm{M1,k}}^{\mathrm{nuc}} - k^{\mathrm{Cplx}}Vp_{\mathrm{M1,i}}^{\mathrm{cyt}}\prod_{k}Vp_{\mathrm{M1,k}}^{\mathrm{cyt}} - k^{\mathrm{Cplx}}Vp_{\mathrm{M1,9}}^{\mathrm{cyt}}\prod_{k}Vp_{\mathrm{M1,k}}^{\mathrm{cyt}} - k_{\mathrm{Rnp}}^{\mathrm{Deg}}Vp_{\mathrm{M1,k}}^{\mathrm{cyt}},$$

$$\frac{\mathrm{d}Vp_{\mathrm{M1,i}}^{\mathrm{cyt}}}{\mathrm{d}t} = k^{\mathrm{Exp}}P_{\mathrm{NEP}}Vp_{\mathrm{M1,i}}^{\mathrm{nuc}} - k^{\mathrm{Cplx}}Vp_{\mathrm{M1,i}}^{\mathrm{cyt}}\prod_{k}Vp_{\mathrm{M1,k}}^{\mathrm{cyt}} - k_{\mathrm{Rnp}}^{\mathrm{Deg}}Vp_{\mathrm{M1,i}}^{\mathrm{cyt}},$$

$$\frac{\mathrm{d}P_{\mathrm{M1}}}{\mathrm{d}t} = \frac{k_{\mathrm{P}}^{\mathrm{Syn}}}{D_{\mathrm{Rib}}}\left(1 - F_{\mathrm{Spl7}}\right)R_{7}^{\mathrm{M}} - k_{\mathrm{M1}}^{\mathrm{Bind}}P_{\mathrm{M1}}\sum_{m=1,\ldots,9}\frac{L_{\mathrm{m}}^{\mathrm{V}}}{N_{\mathrm{M1}}^{\mathrm{Nuc}}}Vp_{\mathrm{m}}^{\mathrm{nuc}}$$

$$- (N_{\mathrm{P_{M1}}} - \sum_{p=1,\ldots,8}\frac{L_{\mathrm{p}}^{\mathrm{V}}}{N_{\mathrm{M1}}^{\mathrm{Nuc}}})r^{\mathrm{Rel}} - (N_{\mathrm{P_{M1}}} - \sum_{p=1,\ldots,i-1,i+1,\ldots,9}\frac{L_{\mathrm{p}}^{\mathrm{V}}}{N_{\mathrm{M1}}^{\mathrm{Nuc}}})r_{\mathrm{D}}^{\mathrm{Rel}},$$

$$\frac{\mathrm{d}V_{\mathrm{Cplx}}^{\mathrm{cyt}}}{\mathrm{d}t} = k^{\mathrm{Cplx}}Vp_{\mathrm{M1,i}}^{\mathrm{cyt}}\prod_{k}Vp_{\mathrm{M1,k}}^{\mathrm{cyt}} - r^{\mathrm{Rel}} - k_{\mathrm{Rnp}}^{\mathrm{Deg}}V_{\mathrm{Cplx}}^{\mathrm{cyt}},$$

$$\frac{\mathrm{d}D_{\mathrm{Cplx}}^{\mathrm{cyt}}}{\mathrm{d}t} = k^{\mathrm{Cplx}}Vp_{\mathrm{M1,9}}^{\mathrm{cyt}}\prod_{k}Vp_{\mathrm{M1,k}}^{\mathrm{cyt}} - r_{\mathrm{D}}^{\mathrm{Rel}} - k_{\mathrm{Rnp}}^{\mathrm{Deg}}D_{\mathrm{Cplx}}^{\mathrm{cyt}}.$$

Continuous production of influenza A virus

This chapter provides additional information on the models for DIP growth during continuous virus production and simulations thereof.

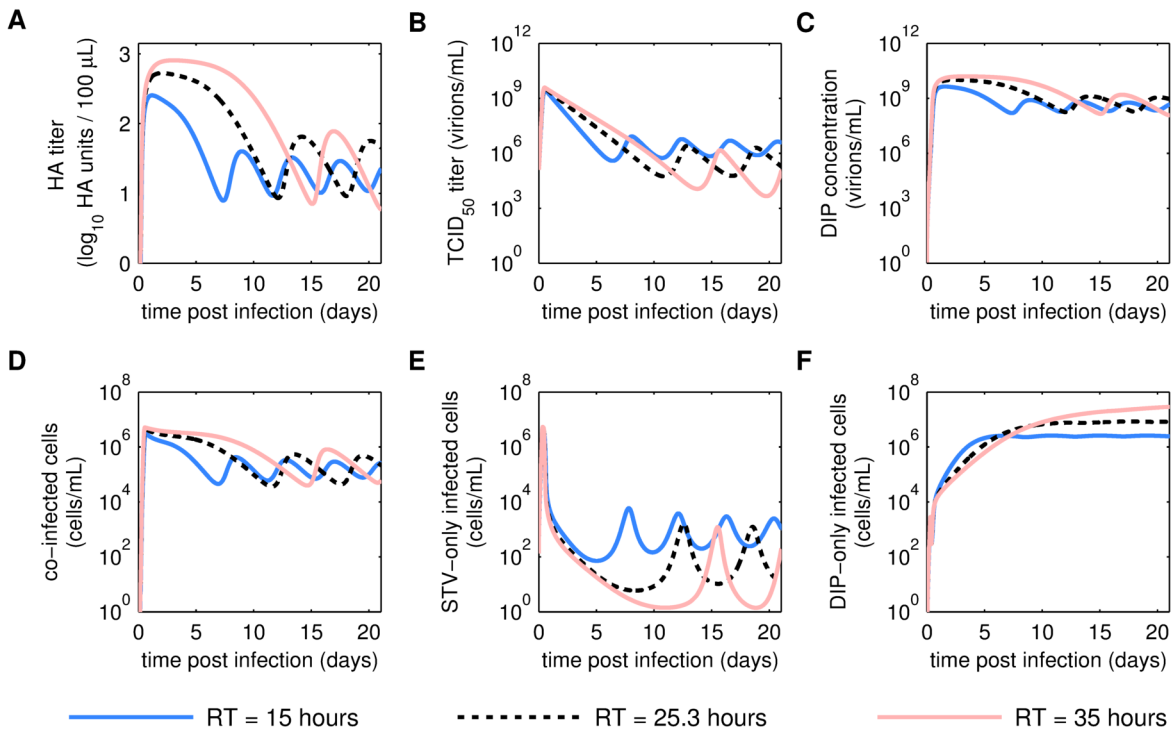## C.1. Influence of residence time on oscillations

Figure C.1.: Simulation of continuous influenza virus production at three different residence times (RTs) neglecting virus degradation. Dynamics of total and infectious virus titers, expressed as HA titer (A) and TCID$_{50}$ titer (B), respectively, as well as concentration of defective interfering particles (DIPs) (C), and concentrations of sub-populations of infected cells, namely co-infected (D), STV-only infected (E) and DIP-only infected (D) cells for a simulated infection at MOI 0.025. Parameters were set according to Table 4.2 except that $k_{V}^{Deg} = 0$. Dependent on the RT, the flow rate of fresh medium from the medium reservoir to the virus bioreactor F_{FM} and the cell concentration in the feed T_{in} were adjusted according to Equation (3.3.11) and Equation (3.3.4), respectively (see Section 3.3.1). Colors according to legend.
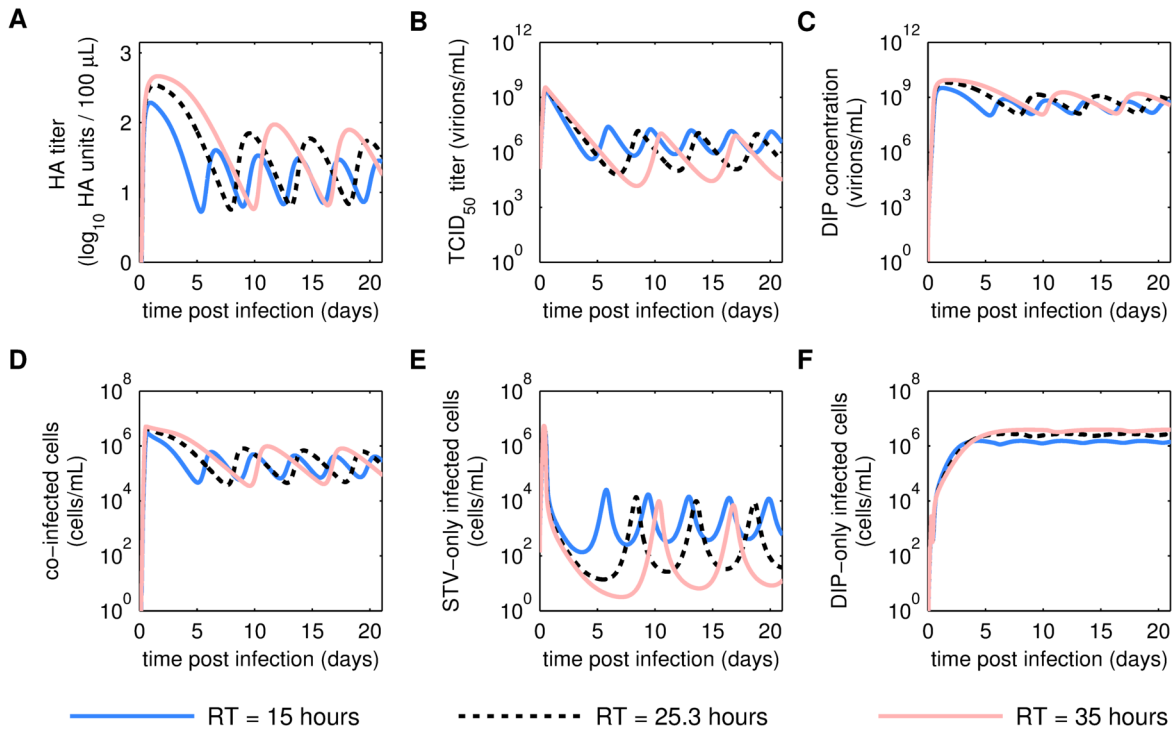
Figure C.2.: Simulation of continuous influenza virus production at three different residence times (RTs) excluding growth of DIP-only infected cells. Dynamics of total and infectious virus titers, expressed as HA titer (A) and $TCID_{50}$ titer (B), respectively, as well as concentration of defective interfering particles (DIPs) (C), and concentrations of sub-populations of infected cells, namely co-infected (D), STV-only infected (E) and DIP-only infected (D) cells for a simulated infection at MOI 0.025. To exclude growth of DIP-only infected cells, the term μI_d in Equation (3.3.6) is neglected. Parameters were set according to Table 4.2. Dependent on the RT, the flow rate of fresh medium from the medium reservoir to the virus bioreactor F_FM and the cell concentration in the feed T_in were adjusted according to Equation (3.3.11) and Equation (3.3.4), respectively (see Section 3.3.1). Colors according to legend.
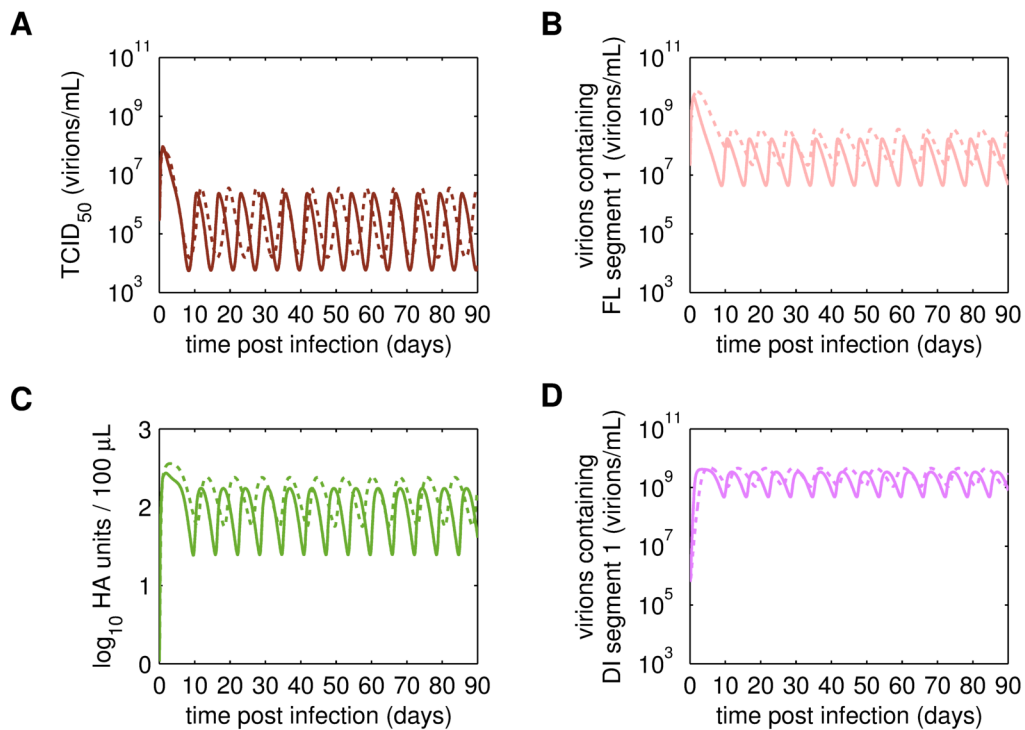
C.2. Model analysis

Figure C.3.: Dynamics of viral sub-populations of A/PR/8/34-delS1(1) produced by MDCK.SUS2 cells in a parallel continuous bioreactor system at residence times of 22 h and 36 h over 90 days. Time courses of infectious STVs (A), FL S1-containing virions (B), sum of all viral sub-populations in $\log_{10}$ HA units/100 μL (C), and DI S1-containing virions (D) are shown for residence times of 22 h (solid lines) and 36 h (dashed lines). The continuous culture was started at 23.4 h p.i.
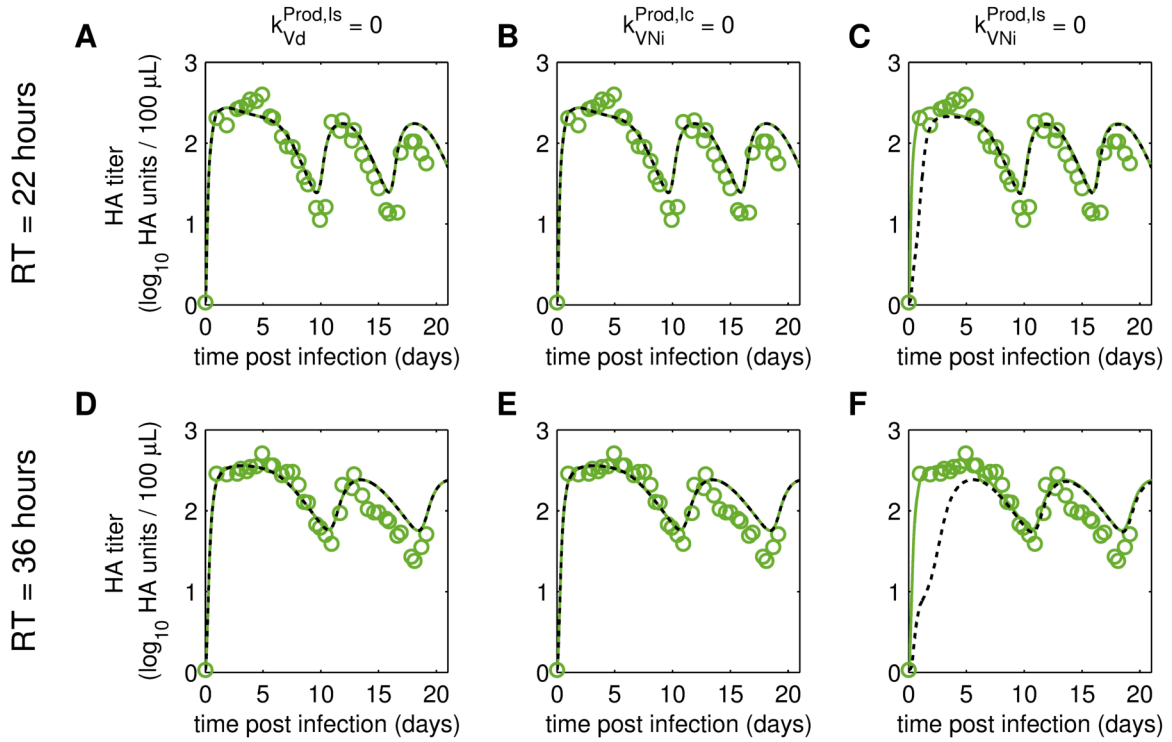
Figure C.4.: Dynamics of the HA titer produced in parallel continuous cultures of MDCK.SUS2 cells infected by A/PR/8/34-delS1(1) at residence times (RTs) of 22 h and 36 h in response to exclusion of different virus production rates. HA titer measurements (open circles), original model fit (solid line) and model simulations (dashed lines) are shown in case of (A, D) the *de novo* generation rate of DIPs by STV-only infected cells $k_{\mathrm{Vd}}^{\mathrm{Prod,Is}}$ is zero, (B, E) the rate of NIP production by co-infected cells $k_{\mathrm{V_{Ni}}}^{\mathrm{Prod,Ic}}$ is zero and (C, F) the rate of NIP production by STV-only infected cells $k_{\mathrm{V_{Ni}}}^{\mathrm{Prod,Is}}$ is zero, for RT 22 h (upper panel) and RT 36 h (lower panel), respectively. For the different simulation scenarios the remaining parameters were fixed according to the values in Table 4.3. For both, experiment and model simulations, the continuous culture was started at 23.4 h p.i.

Table C.1.: Local sensitivities of parameter estimates and initial conditions of the model for production of A/PR/8/34-delS1(1) in continuous cultures of MDCK.SUS2 cells at residence times of 22 h and 36 h, raw values and further analysis in addition to Figure 4.27.

Parameter		RT 22 h		RT 36 h	
		Value	LS (%)	Value	LS (%)
μ^{a}	(h^{-1})	0.0454	0.0052	0.0278	0.0074
D^{a}	(h^{-1})	0.0454	2.1726	0.0278	0.8996
$k_{\text{S}}^{\text{Inf}}$	$(\text{ml/(virion} \cdot \text{h}))$	1.59×10^{-7}	0.0111	5.38×10^{-8}	0.0121
$k_{\text{D}}^{\text{Inf}}$	$(\text{ml/(virion} \cdot \text{h}))$	2.32×10^{-10}	0.0375	7.96×10^{-11}	0.1166
k^{Apo}	(h^{-1})	0.008	0.0111	0.003	0.0039
$k_{\text{Vs}}^{\text{Prod}}$	$(\text{virions/(cell} \cdot \text{h}))$	2.51	0.0265	4.12	0.0447
$k_{\text{Vd}}^{\text{Prod,Ic}}$	$(\text{virions/(cell} \cdot \text{h}))$	203	0.0985	177	0.1194
$k_{\text{Vd}}^{\text{Prod,Is}}$	$(\text{virions/(cell} \cdot \text{h}))$	10^{-5}	3.83×10^{-9}	1.13×10^{-9}	2.14×10^{-19}
$k_{\text{V}_{\text{Ni}}}^{\text{Prod,Ic}}$	$(\text{virions/(cell} \cdot \text{h}))$	4.91×10^{-16}	1.16×10^{-23}	1.41×10^{-8}	1.71×10^{-21}
$k_{\text{V}_{\text{Ni}}}^{\text{Prod,Is}}$	$(\text{virions/(cell} \cdot \text{h}))$	120	0.0074	173	0.0242
$k_{\text{Vs}}^{\text{Deg}}$	(h^{-1})	1.58×10^{-7}	4.45×10^{-9}	0.07	0.0383
$k_{\text{V}}^{\text{Deg}}$	(h^{-1})	3.82×10^{-27}	0	2.02×10^{-9}	1.63×10^{-15}
T_{in}^{b}	(cells/ml)	1.13×10^{6}	0.1536	1.13×10^{6}	0.1496
T_0	(cells/ml)	1.80×10^{6}	0.0321	1.37×10^{6}	0.0640
V_{s0}^{c}	(virions/ml)	3.16×10^{5}	5.06×10^{-5}	3.16×10^{5}	5.99×10^{-5}
V_{d0}^{c}	(virions/ml)	6.41×10^{5}	8.33×10^{-4}	8.06×10^{5}	0.0033
$V_{\text{Ni0}}^{\text{c}}$	(virions/ml)	2.05×10^{7}	1.59×10^{-4}	2.03×10^{7}	1.40×10^{-4}

[a] Although D was estimated from experimental measurements and was fixed during model fitting, the sensitivity of D expresses the sensitivity of the system toward perturbations in flow rates. For continuous cultivation we usually assume $\mu = D$. Here, sensitivity of the two model parameters was evaluated individually.
[b] T_{in} is assumed to be constant during the continuous cultivation. Its local sensitivity expresses how strongly the system responds to perturbations of the cell concentration in the cell bioreactor, see Equation (3.3.4), Section 3.3.1.
[c] Local sensitivity of initial concentrations of STVs, DIPs and NIPs expresses sensitivity of the system toward seed virus composition.
RT - residence time, LS - local sensitivity, represents the normalized change in the model output in response to a perturbation of the parameter or initial condition by $+1\%$ (see Equation (2.3.4) and Equation (2.3.5)).
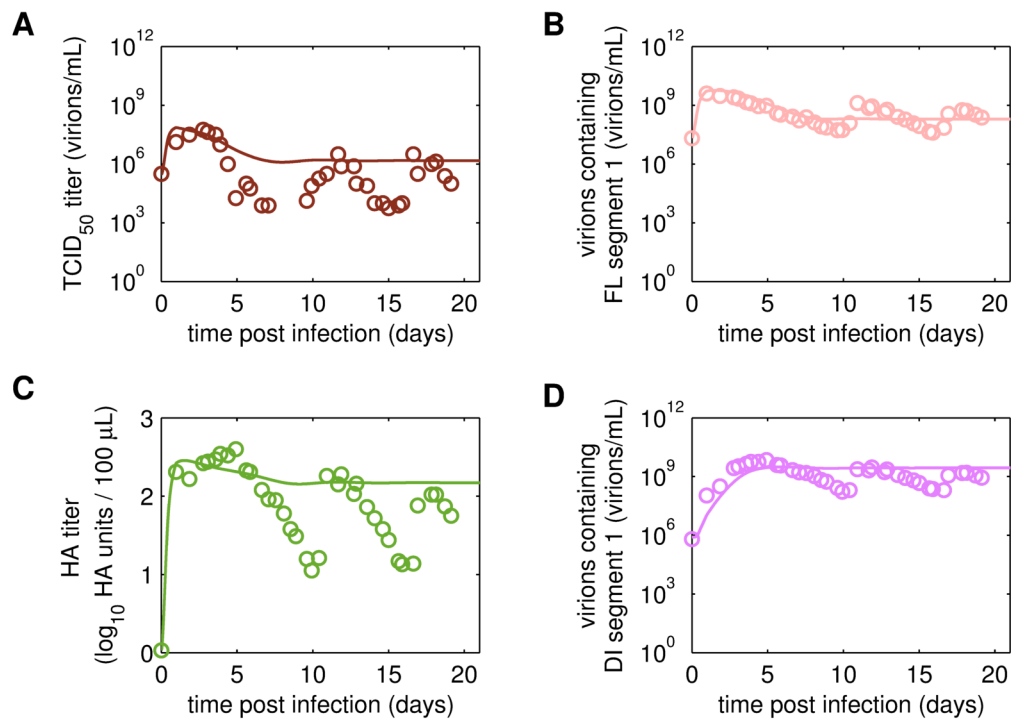
Figure C.5.: Prediction for the dynamics of viral sub-populations of A/PR/8/34-delS1(1) produced by MDCK.SUS2 cells in a parallel continuous bioreactor system at RT 22 h. Experimental data obtained for RT 22 h (open circles) and predictions (lines) using the model fitted previously to the data of RT 36 h with the parameter values in Table 4.3, except that $\mu = D = 0.0454\,h^{-1}$. Shown are time courses of infectious STVs (A), FL S1-containing virions (B), sum of all viral sub-populations as HA titer (C), and DI S1-containing virions (D). For both, experiment and model simulations, the continuous culture was started at 23.4 h p.i.
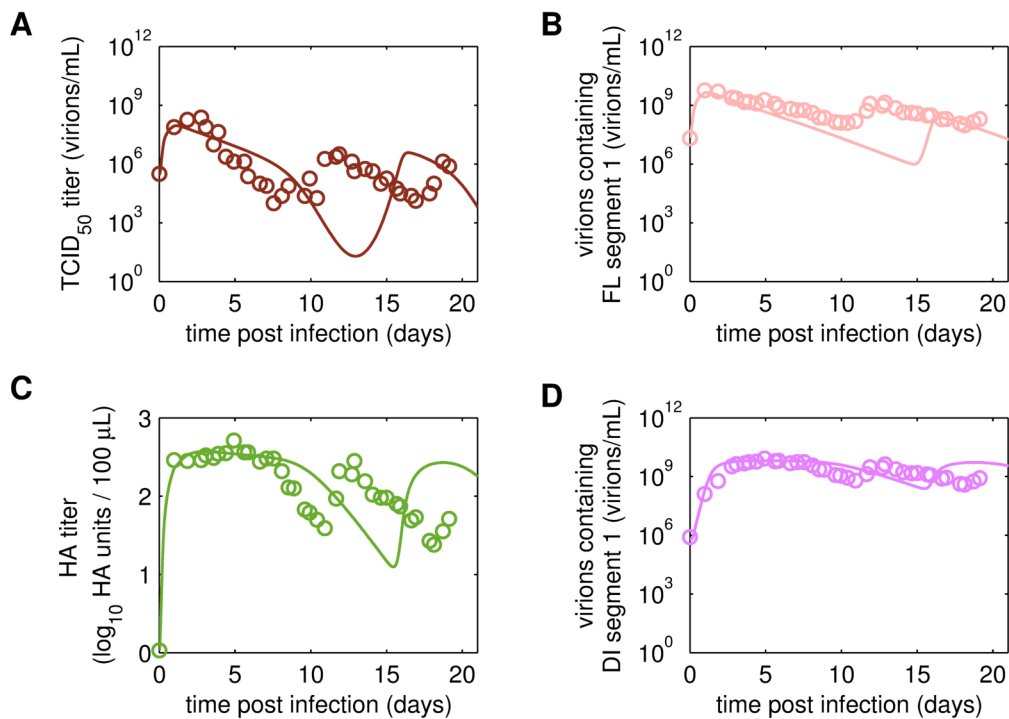
Figure C.6.: Prediction for the dynamics of viral sub-populations of A/PR/8/34-delS1(1) produced by MDCK.SUS2 cells in a parallel continuous bioreactor system at RT 36 h. Experimental data obtained for RT 36 h (open circles) and predictions (lines) using the model fitted previously to the data of RT 22 h with the parameter values in Table 4.3, except that $\mu = D = 0.0278\,h^{-1}$. Shown are time courses of infectious STVs (A), FL S1-containing virions (B), sum of all viral sub-populations as HA titer (C), and DI S1-containing virions (D). For both, experiment and model simulations, the continuous culture was started at 23.4 h p.i.